Development and Application of Uranium X-ray Absorption Spectroscopy to Natural Actinide Titanates

Lucy M. Mottram

Immobilisation Science Laboratory

Department of Materials Science and Engineering

University of Sheffield

A thesis submitted in partial fulfilment of the requirements for the degree of Doctor of Philosophy

January 2023

Abstract

The performance of any potential wasteform for actinide waste arising from civil or military nuclear uses is determined by the ability of the wasteform to immobilise actinides throughout its lifetime. The mobility of actinides, such as U and Pu, is dependent on speciation; higher oxidation states are more mobile. As experiments relevant to the timescale of the lifetime of a wasteform – on the order of hundreds of thousands to millions of years – cannot be practically undertaken, predictions of long-term behaviour of potential actinide wasteforms are based on the properties of analogues. These are uranium minerals, provenanced from well-characterised geological formations, with known geological ages, often 1 billion years old or more. Understanding the speciation of U in these minerals, and how it has evolved over such timescales, opens possibilities to predicting the performance of synthetic wasteforms designed for actinide immobilisation.

X-ray absorption spectroscopy (XAS) is an element-specific measurement that enables the characterisation of U speciation and local chemical environment. In this Thesis, a range of different U XAS measurements have been evaluated in their ability to identify the chemistry of natural U minerals, using a set of U reference compounds and two natural mineral analogues of synthetic titanate wasteforms. The capability of novel laboratory XAS to characterise U speciation in samples and concentrations relevant to synthetic actinide wasteforms, and to investigate the speciation of other elements and materials relevant to nuclear waste disposal, has been established. The application of U M_4-edge M_β HERFD XAS and U L_3-edge XAS to investigate U speciation in a mineral calciopyrochlore sample have enabled the first reported direct characterisation of U^{5+} in a natural mineral. The application of spatially resolved micro-focus X-ray techniques has underpinned the mechanism by which stable U^{4+} brannerite is oxidised to U^{6+} by hydrothermal alteration processes. Combined, these studies have advanced understanding of the capabilities of XAS analysis and demonstrated its suitability and potential for advancing fundamental understanding of U speciation and alteration within mineral analogues for actinide waste.

Acknowledgements

There are many people who I would like to thank, all of whom played an important role in helping me get to the end of my PhD. Most of them, knowing me well by now, would not be surprised that I struggled to write a quick, succinct and coherent thank you, on the day of my submission - but that's what corrections are for! All of them have my heartfelt thanks for their support and understanding throughout my PhD.

Firstly, my supervisors: Professor Claire Corkhill, Professor Neil Hyatt and Dr Martin Stennett. Thank you Claire for taking me on and getting me through the difficult write up process to submission, and thank you Neil for starting me down this path and offering me so many opportunities, changing supervisor wasn't part of the plan but I now feel very lucky that I was able to work with and learn so much from both of you. Thank you Martin for teaching me the ways of XAS, and making it possible for me to get anything done in the lab.

I was so lucky to have had two excellent postdocs helping me: Dr Luke Townsend and Dr Laura Gardner. Luke, thank you for all of your EXAFS help and spending many hours reading my thesis. Laura, thank you for helping me find some semblance of order while writing up, keeping me on track, motivating me and for being there whenever I needed it.

I would like to thank all of the ISL for their friendship and support, especially Malin Christian Dixon-Wilkins, Liam Harnett and Hannah Smith, who were always there to provide a sympathetic ear, make me smile or help me out in the lab.

I would also like to thank the beamline scientists - without whom the majority of my thesis would not exist! Thank you to Dr Bruce Ravel, Dr Ryan Tappero, Dr Sarah Nicholas, Dr Giannantonio Cibin, Dr Steven Parry, Dr Fred Mosselmans, Shu Hayama, Dr Kristina Kvashnina, Dr Sergei Butorin, Dr Tatiana Poliakova, Anastasiia Smirnova and Jurij Galanzew. Special thanks to Bruce, Ryan and Sarah for being such welcoming hosts and for many hours of board games at the beamline!

My very patient friends: Rachael, Amie, Lucy, Maddie, Rebecca, Lucie, Chloe, James, Rob, Emma, James and Aileen, who put up with me vanishing into my PhD for months or years at a time, and welcomed me back when I would sporadically return - thank you and I look forward to seeing more of you all soon!

The Unicorns - thank you for being the most positive and friendly team, becoming my friends and giving me two precious hours each week free from stress, worry or writing up.

Lauren and Kieran - thank you for sharing your friendship, home, food and cats with me, and for keeping Fred company while I was busy writing!

A very special thank you to Fred, for all of your love, support, encouragement, the lifts home late at night and the hot meals delivered to the library, I am so grateful for all of it.

Finally, my family: Rolo, Mum and Dad, thank you for all your support for so many years leading up to this point and all the phone calls to get me started, kept me going and always make me laugh.

List of Abbreviations

BESSY-II	Berlin Electron Storage Ring Society for Synchrotron Radiation-II
BNL	Brookhaven National Laboratory
BSE	Backscattered Electrons
BVS	Bond Valance Sum
DMO	Domestic Microwave Oven
DLS	Diamond Light Source
DRS	Diffuse Reflectance Spectroscopy
DTA	Differential Thermal Analysis
EDX	Energy-Dispersive X-ray Spectroscopy
EELS	Electron Energy Loss Spectroscopy
EPMA	Electron Probe MicroAnalysis
ESRF	European Synchrotron Radiation Facility
EXAFS	Extended X-ray Absorption Fine Structure
FT	Fourier Transform
FWHM	Full Width at Half Maximum
GDF	Geological Disposal Facility
HERFD	High Energy Resolution Fluorescence Detected
HLW	High Level Waste
HZDR	Helmholtz-Zentrum Dresden Rossendorf Laboratory

ILW	Intermediate Level Waste
ITTFA	Iterative Target-Transformation Factor Analysis
LA-ICP-MS	Lase Ablation Inductively Coupled Plasma Mass Spectrometer
LCF	Linear Combination Fitting
LLW	Low Level Waste
MEE	Multi-Electron Excitation
NSLS	National Synchrotron Light Source
NSLS-II	National Synchrotron Light Source-II
PCA	Principal Component Analysis
PEG	Polyethylene Glycol
PFY	Partial Fluorescence Yield
PSI	Paul Scherrer Institute
pXRD	powder X-ray Diffraction
QPA	Quantitative Phase Analysis
SBCA	Spherically Bent Crystal Analyser
SDD	Silicon Drift Detector
SE	Secondary Electron
SEM	Scanning Electron Microscopy
SLS	Swiss Light Source
SNF	Spent Nuclear Fuel

TFY	Total Fluorescence Yield
TGA	Thermogravimetric Analysis
µEXAFS	microfocus Extended X-ray Absorption Fine Structure
µXANES	microfocus X-ray Absorption Near-Edge Spectroscopy
µXAS	microfocus X-ray Absorption Spectroscopy
µXRD	microfocus X-ray Diffraction
µXRF	microfocus X-ray Fluorescence
VLLW	Very Low-Level Waste
XANES	X-ray Absorption Near-Edge Spectroscopy
XFM	X-ray Fluorescence Microscope
XRD	X-ray Diffraction
XRF	X-ray Fluorescence Spectroscopy
XRM	X-ray Microscopy

Publications

Publications

- A.S. Yorkshire, M.C. Stennett, B. Walkley, J.L. Provis, L.T. Townsend, L.T. Haigh, N.C. Hyatt, L.M. Mottram and C.L. Corkhill, Spectroscopic identification of Ca-bearing uranyl silicates formed in C-S-H systems, Scientific Reports – IN REVIEW

- C.L. Corkhill, C. Mann, J.R. Eskelsen, D.N. Leonard, L.M. Mottram, M.C. Stennett, J.M.S. Ayling, C.L. Thorpe, M.R. Cole, S. Nicholas, R. Tappero, E.M. Pierce, Surface interfacial analysis of simulant high level nuclear waste glass dissolved in synthetic cement solutions, NPJ Mater. Degrad. 6(1) (2022) 14.

- H. Ding, C. Gausse, M.C.D. Wilkins, L.M. Mottram, M.C. Stennett, D. Grolimund, R. Tappero, S. Nicholas, S.K. Sun, T. Shiba, C. Paraskevoulakos, N.C. Hyatt, C.L. Corkhill, Chemical characterisation of degraded nuclear fuel analogues simulating the Fukushima Daiichi nuclear accident, NPJ Mater. Degrad. 6(1) (2022) 13.

- A.S. Yorkshire, M.C. Stennett, B. Walkley, S.E. O'Sullivan, L.M. Mottram, D.J. Bailey, J.L. Provis, N.C. Hyatt, C.L. Corkhill, Spectroscopic evaluation of U-VI-cement mineral interactions: ettringite and hydrotalcite, J. Synchrot. Radiat. 29 (2022) 89-102.

- M.E. Seddon-Ferretti, L.M. Mottram, M.C. Stennett, C.L. Corkhill, N.C. Hyatt, HERMES - a GUI-based software tool for pre-processing of X-ray absorption spectroscopy data from laboratory Rowland circle spectrometers, J. Synchrot. Radiat. 29 (2022) 276-279.

- M.C.D. Wilkins, L.M. Mottram, E.R. Maddrell, M.C. Stennett, C.L. Corkhill, K.O. Kvashnina, N.C. Hyatt, Synthesis, Characterization, and Crystal Structure of Dominant Uranium(V) Brannerites in the $UTi_{2-x}Al_xO_6$ System, Inorg. Chem. 60(23) (2021) 18112-18121.

- H. Ding, M.C.D. Wilkins, L.M. Mottram, L.R. Blackburn, D. Grolimund, R. Tappero, S.L. Nicholas, S.K. Sun, C.L. Corkhill, N.C. Hyatt, Chemical state mapping of simulant Chernobyl lava-like fuel containing material using micro-focused synchrotron X-ray spectroscopy, J. Synchrot. Radiat. 28 (2021) 1672-1683.

- S.K. Sun, L.M. Mottram, N.C. Hyatt, On the existence of the compound "$Ce_3NbO_{7+\delta}$" prepared under air atmosphere, J. Rare Earths 39(5) (2021) 596-599.

- H. Ding, M.C.D. Wilkins, C. Gausse, L.M. Mottram, S.K. Sun, M.C. Stennett, D. Grolimund, R. Tappero, S. Nicholas, N.C. Hyatt, C.L. Corkhill, Safely probing the chemistry of Chernobyl nuclear fuel using micro-focus X-ray analysis, J. Mater. Chem. A 9(21) (2021) 12612-12622.

- S.M. Thornber, L.M. Mottram, A.R. Mason, P. Thompson, M.C. Stennett, N.C. Hyatt, Solubility, speciation and local environment of chlorine in zirconolite glass-ceramics for the immobilisation of plutonium residues, RSC Adv. 10(54) (2020) 32497-32510.

- M. Ahmadzadeh, A. Scrimshire, L.M. Mottram, M.C. Stennett, N.C. Hyatt, P.A. Bingham, J.S. McCloy, Structure of $NaFeSiO_4$, $NaFeSi_2O_6$, and $NaFeSi_3O_8$ glasses and glass-ceramics, Am. Miner. 105(9) (2020) 1375-1384.

- L.M. Mottram, M.C. Stennett, S.K. Sun, N.C. Hyatt, Laboratory Based X-ray Absorption Spectroscopy of Iron Phosphate Glasses for Radioactive Waste Immobilisation: A Preliminary Investigation, IOP Conference Series: Materials Science and Engineering 818 (2020) 012020.

- L.M. Mottram, M.C.D. Wilkins, L.R. Blackburn, T. Oulton, M.C. Stennett, S.K. Sun, C.L. Corkhill, N.C. Hyatt, A Feasibility Investigation of Laboratory Based X-ray Absorption Spectroscopy in Support of Nuclear Waste Management, MRS Adv. 5(1-2) (2020) 27-35.

- L.M. Mottram, S. Cafferkey, A.R. Mason, T. Oulton, S.K. Sun, D.J. Bailey, M.C. Stennett, N.C. Hyatt, A feasibility investigation of speciation by Fe K-edge XANES using a laboratory X-ray absorption spectrometer, J Geosci. 65(1) (2020) 27-35.

- L.M.Mottram, D.Z.C. Martin, N. Reeves-McLaren, R. Boston, Low-temperature crystallization of $La_{0.15}Sr_{0.775}TiO_3$ using ionic liquids, J. Am. Ceram. Soc. 101(10) (2018) 4468-4471.

Conference presentations

- Royal Society of Chemistry Spectroscopic Methods in Radiochemistry Research – Manchester, July 2022

- Mineralogical Society of UK & Ireland Environmental Mineralogy Group Research in Progress Meeting: Waste to Resources – Bristol, June 2022

Table of Contents

1. Introduction

Implementing nuclear fission and other renewable energy alternatives is of high importance in light of the eventual exhaustion of fossil fuel reserves and the current climate crisis. Regardless of the future of nuclear fission power, the UK already has legacy waste from 70 years of using nuclear power, including the largest inventory of separated civil Pu in the world, and waste still to be produced from active plants until the end of their lifecycle.

Radioactive waste, largely arising from civil nuclear fission energy generation and associated operations, can be categorised into several groups including: high level waste (HLW); intermediate level waste (ILW); low level waste (LLW) and; very low level waste (VLLW). High level wastes include those materials that contain long-lived (thousands to hundreds of thousands of years) fission products and are heat generating. One type of HLW is spent nuclear fuel (SNF), which consists mainly of the original UO_2 fuel, fission products, plutonium (Pu) and other transuranics produced by neutron capture. Several uranium (U) and Pu isotopes have exceptionally long half-lives, 4.47×10^9, 7.04×10^8, and 2.41×10^4 years for U-238 U-235 and Pu-239 respectively [1], and have significant radioactivity. Until recently, SNF was reprocessed for reuse in the nuclear fuel cycle, where U and Pu were separated from the fission products, the latter being immobilised in a borosilicate glass. Policy decisions have meant that the separated Pu, and much of the reprocessed U, has not been reused. This material is currently in storage awaiting either future re-use or, if UK Government policy is amended, disposal.

It is current UK Government policy that HLW will be managed, in the long-term, by disposal in a geological disposal facility (GDF). In this facility, the radioactive waste will be isolated from the biosphere for long enough to ensure that it has undergone sufficient radioactive decay such that it is no longer hazardous. This requires a wasteform that is resistant to radiation damage and leaching by groundwater, that is chemically compatible with the waste, chemically flexible enough to accommodate contaminants from the waste stream and there should be confidence that these properties will persist over the lifetime of the wasteform. To confidently predict properties over such long-time scales, there must be good understanding of the chemistry of the wasteform and there should be natural analogues available.

Should a decision be taken by UK Government to dispose of the Pu inventory in a GDF, titanate ceramics have been identified as group with potential as wasteforms for this material (including its U daughter products) due to their high leaching and radiation resistance and the prevalence of actinide-bearing natural titanate mineral analogues. The characterisation of theses natural analogues provides underpinning evidence and understanding to predict the properties of potential Pu-wasteforms, and especially the speciation of the actinide within the wasteform, which is the key control on actinide solubility and subsequent mobility in the underground environment. X-ray absorption spectroscopy (XAS) is a unique, element-specific technique that can be used to characterise actinide oxidation state, chemical coordination and also short-range structure.

This Thesis aims to develop an understanding, and evaluation, of the capabilities of different XAS techniques to investigating samples relevant to nuclear waste disposal; additionally, to probe the role of U^{5+} and U^{6+} in charge compensation and alteration of natural actinide titanates. This Thesis was prepared in alternative paper format, whereby the results chapters consist of work that have either been prepared for publication or have been published.

Chapter 2 is a literature review of relevant topics that are common to all of the results chapters (Chapters 4-7). Since the results chapters have each been prepared with their own introductions and focused literature reviews, to avoid unnecessary repetition, Chapter 2 presents a brief literature review that refers to the individual introductions of Chapters 4-7. Chapter 2 introduces the concept of a GDF, the property requirements for an actinide wasteform and the advantages of using analogue materials. XAS measurements are introduced; however, how these are achieved is discussed thoroughly in Chapter 3. Chapter 2 then describes the pyrochlore super-group and brannerite minerals, their structures and properties. There is a discussion of all literature available on the use of U XAS to investigate U speciation in synthetic and natural brannerites and U titanate pyrochlores. One of the gaps in literature identified in Chapter 2 is the use of spatially resolved X-ray techniques to investigate U speciation and alteration in U titanate mineral analogue samples. A discussion of papers that have used these techniques to study synthetic U titanates or relevant natural samples is presented accordingly.

Chapter 3 describes the materials and methods used. This includes detailed descriptions of X-ray sources and how different XAS techniques are achieved.

Chapter 4 consists of a draft publication that describes an investigation into the capabilities of different U XAS experiments to provide information about U speciation using a comprehensive set of U reference compounds. This includes data collected at different absorption edges, using different techniques and different X-ray sources. This Chapter presents comparisons between different data sets and evaluates the information that was obtained from the data, in addition to the benefits and limitations each measurement type. The details of the draft publication are as follows:

Comprehensive evaluation of X-ray absorption spectroscopy approaches and instrumentation to derive uranium speciation by L. M. Mottram, L. T. Townsend, D. J. Bailey, A. S. Yorkshire, K. Kvashnina, J. F. W. Mosselmans, B. Ravel, M. C. Stennett, N. C. Hyatt and C. L. Corkhill. Prepared for submission to Journal of Synchrotron Radiation.

Author contributions: **LMM** – preparation of reference compounds for laboratory U L_3-edge XAS measurements, preparation of reference compounds for U L_3-edge $L_{\alpha1}$ HERFD XAS, collection of laboratory U L_3-edge XAS data, U L_3-edge transmission XAS data at B18, collection of U L_3-edge $L_{\alpha1}$ HERFD XAS data at I20-scanning, all data analysis, draft writing and editing; **LTT** – provided support for EXAFS data analysis and editing; **DJB** – preparation of reference compounds for U L_3-edge $L_{\alpha1}$ HERFD XAS, support with collection of U L_3-edge transmission XAS data at B18; **ASY** - support with collection of U L_3-edge transmission XAS data at B18; **KK** - Operation of BM20 beamline and U M_4-edge M_β XANES data collection; **JFWM** - Operation of I20-scanning beamline and U L_3-edge $L_{\alpha1}$ XANES data collection; **BR** – Operation of X23A2 beamline and U L_3-edge XAS data collection; **MCS** – preparation of reference compounds for U L_3-edge transmission, L_3-edge $L_{\alpha1}$ HERFD and U M_4-edge M_β XAS measurements, provided support with collection of U L_3-edge transmission, L_3-edge $L_{\alpha1}$ HERFD and U M_4-edge M_β XAS data; **NCH** - acquired funding, provided supervision, support with data collection of U L_3-edge laboratory, U L_3-edge transmission and L_3-edge $L_{\alpha1}$ HERFD XAS data, and support with analysis; and **CLC** – provided supervision, support in data collection of U L_3-edge transmission and U M_4-edge M_β XAS data and support in analysis and editing.

Chapter 5 is a draft publication that describes the application of spatially resolved X-ray techniques, including micro-focus XAS, to investigate U speciation and alteration in a heavily altered, metamict U titanate mineral, analogous to synthetic U titanate wasteforms. The study is the first application of these techniques to investigate U speciation in a natural actinide-containing mineral analogue and demonstrates the suitability of these techniques. The majority of U in the U mineral phase was found to be speciated as U^{6+} uranyl. The details of the draft publication are as follows:

X-ray absorption micro-spectroscopy analysis of uranium in a natural analogue for plutonium ceramic wasteforms by L. M. Mottram, L. T. Townsend, H. Ding, R. Tappero, S. L. Nicholas, M. C. Stennett, N. C. Hyatt and C. L. Corkhill. Prepared for submission to Nature Material Degradation.

Author contributions: **LMM** – all data collection, analysis of all data, draft writing and editing; **LTT** – provided support for µEXAFS data analysis and editing; **HD** – provided support for all data collection; **RT** – Operation of XFM beamline, data collection; **SLN** – Operation of XFM beamline, data collection; **MCS** – prepared reference compounds for measurement, provided support for all data collection; **NCH** – acquired funding, provided supervision, support in data collection and analysis; and **CLC** – provided supervision, support in data collection and analysis, editing.

Chapter 6 consists of a draft publication that describes the investigation of U speciation in a metamict calciopyrochlore mineral sample containing U and Ti. Data and analysis from multiple U XAS techniques were discussed. The data and analysis presented in this paper are the first known direct characterisation of U^{5+} in a mineral, and the first U^{5+} natural mineral that contains U^{4+}, U^{5+} and U^{6+}. This is of particular significance due to the age of the sample, of approximately one billion years old. The details of the draft publication are as follows:

Direct characterisation of a 1 billion-year old pentavalent uranium mineral by L. M. Mottram, L. T. Townsend, L. J. Gardner, K. Kvashnina, J. F. W. Mosselmans, M. C. Stennett, N. C. Hyatt and C. L. Corkhill. Prepared for submission, in the first instance, to Nature Geoscience.

Author contributions: **LMM** – preparation of sample for U L_3-edge HERFD XAS, SEM/EDX data collection, U L_3-edge XAS data collection, U L_3-edge HERFD data collection, EPMA data collection and all data analysis, draft writing and editing **LTT** - provided support for XANES data analysis, EXAFS data analysis and editing; **LJG** – editing and formatting; **KK** – Operation of BM20 beamline and U M_4-edge $M\beta$ XANES data collection; **JFWM** – Operation of I20-scanning beamline and data collection; **MCS** – preparation of sample for SEM, preparation of sample and reference compounds for U L_3 edge XAS and U M_4-edge HERFD XAS, preparation of reference compounds for U L_3-edge HERFD data, provided support for all XAS data collection; **NCH** – preparation of sample for and collection of XRD data, acquired funding, provided supervision, provided support for collection of U L_3-edge XAS, U L_3-edge HERFD XAS data and analysis of SEM, XRD, U L_3 edge XANES and EXAFS data; **CLC** – provided supervision and support for collection of U L_3-edge XAS data, U M_4-edge XAS data and analysis of all data.

Chapter 7 comprises three published papers that describe the development and use laboratory XAS for speciation of elements relevant to HLW materials, including U, Ce and Fe. The details of the publications are as follows:

Chapter 7.1: A Feasibility Investigation of Laboratory Based X-ray Absorption Spectroscopy in Support of Nuclear Waste Management by L. M. Mottram, M. C. Dixon Wilkins, L. R. Blackburn, T. Oulton, M. C. Stennett, S. K. Sun, C. L. Corkhill and N. C. Hyatt. *MRS Advances*, 5, 27 – 35 (2020)

This paper describes the feasibility of measuring Ce and U L_3-edge XAS data on a laboratory instrument, with data collected from Ce and U reference compounds and examples of simulant HLW materials, compared to data from synchrotron facilities.

Author contributions: **LMM** – preparation of samples and reference compounds for laboratory XAS, collection of laboratory XAS data, data analysis, draft writing and editing; **MCDW** – Synthesis of samples, preparation of reference compounds for laboratory XAS; **LRB** – synthesis of samples; **TO** – support with collection of laboratory XAS data; **MCS** – preparation of samples and reference compounds for synchrotron measurement, collection of XAS data at synchrotron; **SKS** - support with synthesis of samples; **CLC** – provided funding,

editing; **NCH** – provided funding, supervision, collection of laboratory XAS data, collection of synchrotron XAS data, provided support with data analysis, editing.

Chapter 7.2: A feasibility investigation of speciation by Fe K-edge XANES using a laboratory X-ray absorption spectrometer by L. M. Mottram, S. Cafferkey, A. R. Mason, T. Oulton, S. Sun, D. J. Bailey, M. C. Stennett, and N. C. Hyatt. *Journal of Geosciences,* 65, 27 – 35 (2020).

This paper describes an initial investigation into characterising Fe speciation using laboratory XAS, where Fe K-edge data collected from Fe reference compounds at a synchrotron facility and on a laboratory instrument are compared.

Author contributions: **LMM** – preparation of reference compounds for laboratory XAS, collection of laboratory XAS data, data analysis, draft writing and editing; **SC** – preparation of reference compounds for laboratory XAS, collection of laboratory XAS data; **ARM** – collection of synchrotron XAS data; **TO** – support with collection of laboratory XAS data; **SKS** – preparation of samples; **DJB** – support with collection of laboratory XAS data; **MCS** – preparation of samples and reference compounds for synchrotron measurement, collection of synchrotron XAS data; **NCH** – provided funding, supervision, collection of laboratory XAS data, collection of synchrotron XAS data, provided support with data analysis, editing.

Chapter 7.3 Laboratory Based X-ray Absorption Spectroscopy of Iron Phosphate Glasses for Radioactive Waste Immobilisation: A Preliminary Investigation by L. M. Mottram, M. C. Stennett, S. K. Sun and N. C. Hyatt. *IOP Conference Series: Materials Science and Engineering*, 818, 012020 (2020).

This paper describes the further development of the use of laboratory spectrometers to investigate Fe speciation in samples relevant to nuclear waste disposal. Fe XAS K-edge data were collected at a synchrotron facility and using a laboratory spectrometer from Fe reference compounds and iron phosphate glass samples. The data and subsequent analysis from each measurement were compared.

Author contributions: **LMM** – preparation of reference compounds for laboratory XAS, collection of laboratory XAS data, data analysis, draft writing and editing; **MCS** – preparation

of samples and reference compounds for synchrotron measurement, collection of synchrotron XAS data; **SKS** – preparation of samples; **NCH** – provided funding, supervision, collection of laboratory XAS data, collection of synchrotron XAS data, provided support with data analysis, editing.

2. Literature review

2.1. Wasteforms for actinides

The principle of geological disposal for nuclear waste is to isolate radioactive waste from the biosphere until the radioactivity of the waste has fallen below a threshold safe level [2]. Isolation of waste will be provided by multiple barriers, the innermost of which is the wasteform in which the waste will be incorporated. High-level waste (HLW) is radioactive waste material that has a high activity (~104-106 TBq m^{-3}) and long half-life [3]; the majority of HLW consists of fission products, and a minor amount of U, Pu and other actinides. The latter three are the subject of this Thesis and the remainder of this Chapter. Due to its radiotoxic nature, HLW requires the most stringent isolation; therefore, there are several property requirements a high-level wasteform must fulfil [4].

To prevent movement of actinides, the wasteform must be chemically compatible with the actinides and any waste stream contaminants, chemically compatible with the other containment barriers, and resistant to dissolution by groundwater [5]. These properties must endure over the lifetime of the wasteform, so the wasteform must also be resistant to radiation damage as this would cause a change in structure, which could be detrimental to dissolution resistance. To confidently predict the properties of potential wasteforms over the lifetime of disposal, samples that contain, and have retained, actinides over millions of years should be studied to inform modelling of wasteform performance [6]. These samples should be as chemically and structurally similar to the synthetic wasteform as possible and are referred to as analogues (for actinide wasteforms these are naturally occurring U and Th minerals). The availability of analogue materials is therefore another important requirement for a potential synthetic wasteform, and for this reason some wasteform compositions have been derived from naturally occurring actinide containing minerals. Two groups of potential actinide wasteforms which have readily available mineral analogues are brannerites and pyrochlores, these are discussed in detail later.

The ability of a wasteform to immobilise actinides is largely dependent on the mobility of the actinide once it becomes dissolved from that wasteform. The mobility of both U and Pu is

intrinsically linked to oxidation state; the uranyl U^{6+} and plutonyl Pu^{6+} speciations are both more mobile than their respective uranate U^{4+} [7] and plutonate Pu^{4+} [8] speciations. Therefore, these lower oxidation states are targeted in potential synthetic wasteforms and, in a geological disposal facility (GDF), the wasteforms must be stored under reducing conditions. Determining the speciation of U within minerals, as analogues for Pu wasteforms, supports understanding of long-term wasteform behaviour in a GDF. In particular, the study of wasteforms that have undergone alteration by water, enables prediction of the lifetime performance of a wasteform. It should be noted, however, that the temperatures that can occur in a GDF are limited to maxima of between 100°C [9] and 200°C due to the requirements of the host geology and barrier materials used [10], while the hydrothermal alteration experienced by mineral analogues tends to occur at higher temperatures (typically between 300 and 500°C).

2.2. Mineral analogues

2.2.1. The pyrochlore super-group

Pyrochlore describes a super-group of minerals [11] with the structure $A_{2-m}B_2X_{6-w}Y_{1-s}$ ($Fd\bar{3}m$) [12], a group within this super group, and also synthetic ceramics with the same structure. Assuming full site occupancy, this simplifies to $A_2B_2X_6Y$ with O usually occupying the X site. The pyrochlore structure is a derivative of the fluorite (AX_2) [13] ($Fm\bar{3}m$) structure and can be described, if idealised, as corner linked BX_6 octahedra which have A-site cations in the interstices (Figure 2.1), these A site cations are 8-fold coordinated, and can be considered as distorted cubic polyhedra [13, 14]. Within the pyrochlore super-group there are several mineral groups; betafite, pyrochlore, roméite, microlite, and elsmoreite [11, 15]. These mineral groups are defined by the dominant valence and cation in the B site (Figure 2.2) [11]. Within these groups minerals are differentiated and named with respect to the A site and Y site dominance, e.g. a mineral with the structure $A_{2-m}B_2X_{6-w}Y_{1-s}$ which contained Na as the dominant A site cation, 5+ as the dominant B site valence, Ta as the dominant 5+ B site cation and OH as the dominant Y site occupant, would be named hydroxynatromicrolite [11]. The two different cation sites can accommodate a variety of different cations on the A and B site

with different valences (2+, 3+, 4+ and 5+ are all common [13]) including trivalent and tetravalent actinides. This chemical flexibility allows synthetic pyrochlores to accommodate contaminants from the waste stream and enables the addition of other elements to optimise the material properties of the wasteform; for example, the addition of neutron absorbers such as Gd [16] or Hf [13] to maintain criticality control during storage and disposal.

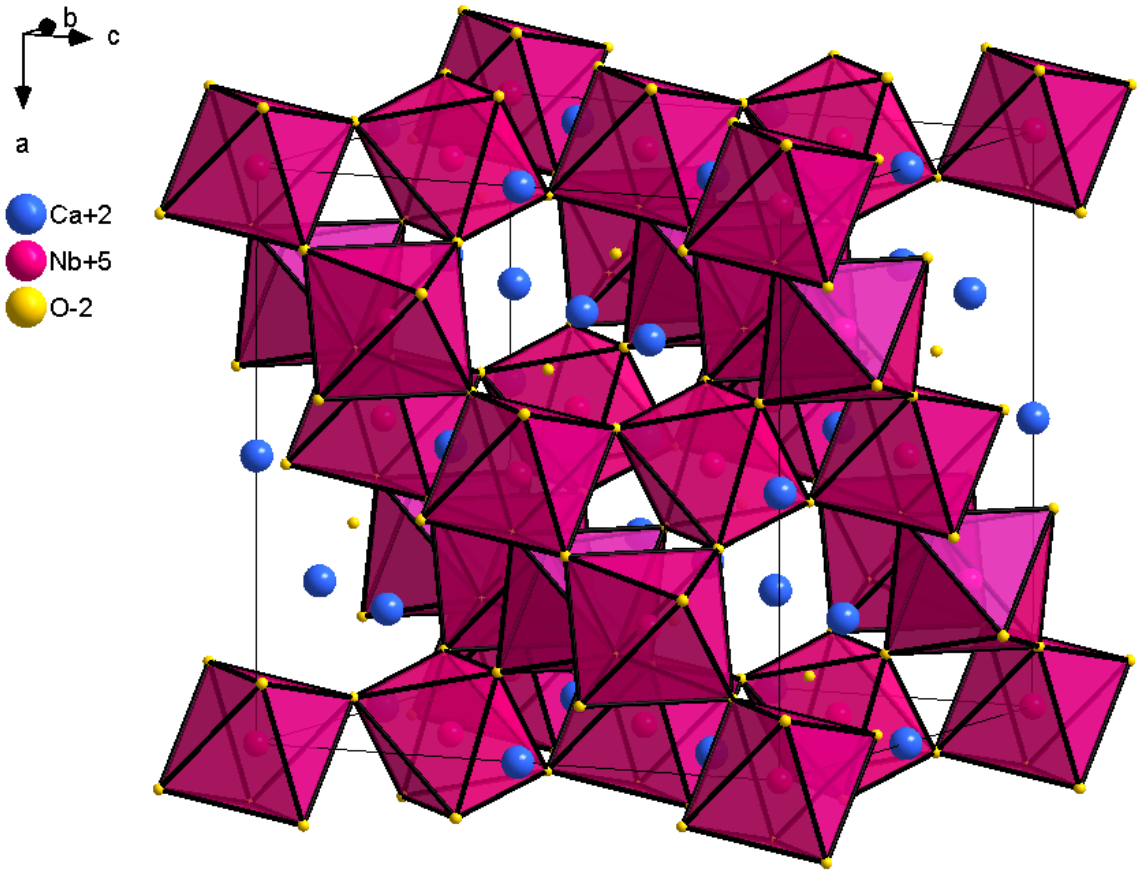

Figure 2.1. Crystal structure of a $Ca_2Nb_2O_7$ pyrochlore ($Fd\bar{3}m$) [17], with: blue A-site Ca^{2+} cations; pink B-site Nb^{5+} cations and distorted octahedra; and yellow O^{2-} anions in the X and Y sites.

Most synthetic compositions of interest for waste disposal contain Ti and Zr on the B site, as compositions with these cations have been found to show good resistance to dissolution [13, 18] and self-radiation damage, originating from α-decay of the actinide elements [16, 19, 20]. For synthetic titanate pyrochlore wasteforms, natural U or Th bearing betafite minerals would be the most relevant analogues. Under new classification proposed by Atencio *et al.* [11] most

mineral samples previously assigned as betafite are no longer classified as such [15], since they contain more net 5+ cations than net 4+ cations. However, these minerals, which contain a significant, if not a majority fraction, of Ti and some U and Th, remain the most compositionally similar to synthetic titanate pyrochlores. In the context of wasteform analogues there is only one pyrochlore supergroup mineral that has been identified with a dominant concentration of U on the A site [15], an oxyuranobetafite ($(U_{0.81}Ca_{0.66}Y_{0.09}REE_{0.14})(Ti_{1.04}Nb_{0.89}Ta_{0.07})O_{7.105}$) from Mare Crisium, the Moon [21].

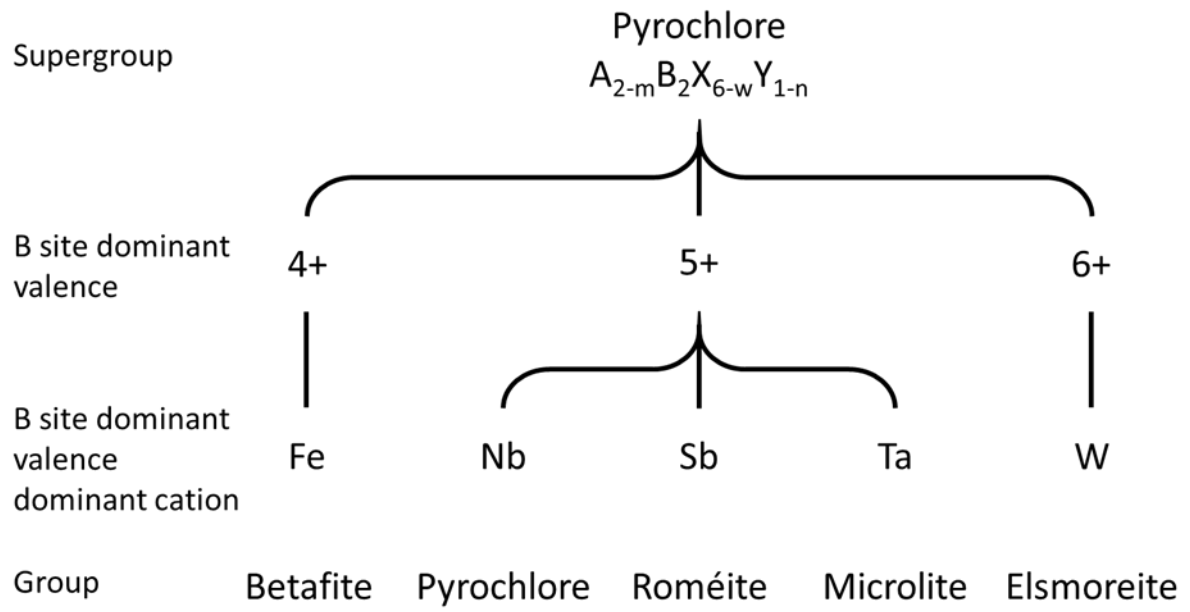

Figure 2.2. Diagram of pyrochlore super-group group categorisation, proposed by Atencio *et al.* where groups are assigned by first the net `dominant valence of B site cations, and then by the highest concentration cation which had that valence [11]

2.2.2. Brannerite

Brannerite has an idealised structure of AB_2O_6 (C2/m), which consists of layers of corner sharing A-site octahedra separated by layers of edge sharing B-site octahedra (Figure 2.3) [22]. The idealised composition of brannerite is $U^{4+}Ti_2O_6$, though mineral samples often contain partially oxidised U [22] and are metamict due to alpha recoil damage [23]. Brannerite

is considered the third most abundant U^{4+} resource after uraninite (UO_2) and coffinite ($USiO_4 \cdot nH_2O$) [22, 24, 25], so there is ample availability of analogous material. While it is possible to recover U from brannerite [26], it is highly refractory and resistant to dissolution [18, 25, 27, 28], making it a good candidate for a wasteform material. Mineral brannerites accommodate impurities including Mg, Ca, Mn, Y, Ba, Pb, Ce, Nd, and Th on the A site and Al, Si, Fe, Ni, and Nb on the B site [23, 29], demonstrating chemical flexibility. Synthetic brannerites have been found to be resistant to radiation damage, if slightly less so than for pyrochlore [30, 31]. The nominal composition of synthetic brannerite (UTi_2O_6) enables a high waste loading (up to 55 wt.% U). This is beneficial since higher waste loadings reduce the volume of a wasteform and, therefore, the amount of space required in a geological disposal facility (GDF).

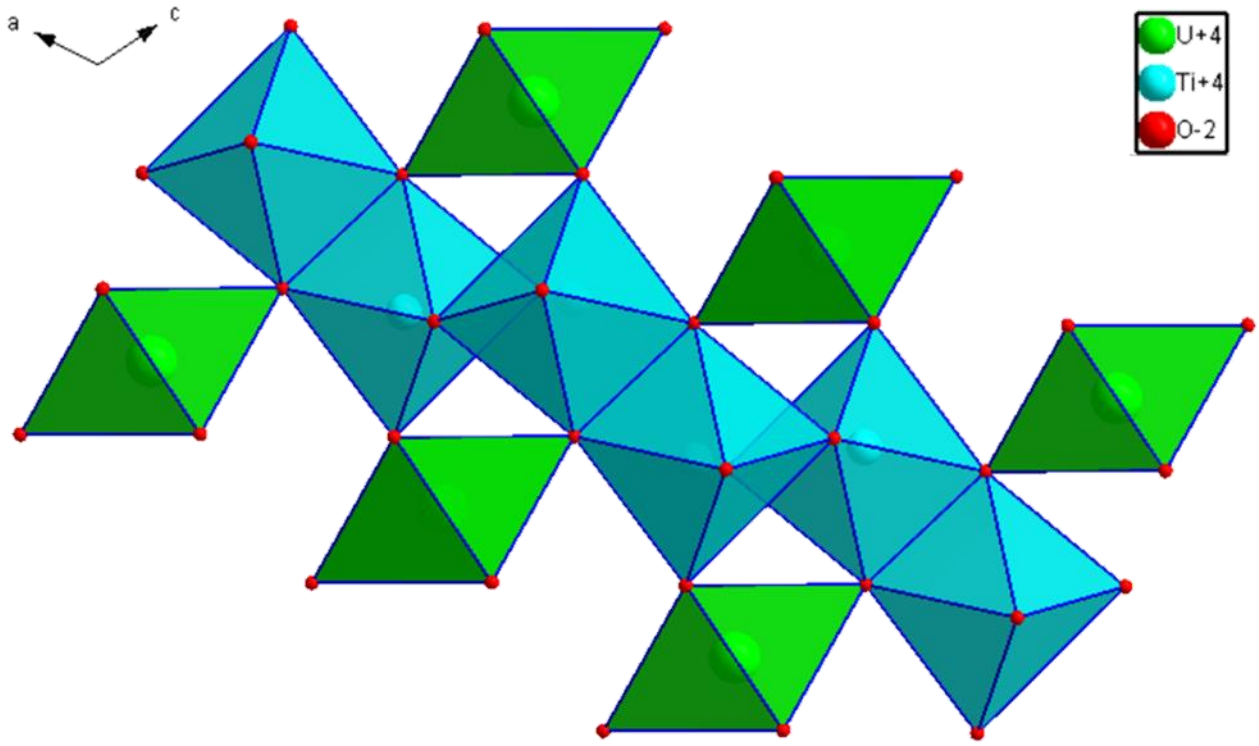

Figure 2.3. Brannerite structure (C2/m), adapted from Mesbah *et al.* [22] with green U^{4+} cations and octahedra, blue Ti^{4+} cations and octahedra, and red O^{2-} anions.

2.3. Characterisation of U in ceramic wasteforms and minerals

2.3.1. X-ray absorption spectroscopy

X-ray absorption spectroscopy (XAS) is a unique method to investigate element speciation, by probing the core electron shells. An X-ray absorption experiment passes X-ray photons through a sample, and some photons are absorbed by electrons, causing them to excite to higher energy levels. As electron energy levels are discrete and different for any given element, the energies at which absorption occurs (referred to as absorption edges) are inherently characteristic. By exploiting the Beer-Lambert law and measuring the intensity of photons before and after the sample whilst changing the energy of incidence photons, it is possible to produce an XAS spectrum which can then be interpreted. Information that can be obtained from an XAS spectrum includes oxidation state, local coordination number, and ligand type of the element being measured. For a complete discussion of the XAS technique, please see Chapter 3.

In this Thesis, the key element of interest is U and, as such, a particular focus will be placed upon the variety of U XAS experiments that can be performed. The most common U XAS experiment is performed at the U L_3-edge as this provides insight into the net U oxidation state, coordination environment, and short-range structure. Uranium $M_{4/5}$-edges may also be probed, often using a specific technique known as high energy resolution fluorescence detected (HERFD) XAS, to more accurately determine U oxidation state and gain some insight into U coordination. For full descriptions of different U XAS measurements the reader is referred to Chapter 3. For discussion of the respective benefits and limitations of each technique to obtain information about U speciation, please see Chapter 4.

Uranium XAS experiments use synchrotrons as X-ray photons sources. Measurements are performed at specialist beamlines equipped to measure radioactive material [32], or some measurements can be achieved with a laboratory instrument where an X-ray tube is used as the photon source [33].

2.3.2. XAS applied to synthetic U titanate materials

Fortner *et al*. collected both U L_3-edge and Pu L_3-edge XAS data in both the X-ray absorption near edge structure (XANES) and extended X-ray absorption fine structure (EXAFS) from synthetic U- and Pu-bearing titanate materials ($Ca_{0.83}Hf_{0.24}Gd_{0.20}U_{0.41}Pu_{0.20}Ti_{2.09}O_7$ and $Ca_{0.88}Hf_{0.24}Gd_{0.20}U_{0.41}Pu_{0.20}(Al,Mg,Ga,Fe,Cr,Ni,K,Na,Mo,Si,Ta,B,W,Zn)_{0.18}Ti_{2.09}O_7(F,Cl)_{0.11}$) in an attempt to investigate U and Pu speciation and their incorporation into the pyrochlore structure [34]. Scanning electron microscopy (SEM) and X-ray diffraction (XRD) analysis identified three actinide bearing phases: brannerite, pyrochlore, and zirconolite (which has the structure $AA'B_2O_7$). Fortner *et al.* stated that the brannerite phase was approximately ≤ 20% ceramic volume and that pyrochlore and zirconolite were 70% of the ceramic volume; however, this data was not included in paper. They found that the Pu was predominately speciated as Pu^{4+} and the results of Pu L_3-edge EXAFS fitting were consistent with Pu substituting onto the A site in the pyrochlore structure. The results of fitting the U L_3-edge EXAFS data were indicative of U substitution onto the B site and a net U oxidation state of 5+. However, these analyses were interpreted assuming that all of the U was present in the pyrochlore structure (it was assumed the zirconolite and pyrochlore structures were too similar to be differentiated).

Stefanovsky *et al.* also attempted to investigate the speciation of a set of multiphase ceramics with a range of target compositions: $La_{0\text{-}0.04}Ce_{0.20\text{-}0.32}Pr_{0\text{-}0.10}Nd_{0.23\text{-}0.32}Sm_{0\text{-}0.06}Eu_{0\text{-}0.01}Gd_{0\text{-}0.04}U_{0.04\text{-}0.48}Ti_2O_6$ (which were characterised by SEM and energy-dispersive X-ray spectroscopy (EDX) as containing several non U-bearing phases, brannerites and an unidentified U-bearing phase) through the collection of XAS data at both the U L_3-edge and the Ce L_2-edge [35]. They concluded from qualitative comparisons of U L_3-edge XANES data from samples and reference compounds that both U^{4+} and U^{5+} were present in their samples. The paper does not describe in detail what comparisons were made, it was indicated that the conclusions drawn were based upon the position of a feature in the XANES region between 17200 eV to 17250 eV. Furthermore, whilst the EXAFS data were fit, from which estimates of U coordination were derived, the overall U speciation was not clearly determined or discussed by the authors. The Ce L_2-edge spectra did evidently show that Ce^{3+} was present in all the samples, supporting the hypothesis that U may be present in a higher oxidation state than U^{4+} due to charge balancing

requirements. As the samples contain multiple U bearing phases, and the basis on which the presence of U^{5+} speciation from qualitative analysis of bulk U L_3-edge XANES is unclear, the conclusion that U^{5+} is present in the brannerite phase does not appear to be supported by the data or analysis provided.

Bulk U XANES with quantitative analysis has been applied to investigate U speciation in synthetic brannerites ($U_{0.9}Ce_{0.1}Ti_2O_6$ and a $UTi_{2-x}Al_xO_6$ system) [36, 37]. These studies used the U L_3-edge position of the synthetic brannerite spectra to estimate U oxidation state. Here, the edge positions of known U reference compounds were used to perform a linear regression analysis from which an estimate of U speciation could be calculated for samples. Bailey (2020) *et al.* [36] also collected Ti K-edge and Ce L_3-edge XAS to support the investigation of U speciation and charge compensation mechanics in samples targeting the synthetic brannerite composition $U_{0.9}Ce_{0.1}Ti_2O_6$, which had been synthesised under different conditions. Linear combination fitting (LCF) of the Ce L_3-edge XANES and peak fitting of the Ti K-edge XANES pre-edge feature provided estimates of Ce and Ti speciation (3+ and 4+ respectively) to support the characterisation of U speciation as 4.0+ and 4.1+ in samples treated under argon and 5% H_2/N_2, respectively. A third sample, which was treated under air, was identified by SEM and EDX as containing U_3O_8 as a major phase and linear regression gave an estimated U oxidation state of 5.4+. Dixon-Wilkins *et al.* produced synthetic brannerites with nominal compositions designed to target U^{5+} speciation through substitution of Ti with Al [37]. They applied U L_3-edge laboratory XAS to provide initial estimates of net U speciation and identify compositions of interest from which to acquire U M_4-edge M_β HERFD XAS. Uranium M_4-edge M_β HERFD XAS data, collected from $UTi_{2-x}Al_xO_6$ samples x = 0.6, 1.0 and 1.2, enabled the direct identification of the presence of U^{4+} and U^{5+}, and LCF analysis was used to produces estimates of 0.21-0.24 and 0.76-0.79 for the relative fractions of U^{4+} and U^{5+} respectively.

These studies demonstrate the benefits of using multiple XAS techniques in an investigation of U speciation to support estimates or investigate speciation further. All the papers discussed here concerned multiphase ceramic samples and some samples contained multiple actinide-bearing phases, which inhibited the characterisation of actinide speciation within the phase of interest. This highlights the potential usefulness of spatially resolved techniques to fully investigate actinide speciation in multi-phase samples.

2.3.3. XAS applied to U-titanate mineral analogues

The extent of application of XAS to determine U speciation in mineral analogues is far less than that of synthetic actinide titanates, with only few studies reported in the literature. Uranium-containing mineral samples are often metamict due to alpha-recoil damage [23, 38-40], which is especially the case for titanate minerals that tend to have high U contents. As such, these samples do not have a long range structure which can be easily characterised. The application of XAS, and EXAFS in particular, is an exteremely important technique for investigating metamict material as it can probe the short-range structure and provide a greater understanding of U speciation and coordination within metamict U minerals. This lack of structure is also the reason why studies of metamict minerals often include attempts to recrystalise them by thermal treatment [27, 28, 41-43], with the treated material characterised in an attempt to aproximate the original structure, or to establish the extent to which the sample has been altered.

Greegor *et al.* used U L_3-edge EXAFS data to investigate the short range structure of a metamict U-bearing mineral sample with the composition $(Ca_{0.46}U_{0.42}Fe_{0.11}Ba_{0.03}Pb_{0.02})(Nb_{1.1}Ti_{0.88}Ta_{0.02})O_{6.0}F_{0.04}\cdot 2.3H_2O$ [44] (a calciopyrochlore under the classification system proposed by Atencio *et al.* [11]) in addition to a sample of the same mineral that had been thermally treated (to attempt to restore the long-range crystal structure). The sample contained a notably high concentration of U; as discussed above, only one pyrochlore super-group mineral has been identified with a majority of U on the A site [15], an oxyuranobetafite which originated on the Moon [21].

Positions of peaks in the Fourier transform of the EXAFS of both samples were used to determine U-O path lengths, which were interpreted by Greegor *et al.* to reflect a uranyl-like structure. However, this thesis finds that the estimated bond lengths (1.94 and 2.37 Å) suggest that the sample may contain U^{5+} speciation, as they are in the range of known U-O path distances of other U^{5+} reference compounds, including pyrochlores [34], possibly with some uranyl speciation also present. The estimated bond lengths of the thermally treated sample (2.03 and 2.51 Å) were greater than the metamict sample and Greegor *et al.* also

found that the increased intensity of features associated with U-metal second shell scatterers in the Fourier transform of EXAFS data from the thermally treated sample indicated that the thermally treated sample had a more ordered structure than the untreated sample. Unfortunately, the analysis performed by Greegor *et al.* did not produce estimates of U coordination or oxidation state, and no XRD data were included to confirm what the thermally treated sample had recrystallised to. However, an estimate of unit cell parameter of a = 10.344(5) was provided, which is within range of unit cell parameters from mineral and synthetic crystalline pyrochlores with similar compositions: a hydroxycalciopyrochlore, $(Ca_{0.73}Na_{0.57}U_{0.4}Ce_{0.05}Fe_{0.02}Y_{0.01}\square_{0.22})_2(Nb_{1.14}Ti_{0.79}Ta_{0.03}Al_{0.01}Mg_{0.01})_2O_{6.2}[(OH)_{1.01}F_{0.09}]_{1.10}$, [45] which had a unit cell parameter of a = 10.381(4) Å and an oxycalciobetafite $(Ca_{1.29}Na_{0.18}U_{0.50}Ce_{0.03})(Ti_{1.09}Nb_{0.79}Zr_{0.14}Fe_{0.04}Ta_{0.01})O_6(O_{0.98}F_{0.02})$ which had a unit cell parameter of a = 10.263(1) Å [46].

Vance *et al.* applied U L_3-edge XANES data to investigate U speciation both a metamict natural mineral sample identified as brannerite, and material that had been heat treated in an attempt to recrystallise UTi_2O_6 [47]. Through qualitative comparison with the edge positions of a U^{4+} and U^{6+} reference compound they found that the metamict, untreated brannerite sample contained a majority of U^{6+} and that the U in the heat-treated version had been reduced, with a net U speciation close to U^{4+}. Further discussion of Vance *et al.*'s findings, and any further conclusions this thesis argues can be drawn from the re-examination of the data can be found in Chapter 5.

2.3.4. Spatially resolved X-ray techniques

Spatially resolved X-ray techniques are a promising and expanding area of characterisation for U materials, where X-ray measurements are collected from a specific area on a sample. A microprobe X-ray beamline utilises an X-ray beam with a spot size on the scale of microns to tens of microns to enable the acquisition of data using various X-ray based spatially-resolved measurements. This includes the collection of microfocus X-ray diffraction (μXRD), X-ray fluorescence (μXRF), XANES (μXANES) and EXAFS (μEXAFS) data, which can be interrogated

using several different analyses. A detailed description of how these measurements are achieved at a microprobe beamline is given in Chapter 3.

2.3.5. Spatially resolved X-ray techniques applied to synthetic U titanates

Bailey (2018) *et al.* utilised U L_3-edge μXAS to investigate the speciation of U in synthetic brannerite in multi-phase ceramic materials [48]. The use of a μXRF mapping technique enabled Bailey (2018) *et al.* to use element emission line intensity maps to identify brannerite phases within their samples and then collect U L_3-edge μXAS data from points within those phases. Bailey (2018) *et al.* then used the edge positions of the μXANES data collected from their samples, and a linear regression of the edge positions and known oxidation state of U reference compounds, to produce estimates of net U oxidation state in the brannerite phases between 4.1+ and 5.2+. This demonstrates the benefit of μXAS over a bulk XAS measurement to investigate the speciation of a specific phase, or area of interest, within a heterogeneous material.

Uranium L_3-edge μXAS has also been used to investigate other nuclear relevant materials, including simulant degraded nuclear fuel from Chernobyl and Fukushima [49-51], U ore concentrate particles [52] and environmental U contamination by depleted uranium munitions [53, 54]. Like Bailey *et al*. these experiments utilised μXRF mapping and μXAS, but they also employed other measurements possible at an X-ray microprobe beamline, including microfocus X-ray diffraction (μXRD), μXRD mapping, oxidation state mapping and microfocus EXAFS (μEXAFS). The method to perform the techniques referred to here, except for oxidation state mapping, are explained in Chapter 3.

The use of μXRD enables the investigation of crystallographic structure at specific points in a sample or even across a whole region of interest. This can be used in combination with μXRF to support the identification and characterisation of different phases, or to determine variation in structure within a sample. Ding *et al.* performed analysis of μXRD map data to produce phase maps of simulant nuclear fuel debris [50, 51] and Crean *et al.* utilised μXRD maps to investigate U speciation by using characteristic reflections to identify regions of U_3O_7

and U_3O_8 within their sample [53]. Spatially dependant variation in U speciation can also be explored using oxidation state mapping. The construction of U oxidation state maps has been thoroughly investigated by Ding *et al.* [50]. It is also possible to collect µEXAFS, several studies [49-51, 54] used U L_3-edge µEXAFS data to investigate the short-range structure at points of interest, an example of which can be found in Crean (2020) *et al.* [54]. This technique would be of particular use in metamict mineral samples, to investigate if there is any variation in short-range structure within a sample.

2.3.6. Spatially resolved X-ray techniques applied to uranium-containing minerals

Syverson *et al.* collected µXRF data from several U minerals, including brannerites, and used µXRF element maps to identify areas of interest within the sample. From these, they collected Pb L_2 and L_3-edge µXANES and µEXAFS [55] to investigate Pb speciation within U minerals and to understand the mobility of radiogenic Pb. They were able to characterise all Pb present within their U mineral samples as Pb^{2+}. Aside from the work undertaken by Syverson *et al.*, to our knowledge, no mineral samples analogous to wasteforms for actinides have been investigated using techniques available at an X-ray microprobe beamline, including the direct investigation of spatially resolved U speciation using µXAS.

Uranium µXAS has been applied to other natural U mineral samples, including U-rich pyrites [56] and in the study of environmental samples in contamination studies [57-59]. Cumberland *et al*. used U L_3-edge µXANES to investigate U speciation in the U rich rims of pyrite (FeS_2) grains [56]. They used LCF analysis of U L_3-edge µXANES data to investigate variation of U speciation across the rim of pyrite grains, the estimates of net U oxidation state they obtained informed their suggestion that U^{6+} has been reduced to U^{4+} at the rim of the pyrite. This work demonstrates how U L_3-edge µXANES data can be used to investigate the mobility of U in mineral samples. However, some of the measures of goodness of fit for their XANES linear combination fits (LCF) were quite high, and some fits presented in the supporting information did not appear to successfully match the data being fitted. This may be due to the absence of a more relevant U reference compound, as LCF is highly reliant on the availability of XANES data collected from reference compounds with similar compositions, structures, and

oxidation states. Cumberland *et al.* also used the LCF analysis from their U L_3-edge μXANES data as a direct estimate of fraction of U^{4+} and U^{6+} speciation, this interpretation is beyond the capabilities of the technique: to estimate net U oxidation and possibly give an estimate of the fraction of uranyl speciation present. This shows that the limitations of both spatially resolved measurements and analysis techniques must be understood to produce accurate and reliable results which can be used with confidence to inform the design of nuclear wasteforms.

2.4. Conclusions

To accurately predict the properties of wasteforms for Pu over their lifetimes of hundreds of thousands of years, the current and original speciation of U (both as U surrogate for Pu and as a Pu daughter nuclide) in relevant mineral analogues is of significance. X-ray absorption spectroscopy is a key technique in investigating the speciation of U within minerals and synthetic wasteform materials, which has been successfully applied in these contexts. A small number of studies have applied XAS to characterise U within mineral analogues for Pu wasteforms, including naturally occurring brannerites and a U and Ti bearing pyrochlore, but there remain many questions surrounding the U local chemical environment and speciation. These should be answered on a wide range of heterogeneous mineral samples to help reach consensus on the speciation of U and, therefore, the performance of synthetic actinide wasteforms over a disposal lifetime.

Techniques of particular relevance to U mineral analogues are U L_3-edge EXAFS, U M_4-edge HERFD, and spatially-resolved techniques available at a microprobe beamline. Uranium L_3-edge EXAFS provides insight into the speciation of U and the associated short-range structure of a sample. When combined with U M_4-edge HERFD data, which enables a more accurate estimation of the fraction of each U oxidation state present within a sample than the L_3-edge, significant insight can be gained into the local U environment in wasteform-relevant samples. To establish the speciation of U in different phases within non-homogenous samples or identify variation in speciation, structure and composition, which would support the investigation of the alteration history of a sample, spatially resolved techniques are required. Thus far this technique has been applied to nuclear waste relevant materials, and to in an investigation of Pb speciation within some U and U rich minerals, including brannerite. Previous work also showed the benefits from the combined use of different techniques, or measurements at different edges and of different elements.

To support the investigation of U environments in mineral analogues first there must be confidence in the methods used to measure and analyse the data, therefore the capabilities and limitations of these techniques for use with environmental samples must be thoroughly investigated and understood.

2.5. References

[1] N.N. Greenwood, A. Earnshaw, The Actinide Elements, Chemistry of the elements, Butterworth-Heinmann, Oxford, UK, 1997, pp. 1253-1267.

[2] J. Birkholzer, J. Houseworth, C.F. Tsang, Geologic Disposal of High-Level Radioactive Waste: Status, Key Issues, and Trends, in: A. Gadgil, D.M. Liverman (Eds.), Annual Review of Environment and Resources, Annual Reviews, Palo Alto, 2012, pp. 79-106.

[3] International Atomic Energy Agency, Classification of Radioactive Waste, 2009.

[4] S.V. Stefanovsky, S.V. Yudintsev, Titanates, zirconates, aluminates and ferrites as waste forms for actinide immobilization, Russ. Chem. Rev. 85(9) (2016) 962-994.

[5] N.C. Hyatt, M.I. Ojovan, Special Issue: Materials for Nuclear Waste Immobilization, Materials 12(21) (2019) 4.

[6] Q.X. Cao, S.V. Krivovichev, B.E. Burakov, X.D. Liu, X.T. Liu, Natural metamict minerals as analogues of aged radioactive waste forms, J. Radioanal. Nucl. Chem. 304(1) (2015) 251-255.

[7] K. Maher, J.R. Bargar, G.E. Brown, Environmental Speciation of Actinides, Inorg. Chem. 52(7) (2013) 3510-3532.

[8] G.R. Choppin, J.-O. Lijenzin, J. Rydberg, Chapter 22 - Behavior of Radionuclides in the Environment, Radiochemistry and Nuclear Chemistry (Third Edition), Butterworth-Heinemann, Woburn, 2002, pp. 642-673.

[9] J. Bel, F. Bernier, Temperature Criterion Related to Clay Based Backfill Materials in the Framework of a Geological Repository of Heat Producing Radioactive Waste (HLW), ASME 2001 8th International Conference on Radioactive Waste Management and Environmental Remediation, 2001, pp. 1327-1331.

[10] Radioactive Waste Management, Geological Disposal: Generic Disposal Facility Design, Nuclear Decommissioning Authority, 2016.

[11] D. Atencio, M.B. Andrade, A.G. Christy, R. Giere, P.M. Kartashov, The Pyrochlore Supergroup of Minerals: Nomenclature, Can. Mineral. 48(3) (2010) 673-698.

[12] B.C. Chakoumakos, Systematics of the Pyrochlore Structure Type, Ideal $A_2B_2X_6Y$, J. Solid State Chem. 53(1) (1984) 120-129.

[13] R.C. Ewing, W.J. Weber, J. Lian, Nuclear waste disposal-pyrochlore ($A_2B_2O_7$): Nuclear waste form for the immobilization of plutonium and "minor" actinides, J. Appl. Phys. 95(11) (2004) 5949-5971.

[14] M.A. Subramanian, G. Aravamudan, G.V.S. Rao, Oxide Pyrochlores - A Review, Prog. Solid State Chem. 15(2) (1983) 55-143.

[15] D. Atencio, Pyrochlore-Supergroup Minerals Nomenclature: An Update, Front. Chem. 9 (2021) 6.

[16] S.X. Wang, B.D. Begg, L.M. Wang, R.C. Ewing, W.J. Weber, K.V.G. Kutty, Radiation stability of gadolinium zirconate: A waste form for plutonium disposition, J. Mater. Res. 14(12) (1999) 4470-4473.

[17] J.T. Lewandowski, I.J. Pickering, A.J. Jacobson, Hydrothermal synthesis of calcium-niobium and tantalum oxides with the pyrochlore structure, Mater. Res. Bull. 27(8) (1992) 981-988.

[18] S.K. Roberts, W.L. Bourcier, H.F. Shaw, Aqueous dissolution kinetics of pyrochlore, zirconolite and brannerite at 25, 50, and 75 degrees C, Radiochim. Acta 88(9-11) (2000) 539-543.

[19] K.E. Sickafus, L. Minervini, R.W. Grimes, J.A. Valdez, T. Hartmann, A comparison between radiation damage accumulation in oxides with pyrochlore and florite structures, Radiat. Eff. Defects Solids 155(1-4) (2001) 133-137.

[20] B.D. Begg, N.J. Hess, W.J. Weber, R. Devanathan, J.P. Icenhower, S. Thevuthasan, B.P. McGrail, Heavy-ion irradiation effects on structures and acid dissolution of pyrochlores, J. Nucl. Mater. 288(2-3) (2001) 208-216.

[21] A.V. Mokhov, P.M. Kartashov, O.A. Bogatikov, N.A. Ashikhmina, L.O. Magazina, E.V. Koporulina, Fluorite, Hatchettolite, Calcium Sulfate, and Bastnasite-(Ce) in the Lunar Regolith from Mare Crisium, Dokl. Earth Sci. 422(1) (2008) 1178-1180.

[22] A. Mesbah, S. Szenknect, N. Clavier, H.T. Lin, F. Baron, D. Beaufort, Y. Batonneau, J. Mercadier, A. Eglinger, M. Turuani, P. Goncalves, F. Choulet, V. Chapon, A.M. Seydoux-Guillaume, M. Pagel, N. Dacheux, Direct synthesis of pure brannerite UTi_2O_6, J. Nucl. Mater. 515 (2019) 401-406.

[23] G.R. Lumpkin, S.H.F. Leung, J. Ferenczy, Chemistry, microstructure, and alpha decay damage of natural brannerite, Chem. Geol. 291 (2012) 55-68.

[24] R. Finch, T. Murakami, Systematics and Paragenesis of Uranium Minerals, Reviews in Mineralogy 38 (1999) 91-179.

[25] R. Gilligan, A.N. Nikoloski, The process chemistry and mineralogy of brannerite leaching, J. S. Afr. Inst. Min. Metall. 117(8) (2017) 765-770.

[26] A. Costine, A.N. Nikoloski, M. Da Costa, K.F. Chong, R. Hackl, Uranium extraction from a pure natural brannerite mineral by acidic ferric sulphate leaching, Miner. Eng. 53 (2013) 84-90.

[27] F.A. Charalambous, R. Ram, S. McMaster, M.I. Pownceby, J. Tardio, S.K. Bhargava, Leaching behaviour of natural and heat-treated brannerite-containing uranium ores in sulphate solutions with iron(III), Miner. Eng. 57 (2014) 25-35.

[28] Y. Zhang, G.R. Lumpkin, H. Li, M.G. Blackford, M. Colella, M.L. Carter, E.R. Vance, Recrystallisation of amorphous natural brannerite through annealing: The effect of radiation damage on the chemical durability of brannerite, J. Nucl. Mater. 350(3) (2006) 293-300.

[29] M. Turuani, F. Choulet, A. Eglinger, P. Goncalves, J. Machault, J. Mercadier, A.M. Seydoux-Guillaume, S. Reynaud, F. Baron, D. Beaufort, Y. Batonneau, S. Gouy, A. Mesbah, S. Szenknect, N. Dacheux, V. Chapon, M. Pagel, Geochemical fingerprints of brannerite (UTi_2O_6): an integrated study, Mineral. Mag. 84(2) (2020) 313-334.

[30] G.R. Lumpkin, K.L. Smith, M.G. Blackford, Heavy ion irradiation studies of columbite, brannerite, and pyrochlore structure types, J. Nucl. Mater. 289(1-2) (2001) 177-187.

[31] J. Lian, L.M. Wang, G.R. Lumpkin, R.C. Ewing, Heavy ion irradiation effects of brannerite-type ceramics, Nucl. Instrum. Methods Phys. Res. Sect. B-Beam Interact. Mater. Atoms 191 (2002) 565-570.

[32] M.A. Denecke, Actinide speciation using X-ray absorption fine structure spectroscopy, Coord. Chem. Rev. 250(7-8) (2006) 730-754.

[33] R. Bes, T. Ahopelto, A.P. Honkanen, S. Huotari, G. Leinders, J. Pakarinen, K. Kvashnina, Laboratory-scale X-ray absorption spectroscopy approach for actinide research: Experiment at the uranium L-3-edge, J. Nucl. Mater. 507 (2018) 50-53.

[34] J.A. Fortner, A.J. Kropf, R.J. Finch, A.J. Bakel, M.C. Hash, D.B. Chamberlain, Crystal chemistry of uranium (V) and plutonium (IV) in a titanate ceramic for disposition of surplus fissile material, J. Nucl. Mater. 304(1) (2002) 56-62.

[35] S.V. Stefanovsky, S.V. Yudintsev, A.A. Shiryaev, V.Y. Murzin, A.L. Trigub, Phase partitioning and uranium speciation in brannerite-based ceramics, J. Eur. Ceram. Soc. 37(2) (2017) 771-777.

[36] D.J. Bailey, M.C. Stennett, S.K. Sun, L.J. Gardner, S.A. Walling, C.L. Corkhill, B. Ravel, N.C. Hyatt, Iop, Ce and U speciation in wasteforms for thermal treatment of plutonium bearing wastes, probed by L_3 edge XANES, THERAMIN Conference - Thermal Treatment of Radioactive Waste, Iop Publishing Ltd, Mech Inst, Manchester, England, 2020.

[37] M.C. Dixon Wilkins, L.M. Mottram, E.R. Maddrell, M.C. Stennett, C.L. Corkhill, K.O. Kvashnina, N.C. Hyatt, Synthesis, Characterization, and Crystal Structure of Dominant Uranium(V) Brannerites in the $UTi_{2-x}Al_xO6$ System, Inorg. Chem. 60(23) (2021) 18112-18121.

[38] G.R. Lumpkin, E.M. Foltyn, R.C. Ewing, Thermal recrystallization of alpha-recoil damaged minerals of the pyrochlore structure type, J. Nucl. Mater. 139(2) (1986) 113-120.

[39] G.R. Lumpkin, R.C. Ewing, Alpha-decay damage in minerals of the pyrochlore group, Phys. Chem. Miner. 16(1) (1988) 2-20.

[40] G.R. Lumpkin, Alpha-decay damage and aqueous durability of actinide host phases in natural systems, J. Nucl. Mater. 289(1-2) (2001) 136-166.

[41] F.A. Charalambous, R. Ram, M.I. Pownceby, J. Tardio, S.K. Bhargava, Chemical and microstructural characterisation studies on natural and heat treated brannerite samples, Miner. Eng. 39 (2012) 276-288.

[42] F. Farges, The structure of metamict zircon: A temperature-dependent EXAFS study, Phys. Chem. Miner. 20(7) (1994) 504-514.

[43] S.A. McMaster, R. Ram, M.I. Pownceby, J. Tardio, S. Bhargava, Characterisation and leaching studies on the uranium mineral betafite (U,Ca)(2)(Nb,Ti,Ta)(2)O-7, Miner. Eng. 81 (2015) 58-70.

[44] R.B. Greegor, F.W. Lytle, B.C. Chakoumakos, G.R. Lumpkin, R.C. Ewing, An Investigation of Uranium L-Edges of Metamict and Annealed Betafite, MRS Proceedings 50 (1985) 387.

[45] G.M. Yang, G.W. Li, M. Xiong, B.M. Pan, C.J. Yan, Hydroxycalciopyrochlore, A New Mineral Species from Sichuan, China, Acta Geol. Sin.-Engl. Ed. 88(3) (2014) 748-753.

[46] F. Camara, C.T. Williams, G. Della Ventura, R. Oberti, E. Caprilli, Non-metamict betafite from Le Carcarelle (Vico volcanic complex, Italy): occurrence and crystal structure, Mineral. Mag. 68(6) (2004) 939-950.

[47] E.R. Vance, J.N. Watson, M.L. Carter, R.A. Day, B.D. Begg, Crystal chemistry and stabilization in air of brannerite, UTi_2O_6, J. Am. Ceram. Soc. 84(1) (2001) 141-144.

[48] D.J. Bailey, M.C. Stennett, B. Ravel, D. Grolimund, N.C. Hyatt, Synthesis and characterisation of brannerite compositions $(U_{0.9}Ce_{0.1})_{1-x}M_xTi_2O_6$ ($M = Gd^{3+}$, Ca^{2+}) for the immobilisation of MOX residues, RSC Adv. 8(4) (2018) 2092-2099.

[49] H. Ding, M.C.D. Wilkins, C. Gausse, L.M. Mottram, S.K. Sun, M.C. Stennett, D. Grolimund, R. Tappero, S. Nicholas, N.C. Hyatt, C.L. Corkhill, Safely probing the chemistry of Chernobyl nuclear fuel using micro-focus X-ray analysis, J. Mater. Chem. A 9(21) (2021) 12612-12622.

[50] H. Ding, M.C.D. Wilkins, L.M. Mottram, L.R. Blackburn, D. Grolimund, R. Tappero, S.L. Nicholas, S.K. Sun, C.L. Corkhill, N.C. Hyatt, Chemical state mapping of simulant Chernobyl lava-like fuel containing material using micro-focused synchrotron X-ray spectroscopy, J. Synchrot. Radiat. 28 (2021) 1672-1683.

[51] H. Ding, C. Gausse, M.C.D. Wilkins, L.M. Mottram, M.C. Stennett, D. Grolimund, R. Tappero, S. Nicholas, S.K. Sun, T. Shiba, C. Paraskevoulakos, N.C. Hyatt, C.L. Corkhill, Chemical characterisation of degraded nuclear fuel analogues simulating the Fukushima Daiichi nuclear accident, NPJ Mater. Degrad. 6(1) (2022) 13.

[52] D.E. Crean, C.L. Corkhill, T. Nicholls, R. Tappero, J.M. Collins, N.C. Hyatt, Expanding the nuclear forensic toolkit: chemical profiling of uranium ore concentrate particles by synchrotron X-ray microanalysis, RSC Adv. 5(107) (2015) 87908-87918.

[53] D.E. Crean, F.R. Livens, M.C. Stennett, D. Grolimund, C.N. Borca, N.C. Hyatt, Microanalytical X-ray Imaging of Depleted Uranium Speciation in Environmentally Aged Munitions Residues, Environ. Sci. Technol. 48(3) (2014) 1467-1474.

[54] D.E. Crean, M.C. Stennett, F.R. Livens, D. Grolimund, C.N. Borca, N.C. Hyatt, Multimodal X-ray microanalysis of a UFeO4 particle : evidence for the environmental stability of ternary U(v) oxides from depleted uranium munitions testing, Environ. Sci.-Process Impacts 22(7) (2020) 1577-1585.

[55] D.D. Syverson, B. Etschmann, W.H. Liu, R. Ram, Y. Mei, T. Lanzirotti, J. Mercadier, J. Brugger, Oxidation state and coordination environment of Pb in U-bearing minerals, Geochimica Et Cosmochimica Acta 265 (2019) 109-131.

[56] S.A. Cumberland, K. Evans, G. Douglas, M. de Jonge, L. Fisher, D. Howard, J.W. Moreau, Characterisation of uranium-pyrite associations within organic-rich Eocene sediments using EM, XFM-μXANES and μXRD, Ore Geol. Rev. 133 (2021) 16.

[57] D.M. Singer, J.M. Zachara, G.E. Brown, Uranium Speciation As a Function of Depth in Contaminated Hanford Sediments - A Micro-XRF, Micro-XRD, and Micro- And Bulk-XAFS Study, Environ. Sci. Technol. 43(3) (2009) 630-636.

[58] O.N. Batuk, S.D. Conradson, O.N. Aleksandrova, H. Boukhalfa, B.E. Burakov, D.L. Clark, K.R. Czerwinski, A.R. Felmy, J.S. Lezama-Pacheco, S.N. Kalmykov, D.A. Moore, B.F. Myasoedov, D.T. Reed, D.D. Reilly, R.C. Roback, I.E. Vlasova, S.M. Webb, M.P. Wilkerson, Multiscale Speciation of U and Pu at Chernobyl, Hanford, Los Alamos, McGuire AFB, Mayak, and Rocky Flats, Environ. Sci. Technol. 49(11) (2015) 6474-6484.

[59] C.L. Corkhill, D.E. Crean, D.J. Bailey, C. Makepeace, M.C. Stennett, R. Tappero, D. Grolimund, N.C. Hyatt, Multi-scale investigation of uranium attenuation by arsenic at an abandoned uranium mine, South Terras, NPJ Mater. Degrad. 1(1) (2017) 7.

3. Experimental Procedures

This Chapter describes the experimental procedures undertaken in the research presented in this Thesis. Any variation from this experimental procedure in specific chapters is detailed in the experimental procedures section of that particular chapter.

3.1. Materials

3.1.1. Reference compounds

All results chapters concern the measurement of reference compounds. Reference compounds were either obtained from stock material, mineral samples or were synthesised, and were required to be in powder form. Reference material from mineral sources was obtained with the use of a titanium needle. Unless specified otherwise, size reduction of powders was achieved by grinding, by hand, with an agate mortar and pestle.

3.1.2. Mineral sample thin sections

Spatially-resolved measurements of samples, (Sections 3.2.1 and 3.2.5) were collected from minerals mounted as thin sections onto a Spectrosil© glass slide. These thin sections were prepared by mounting the sample onto the glass slide, and then cutting, grinding and polishing the sample to achieve a sample thickness of 40µm and a surface finish of 1 µm.

3.1.3. Mineral samples for bulk measurements

For bulk measurements, (Sections 3.2.3, 3.2.4, 3.2.6 and 3.2.7) mineral samples were collected from the source mineral with the use of titanium needle. Unless specified otherwise, size reduction of powders was achieved by grinding by hand with an agate mortar and pestle.

3.2. Methods

3.2.1. Scanning electron microscopy and energy dispersive X-ray spectrometry

Scanning electron microscopy (SEM) and energy dispersive X-ray spectrometry (EDX) use electrons to investigate the microstructure and composition of samples. When a sample is bombarded with electrons, several different interactions occur which can be measured: elastic scattering, where the electron is scattered back towards the detector and is measured, referred to as backscattered electrons (BSE); inelastic scattering, where the incidence electron collides with an electron from an atom in the sample, and the secondary electron is emitted towards the detector, known as secondary electrons (SE); and when a secondary electron is displaced from an atom, the filling of the subsequent hole by a higher energy electron results in the emission of either characteristic X-rays, as described below, or Auger electrons [1]. The different types of electrons have different energies, elastically scattered (BSE) have the most energy and Auger electrons have the least, the higher the energy of the electron the further the depth from which it can escape from the sample (Figure 3.1) [1].

EDX measurements are often performed alongside SEM imaging (including as point spectra or as maps). The EDX technique collects the characteristic X-rays emitted at each point, and quantitative analysis provides estimates of composition.

The SEM and EDX data presented in this Thesis (Chapter 6) were collected on a Hitachi TM3030 in low charge build-up mode using backscattered electrons (BSE) with an accelerating voltage of 15 keV and a working distance of approximately 9 mm. EDX data were collected on a Bruker Quantax Energy Dispersive X-ray Spectrometer.

The sample measured in Chapter 6 was a mineral thin section mounted on a glass slide, no additional coatings were made before SEM-EDX measurements.

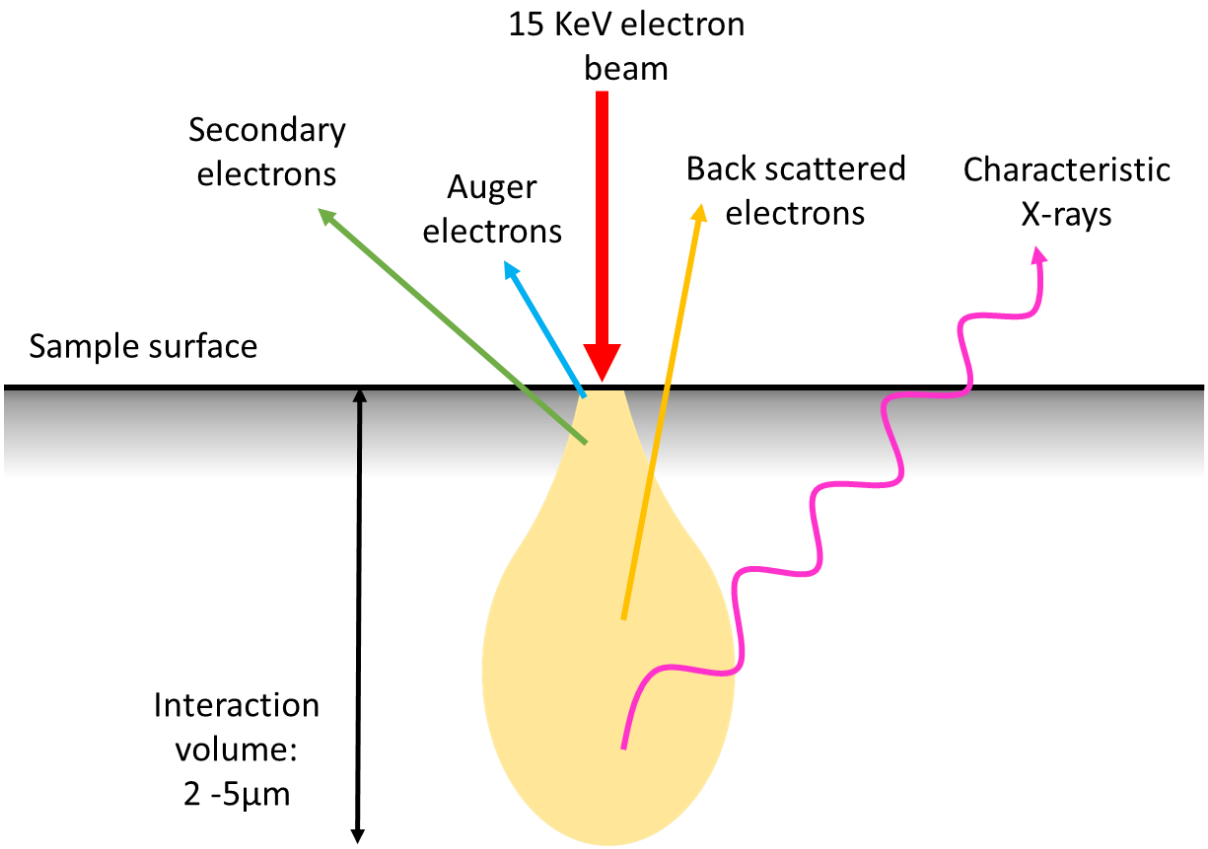

Figure 3.1. Interaction volume and emission depths of electrons and characteristic X-rays in the context of Scanning Electron Microscopy.

3.2.2. X-ray sources

Several of the characterisation methods discussed herein utilise X-rays from different sources: a Cu X-ray tube; a W X-ray tube; synchrotron bending magnets; and synchrotron insertion devices (wigglers and undulators). When discussing X-ray diffraction, and optical set ups, X-rays are treated as waves and discussed with respect to wavelength. Whereas, when discussing the production of X-rays and X-ray absorption spectroscopy, they are treated as particles (X-ray photons) and discussed with respect to energy.

At a synchrotron, electrons are accelerated to relativistic speeds and then forced to follow a curved, rather than a linear, path in a synchrotron storage ring using bending magnets. As a change in direction is equivalent to acceleration, the electrons produce a high intensity beam

of collimated X-ray photons, with a large range of energies, tangential to the electron path, known as synchrotron radiation [2]. X-ray photons can also be produced using insertion devices, wigglers and undulators that also alter the path of the electrons to produce X-ray photons. Beamlines are built along the paths of the X-ray photons and use the synchrotron radiation for a variety of experiments.

In X-ray tubes, electrons are accelerated towards and collide with a metal target, which produces two types of X-ray radiation: continuous radiation, known as Bremsstrahlung radiation, and characteristic radiation, which occurs only at specific wavelengths, dependent on the element used in for the target [3].

Continuous radiation is produced by the incident electrons colliding with the atoms of the target, causing the electrons to decelerate. While decelerating, the kinetic energy of the electron is converted into an X-ray photon and emitted to preserve conservation of energy. The electrons all decelerate differently, so a continuous range of X-ray photons of different energies are produced.

Characteristic radiation occurs when using incident electrons generated above a threshold voltage and is produced by electron bombardment that results in the displacement of core orbital electrons in the atoms of the metal target; the result of which is the production of core-holes. To fill the core-hole a higher energy electron transitions down to the core hole, which requires the electron to release energy in the form of an X-ray photon. As the differences between electron orbitals are discrete, the energies of X-ray photons produced are also discrete and characteristic of both the element from which they are produced and the transition which occurred.

3.2.3. Powder X-ray Diffraction

Powder X-ray diffraction (pXRD) uses X-rays to investigate the long-range structure of materials. In this Thesis, bulk powder X-ray diffraction was performed in reflection mode using an instrument that applied Bragg-Brentano geometry, as described below. A description

of how microfocus X-ray diffraction (μXRD) was achieved at a microprobe beamline is provided later (3.2.5).

An X-ray source is positioned with a sample and detector in Bragg-Brentano geometry; the X-ray source and detector are positioned on the edge of the diffraction circle and top surface of the sample is positioned to be at the centre of the circle. This diffraction method requires monochromatic X-rays, so a filter is used to select a characteristic X-ray wavelength. The X-rays bombard and penetrate the sample and are only scattered back toward the detector when they collide with an atom, at the same angle as the incidence angle. Here, the crystal structure inside a sample is considered to be layers of atoms, or planes of a crystal lattice, and the distance between the layers is referred to d spacing, as shown in Figure 3.2. Diffraction at different depths within the sample causes the scattered X-rays to be out of phase, resulting in destructive interference unless the d spacing and X-ray incidence angle satisfies Bragg's Law (Equation 3.1). If the d spacing and incidence angle (θ) do satisfy Bragg's law, the X-rays scattered by the sample are in phase, resulting in constructive interference. This constructive interference is observed as a peak of intensity in the XRD pattern, these peaks are referred to as reflections. XRD patterns can be used to determine unit cell parameters, phase orientation, structure and composition [3].

$$n\lambda = 2d\sin(\theta) \qquad (3.1)$$

Equation 3.1. Bragg's Law, n – positive integer, λ - wavelength of X-rays, d - spacing between layers of atoms in sample, θ - angle between incident X-rays and sample

The p-XRD data presented in this thesis (Chapter 6) were collected on a Bruker D2 Phaser diffractometer which uses Cu-K_α radiation (λ = 1.5418 Å), a Ni filter and a Lynxeye position sensitive detector. Measurements were made from 5° to 65° 2θ with a step size of 0.02° and a total scan time of 6 hours. Samples were prepared for pXRD by grinding by hand to achieve size reduction, then was deposited in a sample holder and pressed and smoothed with a glass slide to achieve a flat surface.

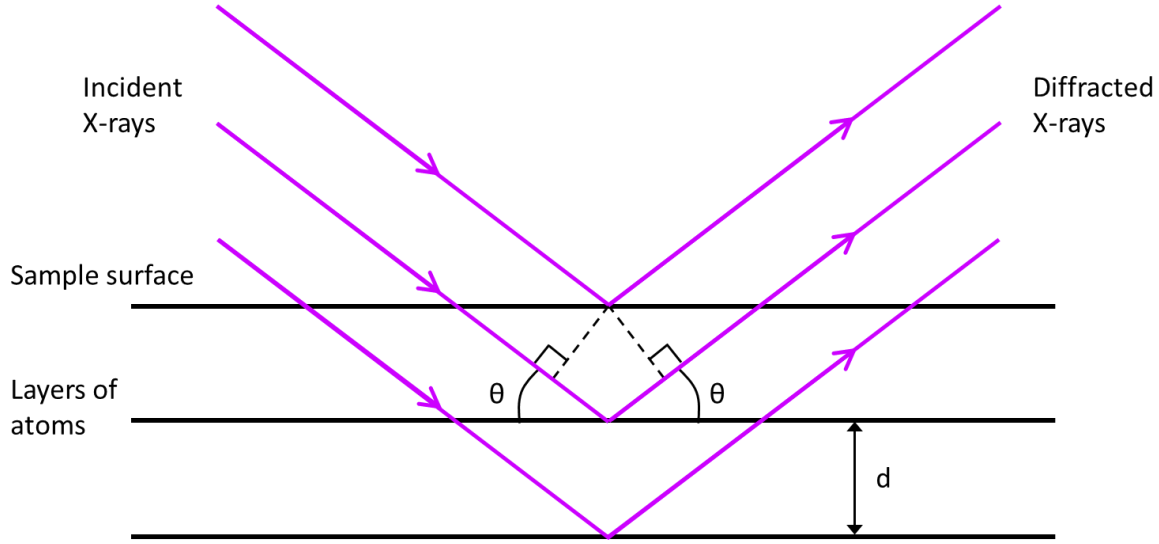

Figure 3.2. Diagram of Bragg diffraction, showing: parallel incident X-rays of the same wavelength; θ – Bragg angle, the angle between the incident X-ray and the sample surface; the layers of atoms in a sample; and d – the regular spacing between atomic layers.

3.2.4. X-ray Absorption Spectroscopy

3.2.4.1. Theory

X-ray absorption spectroscopy (XAS) is an elemental analysis technique that exploits the photoelectric effect and can be utilised to characterise element speciation, local coordination environment, and short-range order. In an XAS measurement, a sample is bombarded by X-ray photons over a range of energies, selected to target a specific element. Core electrons in the atoms of the sample absorb these photons and are excited into the continuum. The ejection of an electron results in the atom assuming an excited state where a core hole is formed and consequently de-excitation occurs, with an electron from a higher energy orbital falling to fill the core hole. During this de-excitation process, energy is released in the form of an X-ray photon, or a second electron is ejected from the atom (referred to as an Auger electron). The energy of electron orbitals and the differences between them are discrete and therefore only specific energies of X-ray photons and are absorbed and emitted. At these discrete energies there will be an increase in X-ray photon absorption, these are referred to as absorption edges. The edges are named with respect to which core orbital the electron

was excited from upon absorption of the incoming X-ray, for example K-edges refer to 1s orbitals (Figure 3.3). The energies of the different orbitals are intrinsically related to the composition of the atom, and therefore are characteristic for different elements. Therefore, measuring an edge probes the transition between orbitals in a given element, so XAS is an element specific technique [3].

From an XAS experiment several different measurements can be performed including transmission mode and fluorescence mode. Transmission mode XAS measurements are made from the initial X-ray photon absorption-excitation event; the energy of incident X-ray photons is varied, and the intensity of the incident X-ray photons (I_0) before the sample and the intensity of X-ray photons transmitted through the sample (I_t) are both measured. These two measurements are used (Equation 3.2) to produce an absorption spectrum (Figure 3.4). Often an in-line reference is collected simultaneously using the same set up to enable energy calibration.

$$\mu(E) = \ln(I_0/I_t) \quad (3.2)$$

Equation 3.2. Equation to calculate absorption ($\mu(E)$) from intensity of incident (I_0) and transmitted X-ray photons (I_t), adapted from the Beer-Lambert law.

X-ray fluorescence measurements probe the secondary transition of an electron dropping down to fill a core hole, which causes the emission of an X-ray photon to be released. The intensity of incident X-ray photons (I_0) and the intensity of X-ray photons emitted from the sample (I_f) are both measured, which can be used to calculate (Equation 3.3) an estimate of absorption. There are two types of fluorescence measurement: partial fluorescence yield (PFY), where at each incidence energy of X-ray photons, only the intensity of emitted X-ray photons with a specific energy are measured; and total fluorescence yield (TFY), where the total intensity of all emitted X-ray photons is measured at each incidence energy of X-ray photons [4].

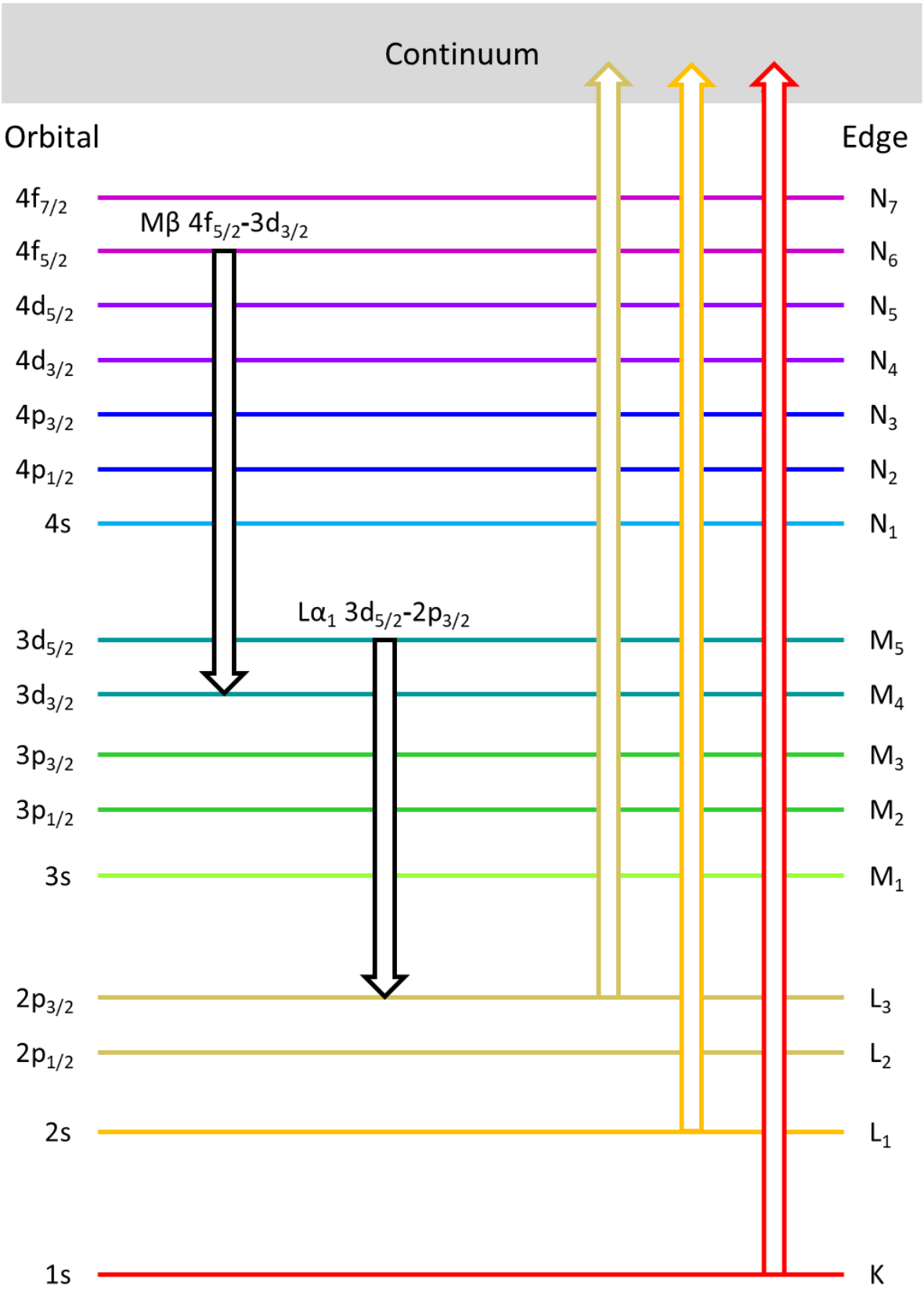

Figure 3.3. Diagram of orbitals and their respective edges, with the arrows to indicate transitions for the K, L_1 and L_3 edges and the $L_{\alpha 1}$ and M_β emission lines.

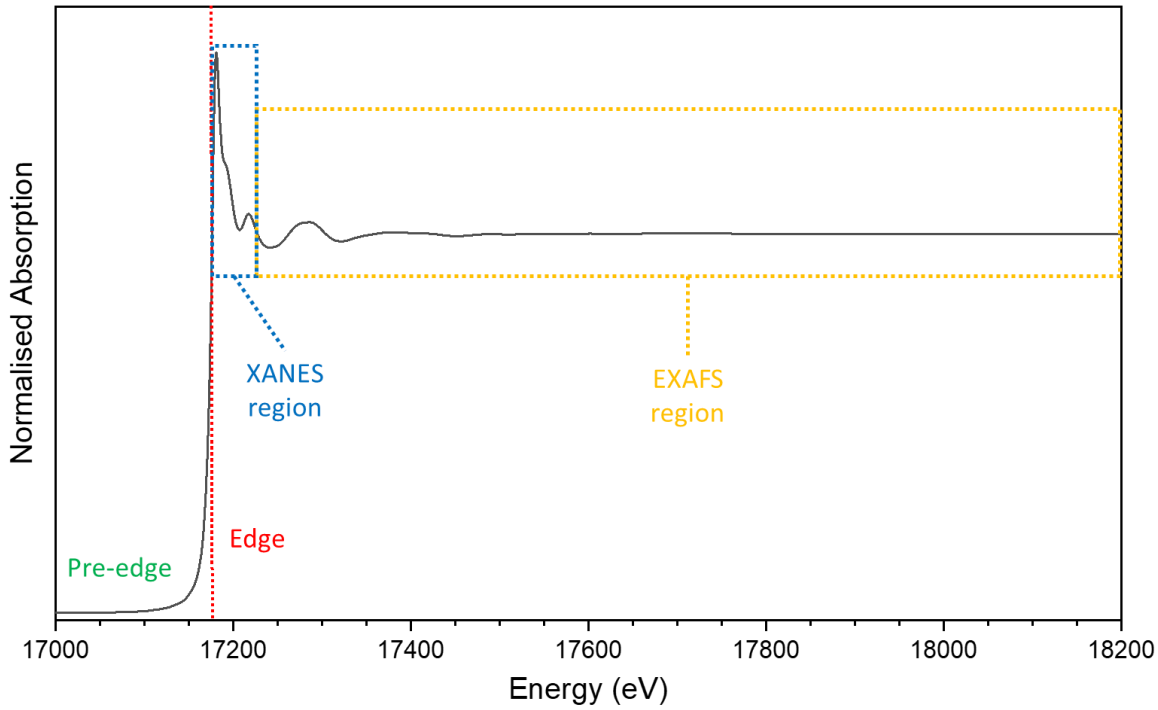

Figure 3.4. Example of XAS data collected at U L_3-edge, with pre-edge, edge, XANES and EXAFS regions indicated.

$$\mu(E) \propto I_f/I_0 \qquad (3.3)$$

Equation 3.3. Equation to calculate absorption (μ(E)) from intensity of incident (I0) and emitted X-ray photons (I_f) [5].

3.2.4.2. The XAS spectrum

An XAS spectrum has several different regions: the pre-edge, the edge, the X-ray absorption near edge structure (XANES) and the extended X-ray absorption fine structure (EXAFS) (Figure 3.4). The XANES region generally covers the range from the edge to 50 eV past the edge, the EXAFS region is from 50 eV past the edge to 1000 eV past the edge. XAS data shown here has been normalised, pre-edge region is fit with a linear component and set to 0 and the post-edge region (XANES and EXAFS) is fit with a polynomial and set to 1, the net increase in absorption between the pre- and post-edge region is referred to as an edge step.

3.2.4.3. Absorption edge characterisation

Both the shape and position of the edge are characteristic of the environment experienced by the element; what oxidation state it is in and what other atoms surround it. Oxidation state affects the energy required to excite the electron, and therefore the position of the absorption edge. The position of the absorption edge, E_0, can be quantified in several different ways.

- E_0 first derivative - the point at which the absorption edge is steepest, which can be found from the maxima in the first derivative or point at which y = 0 in the second derivative. However, if the data collected has a lot of noise, or a low energy resolution, this reduces the accuracy of calculating E_0 using this method. In addition, the presence of pre-edge features can make it difficult to identify the steepest point, or rather, where the steepest point would be without the effect of pre-edge features on the shape of the edge. This in turn reduces the confidence in conclusions drawn from comparison with the E_0 values of other absorption edges without pre-edge features.

- E_0 half - which uses a normalised XAS spectrum and takes the energy value of the edge at which normalised adsorption is 0.5, known as the E_0 half. The value of 0.5 is arbitrary, any value if used consistently for a data set would allow comparison, but 0.5 has been standardised. This point should be independent of effects from noise and

from pre-edge and peak features. The E_0 half values however are highly dependent on the quality of the normalisation of the data, which is affected by human error.

- The E_0 value can also be quantified as the white line, the maximum of absorption. As with using the 1st derivative this is simple to measure however it is also affected by noise and the step size used to collect the data. Furthermore, the peak after the absorption edge can have a multimodal shape, which can make it difficult to differentiate where to assign the true white line position.

The choice of E_0 position with which to analyse data varies throughout the literature, some particular edges may have an E_0 type commonly accepted for use by an academic community, however there are no rules which govern choice, no estimate of edge position has been identified as more or less valid, and all are merely attempts to define the true edge position, so it is always important to always state how E_0 position was assigned.

3.2.4.4. Pre-edge feature characterisation

For spectra collected from certain edges and elements, such as the K-edges from transmission metals including Ti [6] and Fe [7], speciation can also be investigated using features which occur before the white line, these features are referend to as pre-edge or edge features. The intensity and position of pre-edge features, which are determined by peak fitting (Gaussian, Pseudo-Voigto or Lorentzian), have been found to be characteristic of both oxidation state and coordination [6, 7].

3.2.4.5. XANES Characterisation

Features in the XANES region of some spectra can be characteristic of element oxidation state and coordination. These include Ce and U L_3-edge data; the shape of features in the Ce L_3-edge XANES from Ce^{3+} and Ce^{4+} containing material are significantly different and have been attributed to different electron orbital transitions [8], and are therefore characteristic of Ce

oxidation state. Techniques such as linear combination fitting (LCF) or iterative target transformation factor analysis (ITTFA) can be applied to quantify the relative fraction of each characteristic feature in the XANES region of a Ce L_3-edge spectra, and therefore determine the relative concentrations of Ce^{3+} and Ce^{4+} present in a sample. Additionally, at the U L_3-edge two specific features (which occur between 17184.0 and 17202.0 eV and 17205.0 and 17230.0 eV respectively) have been found to be diagnostic of the presence of uranyl speciation [9].

3.2.4.6. EXAFS characterisation

Oscillations in the EXAFS region are caused by photoelectron scattering. The X-ray absorbing atom ejects an electron, which then scatters off nearby atoms before returning to the initial absorbing atom. The electron can be treated as a wave and on its return to the absorbing atom can produce constructive or destructive interference. Constructive interference creates greater electron density at the absorbing atom and therefore a higher probability of X-ray absorption which results in a peak in the EXAFS region. Destructive interference creates lower electron density at the absorbing atom and therefore a lower probability of X-ray absorption resulting in a trough in the EXAFS region. The result of this is the EXAFS region which can be modelled as a combination of sinusoidal waves, with each individual component coming from single or multiple scattering pathways from the elements that surrounding the central absorbing atom. Depending on the distance and position of the atoms surrounding the absorbing atom different interference patterns and therefore EXAFS will occur. Therefore, the EXAFS region of the XAS spectrum is characteristic of the sample's structure.

To interpret this data, attempts are made to replicate the EXAFS region using the EXAFS equation to reproduce the oscillations of different scattering paths, and sum them to recreate the overall fit, a simplified version of this is shown in Equation 3.4. Here only single scattering paths are considered.

$$\chi(k) = S_0^2 \sum_i N_i \frac{f_i(k)}{kd_i^2} e^{\frac{2d_i}{\lambda(k)}} e^{-dk^2\sigma_i^2} \sin\left(2kd_i + \delta_i(k)\right) \quad (3.4)$$

Equation 3.4. The EXAFS equation, with notation from Calvin [10], k = wavenumber, other terms discussed below

For each path, a series of parameters, which describe the scattering path must be fit.

N – The number of scattering atoms present, often the coordination number, also referred to as the degeneracy.

d – The half length of the path, for a single scattering path it can be treated as the distance between the absorption and scattering atom.

σ^2 – Mean square relative displacement, also known as the Debye-Waller factor, the variance in the half path length, a measure of static and thermal disorder.

S_0^2 – The amplitude reduction factor, this accounts for the difference between the initial and final state of the absorbing atom, this difference is caused by a large range of different intrinsic losses so this is a complex term [10].

When modelling EXAFS spectra (i.e. the process of EXAFS fitting), the same S_0^2 value is applied to all the paths, in addition another parameter ΔE_0 is also applied to the fit, this parameter accounts for any difference between the selected edge position of the data and the edge position of the calculated fit.

3.2.5. Spatially-resolved X-ray techniques

Spatially-resolved XAS techniques, which can be performed at a microprobe beamline, utilise an X-ray beam with a smaller spot size, which is focused by Kirkpatrick-Baez mirrors, to investigate specific areas or spatial variation within a sample [11]. Several X-ray measurements can be made, including microfocus XAS (μXAS), microfocus XRD (μXRD), and microfocus X-ray fluorescence spectroscopy (μXRF). The μXAS data discussed in Chapter 5 were produced from fluorescence mode, TFY measurements.

X-ray fluorescence (XRF) measurements also probe the secondary transitions after electron excitation. A sample is bombarded with X-ray photons of a fixed energy and the intensity of X-ray photons emitted at different energies is measured. As the energies of emitted X-ray photons are characteristic of different elements, peaks can be observed in an X-ray fluorescence spectrum, referred to as emission lines, which diagnostic of the elements present within a sample. An XRF spectrum cannot be quantitatively analysed without the use of well quantified reference compounds, but comparison of spectra indicates relative differences in concentration of elements. Which elements can be detected by XRF is limited by the energy of incident X-ray photons, so the incident energy used should always be given [12].

The μXRD measurements performed in this Thesis were performed at a microprobe beamline and so do not use the same instrumentation and geometry as pXRD discussed above. Here, XRD data were collected in transmission. The sample is positioned perpendicular to the monochromatic X-ray beam and X-rays, which pass through the sample, are either directly transmitted or are diffracted at specific angles dependant on the d spacing (Equation 3.2). Diffracted X-rays occur as cones projecting from the sample (Figure 3.5a) and a detector positioned perpendicular to the X-ray beam (parallel to the sample) intersects the diffraction cones. This allows for the observation of the diffraction cones as circular rings, known as Debye-Scherrer rings, or more commonly referred to as 2D diffraction patterns [13]. For thin section mineral samples, crystals within a sample are often preferentially orientated in specific directions, which results in hot spots of diffraction on a diffraction cone, rather than a diffuse ring (Figure 3.5a). Using the known dimensions of the Debye-Scherrer rings, and the

distance between the sample and the detector, the angle of diffraction for each ring can be calculated, and the data are processed to produce an intermediate 2D diffraction data 'cake' (Figure 3.5b) and then further processed to produce 1D diffraction patterns (Figure 3.5c).

It is possible to also collect µXRF and µXRD in mapping mode, where the sample is moved in front of the beam to achieve a raster-like motion, and µXRF or µXRD data are collected at regular spatial integrals to produce a mapped area of interest which has an µXRF spectra or µXRD pattern for each point.

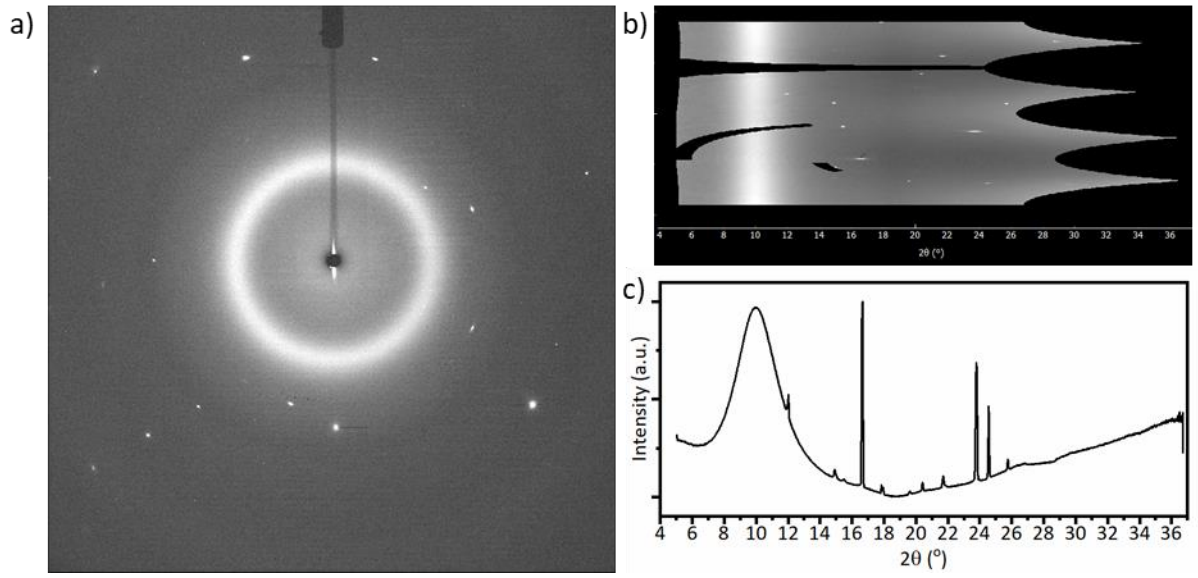

Figure 3.5. (a) Example of 2D diffraction patterns collected at the X-ray Fluorescence Microprobe (XFM) beamline, National Synchrotron Light Source II (NSLS-II), Brookhaven National Lab (BNL), USA, collected from mineral thin section, showing diffuse scattering (glass slide) and preferred orientation (diffraction spots) **(b)** partially processed 2D diffraction data 'cake', **(c)** the resultant 1D diffraction data.

3.2.6. Laboratory based XAS

Laboratory XAS instruments exploits Bragg's Law to select photon energy [14]. The detector, sample and monochromator (a spherically bent crystal analyser (SBCA)) are all positioned in

Rowland circle geometry, shown in Figure 3.6. The Rowland circle radius is the same as the SBCA's radius of curvature and, for the instrument used in Chapters 4 and 7, this is 1 m. The continuous X-ray source (X-ray tube) is dispersive, not collimated, so a spherically bent crystal analyser (SBCA) is used to both discriminate in energy and focus the dispersed X-ray photons to a point on the sample, increasing the intensity and improving efficiency of the instrument. As incident X-rays to the SBCA, which has a fixed d spacing, are dispersed and have a range of wavelengths, at a given angle only one wavelength (λ) of X-rays (and any harmonics with wavelengths of nλ) will be diffracted. Therefore, by moving the sample and detector to change the angle while maintaining a Rowland circle geometry with a radius of 1m, it is possible to scan in energy [14]. The energy range which can be measured is limited by the range of motion of the detector (55-85° for the instrument used in this Thesis) and the availability of monochromator crystals with different d spacings. Due to the significantly lower intensity X-ray source used and the use of a single detector, it is not possible to measure I_0, I_t and a reference material on the laboratory spectrometer described here. However, absorption is still calculated as described above in Equation 3.2.

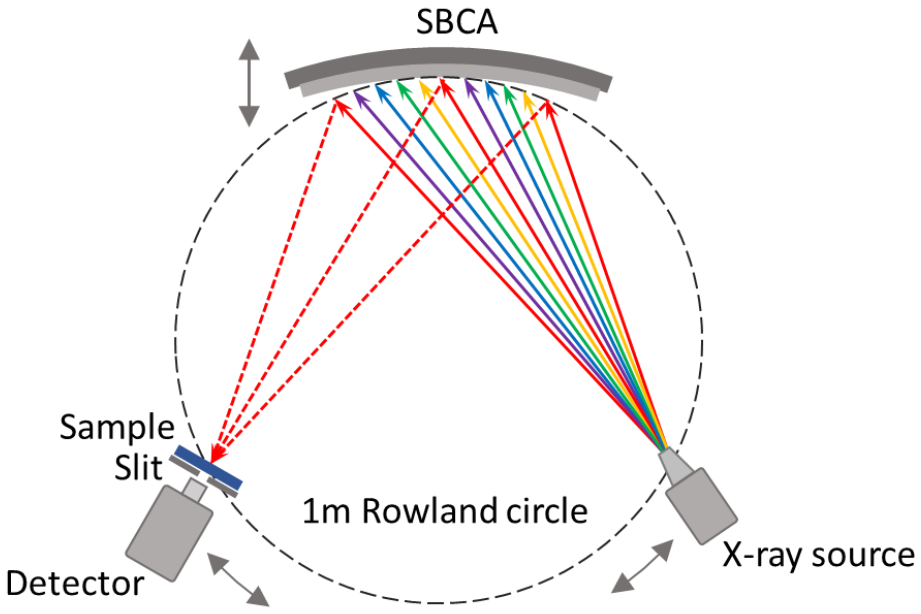

Figure 3.6. Simplified diagram of Rowland circle geometry for transmission X-ray absorption spectroscopy, taken from Mottram *et al.* [15] (Chapter 7.1).

3.2.7. High Energy Resolution Fluorescence Detected XAS

High Energy Resolution Fluorescence Detected (HERFD) XAS is a fluorescence, PFY technique that measures the intensity of X-ray photons emitted at a single chosen energy associated with a specific secondary transition [5]. This reduces the effects of core-hole lifetime broadening, which is thoroughly discussed in Chapter 4. Only the intensity of X-ray photons emitted at a selected energy are measured at each incident photon energy and this is achieved by use of an energy discriminating detector. In Chapters 4 and 5, the energy detectors used are a Johann-type spectrometer arranged to collect X-ray emission spectroscopy (XES) data. The sample, spherically bent crystal analysers (SBCA) and detector are arranged in Rowland circle geometry as shown in Figure 3.7, similar to that described for Laboratory XAS, enabling the selection of a specific wavelength, and therefore energy of X-ray photon. HERFD XAS also requires a higher energy resolution of incident X-ray photons, which can be achieved by using additional monochromators [16] [17].

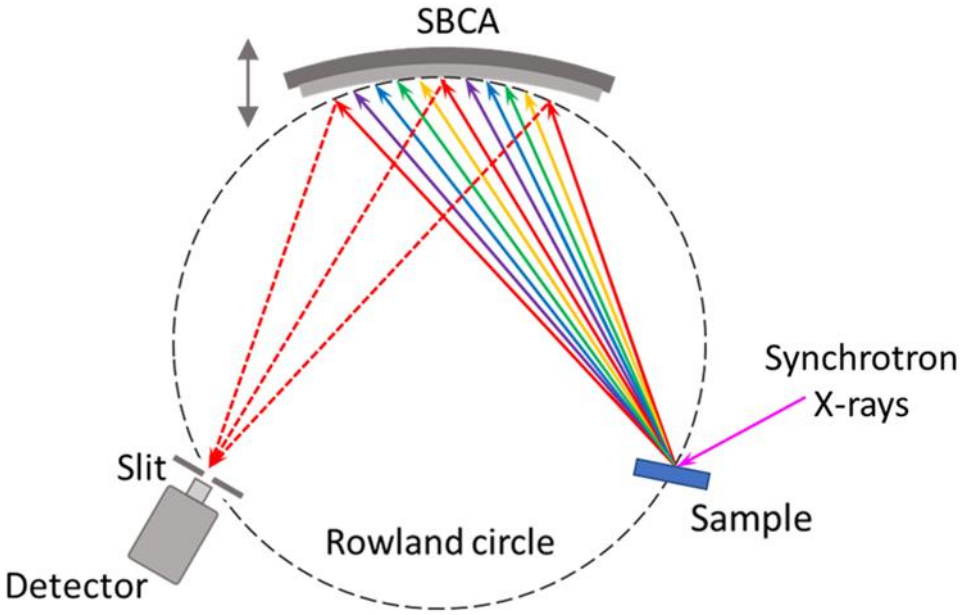

Figure 3.7. Simplified diagram of Rowland circle geometry for X-ray emission spectroscopy, as is used as a discriminating energy detector for HERFD measurements.

3.3. References

[1] R.F. Egerton, Physical principles of electron microscopy : an introduction to TEM, SEM, and AEM, Springer, New York, NY, 2005.

[2] P. Willmott, An introduction to synchrotron radiation : techniques and applications, Wiley, Chichester, West Sussex, U.K., 2011.

[3] D. McMorrow, J. Als-Nielsen, Elements of modern X-ray physics, John Wiley, Chichester, West Sussex, 2011.

[4] P. Glatzel, T.C. Weng, K. Kvashnina, J. Swarbrick, M. Sikora, E. Gallo, N. Smolentsev, R.A. Mori, Reflections on hard X-ray photon-in/photon-out spectroscopy for electronic structure studies, J. Electron Spectrosc. Relat. Phenom. 188 (2013) 17-25.

[5] W. Grunert, K. Klementiev, X-ray absorption spectroscopy principles and practical use in materials analysis, J. Taibah Univ. Med. Soc. 5(4) (2020) 35.

[6] F. Farges, G.E. Brown, J.J. Rehr, Ti K-edge XANES studies of Ti coordination and disorder in oxide compounds: Comparison between theory and experiment, Phys. Rev. B 56(4) (1997) 1809-1819.

[7] M. Wilke, F. Farges, P.E. Petit, G.E. Brown, F. Martin, Oxidation state and coordination of Fe in minerals: An FeK-XANES spectroscopic study, Am. Miner. 86(5-6) (2001) 714-730.

[8] A. Bianconi, A. Marcelli, H. Dexpert, R. Karnatak, A. Kotani, T. Jo, J. Petiau, Specific intermediate-valence state of insulating 4f compounds detected

by L_3 x-ray absorption, Phys. Rev. B 35(2) (1987) 806-812.

[9] M.A. Denecke, T. Reich, M. Bubner, S. Pompe, K.H. Heise, H. Nitsche, P.G. Allen, J.J. Bucher, N.M. Edelstein, D.K. Shuh, Determination of structural parameters of uranyl ions complexed with organic acids using EXAFS, J. Alloy. Compd. 271 (1998) 123-127.

[10] S. Calvin, XAFS for Everyone, Taylor and Francis, Boca Raton, 2013.

[11] D. Grolimund, M. Senn, M. Trottmann, M. Janousch, I. Bonhoure, A.M. Scheidegger, M. Marcus, Shedding new light on historical metal samples using micro-focused synchrotron X-ray fluorescence and spectroscopy, Spectroc. Acta Pt. B-Atom. Spectr. 59(10-11) (2004) 1627-1635.

[12] S. Majumdar, J.R. Peralta-Videa, H. Castillo-Michel, J. Hong, C.M. Rico, J.L. Gardea-Torresdey, Applications of synchrotron mu-XRF to study the distribution of biologically important elements in different environmental matrices: A review, Anal. Chim. Acta 755 (2012) 1-16.

[13] N. Tamura, M. Kunz, A concise synchrotron X-ray microdiffraction field guide for the Earth scientists, Bol. Soc. Geol. Mex. 67(3) (2015) 467-478.

[14] G.T. Seidler, D.R. Mortensen, A.J. Remesnik, J.I. Pacold, N.A. Ball, N. Barry, M. Styczinski, O.R. Hoidn, A laboratory-based hard x-ray monochromator for high-resolution x-ray emission spectroscopy and x-ray absorption near edge structure measurements, Rev. Sci. Instrum. 85(11) (2014) 12.

[15] L.M. Mottram, M.C.D. Wilkins, L.R. Blackburn, T. Oulton, M.C. Stennett, S.K. Sun, C.L. Corkhill, N.C. Hyatt, A Feasibility Investigation of Laboratory Based X-ray Absorption Spectroscopy in Support of Nuclear Waste Management, MRS Adv. 5(1-2) (2020) 27-35.

[16] S. Hayama, G. Duller, J.P. Sutter, M. Amboage, R. Boada, A. Freeman, L. Keenan, B. Nutter, L. Cahill, P. Leicester, B. Kemp, N. Rubies, S. Diaz-Moreno, The scanning four-bounce monochromator for beamline I20 at the Diamond Light Source, J. Synchrot. Radiat. 25 (2018) 1556-1564.

[17] A.C. Scheinost, J. Claussner, J. Exner, M. Feig, S. Findeisen, C. Hennig, K.O. Kvashnina, D. Naudet, D. Prieur, A. Rossberg, M. Schmidt, C.R. Qiu, P. Colomp, C. Cohen, E. Dettona, V. Dyadkin, T. Stumpf, ROBL-II at ESRF: a synchrotron toolbox for actinide research, J. Synchrot. Radiat. 28 (2021) 333-349.

4. Comprehensive evaluation of X-ray absorption spectroscopy approaches and instrumentation to derive uranium speciation

L. M. Mottram[1], L. T. Townsend[1], L. J. Gardner[1], D. J. Bailey[1], A. S. Yorkshire[1], K. Kvashnina[2,3], J. F. W. Mosselmans[4], B. Ravel[5,6], M. C. Stennett[1], N. C. Hyatt[1] and C. L. Corkhill[1]

[1]NucleUS Immobilisation Science Laboratory, Department of Materials Science and Engineering, University of Sheffield, S1 3JD, UK

[2]Helmholtz-Zentrum Dresden-Rossendorf (HZDR), Institute of Resource Ecology, PO Box 510119, 01314, Dresden

[3]The Rossendorf Beamline at ESRF – The European Synchrotron, CS40220, 38043 Grenoble Cedex 9, France

[4]Diamond Light Source, Harwell Science and Innovation Campus, Didcot, UK

[5]Brookhaven National Laboratory, NSLS-II, Upton, NY 11973, USA

[6]Material Measurement Science Division, Material Measurement Laboratory, National Institute of Standards and Technology, Gaithersburg, MD 20899, USA

Abstract

X-ray absorption spectroscopy (XAS) measurements have been collected from a set of uranium (U) reference compounds at the U L_1, U L_3 and U M_4-edge. Different measurement approaches (transmission and high energy resolved fluorescence detected (HERFD) XAS) and different instrumentation (synchrotron and laboratory spectrometers) have been applied to a suite of U reference compounds to enable comparison and establish the capabilities of each technique. Of all the measurements the U L_3-edge transmission data were found to provide the widest range of information about the U environment, including structural information from fitting the EXAFS region. The U L_3-edge transmission XANES data collected on a lab spectrometer were in excellent agreement with U L-edge transmission data collected on a synchrotron, and provide an appealing alternative to a synchrotron measurement, apart from the lack of EXAFS measurement. The best estimates of U oxidation state by edge position can be obtained using the edge position at intensity = 0.5 (E_0 half) on the U L_3-edge HERFD XANES data and the first peak in the first derivative (E_0 1^{st} deriv.) To determine the presence of different U oxidation states in a sample and confirm the presence of U^{5+} analysis of U M_4-edge HERFD XANES data is required. An investigation into U environment using XAS should ideally utilise multiple different measurements to increase the amount of different information which can be discerned. Such findings are of key importance as the characterisation of U speciation is relevant to nuclear waste management, contaminated land studies, and fundamental uranium chemistry.

4.1. Introduction

X-ray absorption spectroscopy (XAS) is a unique tool that enables the investigation of U oxidation state, speciation and short-range structure. This is pertinent to a range of disciplines within the nuclear fuel cycle including mining, fuel fabrication and reprocessing, radioactive waste management and disposal, contaminated land studies, and also pure U chemistry. Many stages of the U nuclear fuel cycle are dependent on the speciation of U: U^{6+} (as uranyl (UO_2^{2+})) is more soluble and, therefore, more environmentally mobile, than the relatively insoluble U^{4+}, which exists as non-crystalline or crystalline uraninite (UO_2) [1]. This fundamental chemistry is exploited during mining, extraction and reprocessing but may be detrimental for waste disposal or in the case of accidental release or contamination. Uranium is also used as a surrogate for Pu in Pu research, the plutonyl Pu^{6+} speciation is more mobile than plutonate Pu^{4+} [2], similar to U. For environmental chemistry Pu^{3+}, which is stable under reducing conditions [2], is also of interest. As such, XAS has been extensively utilised to investigate the speciation of U (and to infer the speciation of Pu) in potential wasteforms [3-16], to predict their performance in geological disposal facilities [4, 17-19], and has also been utilised in nuclear fuel research [20-22]. In contaminated land studies, XAS has been applied to investigate the environmental behaviour of U as a contaminant [19, 23] in addition to gaining an understanding of the mechanisms of potential remediation technologies [24]. Spectroscopy also facilitates chemical research to gain a better understanding of the complex chemistry of U; the U electronic structure, the occurrence of U^{5+} and how 5f orbital electrons act during bonding [25-33].

X-ray absorption spectroscopy exploits the photoelectric effect; measuring the intensity and energies of X-ray photons before and after being passed through a sample, as electron orbitals are discrete and characteristic to each element at a known energy it is possible to probe the excitation of electrons from specific orbitals, known as edges, to unoccupied orbitals [34, 35]. Examination of the excitation or other transitions of an electron provides understanding of the oxidation state, coordination and the short-to-medium range structure of an element with a sample.

The main edges commonly used to investigate U speciation are the U L_3 ($2p_{3/2}$) and U M_4-edge ($3d_{3/2}$). Uranium L_3-edge transmission XAS involves the direct measurement of absorption, as described above, and it is possible to collect both data in the X-ray absorption near edge structure (XANES) and extended X-ray absorption fine structure (EXAFS), which provide information about U speciation and short-range structure [36]. The U M_4-edge is typically investigated with high energy resolution fluorescence detected (HERFD) XAS measurements [13, 25, 27, 29, 37-44]. A HERFD measurement enables the resolution of features that could not be observed in a standard transmission XAS experiment. This is achieved by measuring a different, secondary transition [35] and using instrumentation with an energy resolution equal to or less than the core-hole lifetime broadening [45]. For example, U M_4-edge HERFD data can be measured by fixing the emission energy to that of the U M_β emission line ($4f_{5/2}$-$3d_{3/2}$), rather than the U M_4 edge ($3d_{3/2}$), so broadening of features is dependent on the core-hole lifetime of the $4f_{5/2}$ orbital (23.12 fs, 0.27 eV) rather than that of the $3d_{3/2}$ orbital (1.77 fs, 3.54 eV), which is shorter and therefore causes greater broadening. Combined with instrumentation that provides high energy resolution, features are better resolved. Notably, unlike a transmission XAS measurement that measures the intensity of all photons transmitted by the sample at each incident photon energy, HERFD measures the intensity of emitted photons with a single fixed energy, or fixed transfer energy and, as such, is known as a partial fluorescence yield technique (PFY) [45]. Therefore, a HERFD spectrum is not a representation of a transmission XAS spectrum and the two cannot be directly compared, though HERFD in of itself can still provide important information relating to speciation (oxidation state and coordinating ligands). Other measurements used to investigate U environment include: U L_1-edge (2s), U L_1-edge HERFD ($L_{\beta4}$, $3p_{1/2}$-$2s_{1/2}$) [46], U L_2-edge XANES ($2p_{1/2}$) [47], U L_3-edge HERFD (U $L_{\alpha1}$, $3d_{5/2}$-$2p_{3/2}$ [27, 46], U $L_{\beta2}$, 4d-$2p_{3/2}$ [37] and $L_{\beta5}$, 5d-$2p_{3/2}$ [37]), U $N_{4,5}$-edge XAS (4d) [20] and also XAS of ligand K-edges (1s), such as O K-edge XAS [44].

To perform XAS experiments, the most common method is to utilise one of the many international synchrotrons that are central user facilities and, as such, require successful allocation of time through a competitive process. Such central user facilities are often oversubscribed and highly competitive. If successful, the time between application and conducting an experiment can be several months or longer. This can cause a significant delay

in a research timeline, especially in areas of research such as actinide wasteforms where the optimisation of a composition or process is achieved through the iterative production and characterisation of samples. Furthermore, access for radioactive work is limited by the number of beamlines with the capabilities to handle radioactive material [36] in addition to restrictions on the amount and activity of samples permitted by the synchrotron facility or transportation requirements. As such, laboratory X-ray spectroscopy instruments provide a promising approach to complement the available options for characterisation in actinide research [48], enabling quick access to U L_3-edge XAS. Having confidence in the accuracy and precision of these instruments when compared to synchrotron XAS is imperative in developing and utilising lab-based techniques. Thus far, U L_3-edge XAS data have been successfully collected from reference compounds [49, 50] and also wasteform relevant materials with lower U concentrations [13, 51] using laboratory instruments.

Here, a variety of XAS measurements were undertaken using a comprehensive suite of U-containing reference compounds: multiple U edges, U L_1, U L_3 and U M_4; different techniques, transmission XAS and HERFD-XAS; different data ranges, XANES and EXAFS; and different instrumentations, three synchrotron facilities, five beamlines and one laboratory instrument, to enable comparison between measurements, identify what can be achieved from each technique and which may be complimentary.

4.2. Materials and methods

4.2.1. Reference Compounds

The suite of reference compounds, comprising a range of U oxidation states and coordination environments (Table 1), were either obtained from stock material (UO_2, purchased from International Bio-Analytical Industries, Inc. with a 99.99% purity and metaschoepite ($(UO_2)_8O_2(OH)_{12}\cdot 10H_2O$))), mineral samples (soddyite ($(UO_2)_2SiO_4\cdot 2H_2O$)) or synthesised (UTi_2O_6, $CrUO_4$, $USbO_5$, $LaUO_4$, U_3O_8 $MgUO_4$, $BaUO_4$, Ca_3UO_6, $SrUO_4$, $CaUO_4$ and $UMoO_6$). For the latter, the synthesis routes have been previously described [11, 52, 53]. The soddyite mineral was obtained from Excalibur minerals Co. and originated from Musonoi Mine, Kolwezi, Lualaba Province, DR Congo. Material was collected from the mineral sample using a titanium needle.

4.2.2. X-ray absorption spectroscopy

XAS measurements were conducted at several different beamlines, including: B18, Diamond Light Source (DLS), UK; I20-scanning, Diamond Light Source (DLS), UK; BM20, The Rossendorf Beamline, European Synchrotron Radiation Facility (ESRF), France; and X-23A, National Synchrotron Light Source (NSLS), Brookhaven National Laboratory, USA (Table 2). Data were also collected using an easyXES100-extended laboratory X-ray spectrometer, at the University of Sheffield. The configuration of each beamline / instrument is given in Table 2. All beamlines utilised a double crystal Si monochromator with collimating and focusing mirrors to configure synchrotron radiation for measurements.

All XAS transmission measurements used three ion chambers, positioned before the sample, after the sample and after both the sample and a reference foil, enabling the near-simultaneous measurement of I_0, I_t and I_r. The sample and foil were both orientated perpendicular to the beam.

The high energy resolved fluorescence detected (HERFD) XAS measurements were performed at I20-scanning (DLS) and the Rossendorf Beamline (BM20, ESRF). HERFD measurements were

collected using an emission spectrometer. Both beamlines used a vertically orientated Johann-type spectrometer, in which the sample, spherically bent crystal analysers (SBCA) and detector are arranged in Rowland circle geometry to enable the collection of XES data with a fixed emission energy.

For the U L_3-edge HERFD experiment at I20-scanning (DLS) the data were collected at an emission energy of 13614.10 eV, the maximum intensity of the U $L_{\alpha 1}$ emission line ($2p_{3/2}$-$3d_{5/2}$). The high energy resolution required for HERFD was provided by a four bounce crystal monochromator [54], consisting of two double Si(111) counter-rotating crystals. The sample was orientated at 45^o to the incident beam, the vertical Rowland circle was orientated at 90^o to the incident beam. To reduce the loss of photons, a He bag was positioned in the beam flight path between the sample, SBCAs and the detector. To prevent photon-induced reduction of U in the sample, or any other potential damage, the sample was moved between each measurement so that a fresh region was always in the path of the beam.

For the U M_4-edge HERFD experiment at BM20 (ESRF) the data were collected at an emission energy of 3337 eV, the maximum intensity of the U M_β emission line. The five striped Si(220) SBCAs were aligned at a 75^o Bragg angle and had a curvature and were positioned on a Rowland circle with a radius of (1.0 m) [55]. Helium was used to reduce resistance and photon loss.

The laboratory instrument (easyXES100-extended) is also a Johann-type spectrometer; however, for XAS measurements Rowland circle geometry and SBCAs are employed to select the incident energy and optimise the number of photons which arrive at the sample, enabling energy scanning measurements using a low power dispersive X-ray source [56]. The X-ray source (100 W Pd X-ray tube), SBCA and sample are arranged on the Rowland circle, with the detector positioned directly behind the sample to collect XAS transmission data. A He tank provided a photon flight path with reduced resistance and photon loss. This instrumentation requires the separate, consecutive measurement of I0, It and Ir scans, additional I0 and It scans were also collected with the detector offset at 4.00^o to enable correction for leakage effects [51].

Table 4.1: List of U reference compounds, oxidation states, coordination number and the instruments on which they were measured. Trans = transmission.

	Instrument		DLS B18	DLS B18	DLS I20	ESRF BM20	NSLS 6BM	EasyXES 100-extended
	Edge/Transition		U L_1	U L_3	U L_3 $L_{\alpha1}$	U M_4 M_β	U L_3	U L_3
	Measurement type		Trans	Trans	HERFD	HERFD	Trans	Trans
Standard	**Oxidation state**	**Coordination number**						
UTi_2O_6	4	6	Y	Y	Y	Y	Y	Y
UO_2	4	8	Y	Y	Y	Y	Y	Y
U_4O_9	4.5	8				Y	Y	
KUO_3	5	6				Y		
$CrUO_4$	5	6	Y	Y	Y	Y		Y
$USbO_5$	5	7	Y	Y	Y	Y		Y
$LaUO_4$	5	8	Y	Y	Y	Y		Y
β-U_3O_8	5.33	6.67	Y			Y	Y	
$MgUO_4$	6	6		Y	Y			
$BaUO_4$	6	6	Y	Y	Y	Y		Y
α-Ca_3UO_6	6	6	Y	Y	Y	Y	Y	Y
α-$SrUO_4$	6	8	Y	Y	Y	Y		Y
$CaUO_4$	6	8	Y	Y	Y	Y	Y	Y
Metaschoepite $(UO_2)_8O_2(OH)_{12} \cdot 10H_2O$	6	7	Y	Y	Y	Y	Y	Y
$UMoO_6$	6	7	Y	Y	Y	Y		Y
Soddyite $(UO_2)_2SiO_4 \cdot 2H_2O$	6	7		Y	Y			Y

Table 4.2: Details of instruments / beamlines utilised to collect XAS data for U reference compounds. vert. – vertical; horiz. – horizontal; DMC – Double monochromator crystal; DMM – double multilayer monochromator

Instrument	**B18 (DLS)**	**B18 (DLS)**	**I20 (DLS)**	**BM20 (ESRF)**	**X-23 (NSLS)**	**EasyXES-100 extended**
Edge	**U L_1**	**U L_3**	**U L_3**	**U M_4**	**U L_3**	**U L_3**
Source						
Type	Bending magnet	Bending magnet	Wiggler	Short Bending magnet	Bending magnet	W anode X-ray tube
Source energy (GeV)	3	3	3	6	2.8	25 $x10^{-6}$
Source current (mA)	300	300	300	200	300-150	3.2
Theoretical maximum flux (photons.s^{-1})	5 x 10^{11}	5 x 10^{11}	1 x 10^{12} (at 10 keV)	1.4x10^{13} (at 18 keV)	6 x 10^{9} (at 8 keV)	5 x10^{4} (6-8 keV, 85°)
Optics						
Collimating mirror (orientation, shape,	flat cylindrically bent	flat, cylindrically bent	upwards deflecting vert. downwards deflecting, flat	Vert.	None*	-
coating)	Pt	Pt	Rh	Rh/Si/Pt		
Monochromator	DMC Si(111)	DMC Si(111)	2x DMC Si(111)	DMC Si(111) and DMM	Si(311)	-
Focusing mirrors (orientation,			horiz. long sagittal focusing cylinder	vert./horiz.		
shape,	double bent cylinder	double bent cylinder	vert. flat, mechanically deformed	double-toroid	none	-
coating)	Pt	Pt	Rh	Rh/Pt		
Harmonic rejection	-	-	Si	-		-
Spot size (h x v) (µm)			< 1x1mm	21 x 69	10,000 x 500	
Measurement						
mode	Transmission	Transmission	HERFD	HERFD	Transmission	Transmission
Detector type	Ion chambers	Ion chambers	64-element Ge detector	Ketek SDD	Ion chambers	Vortex SDD
Spectrometer type	-	-	Johann	Johann	-	Johann
Rowland circle radius (m)			1.0	1.0		1.0
SBCA	-	-	5x Si(111) striped	3x Si(220) striped	-	1x Si(1266)
Beam path	Air	Air	He	He	Air	Al attenuation He
Calibrant		Y foil			$Ca_{0.8}U_{0.2}$-$Ti_{1.6}Fe_{0.4}O_7$	UTi_2O_6
Reference	[57]	[57]	[54, 58]	[55, 59]	[60]	[51, 61, 62]

4.2.3. Sample preparation

Reference compounds were prepared for measurement by grinding and then combining with polyethylene glycol (PEG) to form homogenous dispersions that were pressed under 1 tonne for 1 minute to form pellets, (PEG amounts and pellet diameters are listed in Table 4.3). Reference compounds prepared for HERFD measurements (I20-scanning, DLS and BM20, ESRF) and for laboratory XAS (easyXES100-extended) also required further size reduction, by ball milling in a Fritsch Pulverisette 23 Micro Mill for 10 minutes at 30 RPM in IPA. Samples were prepared to either obtain a specific absorber concentration, calculations for which were performed in Hephaestus [1], or a specific mass (Table 4.3).

4.2.4. Data processing

HERMES [63] was used to process the laboratory XAS data prior to analysis, where the individual I0 and It scans were merged, the I0 and It data offset were fitted with 3rd order polynomials, which were subtracted from the respective I0 and It merged data. All data were calibrated to the absolute energy scale by performing a theta shift correction and all data were converted to a file containing I0 and It, enabling plotting of absorption as a function of energy.

Athena, from the Demeter software suite was used to calibrate, align and merge data acquired on synchrotron instruments. Athena was also used to identify the E_0 1st derivative positions and too normalise all XAS data. The E_0 half position values, taken at the energy on the edge where normalised intensity is 0.5, were determined from the normalised data. The U M_4-edge M_β HERFD XANES data produce such a high white line intensity that the data is normalised to the peak of the absorption edge, rather than normalised between the pre-edge range and the post edge region, as is used to process the U L_1 and U L_3-edge data. Prior to fitting of U L_3-edge EXAFS transmission data from B18 (DLS), data were examined in Athena and necessary multi-electron excitation (MEE) removal was performed. EXAFS data were fit in Artemis from the Demeter Suite [64] in combination with FEFF6 [65].

Table 4.3: List of measurements made, with details of the instrumentation, source and measurement conditions.

Instrument	**B18 (DLS)**	**B18 (DLS)**	**I20 (DLS)**	**BM20 (ESRF)**	**X-23 (NSLS)**	**EasyXES-100 extended**
Edge/Transition	**U L_1**	**U L_3**	**U L_3 $L_{\alpha 1}$**	**U M_4 M_β**	**U L_3**	**U L_3**
Mode	**Transmission**	**Transmission**	**HERFD**	**HERFD**	**Transmission**	**Transmission**
Sample prep						
Size reduction	Hand ground	Hand ground	Milled	Milled	Hand ground	Milled
Pellet diameter (mm)	3/6	3/6	10	6	10	13
Conc. (mx)	1.4-2.2	1	0.08-0.13	5.4-8.9	1	1
Mass (mg)	1.7-9.2	1.7-9.2	2	50	15.6-26.0	26.6-44.3
PEG (mg)	50	50	100	50	50	60
Scan parameters						
Step size over edge	0.5	0.5	0.2	0.1	0.5	0.5
Scan time (h:min:sec)	01:30	05:20	18:20	02:30	15:00	2:00:00
No. scans	3	6	4-8	24	2	18*
total time (h:min:sec)	04:30	32:00	1:13:20-2:24:40	01:00:00	00:30:00	36:00:00*

*8 I0 scans, 8 It scans, 1 I0 offset scan and 1 It offset scan give a total of 18 scans, however with the use of a sample wheel a total of six samples can be measured per experiment, and the same I0 scans can be used for each measurement (63 scans total, 10.5 scans per sample), so if the experiment is optimised the total collection time is 126 hours for six samples (21 hours per sample).

4.3. Results and Discussion

A comprehensive evaluation of the efficacy of different XAS approaches and instrumentation to understand U speciation was undertaken through measurement of a range of reference U compounds. To aid in data analysis and comparison between the data sets, each of the sixteen reference compounds were given the same y offset position in all spectra plots. The reference compound spectra were arranged on the y axis in accordance with the oxidation state and coordination environment (with respect to the first shell of oxygen backscatterers) (Table 4.1), to assist the observation of any trends in E_0 position or spectral features that depend on the U environment. Herein, the edge positions of spectra and their XANES features are discussed and described, any XANES features that occur on the peak of the edge, also known as the while line region, are referred to as absorption edge features. These are discussed separately to features that occur in the XANES region past the edge (over 21840 eV at the U L_1-edge and 17190 at the U L_3-edge).

The following sections provide a detailed analysis of each data set and a comparison between different measurements, their benefits and limitations is summarised in Table 4.4. It should be noted that the reference compounds studied here all contain high concentrations of U (and therefore could easily be prepared to 1 absorption length for transmission analysis), so all the conclusions drawn from results discussed here may not be analogous to data collected from lower concentration samples. The reference compound also only included a small number of example of U^{4+}, U^{5+} coordinate reference compounds, and no U^{5+} uranyl compounds, which limits the capacity to identify trends in XAS data with U speciation.

Table 4.4: Summary of measurements made, with a summary of the information that can be obtained, including a comparative ranking (1-4 best-worst, 5-not possible) in addition to and benefits and limitations. *Apart from mixed oxidation with U^{4+}

Instrument	**Synchrotron**	**B18 (DLS)**	**EasyXES 100-extended**	**I20 (DLS)**	**BM20 (ESRF)**
Edge	**U L_1**	**U L_3**	**U L_3**	**U L_3**	**U M_4**
Mode	**Transmission**	**Transmission**	**Transmission**	**HERFD**	**HERFD**
E_0 half position: Oxidation state	5	3	3	1	3*
E_0 1st deriv. position: Oxidation state	1	4	4	2	3*
XANES: Oxidation state (LCF/ITTFA)	5	2	2	2	1
XANES: uranyl U^{6+} feature	5	2	2	1	2
EXAFS: structure	Not measured	1	5	5	5
Specialist information				Possible coordination trend in absorption edge features	Direct observation of U^{4+}, U^{5+} and U^{6+} fraction
Benefits	Best net U oxidation state by edge position	Good all-round measurement	XANES results comparable to synchrotron data without synchrotron	Greater resolution good for low concentrations or small amounts e.g. environmental samples	Direct determination of specific U oxidation state concentrations
Limitations	Only get net U oxidation state from measurement Calibration difficult	Does not provide specific U oxidation state, only net	Does not provide specific U oxidation state, only net Can only measure XANES Long measurement time	Measurement too sensitive for some analysis techniques (LCF/ ITTFA)	Limited structural information

4.3.1. Uranium Edges

4.3.1.1. U L_1-edge XANES

The U L_1-edge (original orbital of excited electron: 2s, core-hole lifetime: 0.36 fs, core-hole lifetime broadening: 17.53 eV) can be used to confidently estimate net U oxidation states. The E_0 first derivative (herein referred to as E_0 1st deriv.) values were found to follow a clear trend when plotted against the known oxidation state of reference compounds (Figure 4.1d). There was also a clear distinction between the ranges of E_0 1st deriv. positions for each oxidation state (21790.7 – 21792.2 eV, 21795.0 – 21795.2 eV and 21796.6 – 21798.0 eV for U^{4+}, U^{5+} and U^{6+}, respectively). The difference between the E_0 1st deriv. ranges of U^{4+} and U^{5+} (2.8 eV) is double that which occurs between U^{5+} and U^{6+} (1.4 eV). These large differences between oxidation states, which are greater than the uncertainty of each data point (0.5 eV, taken from the step size over the edge) enable the net U^{4+}, U^{5+} and U^{6+} oxidation states to be identified confidently, as can U oxidation states that fall between 4+ and 5+, or 5+ and 6+. The U L edge probes the 2s orbital and is thought to be more similar to the K edge, which probes the 1s orbital and, therefore, is more diagnostic of U oxidation state than the U L_2 or U L_3-edges, which probe the 2p orbitals.

E_0 values that were obtained from the point on the edge at which normalised intensity = 0.5 (herein referred to as E_0 half) did not present the same trend observed for the E_0 1st deriv. data (Figure 4.1c). The range of E_0 half positions for U^{6+} reference compounds (21788.0 – 21791.8 eV) overlaps that of the U^{5+} reference compounds (21789.2 – 21790.5 eV) and also extends beyond the range of U^{4+} reference compounds (21786.9 – 21788.0 eV). As such, the E_0 half values cannot not reliably be used to estimate U oxidation state. It is possible that core-hole lifetime broadening has caused the shape of the peak to widen and distort, resulting in E_0 half values that do not follow a liner trend. However, the E_0 1st deriv. positions, which are highly dependent on edge shape, do present a linear trend.

The width of the U L_1-edge is also caused by the presence of two shoulder features that occur before the white line, these can be resolved by measuring U L_1-edge HERFD [46]. Bes *et al.* collected U L_1-edge HERFD data from KUO_5 (U^{5+} uranate, octahedral coordination) and attributed the first feature, at 21757 eV, to a U-p orbital with mixing of U-d/f and U-p, and

hybridisation of the O-p states [46]. They concluded that the second feature, at 21770 eV, appeared to be related to the splitting of U-p states into two bands, one at 21774 (3) eV and the other at 21790 eV [46]. It is possible that the E_0 1st deriv. values determined here are actually estimates of the position of the second feature, which could explain why these values are better estimates U oxidation state than E_0 half position.

One limitation to the use of U L_1-edge E_0 1st deriv. positions is the lack of reliable elements with a similar edge energy to use as a reference for calibration. Tc metal (21044 eV, a radioactive soft β-emitter) and Ru metal (22117 eV) are both possible calibration standards. The magnitude of the shifts in E_0 1st deriv. positions between different U oxidation states does, however, make this measurement less susceptible to the effects of beam drift than the other edges, which have smaller shifts in edge position.

Uranium L_1-edge XANES data (Figures 4.1a and 4.1b) showed some sensitivity to variations in U coordination and crystallographic structure; however, there was no discernible trend in XANES features with oxidation state, coordination or short-range structure. $BaUO_4$ and Ca_3UO_6, reference compounds, which have the same U oxidation state (U^{6+} uranate) and coordination (6) but different crystallographic structures, presented differences in spectral features (Figure 4.1b). Similarly, metaschoepite and $UMoO_6$, which have the same U speciation (U^{6+} uranyl) but different U coordination (6 and 7, respectively), also displayed different L_1-edge spectral features. Despite these observations, comparison across the whole data set showed that these features were not significantly distinctive to enable characterisation of a specific crystallographic structure, coordination or speciation; for example, the spectra of metaschoepite, while clearly different to $UMoO_6$, was not dissimilar to $BaUO_4$, $SrUO_4$ and $CaUO_4$, and confidently distinguishing between these different U^{6+} environments in an unknown sample would not be possible. The sets of U L_1-edge XANES data from U^{4+} and U^{5+} reference compounds (Figure 4.1a) all displayed distinguishing features from each other; however, due to the limited number of reference compounds measured, with only one or less standard to represent each possible occurrence of U oxidation state and coordination, no definitive conclusion about the sensitivity of U L_1-edge XANES to variations in U coordination and structural differences in U^{4+} and U^{5+} samples can be made.

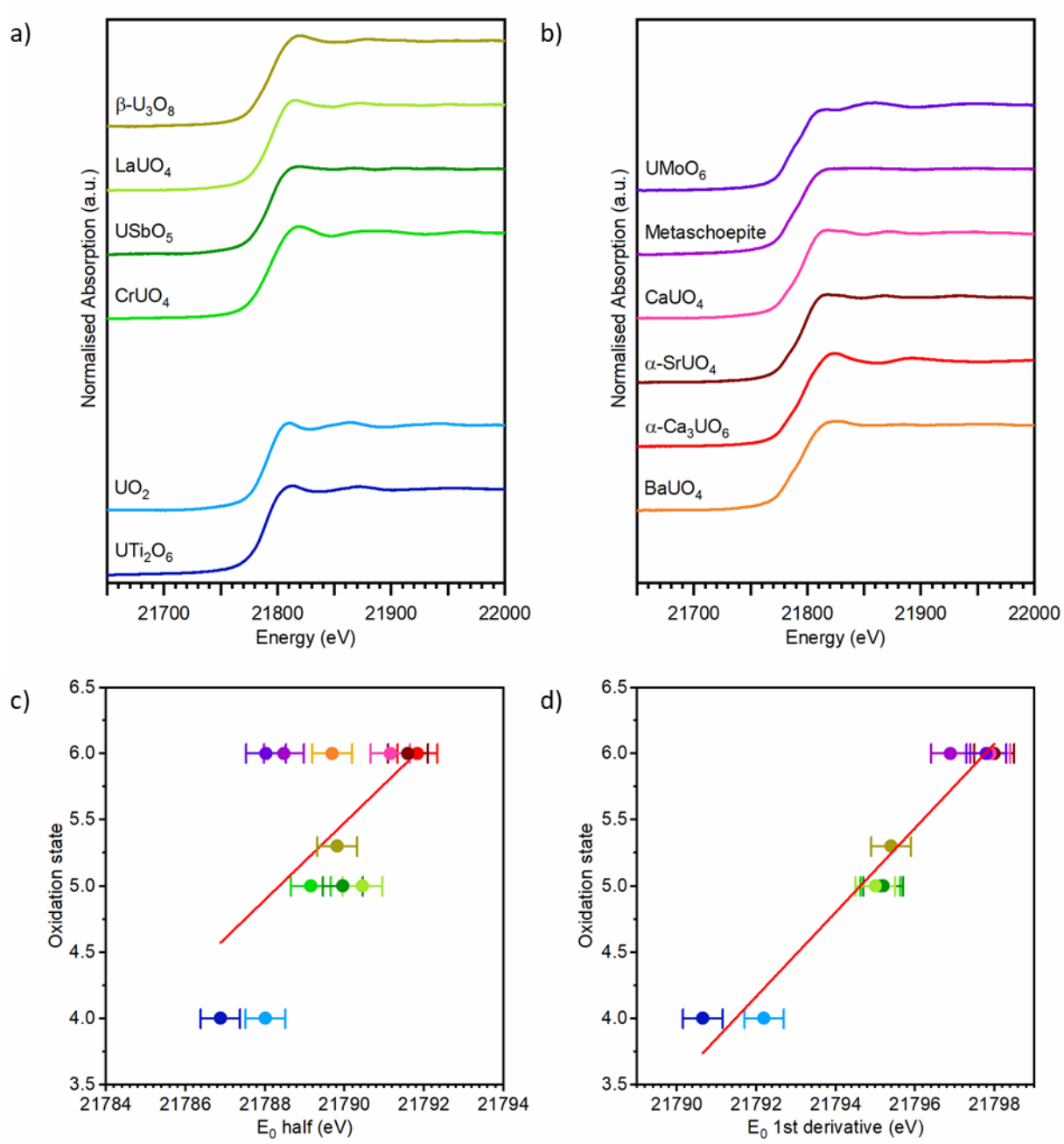

Figure 4.1. (a) U L_1-edge XANES of U^{4+} and U^{5+} reference compounds; **(b)** U L_1-edge XANES of U^{6+} reference compounds; **(c)** E_0 half positions derived from U L_1-edge data of reference compounds plotted against their known oxidation states; and **(d)** E_0 first derivative positions from U L_1-edge data of reference compounds plotted against their known oxidation states. Data were collected on B18, DLS. Colours used for reference compounds are consistent across all plots.

The U L_1-edge has a core-hole lifetime of ~0.36 fs, which is shorter than both the U L_3 and U M_4-edge, resulting in a greater core-hole lifetime broadening effect (17.53 eV). This contributes in part to the broad and low intensity XANES features. The U L_1-edge is at 21757 eV and is more difficult to measure than the U L_3-edge (17166 eV) since it is close to the U L_2-edge (20948 eV) and, consequently, the U L_1-edge data has a higher background (and therefore a lower signal-to-noise ratio) than the U L_3-edge or U M_4-edge (M_β) HERFD data. Therefore, obtaining information of the U environment from the XANES of U L_1-edge XAS data may not be possible. In addition, the data discussed here were collected from reference compounds with high concentrations of U and only one U environment (apart from U_3O_8) and XANES from any lower concentration sample with a mixed U environment will have broader and even less distinct features, with a worse signal-to-noise ratio than the reference compounds.

A U L_1-edge HERFD $L\beta_4$ ($3p_{1/2}$-$2s_{1/2}$) experiment has been successfully conducted to measure KUO_5 [46]. A U L_1-edge HERFD measurement could produce a better estimate of U oxidation state, improvements in energy resolution over a U L_1-edge XAS measurement would provide smaller uncertainties by enabling a smaller step size over the edge. The increased energy resolution may also facilitate the observation of distinctive features not visible with a standard U L_1-edge measurement, so a U L_1-edge HERFD experiment with multiple U reference compounds would be of interest. Investigations into U L_1-edge EXAFS, to determine if any structural information can be gleaned from the U L_1-edge is another area potential area of research.

Analysis of the U L_1-edge transmission E_0 1^{st} deriv. position to determine net U oxidation state has been revealed to be a promising technique, better than the use of U L_3-edge transmission E_0 positions (Table 4.4). Apart from this it was not possible to ascertain any other information which could be derived from U L_1-edge XANES, due to a lack of distinctive features.

4.3.1.2. U L_3-edge XANES

The XANES region of the U L_3-edge XAS ($3p_{3/2}$, 0.77 fs, 8.16 eV) data (Figures 4.2a and 4.2b) was found to have more distinctive features than the U L_1-edge, with some features that could be used to characterise specific U environments. Several reference compounds presented multiple features in the absorption edge such as $USbO_5$ (Figure 4.2a) and Ca_3UO_6 (Figure 4.2b). These more distinct features are partially the result of the longer core-hole lifetime at the L_3-edge (~0.77 fs) that results in less broadening (8.16 eV). This makes it easier to qualitatively distinguish different reference compounds, which is exemplified when comparing the U L_3-edge XAS data acquired from $Mg^{6+}UO_4$ and $BaU^{6+}O_4$ (Figure 4.2b). These compounds share the same U oxidation state and coordination environment (6) but displayed different white line shapes. The U^{6+} uranyl reference compounds (metaschoepite, $UMoO_6$ and Soddyite) all displayed a shoulder feature between 17184.0 and 17202.0 eV (Figure 4.2b), which is widely understood to be characteristic of the uranyl speciation (UO_2^{2+}) and manifests from the presence of the two strong formally triple-bonded U-O_{ax} backscatters [66]. The U L_3-edge is the most widely studied edge for U and commonly employed XANES analysis methods include linear combination fitting (LCF) and principal component analysis (PCA) with iterative target-transformation factor analysis (ITTFA) that attempt to quantify and extrapolate speciation information from the XANES data. These methods produce fits that best describe an unknown sample by combining the real XANES of reference compounds (LCF) or generated principal components of a sample and set of reference compounds (PCA and ITTFA). From the best fits of U L_3-edge data estimates of net U oxidation state and fraction of U^{6+} uranyl speciation present can be calculated.

As with the U L_1-edge E_0 1^{st} deriv., the U L_3-edge E_0 half and E_0 1^{st} deriv. positions (Figures 4.2c and 2d) followed a linear trend that could be used to estimate the U oxidation state in unknown U samples. However, the U L_3-edge E_0 positions do not provide as robust of an estimate of U oxidation state as the U L_1-edge. While there was no overlap between the ranges of edge positions for each oxidation state for the U L_3-edge E_0 half or E_0 1^{st} deriv. positions, when uncertainties are added to the ranges there is significant extension of the E_0 half positions (Figure 4.2c) of U^{5+} with U^{6+} and the E_0 1^{st} deriv. positions (Figure 4.2d) of U^{4+}

with U^{5+} and U^{5+} with U^{6+}. In particular, the E_0 1st deriv. positions of $U^{5+}SbO_5$ (17171.8 eV) and $Ca_3U^{6+}O_6$ (17172.0 eV) are very close.

The E_0 half positions (Figure 4.2c) for U^{4+}, U^{5+}, and U^{6+} are all more closely clustered (ranges of 0.6, 0.5 and 0.7 eV, respectively) than the E_0 1st deriv. positions for U^{4+}, U^{5+}, and U^{6+} (ranges of 0.8, 1.1 and 1.2 eV, respectively). Also, the gaps between the ranges of U L_3-edge E_0 half positions (1.1 eV and 0.6 eV for U^{4+} to U^{5+} and U^{5+} to U^{6+}, respectively) of each oxidation state are greater than the respective gaps between ranges in the U L_3-edge E_0 1st deriv. positions. As the U L_3-edge E_0 half position ranges for each oxidation state are shorter and more distinct, the use of this E_0 position is preferable to E_0 1st deriv., to enable more confident identification of net U oxidation in a sample, especially those that fall between 4+ and 5+ or 5+ and 6+.

The U L_3-edge E_0 half and 1st deriv. positions both can be used to provide estimates of net U oxidation state; of these, the E_0 half position would provide a better estimate. Neither provides as good an estimate of the mean oxidation state as the first derivative at the U L_1-edge (Table 4.4). The U L_3-edge measurements do, however, allow the collection and analysis of data in the EXAFS region, from which the short-range structure can be investigated, which is discussed further below.

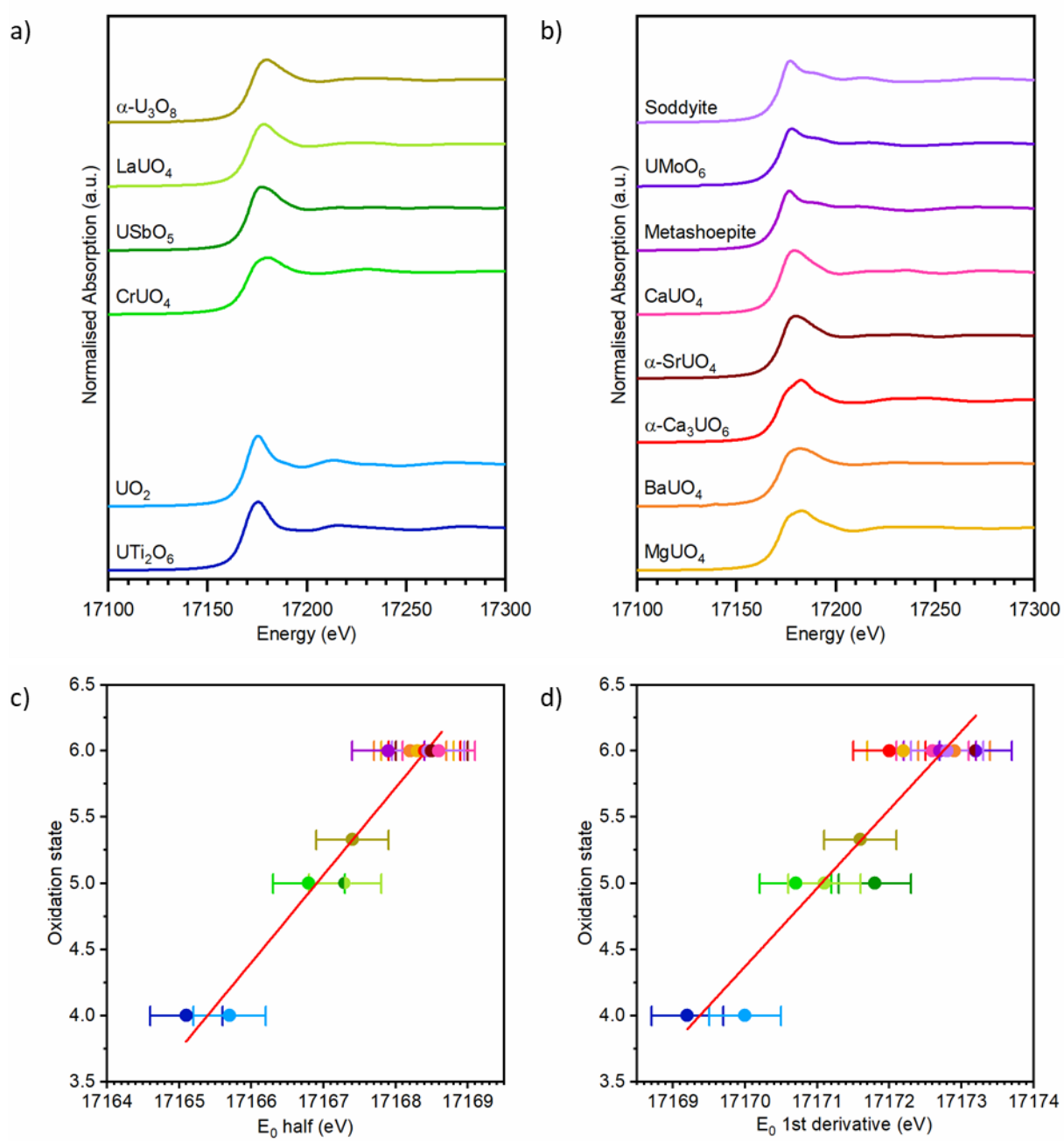

Figure 4.2. (a) U L_3-edge XANES of U^{4+} and U^{5+} reference compounds; **(b)** U L_3-edge XANES of U^{6+} reference compounds; **(c)** E_0 half positions derived from U L_3-edge data of reference compounds plotted against their known oxidation states; and **(d)** E_0 first derivative positions from U L_3-edge data of reference compounds plotted against their known oxidation states. Data were collected at B18, DLS. Colours used for reference compounds are consistent across all plots.

4.3.1.3. U M_4-edge $M\beta$ HERFD XANES

The U M_4-edge HERFD (Emission line: $M\beta$, transition: $4f_{5/2}$-$3d_{3/2}$, 23.12 fs, 0.27 eV) XANES data (Figures 4.3a and 4.3b) presented a variety of well resolved distinctive features, enabling direct observation of relative concentrations of U^{4+}, U^{5+} and U^{6+}. The U M_4-edge HERFD data is different to the U L_1 and U L_3-edge data, due to the edge being probed (M_4), the transition being exploited to measure it ($4f_{5/2}$-$3d_{3/2}$, a secondary transition), the type of data collected (PFY) and the instrumentation used (greater energy resolution). Therefore, these data cannot be directly compared with those of transmission U L-edges. However, from the U M_4 edge HERFD XANES data (Figures 4.3a and 4.3b) it can be seen that the features associated with each U oxidation state are sharp and well resolved and, therefore, the shift in edge position with oxidation state observed in Figures 4.3a and 4.3b is more readily apparent than in Figures 4.1a, 4.1b, 4.2a and 4.2b.

The spectra acquired from each standard were distinctive, including $SrUO_4$ and $CaUO_4$ (Figure 4.3b), which have the same U oxidation state (U^{6+}, uranate), coordination (8, distorted cubic) and structure (R-3m) [67], demonstrated discernible differences, unlike the spectra from same reference compounds collected at the U L_1 and U L_3-edges (Figures 4.1b and 4.2b). This demonstrates that the U M_4-edge ($4f_{5/2}$-$3d_{3/2}$) HERFD measurement is more sensitive to variations in composition.

The narrower features also enable direct observation of multiple U oxidation states within a sample. The U M_4-edge $M\beta$ HERFD XANES from U_4O_9 ($U^{4+}{}_2U^{5+}{}_2O_9$) presented two distinct peaks, one at a position characteristic of U^{4+} (3725.3 eV) and the other at a position characteristic of U^{5+} (3726.4 eV). The U M_4-edge $M\beta$ HERFD XANES from U_3O_8 ($U^{5+}{}_2U^{6+}O_8$) displayed a broader white line shape (3725.4-3725.8 eV) than those from single oxidation state reference compounds, indicative of contributions from U^{5+} and U^{6+}. Measuring U M_4-edge $M\beta$ HERFD XANES enables direct investigation of U speciation and to determine the presence of U^{5+} [44], which cannot be achieved by U L_3-edge XAS (or U L_3-edge L1α HERFD) due to the greater extent of broadening present at this edge, as previously discussed by Pidchenko *et al.* [39].

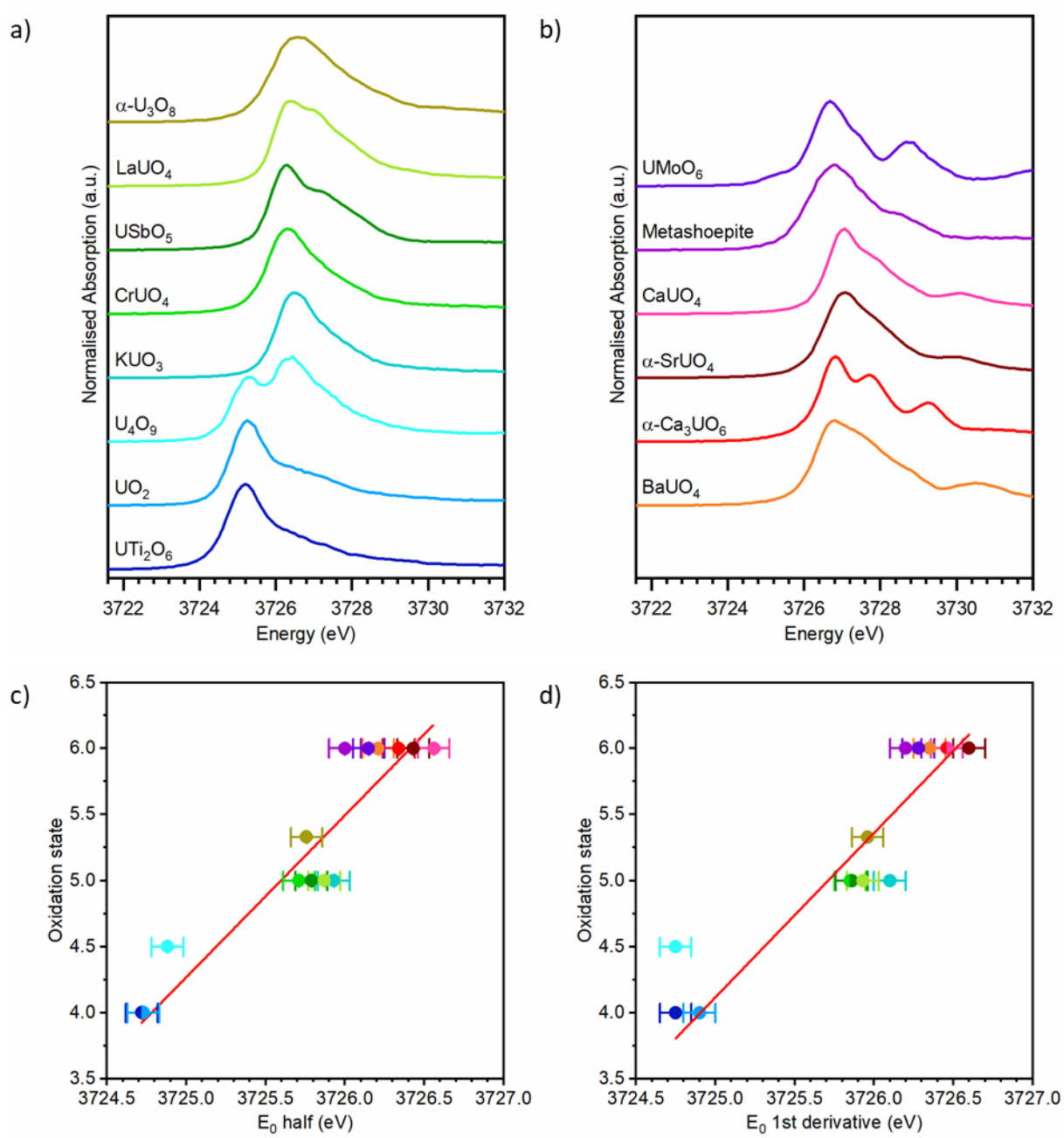

Figure 4.3. (a) U M_4-edge M_β XANES of U^{4+} and U^{5+} reference compounds **(b)** U M_4-edge M_β HERFD XANES of U^{6+} reference compounds **(c)** E_0 half positions from U M_4-edge M_β HERFD data of reference compounds plotted against their known oxidation states **(d)** E_0 first derivative positions from U M_4-edge M_β HERFD data of reference compounds plotted against their known oxidation states. Data were collected on BM20, ESRF. Colours used for reference compounds are consistent across all plots.

Further data analysis of U M_4-edge M_β HERFD XANES data by LCF or PCA with ITTFA enables determination of the relative fraction of each U oxidation state present, which is an approach successfully applied in several studies [13, 22, 25, 27]. The use of LCF or PCA with ITTFA can be inhibited by lack of appropriate reference compounds to provide relevant spectra, especially for better resolved data. The U M_4-edge M_β HERFD XANES data contain well resolved features; however, these data are normalised differently to U L_1 and L_3-edge data, so that the maximum intensities of each spectrum are the same. This may reduce the need for relevant reference compounds. Also, despite the high resolution, the energy range measured is much shorter than the U L_1 or L_3-edge, so there are fewer data points to vary.

The E_0 half and E_0 1st deriv. positions of U M_4-edge M_β HERFD data (Figures 4.3c and 4.3d) follow a linear trend; however, these data would only enable the identification of samples with a single oxidation state. The ranges of E_0 half positions (Figure 4.3c) of each oxidation state (U^{4+}: 3724.7 – 3724.7 eV, U^{5+}: 3725.7 – 3725.9 eV and U^{6+}: 3726.0 – 3726.6 eV) do not overlap but when uncertainties (0.1 eV) are included, the U^{5+} and U^{6+} ranges cannot be distinguished. The same was also found for the E_0 1st deriv. positions (U^{4+}: 3724.8 – 3724.9 eV, U^{5+}: 3725.9 – 3726.1 eV and U^{6+}: 3726.2 – 3726.6 eV), shown in Figure 4.3d.

As is demonstrated by the E_0 positions of U_4O_9 (Figures 4.3c and 4.3d), the separation between the U^{4+} and U^{5+} peaks prevent the use of E_0 position at the U M_4-edge to estimate the net U oxidation state of a sample that contains a mixture of U^{4+} and U^{5+}. It may be possible to determine the net oxidation state of samples containing a mixture of U^{5+} and U^{6+}, using the white line E_0 position as there is sufficient overlap between the U^{5+} and U^{6+} peaks to produce a monomodal shape.

The U M_4-edge M_β HERFD XANES data presented a variety of well-resolved distinctive features, enabling direct observation of relative concentrations of U^{4+}, U^{5+} and U^{6+}. This is exceptionally useful for investigating mixed U oxidation states in a sample and confirming the presence of U^{5+}, which cannot be explicitly achieved using data collected at the U L_1 or U L_3-edge. The E_0 positions can be used to identify the oxidation state when one U environment is present and estimate the net U oxidation state, but only for single U oxidation states or possibly a mixture of U^{5+} and U^{6+}, as is discussed above. However, the limited use of E_0

position to investigate U oxidation state is not a significant disadvantage as much more extensive characterisation of the U oxidation state in the sample can be achieved by analysis of the XANES features. The XANES region also displays the distinctive U^{6+} uranyl features that can be used to determine the presence of U^{6+} uranyl and estimate the relative fraction of U^{6+} uranyl speciation present.

4.3.1.4. Comparison of different U edges

If using E_0 position to estimate U oxidation state, of the three edges investigated, the U L_1-edge E_0 first derivative position (Figure 4.1d) is preferable to characterise U oxidation state (Table 4.4). The ranges in U L_3-edge E_0 positions (3.5 eV and 4 eV for E_0 half and E_0 1st deriv., respectively) are smaller than at the U L_1-edge, and both sets of measurements have the same uncertainty (0.5 eV). For both the U L_1 and U L_3-edge, the difference in ranges of E_0 positions for different oxidation states was found to be greater between the U^{4+} and U^{5+} reference compounds than the U^{5+} and U^{6+} reference compounds. Therefore, there should be a greater inherent confidence given to any estimates of net U oxidation state between 4+ and 5+ from the U L_1-edge and U L_3-edge E_0 position. The limitations of the use of E_0 position alone to estimate U oxidation state from U M_4 HERFD E_0 data are discussed above.

Through qualitative analysis of the U L_3-edge transmission and U M_4-edge ($4f_{5/2}$-$3d_{3/2}$) HERFD data, some distinct features (such as uranyl speciation) can be observed, however absolute determination of structure is challenging without complex analysis (such as computational modelling). For the direct determination of U oxidation state, the combined analysis of U M_4-edge position and U M_4-edge HERFD XANES provides the most conclusive results; analysis can ascertain the presence of different U species in a mixed U oxidation state sample, whereas it is only possible to establish net U speciation from analysis of the U L_1 and U L_3-edge transmission data.

4.3.2. Techniques and Instrumentation

To assess the influence of XAS technique and instrument on the ability to determine U speciation, the reference compounds were measured at the L_3-edge using transmission XAS and L_3-edge $L_{\alpha1}$ HERFD XAS. Moreover, data collected at synchrotron facilities were compared with those acquired using a laboratory spectrometer. Data presented in Figures 4.4 to 4.6 have been organised in each plot as described before, ordered with respect to the oxidation state, coordination and speciation of U in each reference compound to enable comparison between plots. From these data the E_0 half and E_0 first deriv. positions were determined, as described above, and plotted against the known oxidation state of each reference compound, a linear fit was then calculated to attempt to construct an E_0 position to oxidation state calibration line. A summary of comparison between different measurements, their benefits and limitations are shown in Table 4.4.

4.3.2.1. U L_3-edge transmission XAS - Synchrotron data vs Synchrotron data

Two sets of U L_3-edge XAS transmission data are shown in Figure 4.4, collected on bending magnet beamlines at two different synchrotrons with similar instrumentation (Table 4.1). This demonstrates the degree of variation in data between collected on different instruments, independent of technique. There was strong visual and statistical agreement between the XANES data (Figures 4.4a and 4.4b); the white line features and features in the XANES region appeared very similar and the edge position values of each data set were in good agreement. There were slight variations in intensity of white light features in some of the spectra (Ca_3UO_6, $CaUO_4$ and metaschoepite); however, the agreement of all features past the white line was found to be excellent. The E_0 half data (Figure 4.4c) collected from X23A2 (NSLS, USA) appeared to be systematically at lower energy than the B18 (DLS, UK) data, with a mean difference of -0.6 eV. The E_0 1^{st} deriv. position data (Figure 4.4d) sets were found to be in better agreement than the E_0 half positions, with the data clustering closely around the comparative x=y line, and a mean difference of 0.1 eV. The E_0 1^{st} deriv. positions of UO_2, however, did not show as good agreement as the rest of the data set, with a difference of 0.9 eV. It is possible that the UO_2 sample measured at X23A2 comprised UO_{2+x} rather than UO_2,

resulting in a shift in edge position. This explanation is not consistent with the UO_2 E_0 half positions, which showed good agreement between the data sets. The difference in E_0 could also be the result in variation in sample preparation, either in the mass of UO_2 in the pellet, or the level of homogeneity achieved, either of which could result in a different concentration of UO_2 in the path of the beam, causing a difference in absorption intensity at the white line, and therefore edge position. Selection of the E_0 1^{st} deriv. position, the first peak in the first derivative, is much more susceptible to the effects of glitches in the data than the E_0 half position so this is also a possible cause in the difference in UO_2 E_0 positions.

4.3.2.2. U L_3-edge transmission XAS - Synchrotron data vs Lab Spectrometer data

Comparison of U L_3-edge transmission data collected on a synchrotron instrument (B18, DLS, UK) and a laboratory spectrometer (EasyXES100-extended) are shown in Figure 4.5. Despite the differences in X-ray sources and collection set ups, the data were found to be in excellent agreement with the edge positions and features matching well. The lab XAS XANES data (Figures 4.5a and 4.5b) had more noise than the synchrotron data, which is a result of the lower photon flux from the lab X-ray source. Some discrepancy was observed in the intensities of absorption edge features, with the lab XAS data displaying showing a slight decrease in intensity in this region for several reference compounds (UTi_2O_6, UO_2, $SrUO_4$, $CaUO_4$, metaschoepite and soddyite). This difference in intensity is unlikely to be caused by leakage or sample thickness effects since leakage correction has been applied to the data and the samples were prepared to achieve an absorption length (μx) of 1. Therefore, it is thought that these differences in intensity are the result of some reference compounds being more strongly self-absorbing, as has been discussed in previous work [51]. The data are in better agreement in the XANES region past the edge, which was also observed in the comparison between the two sets U L_3-edge transmission XAS synchrotron data (Figures 4.4a and 4.4b). XANES data from laboratory measurements have previously been successfully analysed by LCF [51].

The E_0 1^{st} deriv. position of UTi_2O_6 was used a calibration standard for the lab XAS data set. Therefore, the UTi_2O_6 points in Figures 4.5c and 4.5d should not be considered when assessing

the agreement of the data sets; however, the data point has been included in the plot, for completeness.

Both sets of E_0 positions (Figure 4.5c and 4.5d, disregarding UTi_2O_6) showed strong agreement; comparisons of the E_0 half data in particular were excellent, with a mean difference of -0.2 eV. This difference is less than the difference between the E_0 half positions of the two transmission data sets (-0.6 eV); however, the data compared are comprised of a greater number of standards than were measured for the two synchrotron transmission measurements. The E_0 1^{st} deriv. data (Figure 4.5d) (disregarding UTi_2O_6) also show good agreement, comparable with that between the two synchrotron U L_3-edge transmission measurements (Figure 4.4d) and as with the transmission measurements there is less good agreement between the UO_2 values (0.7 eV) and also $LaUO_4$ (1.0 eV).

The good agreement between U L_3-edge transmission XANES data collected on a laboratory instrument and at a synchrotron creates confidence in the use of laboratory spectrometers to investigate U speciation and that the analysis of these laboratory data will produce results with a similar level of accuracy as data collected at a synchrotron. If access to a laboratory spectrometer is possible, while lab measurements take significantly longer than synchrotron measurements and a relatively high concentration of U in the sample of interest is necessary, the wait time to perform measurements could be days or weeks, rather than many months for a synchrotron measurement. Direct access and the removal of limitations on number or activity of samples by synchrotrons or travel requirements makes lab spectrometers an especially appealing alternative to synchrotron experiments for U and work with other radioactive elements

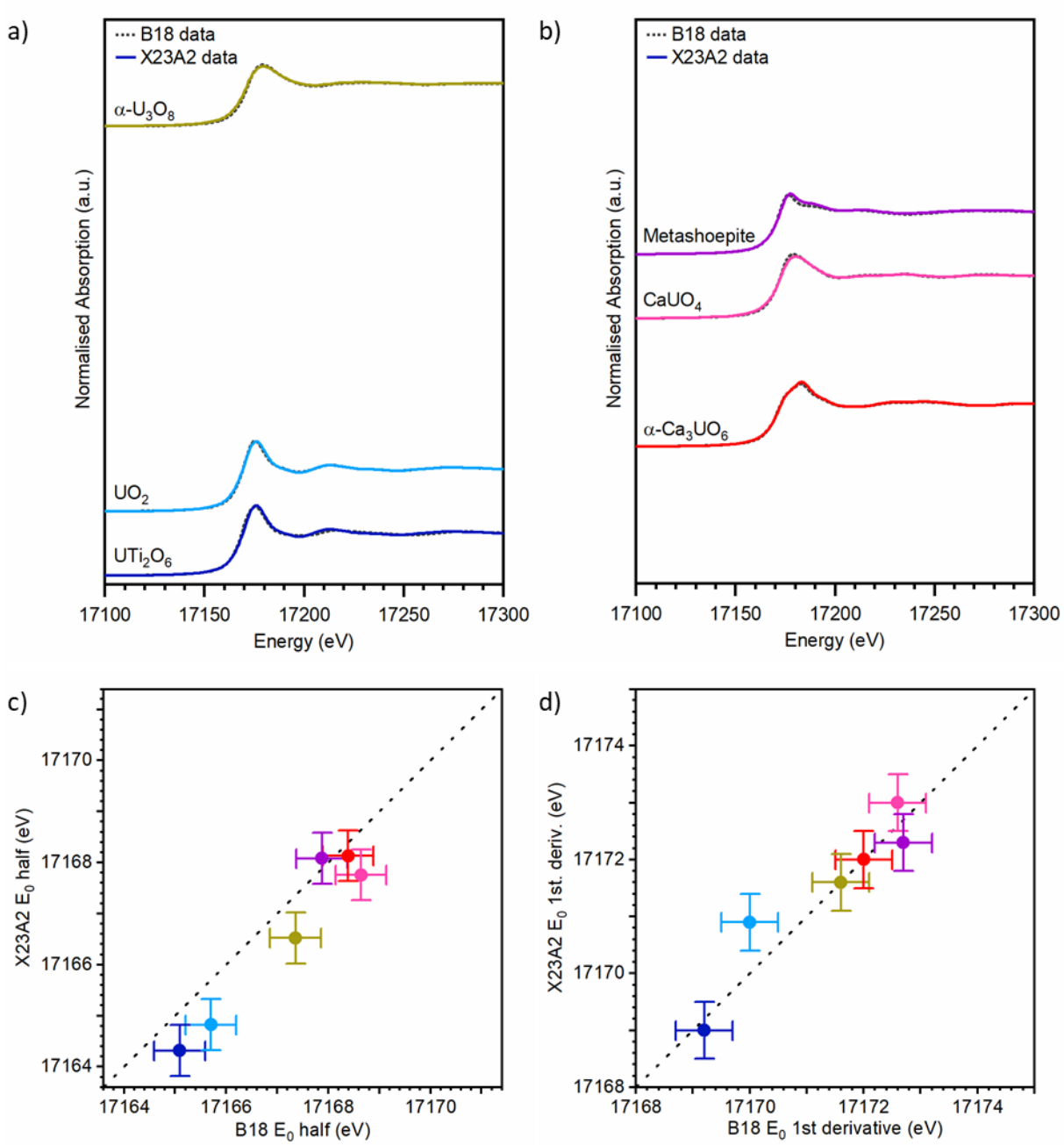

Figure 4.4. Comparison plot of **(a)** U L_3-edge XANES of U^{4+} and U^{5+} reference compounds (indicated on plots) and **(b)** U L_3-edge XANES of U^{6+} reference compounds (indicated on plots) measurements were performed at B18, DLS, Oxford, UK and X23A2, NSLS, BNL, USA. Comparison plots of the **(c)** E_0 half and **(d)** E_0 1st deriv. positions of U reference compounds from U L_3-edge transmission measurements. Colours used for reference compounds are consistent across all plots.

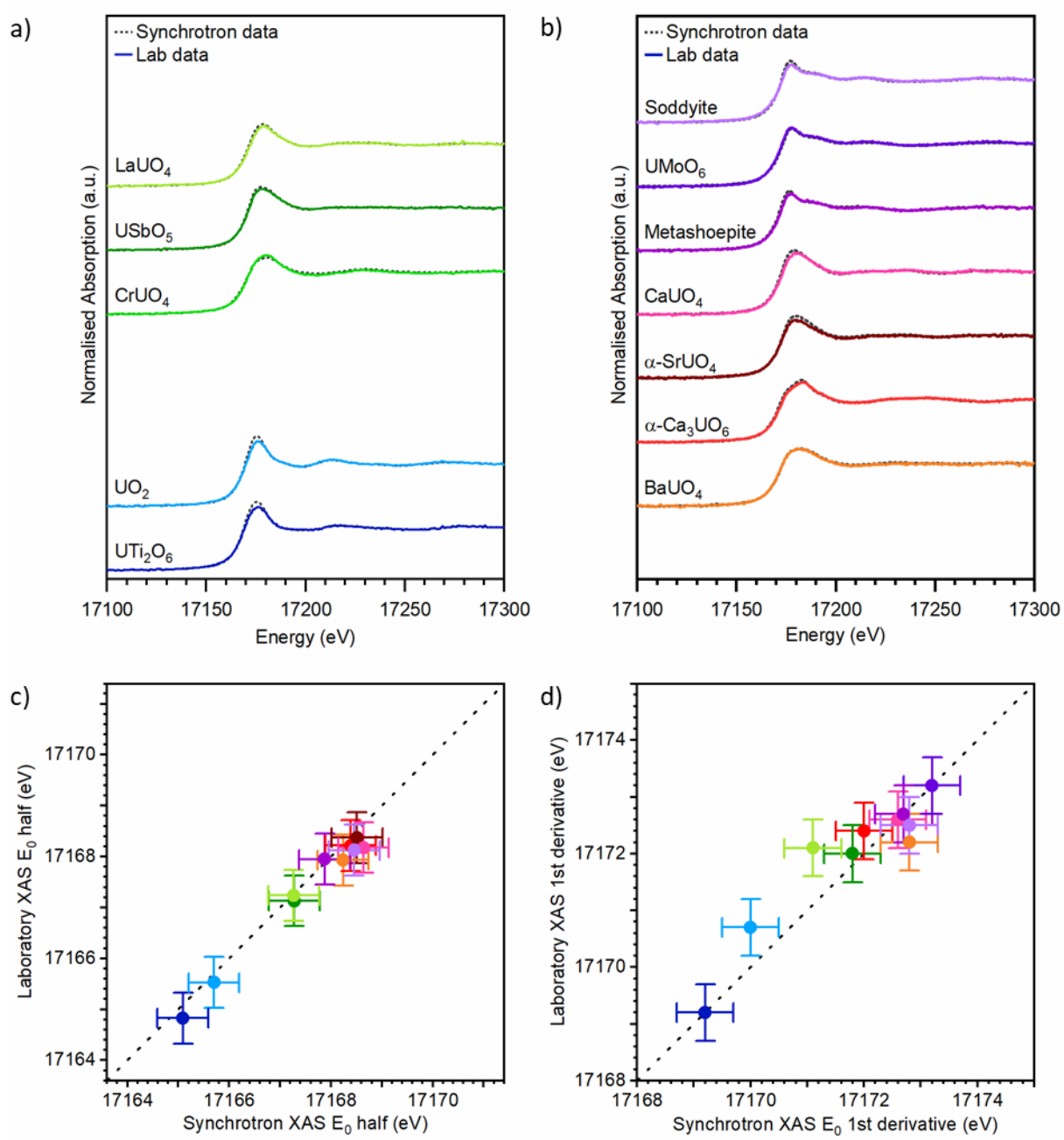

Figure 4.5. Comparison plot of **(a)** U L_3-edge XANES of U^{4+} and U^{5+} reference compounds (indicated on plots) and **(b)** U L_3-edge XANES of U^{6+} reference compounds (indicated on plots), measurements were performed at B18, DLS, Oxford, UK and on the EasyXES100-extended laboratory instrument. Comparison plots of the **(c)** E_0 half and **(d)** E_0 1st deriv. positions of U reference compounds from U L_3-edge transmission measurements. Colours used for reference compounds are consistent across all plots

All measurements made were from concentrated U reference compounds, and measurements on lower concentration samples may not be possible or may take longer to provide good single to noise ratios than the lab XAS data shown here. The lowest concentration sample successfully measured on the easyXES100-extend at the University of Sheffield contained 3 wt. % U in a glass ceramic material [51]. The easyXES100-extended instrument cannot collect U L_3-edge XAS data in the EXAFS region, unlike a synchrotron experiment; however, other lab spectrometers have been used to collected EXAFS data at lower energies (4-10 keV) [68]. Instrumentation could improve to enable the measurement of lab U L_3-edge EXAFS data, or lab instrument could be utilised to investigate short-range structure by probing the edge of another element which can be measured, such as Cu K edge [68] or Ti L_3-edge EXAFS [69].

4.3.2.3. U L_3-edge transmission vs U L_3-edge $L_{\alpha1}$ HERFD

Uranium L_3-edge HERFD ($L_{\alpha1}$, $3d_{5/2}$-$2p_{3/2}$, 1.59 fs, 3.94 eV) data (I20, UK), [45] are shown in Figures 4.6a and 4.6b, alongside U L_3-edge transmission XAS data collected from the same reference compounds. As discussed above a HERFD measurement is a partial fluorescence yield technique (PFY) and, therefore, HERFD XANES cannot be directly compared to transmission XANES data. However, it was apparent that the features in the U L_3-edge $L_{\alpha1}$ HERFD XANES have a higher intensity in the white line region, with much sharper features than the transmission data, enabling a greater distinction between different spectra than the transmission XANES.

Spectra from all reference compounds, with the possible exception of UO_2, displayed multiple features in the white line region. For example, the HERFD data from $SrUO_4$ and $CaUO_4$ (Figure 4.6b) had observable differences, demonstrating that features on the absorption edge in HERFD XANES are more sensitive to differences in composition than U L_3-edge transmission XANES. Interestingly, there appeared to be characteristic trends in the intensity and position of features on the absorption edge. All the uranate 6-fold coordinate (octahedral) reference compounds (UTi_2O_6, $CrUO_4$, $MgUO_4$, $BaUO_4$ and αCa_3UO_6) had two features of similar intensity on the absorption edge, which are clearly distinguishable. Unlike the spectra from

uranate octahedral reference compounds, the uranate 8-fold U reference compounds (UO_2, $LaUO_4$, $\alpha SrUO_4$ and $CaUO_4$) had absorption edges which appeared to consist of one main feature, with a low, or no, contribution from a secondary feature.

These observations are consistent with previous work by Kvashnina *et al.* [37], Bes *et al.* [46] and Yomogida *et al*. [33]. Bes *et al.* collected U L_3-edge $L_{\alpha 1}$ HERFD XANES data from KUO_5, a U^{5+} uranate octahedral coordinated U reference compound, in the XANES a 'bimodal white line shape' was observed [46], the same as was observed here in the XANES of all uranate octahedral coordinated U reference compounds (Figures 4.6a and 4.6b). Bes *et al.* and used density of states calculations (DOS) to identify that the two peaks observed in the white line the KUO_5 XANES data were caused by the crystal field splitting of the 6d orbitals, a result of the octahedral geometry. The first peak in the white line region could be attributed to the U-d_{z^2} and U-$d_{x^2-y^2}$ orbitals (t_{2g}) and the second to the U-d_{xy}, U-d_{yz} and U-d_{yz} (e_g) [46]. Yomogida *et al*. collected U L_3-edge $L_{\alpha 1}$ HERFD data from $FeUO_4$, a transition metal U^{5+} monouranate in which U has 6-fold octahedral coordination, very similar to $CrUO_4$; both Fe and Cr are trivalent [32]. The spectra collected from $FeUO_4$ by Yomogida *et al*. displayed two features in the white line region which they also attributed to crystal field splitting of the 6d orbital [33], the features also had relative intensities similar to the features in the white line of $CrUO_4$.

Works by Kvashnina *et al.* [21, 37] investigated U L_3-edge $L_{\alpha 1}$ HERFD XANES data collected from UO_2 and $UO_2(NO_3)_2{\cdot}6H_2O$ (U^{6+} uranyl, five unique U environments, two octahedral and three 7-fold coordinated) using DOS calculations. They found that while estimations suggested two features would be present in the spectra of UO_2, due to crystal-field splitting of the U 6d states, the two features were not experimentally resolved [37]. This could be in part due to the first feature being shifted into the edge itself and therefore is hidden. Whereas with $UO_2(NO_3)_2{\cdot}6H_2O$ they found that the effects of crystal-field splitting were not apparent due to lower local symmetry at the U site [21]. Kvashnina *et al.* also found it was possible to observe these features in the U L_3-edge $L\beta_5$ ($5d_{3/2,5/2}$-$2p_{3/2}$) HERFD XANES spectra of UO_2 [37].

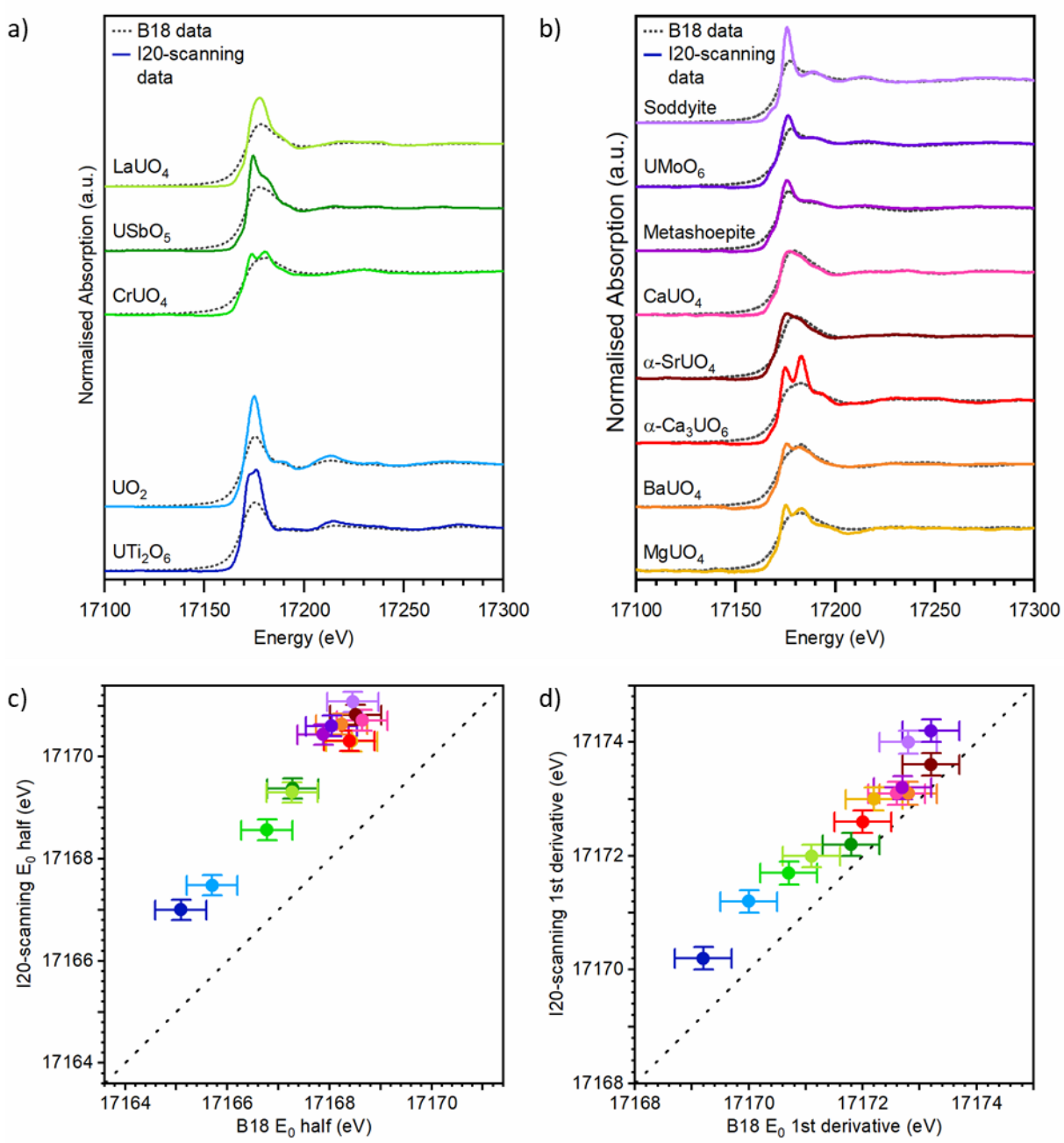

Figure 4.6. Comparison plot of U L_3-edge transmission XANES data collected from U reference compounds (indicated on plots) measured at B18, DLS, Oxford, UK and U L_3-edge $L_{\alpha 1}$ HERFD XANES data measured at I20-scanning, DLS, Oxford, UK, collected from the same set of **(a)** U^{4+} and U^{5+} reference compounds (indicated on plots) and **(b)** U^{6+} reference compounds (indicated on plots). Comparison plots of the **(c)** E_0 half and **(d)** E_0 1st deriv. positions of U reference compounds from U L_3-edge transmission measurements. Colours used for reference compounds are consistent across all plots.

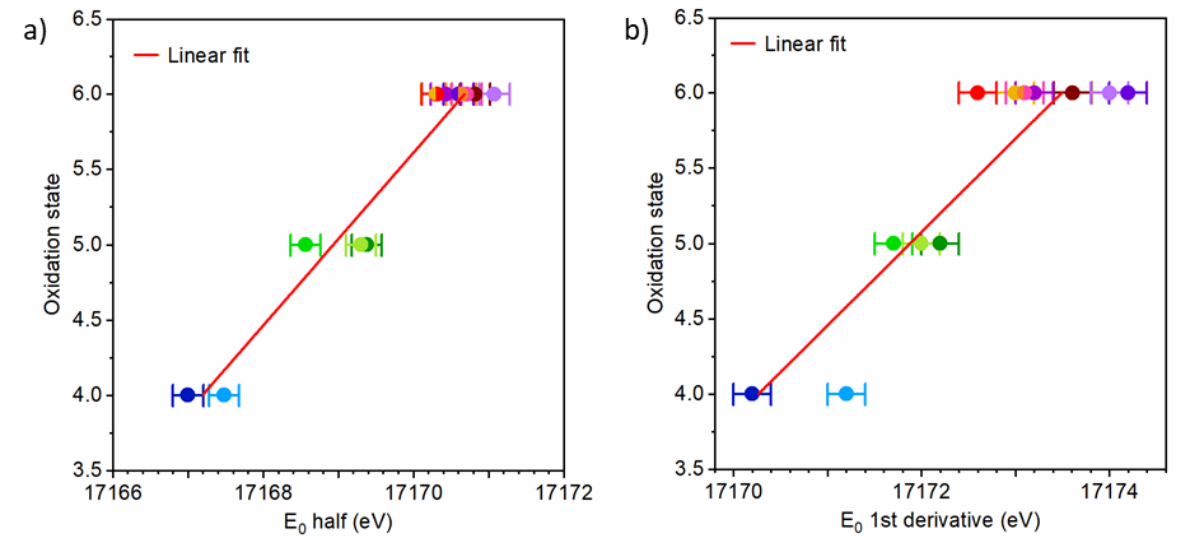

Figure 4.7. (a) E_0 half positions derived from U L_3-edge $L_{\alpha1}$ HERFD data of reference compounds plotted against their known oxidation states; and **(b)** E_0 first derivative positions from U L_3-edge $L_{\alpha1}$ HERFD data of reference compounds plotted against their known oxidation states. Data were collected at I20-scanning, DLS. Colours used for reference compounds are consistent

It is possible that the number of features in the white line region could be used to distinguish between different coordination states. However, not enough U^{4+}, U^{5+}, or 7-fold coordinate reference compounds were measured in the present study to confirm that these observed trends persist, or to determine if a similar trend occurs in the spectra from 7-fold coordinate U reference compounds. Any identified trends would also require underpinning with knowledge in trends in crystal field splitting of the U 6d orbital with coordination.

A pre-edge feature was also apparent between 17164 eV and 17170 eV, more pronounced in some spectra (αCa_3UO_6 and soddyite) than others, which appears to occur in all spectra from the U^{5+} and U^{6+} reference compounds (Figures 4.6a and 4.6b). Features in this region were assigned by Vitova *et al*. to $2p_{3/2}$-5f electronic transitions [70]. Vitova *et al*. speculated that the position and relative intensity of these features could be used to characterise U speciation, as is done with the K-edge spectra of 3d and 4d metals and, furthermore, could provide insight into types of ligands and bonds formed [70].

Features beyond the white line were also found to be better resolved than features in U L_3-edge transmission XANES data, especially intensities of features in XANES from UTi_2O_6 and UO_2. The same uranyl features that were observed in U L_3-edge transmission data were also apparent in the HERFD data from U^{6+} uranyl reference compounds (metaschoepite, $UMoO_6$ and soddyite), with a greater degree of resolution. The high resolution of features, while enabling greater distinction between samples which contain U with a similar speciation, could cause difficulty in performing LCF or PCA with ITTFA. These analysis techniques are limited by the availability of relevant reference compounds and, as there is such significant variation in the U L_3-edge $L_{\alpha1}$ HERFD XANES features and especially features on the absorption edge, it may to be difficult to recreate the shape of the spectra using generic reference compounds.

The E_0 half (Figure 4.6c) and E_0 1st deriv. (Figure 4.6d) positions of reference compounds from U L_3-edge transmission and HERFD data, plotted against each other. Both comparisons found that the E_0 positions from HERFD data were systematically higher than the transmission data. The mean difference between the E_0 half data (2.19 eV) was greater than the mean difference between the E_0 1st deriv. data (0.75 eV) and both data sets, apart from the systematic shifts in position, appeared follow the x=y trend line well. These systematic shifts are artefacts of the U L_3-edge $L_{\alpha1}$ HERFD data being a PFY measurement, which only observes the intensity of X-ray photons emitted at the energy of the $3d_{5/2}$-$2p_{3/2}$ transition. This U L_3-edge $L_{\alpha1}$ HERFD measurement can also be considered as a horizontal slice from a resonant inelastic X-ray plane, as was illustrated by Kvashnina *et al.* for UO_2 [37]. Notably, the impact of the PFY measurement type on both E_0 half and E_0 1st deriv. estimates of position for a U L_3-edge $L_{\alpha1}$ HERFD is systematic, so within a HERFD data set E_0 position could be used to estimate U oxidation state.

The E_0 half (Figure 4.7a) and E_0 1st deriv. (Figure 4.7b) data were used to construct calibration lines, to investigate the suitability of U L_3-edge $L_{\alpha1}$ HERFD edge positions to characterise U oxidation state. The E_0 half data (Figure 4.7a) is promising, with small ranges of E_0 position for each U oxidation state (U^{4+}: 17167.00 – 17167.48 eV, U^{5+}: 17168.57 – 17169.38 eV and U^{6+}: 17170.31 – 17171.08 eV) with large gaps between ranges (1.09 eV and 0.93 eV), which enables more confident estimates of mixed U oxidation states.

The E_0 1st deriv. data (Figure 4.7b) were more broadly spread for U^{4+} and U^{6+} (U^{4+}: 17170.2 – 17171.2 eV, U^{5+}: 17171.7 – 17172.2 eV and U^{6+}: 17172.6 – 17174.2 eV), which resulted in smaller gaps between ranges (0.5 eV and 0.4 eV for U^{4+}-U^{5+} and U^{5+}-U^{6+}, respectively). For both sets of E_0 positions the separations between the U^{4+} and U^{5+} edge positions are slightly greater than between the U^{5+} and U^{6+} reference compounds; however, the extent of the separation is less, which is in contrast to the 2:1 ratio observed in the U L_1-edge E_0 1st deriv. data (Figure 4.1d). The gaps between ranges in the E_0 half data (1.09 eV and 0.93 eV for U^{4+} to U^{5+} and U^{5+} to U^{6+}, respectively) are greater relative to the uncertainty (0.2 eV) than the U L_1-edge E_0 1st deriv. positions (2.8 eV and 1.4 eV for U^{4+} to U^{5+} and U^{5+} to U^{6+}, respectively, with an uncertainty of (0.5 eV). This suggests that of all the E_0 positions from different measurements discussed here, the E_0 half position of the U L_3-edge $L_{\alpha1}$ HERFD data would be the best to use to estimate the U oxidation state (Table 4.4).

The U L_3-edge $L_{\alpha1}$ HERFD XAS spectra were found to have very well resolved features, which enables observation of crystal field splitting caused by octahedral coordination geometry [46]. A possible trend in the intensity of features on the absorption edge could be explored to understand the applicability to determine U coordination. The well-resolved features also enable definitive identification of the presence of U^{6+} uranyl speciation. The high energy resolution could also enable the investigation of small variations in U environment which would not be possible to resolve using a transmission measurement. The use of LCF or PCA with ITTFA to analyse samples may either be very informative or difficult to achieve, depending on the availability of relevant reference compounds with similar U environments to support analysis.

One area in which U L_3-edge $L_{\alpha1}$ HERFD XANES may be of particular use is the measurement of low concentration samples, such as environmental samples, or samples where only small amounts are available as only small amounts of concentrate reference compounds (2 mg) were required for measurement. However, preparation for HERFD measurements requires milling of the sample, which results in loss of sample and would also have to be taken into consideration if planning a measurement with only a small amount of sample available. HERFD XAS measurements can also cause beam damage to the samples, which was

observed during measurement of the U L_3-edge $L_{\alpha 1}$ HERFD data, but was not observed during the measurement of the transition U L_3-edge data.

4.3.3. U L_3-edge EXAFS

For completeness, the EXAFS region of U L_3-edge transmission data is shown in Figures 4.8 to 4.10, with fitting results summarised in Table 4.5. These data were fit to investigate the short-range structure within each reference compound. All the EXAFS data were successfully fit with CIF files of the solved structure of each reference compound. For the majority of reference compounds, it was possible to fit the first two shells to a scattering distance of ~4 Å. Fitting the first shell enabled an approximation of U coordination, from the total degeneracy of the first shell, and estimation of U oxidation state by calculating the bond valence of each U-O first shell path from the final path length (d_{final}). The Bond Valence Sum (BVS) estimates were shown to give reasonable estimates of the known U oxidation states of the reference compounds, but the accuracy has an error of up to ± 0.3. It was found that the inclusion of multiple scattering paths was significantly beneficial to the fit and, for some fits, essential to produce a successful fit. A U L_3-edge transmission synchrotron experiment, with EXAFS, produces data from which speciation and structure can all be determined. Although the estimates of U oxidation state from EXAFS fitting may not be as robust as other analysis techniques (E_0 positions), EXAFS analysis provides a greater range of information (Table 4.4). An overview of the information which can be derived from EXAFS fitting is shown in Table 4.5, a more thorough description of fits achieved and fitting results are available in the SI.

Table 4.5: Summary of the known short range structure of U reference compound and the EXAFS fitting results, including: R factor – a measure of goodness of fit; total degeneracy of the first shell – an estimate of U coordination; and BVS – an estimate of U oxidation state from the sum of the bond valence calculated for each U-O path in the first shell.

Reference Compound	Reference Compound Nominal Speciation			Fit		
	Oxidation state	Coordination number	Coordination geometry	R factor	Total degeneracy of first shell	BVS
UTi_2O_6	4	6	Octahedral [71]	0.0074	6	3.80(5)
UO_2	4	8	Cubic [72]	0.0159	8	4.05(5)
$CrUO_4$	5	6	Octahedral [28]	0.0107	6	4.82(7)
$USbO_5$	5	7	Pentagonal bipyramid [73]	0.0141	7	5.22(12)
$LaUO_4$	5	8	Cubic [74]	0.0229	8	4.80(22)
β-U_3O_8	5.33	6.67	Pentagonal bipyramid and octahedral [75]	0.0151	6.67	4.96(2)
$MgUO_4$	6	6	Distorted octahedral [47]	0.0065	6	5.79(2)
$BaUO_4$	6	6	Distorted octahedral [67]	0.0227	6	5.71(4)
α-Ca_3UO_6	6	6	Octahedra [76]	0.0075	6	5.88(21)
α-$SrUO_4$	6	8	Distorted cubic [77]	0.0114	8	5.91(4)
$CaUO_4$	6	8	Distorted cubic [67]	0.0120	8	6.06(4)
Metaschoepite $(UO_2)_8O_2(OH)_{12}\cdot 10H_2O$	6	7	Pentagonal bipyramids [78]	0.0180	7	5.89(7)
$UMoO_6$	6	7	Pentagonal bipyramid [79, 80]	0.0188	7	5.89(6)
Soddyite $(UO_2)_2SiO_2 \cdot 2H_2O$	6	7	Pentagonal bipyramid [81]	0.0157	7	6.01(9)

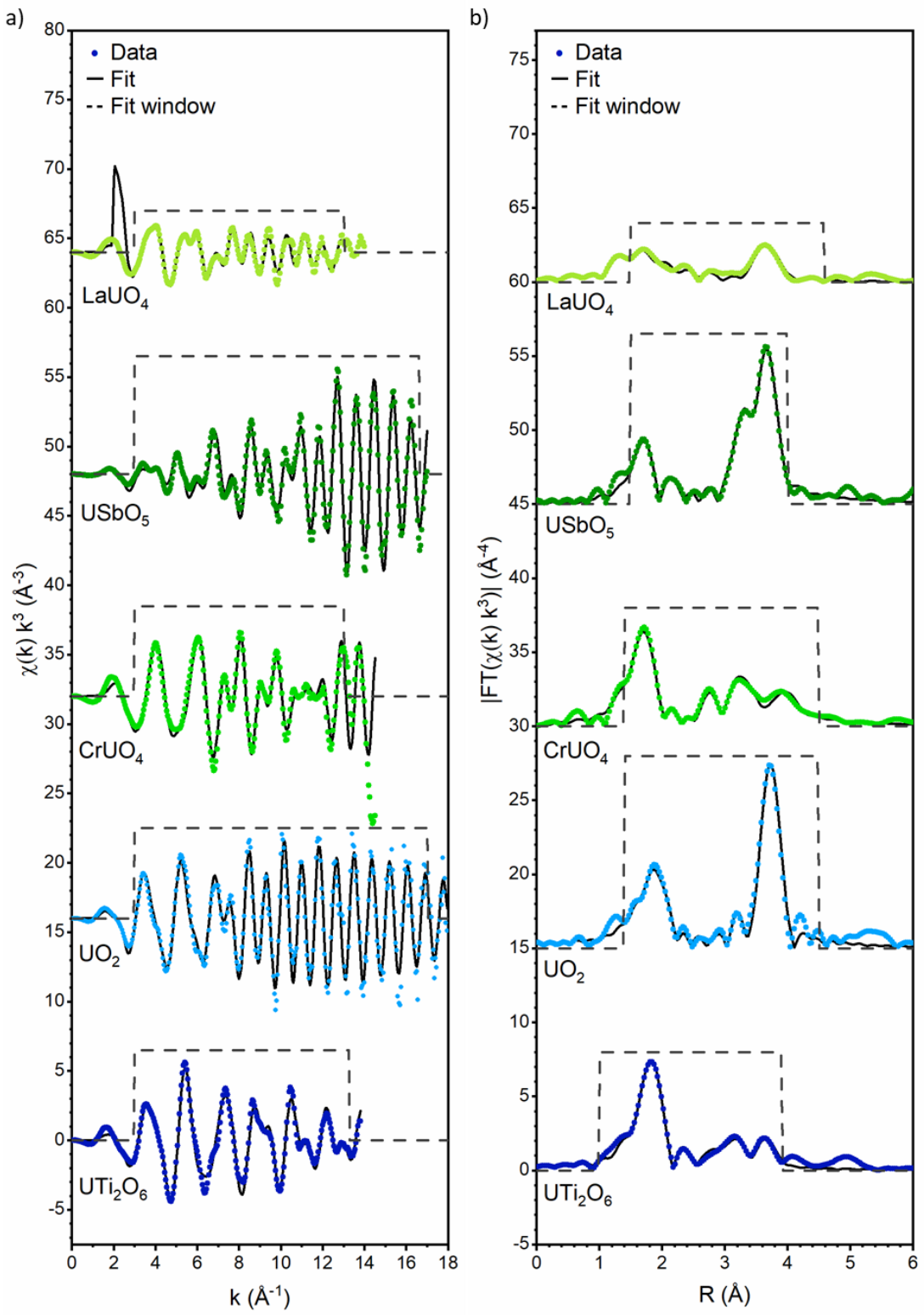

Figure 4.8. Fits of U L_3-edge EXAFS spectra from reference compounds UTi_2O_6, UO_2, $CrUO_4$, $USbO_5$ and $LaUO_4$ presented as **(a)** k^3 EXAFS data and **(b)** as the magnitude of the respective Fourier transform. Colours used for reference compounds are consistent across all plots.

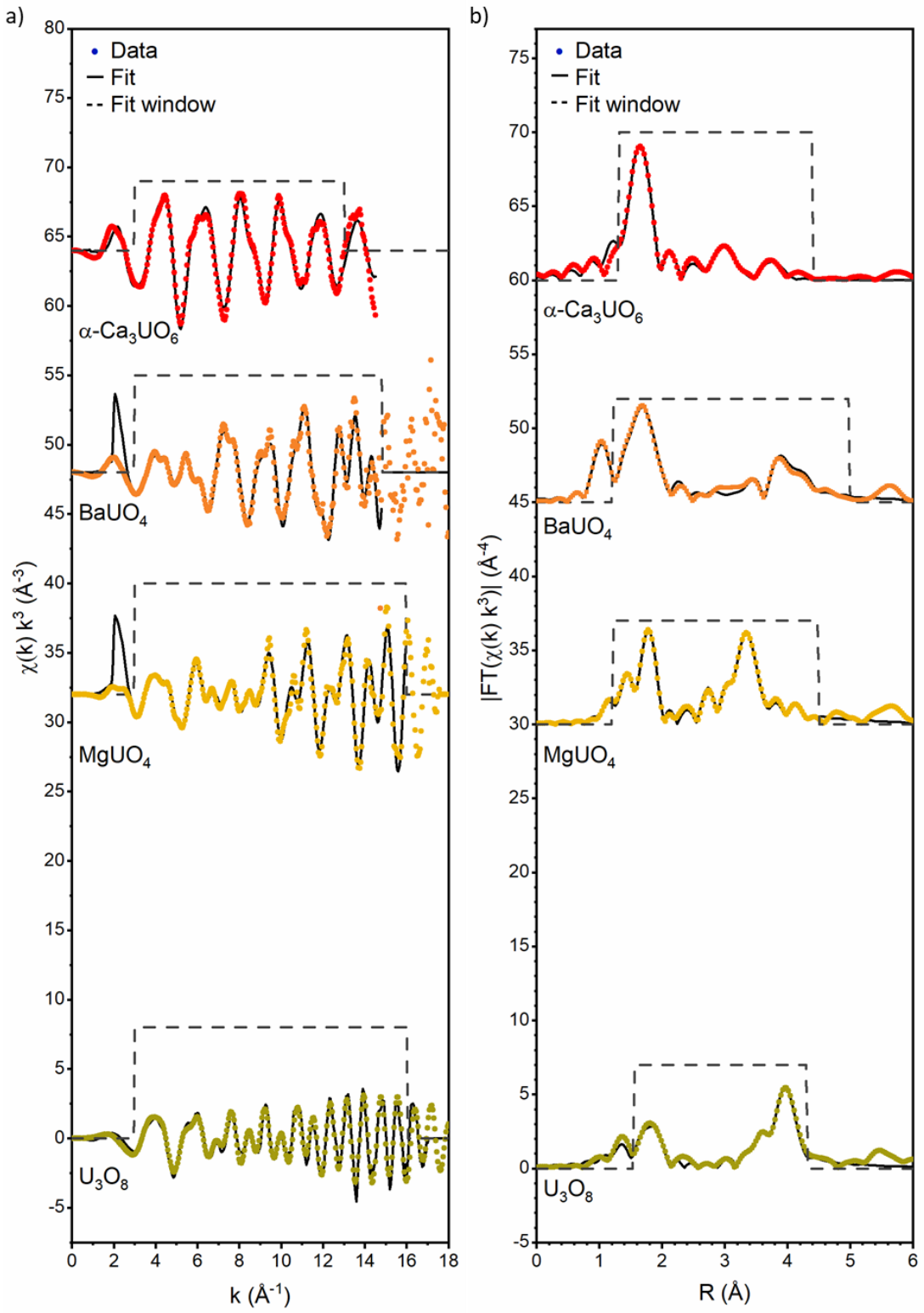

Figure 4.9. Fits of U L_3-edge EXAFS spectra from reference compounds U_3O_8, $MgUO_4$, $BaUO_4$, α-Ca_3UO_6, presented as **(a)** k^3 EXAFS data and **(b)** as the magnitude of the respective Fourier transform. Colours used for reference compounds are consistent across all plots.

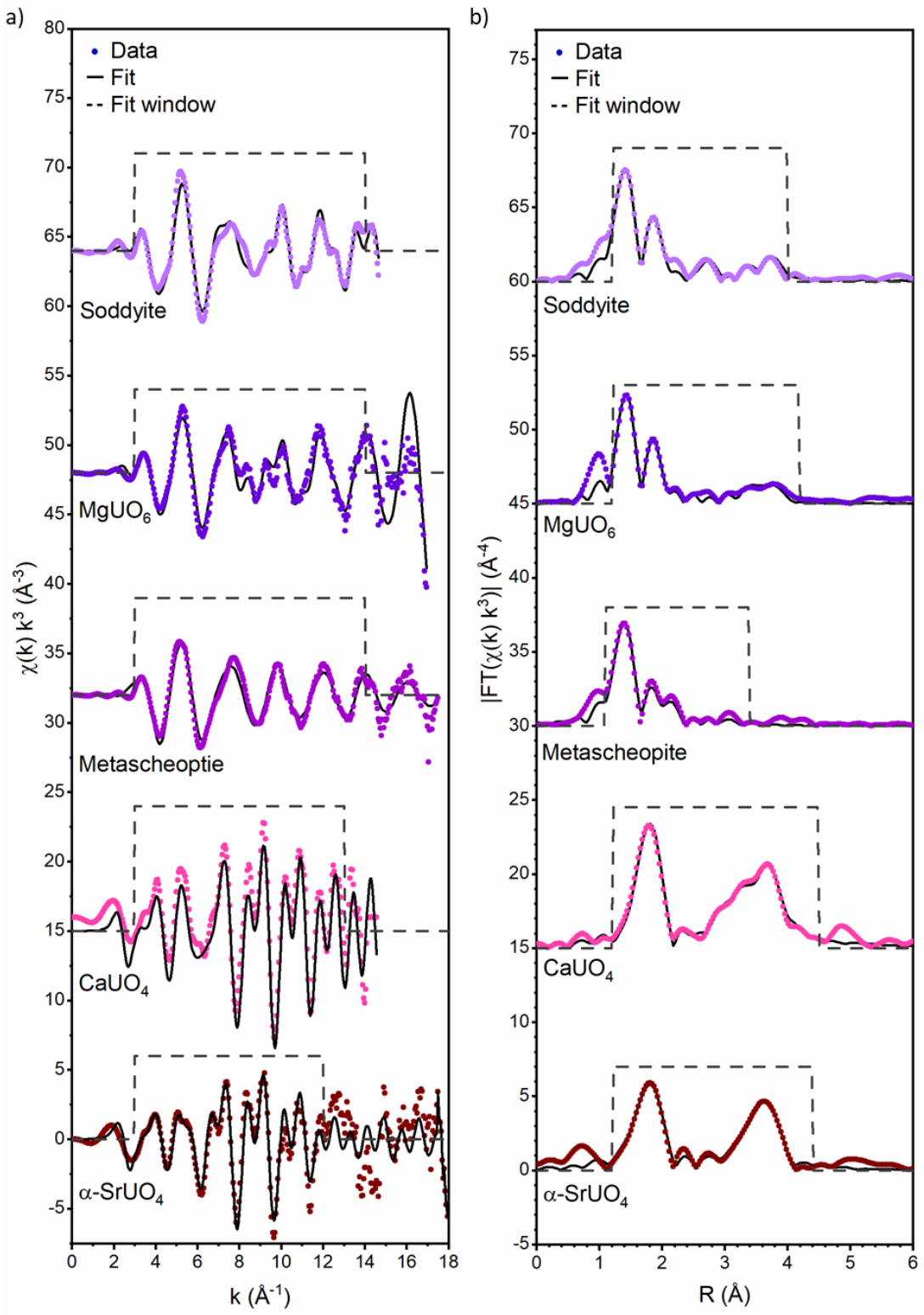

Figure 4.10. Fits of U L_3-edge EXAFS spectra from reference compounds α-$SrUO_4$, $CaUO_4$ metaschoepite ($(UO_2)_8O_2(OH)_{12}\cdot 10H_2O$), $UMoO_6$ and soddyite presented as **(a)** k^3 EXAFS data and **(b)** as the magnitude of the respective Fourier transform. Colours used for reference compounds are consistent across all plots.

4.4. Conclusions

Uranium XAS data have been collected from a suite of U reference compounds using a variety of measurements using different edges, modes and instrumentation. These data have been analysed and compared to investigate the capabilities of each measurement and to discern their benefits and limitations. Each measurement type was found to have a unique benefit, which can be applied to investigate different aspects of U environment in a sample. For net estimates of U oxidation state using edge positions, the U L_3-edge $L_{\alpha1}$ HERFD E_0 half and U L_1-edge transmission E_0 1st deriv. data were found to be the best techniques to apply. The U L_3-edge $L_{\alpha1}$ HERFD XANES data also appeared to display a feature at the beginning of the edge, and the intensity of features on the absorption edge appeared to follow a trend that could be used to determine U coordination. The majority of E_0 positions investigated presented a larger shift in edge position between U^{4+} and U^{5+} than between U^{5+} and U^{6+}; therefore, with this technique, and others dependent on edge position, there is a greater sensitivity to variations in net oxidation state between U^{4+} and U^{5+} than U^{5+} and U^{6+}. The U L_1-edge XANES did not have distinct enough features to gain any insight apart from edge position; however, sensitivity of features to changes in U coordination and structure suggested attempts to measure U L_1-edge EXAFS data or conduct a U L_1-edge HERFD XAS experiment could produce more informative data.

The U L_3-edge transmission measurement was found to provide the largest range of possible information to obtain from the data: U oxidation state from E_0 position; the presence of U^{6+} uranyl from XANES features; and short-range structure from EXAFS fitting. The U L_3-edge transmission laboratory spectrometer data were found to be in good agreement with the U L_3-edge synchrotron data collected to investigate the suitability of different measurements, giving confidence to future use of these instruments to characterise U speciation. The U M_4-edge M_β HERFD XANES data was the only measurement that enabled the direct observation of contributions from different U oxidation states, and therefore could be used to determine the fraction of different U oxidation states present and confirm the presence of U^{5+}. Any attempt to fully examine the U environment of a sample would benefit from the use of multiple of the techniques demonstrated here, ideally including U L_3-edge EXAFS and U M_4-edge M_β HERFD XAS measurements.

4.5. Supporting Information

To optimise the fit and reduce the number of parameters used in some fits single scattering paths were constrained to share parameters. Multiple scattering paths were assigned parameters which were defined as the sum or multiples of parameters from single scattering paths. When discussing the number of unique scattering paths present in each shell this is using the paths which Artemis has identified from FEFF calculations as different enough to be treated as a unique path. One limitation to fitting of the EXAFS data was the presences of a Zr K-edge absorption edge (17998 eV) in several spectra, which required truncation and reduced the range of EXAFS data available for fitting. The presence of a Zr K-edge was attributed to Zr contamination during preparation of the reference compounds for measurement.

4.5.1. UTi_2O_6

UTi_2O_6 (brannerite) has a monoclinic (C2/m) contains one unique U^{4+} octahedral site and one unique Ti octahedral site, the structure of UTi_2O_6 can be described as layers of corner sharing U octahedra separated by layers of edge sharing Ti octahedra [82]. The data were windowed between 3.00 and 13.25 $Å^{-1}$ and the resultant Fourier transform data were fit between 1.00 and 3.90 $Å^{-1}$. The fit was constructed using a CIF file from Szymanski *et al.* [71]. The best fit used one U-O scattering path (O1) with an initial path length of 2.296 Å to represent the two unique U-O scattering paths in the first shell. A second U-O path with an initial path length of 2.824 Å, not in the first shell, was also added, the two U-O paths did not share ΔR or σ^2 parameters. The two unique U-Ti scattering paths could not be adequately represented with one scattering path, so two were used, these two scattering paths (Ti1 and Ti2) were constrained to share a σ^2 parameter. A U-U scattering path (U1) was used to represent one unique U-U scattering path.

4.5.2. UO_2

UO_2 (uraninite) has a cubic structure ($Fm\bar{3}m$) which contains one unique U^{4+} 8-fold cubic site [72]. The data were windowed between 3.00 and 17.00 $Å^{-1}$ and the resultant Fourier transform data were fit between 1.40 and 4.50 $Å^{-1}$. The fit was constructed using a CIF file from Wyckoff [83]. The first three shells each had one unique single scattering path, and one scattering path (O1, U1 and O2) was used to represent each of them. The two U-O paths were constrained to share a σ^2 parameter. Three multiple scattering O1-O1 paths, two double and one forward through multiple scattering path were also included in the fit. These multiple scattering paths all had ΔR parameters defined as $2x\Delta R_{O1}$ and σ^2 which were defined as $2x\sigma^2_{O1}$.

4.5.3. $CrUO_4$

$CrUO_4$ has an orthorhombic structure (Pbcn) with one unique U^{5+} octahedral site and one unique Cr octahedral site [28]. The fit was constructed using an adapted CIF file for $FeUO_4$ from Bacmann and Bertaut [84], $FeUO_4$, like $CrUO_4$, is a transition metal U^{5+} monouranate and Fe and Cr both have an oxidation state of 3+ [32]. $CrUO_4$ and $FeUO_4$ have similar structures, both $BiVO_4$ [32], and the U L_3-edge HERFD ($L_{\alpha1}$) XANES of $CrUO_4$ presented in this work (Figure 4.5c) are very similar to that the U L_3-edge HERFD ($L_{\alpha1}$) XANES measured from $FeUO_4$ in previous work by Yomogida et al [33]. The data were windowed between 3.00 and 13.00 $Å^{-1}$ and the resultant Fourier transform data were fit between 1.40 and 4.50 $Å^{-1}$. The fit used one scattering path (O1) to represent the three unique U-O single scattering paths in the first shell. A second U-O scattering path (O2) was added to represent one unique U-O path and a third (O3) was used to represent four unique O-U scattering paths with original path lengths 3.692-3.994Å. The three U-O paths used (O1, O2 and O3) were constrained to share the same σ^2 parameter (σ^2_U). Each unique U-Cr scattering path was represented with a separate scattering path (Cr1, Cr2 and Cr3), these paths were constrained to share the same σ^2 parameter. Four multiple-scattering O1-O1 paths were included in the fit. All of the multiple-scattering fits, including the rattle O1-O1 path, had ΔR and σ^2 parameters which were defined as $2x\Delta R_{O1}$ and $2x\sigma^2_U$.

Table 4.SI.1. Fit parameters and uncertainties from EXAFS fits of UTi_2O_6, UO_2, $CrUO_4$ and $USbO_5$. Fit parameters: R-factor – measure of goodness of fit; ΔE – shift in E_0, which was constrained to be the same for all paths; S_0^2 – the amplitude reduction factor; N – degeneracy of a path; R – original path length; R_{calc} –calculated path length, sum of the calculated parameter ΔR and R; σ^2 – the Debye-Waller Factor; V_i – calculated individual valence of a path; and BVS – sum of the valences for all paths in the first shell. Symbols * † ‡ ¤ § have been used to indicate the same parameter has been used. In the R_{calc} column any paths within a fit which share the same symbol share the same ΔR parameters, in the σ^2 column any paths within a fit which share the same symbol share the same σ^2 parameter. For paths which had ΔR and σ^2 parameters which were defined as the sum of more than one shared parameter, multiple symbols were used to indicate this. A through explanation of parameters used for each fit is given in the text.

Reference Compound	R factor	S_0^2	ΔE (eV)	Path	N	R (Å)	R_{Calc} (Å)	σ^2 (Å^2)	V_i	BVS
UTi_2O_6	0.0074	0.85	4.3(6)	O1	6	2.296	2.270(5)	0.0044(3)	0.63(1)	3.80(5)
				O2	2	2.824	2.854(5)	0.0194(94)		
				Ti1	4	3.556	3.528(12)	0.0097(32)*		
				Ti2	2	3.703	3.658(48)	0.0097(32)*		
				U1	2	3.770	3.769(9)	0.0040(9)		
UO_2	0.0161	0.85	5.1(5)	O1	8	2.368	2.353(6)*	0.0093(5)*	0.51(1)	4.05(5)
				O1-O1 MS other double	24	3.735	3.706(12)*	0.0186(10)*		
				U1	12	3.867	3.871(3)	0.0048(2)		
				O1-O1 MS double	24	4.301	4.272(12)*	0.0186(10)*		
				O2	24	4.534	4.447(10)	0.0093(5)*		
				O1-O1 MS forward through	8	4.736	4.707(12)*	0.0186(10)*		
$CrUO_4$	0.0107	0.85	6.5(11)	O1	6	2.183	2.159(10)*	0.0074(6)*	0.80(1)	4.82(7)
				Cr1	1	3.295	3.205(21)	0.0027(10)†		
				O2	2	3.309	3.375(37)	0.0074(6)*		
				O1-O1 other double	2	3.578	3.529(20)*	0.0149(12)*		
				Cr2	2	3.623	3.612(24)	0.0027(10)†		
				O1-O1 other double	8	3.665	3.616(20)*	0.0149(12)*		
				O1-O1 other double	8	3.666	3.618(20)*	0.0140(12)*		
				O3	8	3.693	3.807(28)	0.0074(6)*		
				Cr3	4	3.755	3.723(12)	0.0027(10)†		
				U1	2	4.077	4.037(11)	0.0018(10)		
				O1-O1 rattle	2	4.095	4.047(20)*	0.0140(12)*		
$USbO_5$	0.0141	0.85	3.4(9)	O1	2	2.024	1.971(7)*	0.0041(5)*	1.06(8)	5.22(12)
				O2	3	2.303	2.261(7)	0.0041(5)*	0.68(4)	
				O3	2	2.429	2.434(10)	0.0024(9)	0.53(1)	
				Sb1	2	3.550	3.543(7)	0.0029(3)†		
				U1	2	3.635	3.665(14)	0.0034(10)		
				Sb2	4	3.960	3.975(6)†	0.0029(3)†		
				O1-O1 non forward	2	3.953	3.848(13)*	0.0081(11)*		
				O1-O1 hinge	2	3.957	3.852(13)*	0.0081(11)*		
				O1-Sb2 non forward	2	3.962	3.924(13)*†	0.0070(8)*†		
				O1-Sb2 forward	2	3.963	3.925(13)*†	0.0070(8)*†		
				O1-Sb2-O1 double forward scattering	1	3.963	3.873(20)*†	0.0111(13)*†		
				O1-Sb2-O1 forward triangle	1	3.969	3.924(10)*†	0.0055(7)*†		

4.5.4. $USbO_5$

$USbO_5$ has a triclinic structure ($P\bar{1}$) which contains one unique U^{5+} site which is 7-fold coordinated and two unique Sb sites, which are both octahedral [73]. The fit was constructed using a CIF file from Dickens *et al.* [73]. The data were windowed from 3.00 - 16.60 $Å^{-1}$ and the resultant Fourier transform data were fit between 1.50 and 4.00 Å. The best fit used three U-O paths to represent the seven unique U-O scattering paths in the first shell. To reduce the number of parameters used the O1 and O2 paths were constrained to share the same σ^2 parameter (σ^2_{O1}). A second shell was fit using two Sb paths, a U path and several multiple scattering O1-O1 and O1-Sb paths. Two Sb paths were used to represent four unique Sb scattering paths these Sb paths were constrained to share a σ^2 parameter. One U path was used to represent two unique U scattering paths. The ΔR and σ^2 parameters of the two O1-O1 multiple scattering paths were defined as $2x\Delta R_{O1}$ and $2x\sigma^2_{O1}$. The ΔR and σ^2 parameters for the O1-Sb1 multiple scattering forward and non-forward paths were defined as $\Delta R_{O1}+\Delta R_{Sb2}$ and $\sigma^2_{O1}+\sigma^2_{Sb2}$. The ΔR and σ^2 parameters for the O1-Sb1-O1 double forward scattering path were defined as $2x\Delta R_{O1}+\Delta R_{Sb1}$ and $2x\sigma^2_{O1}+\sigma^2_{Sb2}$. The ΔR and σ^2 parameters of the O1-Sb1-O1 forward triangle path were defined as $\Delta R_{O1}+0.5x\Delta R_{Sb1}$ and $x\sigma^2_{O1}+0.5x\sigma^2_{Sb2}$.

4.5.5. $LaUO_4$

$LaUO_4$ has a cubic structure ($Fm\bar{3}m$) where La and U^{5+} both have one unique cubic site [74]. The fit was constructed using an adapted CIF file from Garcia-Chain *et al.* [74]. The data were windowed from 3.00 – 13.00 $Å^{-1}$ and the resultant Fourier transform data were fit between 1.50 and 4.60 Å. Fitting the first shell proved difficult, from the FEFF calculation only one unique U-O single scattering path was identified, however using one single scattering path to represent the first shell was not successful. Using multiple scattering paths to represent the first shell was also unsuccessful, so one U-O scattering path with additional 3rd and 4th cumulant parameters (c_3 and c_4) was used. The c_3 and c_4 parameters describe the skew and kurtosis of the distribution of path distances, where these parameters are not included for a path, they are set to $c_3 = 0$ and $c_4 = 0$, so the distribution of path distances is assumed to be Gaussian. The second shell was fit using three single scattering paths to represent unique

single scattering paths: U-La, La1; U-U, U1; and U-O, O2, the O2 path was constrained to share a σ^2 parameter with the O1 path (σ^2_O).

Table 4.SI.2. Fit parameters and uncertainties from the EXAFS fit of $LaUO_4$. Fit parameters: R-factor – measure of goodness of fit; ΔE – shift in E_0, which was constrained to be the same for all paths; S_0^2 – the amplitude reduction factor; N – degeneracy of a path; R – original path length; R_{calc} –calculated path length, sum of the calculated parameter ΔR and R; σ^2 – the Debye-Waller Factor; C3 – 3rd cumulant; C4 – 4th cumulant; V_i – calculated individual valence of a path; and BVS – sum of the valences for all paths in the first shell. Symbols * † ‡ ¤ § have been used to indicate the same parameter has been used. In the R_{calc} column any paths within a fit which share the same symbol share the same ΔR parameters, in the σ^2 column any paths within a fit which share the same symbol share the same σ^2 parameter. For paths which had ΔR and σ^2 parameters which were defined as the sum of more than one shared parameter, multiple symbols were used to indicate this. A through explanation of parameters used for each fit is given in the text.

Reference Compound	R factor	S_0^2	ΔE (eV)	Path	N	R (Å)	R_{final} (Å)	σ^2 (Å^2)	C_3 (Å^3)	C_4 (Å^4)	V_i	BVS
$LaUO_4$	0.0229	0.85	7.0(16)	O1	8	2.419	2.346(30)	0.0243(31)*	0.0037(14)	0.0001(2)	0.60(3)	4.80(22)
				La1	8	3.949	3.998(40)	0.0154(66)				
				U1	4	3.949	3.818(26)	0.0070(16)				
				O2	24	4.631	4.449(25)	0.0243(31)*				

4.5.6. β-U_3O_8

β-U_3O_8 has a orthorhombic structure (Cmcm) three unique U sites, one U^{5+} octahedral site, one U^{5+} pentagonal bipyramid site and one U^{6+} pentagonal bipyramid site [75]. The fit was constructed using a CIF file from Loopstra *et al.* [75]. The fit used four U-O paths (O1, O2, O3 and O4) to attempt to represent the three unique U sites, the O1 and O2 paths were constrained to share a same σ^2 parameter (σ^2_{O1}) and the four paths had a total degeneracy of 6.67. One U-O path (O5) was included from the U^{5+} octahedral site which had an original degeneracy of N = 2, this path was not present in the FEFF calculations for the other two sites, so was set a degeneracy of N = 0.67. All of the U sites experienced U-U scattering paths between 3.640 and 4.157 Å, for each site the total degeneracy of these U-U paths was 8. To represent these U-U single scattering paths three U-U scattering paths (U1, U2 and U3) were used, these paths were constrained to share the same σ^2 parameter (σ^2_U). Four O-U multiple scattering paths were included, one forward scattering path, one double forward scattering path and two non-forward linear scattering paths, all of the degeneracies of these paths were adjusted to their fraction within the whole structure. The ΔR and σ^2 parameters of the O1-U3

forward scattering path were defined as $\Delta R_{O1}+\Delta R_{U3}$ and $\sigma^2_{O1}+\sigma^2_{U}$, respectively. The ΔR and σ^2 parameters of the O_1-U_1 double forward scattering path were defined as $2x\Delta R_{O1}+2x\Delta R_{U1}$ and $\sigma^2_{O1}+\sigma^2_{U}$, respectively. The ΔR and σ^2 parameters of the O1-U1 non-forward linear scattering path were defined as $\Delta R_{O1}+\Delta R_{U1}$ and $\sigma^2_{O1}+\sigma^2_{U}$, respectively. The ΔR and σ^2 parameters of the O3-U1 non-forward linear scattering path were defined as $\Delta R_{O4}+\Delta R_{U1}$ and $\sigma^2_{O3}+\sigma^2_{U}$, respectively.

4.5.7. $MgUO_4$

$MgUO_4$ has an octahedral structure (Imma) which contains one unique U^{6+} site, a distorted octahedral and one unique octahedral Mg site [47]. The fit was constructed using a CIF file produced by Murphy *et al.* [47]. The data were windowed from 3.00 – 15.00 $Å^{-1}$ and the resultant Fourier transform data were fit between 1.20 and 4.50 Å. The first shell contained two unique U-O scattering paths which were represented by two U-O paths (O1 and O2), these paths had separate ΔR and σ^2 parameters. A single U-O path (O3) and single U-U path (U1) were used to represent one unique single scattering U-O path and one unique U-U path. Three U-Mg scattering paths (Mg1, Mg2 and Mg3) were used to represent three unique U-Mg scattering paths, these three paths were constrained to share the same σ^2 parameter. Paths Mg2 and Mg3 were constrained to share the same ΔR parameter (ΔR_{Mg}) and path Mg1 had a ΔR parameter which was defined as $-\Delta R_{Mg}$. Three U-O paths (O4, O5 and O6) were used to represent 4 unique U-O scattering paths with original path lengths of 3.842-4.234 Å, these paths were constrained to share the same σ^2 parameter as O3. A second U-U path was used to represent one unique U-U path with an original path length of 4.426 Å, this path was constrained to share the same σ^2 parameter as U1. An O1-O2 multiple scattering double scattering path was included, the ΔR and σ^2 parameters were defined as $\Delta R_{O1}+\Delta R_{O2}$ and $\sigma^2_{O1}+\sigma^2_{O2}$ respectively.

Table 4.SI.3. Fit parameters and uncertainties from EXAFS fits of β-U_3O_8, $MgUO_4$ and $BaUO_4$. Fit parameters: R-factor – measure of goodness of fit; ΔE – shift in E_0, which was constrained to be the same for all paths; S_0^2 – the amplitude reduction factor; N – degeneracy of a path; R – original path length; R_{calc} –calculated path length, sum of the calculated parameter ΔR and R; σ^2 – the Debye-Waller Factor; V_i – calculated individual valence of a path; and BVS – sum of the valences for all paths in the first shell. Symbols * † ‡ ¤ § have been used to indicate the same parameter has been used. In the R_{calc} column any paths within a fit which share the same symbol share the same ΔR parameters, in the σ^2 column any paths within a fit which share the same symbol share the same σ^2 parameter. For paths which had ΔR and σ^2 parameters which were defined as the sum of more than one shared parameter, multiple symbols were used to indicate this. A through explanation of parameters used for each fit is given in the text.

Reference Compound	R factor	S_0^2	ΔE (eV)	Path	N	R (Å)	R_{final} (Å)	σ^2 (Å^2)	V_i	BVS
β-U_3O_8	0.0151	0.85	-1.3(9)	O1	1	2.014	1.934(14)*	0.0026(19)*	1.12(2)	4.96(2)
				O2	2	2.080	2.097(10)	0.0026(19)*	1.75(1)	
				O3	2	2.283	2.228(9)†	0.0020(13)†	1.44(1)	
				O4	1.67	2.396	2.631(23)	0.0125(43)‡	0.65(1)	
				O5	0.67	3.535	3.368(113)	0.0125(43)‡		
				U1	1	3.674	3.734(13)¤	0.0045(3)¤		
				U2	2	3.876	3.988(14)	0.0045(3)¤		
				O1-U3 forward scattering	2	4.150	4.084(21)*§	0.0072(22)*§		
				U3	5	4.150	4.164(7)§	0.0045(3)¤		
				O1-U1 double forward scattering	1	4.150	4.111(27)*¤	0.0072(22)*¤		
				O1-U1 non-forward linear	1.33	4.160	4.140(27)*¤	0.0072(22)*¤		
				O3-U1 non-forward linear	1.33	4.160	4.165(22)†¤	0.0065(16)†¤		
$MgUO_4$	0.0065	0.85	0.3(6)	O1	2	1.939	1.931(3)*	0.0016(3)*	1.28(1)	5.79(2)
				O2	4	2.162	2.146(4)†	0.0038(3)†	0.81(1)	
				O3	2	3.267	3.208(37)	0.0074(24)‡		
				U1	2	3.475	3.465(3)	0.0015(3)		
				O1-O2 double	16	3.503	3.478(7)*†	0.0054(6)*†		
				Mg1	2	3.591	3.370(11)	0.0041(18)¤		
				Mg2	4	3.694	3.595(23)	0.0041(18)¤		
				Mg3	2	3.859	4.079(32)	0.0041(18)¤		
				O4	6	3.980	4.021(28)	0.0074(24)‡		
				U2	2	4.426	4.290(24)	0.0096(27)		
$BaUO_4$	0.0227	0.85	-0.8(1.7)	O1	2	1.897	1.903(6)*	0.0042(7)*	1.35(2)	5.71(4)
				O2	4	2.198	2.181(7)†	0.0026(4)†	0.75(1)	
				O1-O2 double	8	3.468	3.457(13)*†	0.0068(11)*†		
				O1-O2 double	8	3.529	3.518(13)*†	0.0068(11)*†		
				Ba1	2	3.790	3.773(19)	0.0028(13)‡		
				O1-O1 non-forward linear	2	3.794	3.807(12)*	0.0084(13)*		
				O1-O1 forward through absorber	2	3.794	3.807(12)*	0.0084(13)*		
				O1-O1 rattle	2	3.794	3.807(12)*	0.0084(13)*		
				O3	4	3.886	3.914(26)	0.0026(4)†		
				Ba2	2	3.991	3.930(24)	0.0028(13)‡		
				U1	4	4.067	4.132(2)	0.0046(22)		
				Ba3	2	4.215	4.116(32)	0.0028(13)‡		
				Ba4	2	4.396	4.412(21)	0.0028(13)‡		

4.5.8. $BaUO_4$

$BaUO_4$ has an orthorhombic structure (Pbcm) with one unique U^{6+} site a distorted octahedral with an orthorhombic structure [67]. The fit was constructed using a CIF file produced by Murphy *et al.* [67]. The data were windowed from 3.00 – 14.80 $Å^{-1}$ and the resultant Fourier transform data were fit between 1.20 and 5.00 Å. The first shell was fit using two U-O paths (O1 and O2) to represent the two unique U-O single scattering paths, these paths had independent ΔR and σ^2 parameters. One U-U path (U1) was included to represent one unique U-U single scattering path. One U-O path (O3) was added to represent two unique U-O single scattering paths, the O3 path was constrained to share a σ^2 parameter with the O2 path (σ^2_2). Four U-Ba paths (Ba1, Ba2, Ba3 and Ba4) were included to represent four unique single scattering U-Ba paths, these paths were constrained to share a σ^2 parameter (σ^2_{Ba}). Two O1-O2 multiple scattering paths were included in the fit, the ΔR and σ^2 parameters for these paths were defined as $\Delta R_{O1}+\Delta R_{O2}$ and $\sigma^2_{O1}+\sigma^2_{O2}$, respectively. Three O1-O1 multiple scattering paths were included in the fit, a non-forward linear, a forward through and rattle multiple scatterer. The ΔR and σ^2 parameters for these O1-O1 multiple scattering paths were all defined as $2x\Delta R_{O1}$ and $2x\sigma^2_{O1}$.

4.5.9. α-Ca_3UO_6

α-Ca_3UO_6 has a trigonal structure ($R\bar{3}$) which contains two unique U^{6+} sites, both octahedral and one unique octahedral Ca site [76]. The fit was constructed using a CIF file produced by Holc and Golič [76]. The data were windowed from 3.00 – 13.00 $Å^{-1}$ and the resultant Fourier transform data were fit between 1.30 and 4.40 Å. The two U octahedral sites are very similar so the FEFF calculations for each U site produced lists of paths which were the same types, had the same degeneracy and similar distances distance up to 5Å. Therefore, it was possible to use one path from one FEFF calculation to represent a similar path from both U sites. The first shell of both U sites contained one unique scattering U-O path, however it was not possible to accurately represent the first shell with one U-O path. Attempts to add C_3 and C_4 parameters to the first shell path to improve the fit were not successful. Instead it was found the first shell was best fit by using two U-O paths, O1 and O2, which each had a degeneracy

of N=3, these paths had separate ΔR and σ^2 parameters. Each U site had two unique U-Ca paths in the second shell, it was possible to represent these with two scattering paths, Ca1 and Ca2, these paths were constrained to share a σ^2 parameter (σ^2_{Ca}). Each U site had one unique U-O paths in the second shell, it was possible to represent these two paths with one scattering paths, O3, this path was constrained to share a σ^2 parameter with the O1 path (σ^2_{O1}). It was possible to represent the O-O multiple scattering paths from the two U sites with one path each. The ΔR and σ^2 parameters for the O-O multiple scattering paths were defined as $\Delta R_{O1}+\Delta R_{O2}$ and $\sigma^2_{O1}+\sigma^2_{O2}$. Each U site calculation had one O-Ca2 unique multiple scattering path, one O-Ca path was used to represent these paths. The ΔR and σ^2 parameters for the O-Ca2 multiple scattering paths were defined as $0.5x(\Delta R_{O1}+5x\Delta R_{O2})+0.5x\Delta R_{Ca2}$ and $0.5x(\sigma^2_{O1}+\sigma^2_{O2})+0.5x\sigma^2_{Ca}$, respectively.

4.5.10. α-$SrUO_4$

α-SrUO4 has a rhombohedral structure (R3̄m) with one unique U^{6+} 8-fold coordinated site, which has with two shorter U-O paths [77]. The fit was constructed using a CIF file from Murphy *et al.* [77]. The data were windowed from 3.00 – 12.00 $Å^{-1}$ and the resultant Fourier transform data were fit between 1.20 and 4.40 Å. The first shell was fit using two U-O paths (O1 and O2) to represent the two unique U-O single scattering paths, these paths had independent ΔR and σ^2 parameters. In the second shell three paths: U-Sr, Sr1; U-U, U1; and U-O, O3 were used to represent on unique single scattering path each. The O3 path was constrained to share the same σ^2 parameter as O2 (σ^2_{O2}). Two multiple scattering O1-O2 double paths were included to improve the fit, for both paths the ΔR and σ^2 parameters of these paths were defined as $\Delta R_{O1}+\Delta R_{O2}$ and $\sigma^2_{O1}+\sigma^2_{O2}$ respectively. One O1-O1 multiple scattering forward path was also included, for this path the ΔR and σ^2 parameters were defined as $2x\Delta R_{O1}$ and $2x\sigma^2_{O1}$ respectively.

Table 4.SI.4. Fit parameters and uncertainties from EXAFS fits of Ca_3UO_6, α-$SrUO_4$ $CaUO_4$ and metaschoepite ($(UO_2)_8O_2(OH)_{12} \cdot 10H_2O$)). Fit parameters: R-factor – measure of goodness of fit; ΔE – shift in E_0, which was constrained to be the same for all paths; S_0^2 – the amplitude reduction factor; N – degeneracy of a path; R – original path length; R_{calc} –calculated path length, sum of the calculated parameter ΔR and R; σ^2 – the Debye-Waller Factor; V_i – calculated individual valence of a path; and BVS – sum of the valences for all paths in the first shell. Symbols * † ‡ ¤ § have been used to indicate the same parameter has been used. In the R_{calc} column any paths within a fit which share the same symbol share the same ΔR parameters, in the σ^2 column any paths within a fit which share the same symbol share the same σ^2 parameter. For paths which had ΔR and σ^2 parameters which were defined as the sum of more than one shared parameter, multiple symbols were used to indicate this. A through explanation of parameters used for each fit is given in the text.

Reference Compound	R factor	S_0^2	ΔE (eV)	Path	N	d (Å)	d_{final} (Å)	σ^2 (Å^2)	V_i	BVS
α-Ca_3UO_6	0.0075	0.85	4.1(1.7)	O1	3	2.077	2.075(4)*	0.0009(4)*	0.94(1)	5.88(21)
				O2	3	2.081	2.037(45)†	0.0156(48)†	1.02(9)	
				O-O double	12	3.478	3.432(49)*†	0.0165(52)*†		
				Ca1	6	3.488	3.471(19)	0.0128(11)‡		
				O-O double	12	3.624	3.578(49)*†	0.0165(52)*†		
				Ca2	6	4.081	4.152(24)¤	0.0128(11)‡		
				O-O non-forward linear	6	4.162	4.116(49)*†	0.0165(52)*†		
				O-O forward through absorber	6	4.162	4.116(49)*†	0.0165(52)*†		
				O-O rattle	6	4.162	4.116(49)*†	0.0165(52)*†		
				O-Ca2	12	4.234	4.246(49)*†¤	0.0146(37)*†‡		
				O3	6	4.423	4.341(63)	0.0156(48)†		
α-$SrUO_4$	0.0114	0.85	6.7(1.0)	O1	2	1.938	1.955(6)*	0.0032(7)*	1.21(2)	5.91(4)
				O2	6	2.315	2.303(7)†	0.0068(6)†	0.58(1)	
				O1-O2 double	12	3.475	3.480(13)*†	0.0100(13)*†		
				O1-O2 double	12	3.782	3.787(13)*†	0.0100(13)*†		
				Sr1	6	3.819	3.828(11)	0.0074(12)		
				O1-O1 forward through absorber	2	3.876	3.910(12)*	0.0063(11)*		
				U1	6	3.925	3.937(21)	0.0056(10)		
				O3	12	4.377	4.453(36)	0.0068(6)†		
$CaUO_4$	0.0120	0.85	5.2(8)	O1	2	1.961	1.956(6)*	0.0021(7)*	1.21(2)	6.06(4)
				O2	6	2.295	2.283(5)†	0.0038(5)†	0.61(1)	
				O1-O2 double	12	3.459	3.441(12)*†	0.0060(12)*†		
				Ca1	6	3.681	3.684(12)	0.0062(11)		
				O1-O2 double	12	3.797	3.780(11)*†	0.0060(12)*†		
				U1	6	3.873	3.886(6)	0.0035(5)		
				O1-O1 forward through absorber	2	3.922	3.912(12)*	0.0042(15)*		
				O3	24	4.341	4.411(15)	0.0114(29)		
Metascheopite	0.0180	0.85	8.4(16)	O1	2	1.785	1.794(8)*	0.0022(6)*	1.70(3)	5.89(7)
				O2	2	2.309	2.287(27)	0.0060(28)†	0.60(3)	
				O3	3	2.429	2.451(22)	0.0060(28)†	0.42(2)	
				O1-O1 rattle	1	3.483	3.500(16)*	0.0045(11)*		
				O1-O1 non-forward linear	2	3.542	3.559(16)*	0.0045(11)*		
				O1-O1 forward throught	2	3.542	3.560(16)*	0.0045(11)*		
				O1-O1 rattle	1	3.593	3.611(16)*	0.0045(11)*		

4.5.11. $CaUO_4$

CaUO4 has a rhombohedral structure ($R\bar{3}m$) with one unique U^{6+} 8-fold coordinated site, which has with two shorter U-O paths, very similar to α-SrUO4 [67]. The constructed fits are also very similar. The fit was constructed using a CIF file from Murphy *et al.* [67]. The data were windowed from 3.00 – 13.00 $Å^{-1}$ and the resultant Fourier transform data were fit between 1.20 and 4.50 Å. The first shell was fit using two U-O paths (O1 and O2) to represent the two unique U-O single scattering paths, these paths had independent ΔR and σ^2 parameters. In the second shell three paths: U-Ca, Ca1; U-U, U1; and U-O, O3 were used to represent one unique single scattering path each. The O3 path was constrained to share the same σ^2 parameter as O2 (σ^2_{O2}). Two multiple scattering O1-O2 double paths were included to improve the fit, for both paths the ΔR and σ^2 parameters of these paths were defined as $\Delta R_{O1}+\Delta R_{O2}$ and $\sigma^2_{O1}+\sigma^2_{O2}$ respectively. One O1-O1 multiple scattering forward path was also included, for this path the ΔR and σ^2 parameters were defined as $2x\Delta R_{O1}$ and $2x\sigma^2_{O1}$ respectively.

4.5.12. Metaschoepite

Metaschoepite ($(UO_2)_8O_2(OH)_{12}\cdot 10H_2O$) has an orthorhombic structure (Pbcn) with four unique U^{6+} 7-fold coordinated pentagonal bipyramid sites [78]. The fit was constructed using a CIF file from Klingensmith *et al.* [78]. The data were windowed from 3.00 – 14.00 $Å^{-1}$ and the resultant Fourier transform data were fit between 1.10 and 3.4 Å. Artemis FEFF calculations identified that for the four unique U sites, one site had five unique U-O single scattering paths, two had six unique U paths and one had seven unique U-O scattering paths in the first shell. Three single U-O scattering paths (O1, O2 and O3) were used to attempt to represent these four first shells. The O1 path represented the scattering paths of the two axial oxygens in each of the four U sites. The O2 and O3 paths represented the scattering paths of five equatorial oxygens in in each of the four U sites, these two paths were constrained to share a σ^2 parameter(σ^2_{O2}). Four O1-O1 multiple scattering paths, two O1-O1 rattle paths a non-forward linear path and a forward through path were included, to represent four O1-O1 multiple scattering present in the FEFF calculations for each U site. The ΔR and σ^2 parameters for all O1-O1 multiple scattering sites were defined as $2x\Delta R_{O1}$ and $2x\sigma^2_{O1}$ respectively. The

multiple scattering O-O non-forward linear path and a forward through path do share the same σ^2, ΔR value, have very similar original path lengths (3.5416 and 3.5419 Å) and therefore very similar final R values, however using one path to these two paths with different geometries was significantly detrimental to the fit (resulted in an R factor of 0.0247).

4.5.13. $UMoO_6$

$UMoO_6$ has a triclinic ($P\bar{1}$) space group with four unique U 7-fold coordinate sites [85]. The fit was constructed using a CIF file obtained from the materials project. [85, 86]. The data were windowed from 3.00 – 14.00 $Å^{-1}$ and the resultant Fourier transform data were fit between 1.20 and 4.20 Å. Artemis FEFF calculations identified that all four U sites had five unique scattering paths: two single scattering paths for each of the axial oxygens and three single scattering paths for the five equatorial oxygens. The best fit achieved used two single scattering U-O paths (O1 and O2) to represent the first shell. The O1 path represented the eight different U-O axial oxygen scattering paths and used a C_3 and C_4 parameter to help account for the variations between these eight paths. The O2 path was used to represent the five axial oxygens. All four U sites had four unique single scattering U-Mo paths in the second shell, with the same total degeneracy of N=6, two U-Mo paths (Mo1 and Mo2) were used to represent these paths, these two paths were constrained to share a σ^2 parameter (σ^2_{Mo}). Three O1-O1 multiple scattering paths were included, a forward through absorber, a non-forward linear and a rattler. The ΔR and σ^2 parameters for all of the O1-O1 multiple scattering paths were defined as $2x\Delta R_{O1}$ and $2x\sigma^2_{O1}$ respectively. Three O1-O2 multiple scattering paths were included, the ΔR and σ^2 parameters for these paths were defined as $\Delta R_{O1}+\Delta R_{O2}$ and $\sigma^2_{O1}+\sigma^2_{O2}$ respectively. One O2-O2 double scatterer multiple scattering path was included, the ΔR and σ^2 parameters were defined as $2x\Delta R_{O2}$ and $2x\sigma^2_{O2}$ respectively. Two O2-Mo2 multiple scattering paths, with forward triangle and obtuse triangle geometries were included in the fit. The ΔR and σ^2 parameters of these two O2-Mo2 paths were defined as $\Delta R_{O2}+0.5x\Delta R_{Mo2}$ and $\sigma^2_{O2}+0.5x\sigma^2_{Mo2}$.

4.5.14. Soddyite

Soddyite ($(UO_2)_2SiO_4 \cdot 2H_2O$)) has an orthorhombic structure (Fddd) which has one unique 7-fold coordinated U site, a pentagonal bipyramid [81]. The fit was constructed using a CIF file from Demartin *et al.* [81]. The data were windowed from 3.00 – 14.00 $Å^{-1}$ and the resultant Fourier transform data were fit between 1.20 and 4.00 Å. The fit of the first shell used three paths (O1, O2 and O3) to represent three unique U-O single scattering paths; the O1 path represented the scattering paths of the two axial oxygens and the O2 and O3 paths represented the scattering paths of the five equatorial oxygens. The O2 and O3 paths were constrained to share a σ^2 parameter (σ^2_{O2}). Beyond the first shell three single scattering paths: Si1, Si2 and U1 were used to represent one unique single scattering path each. The two Si paths (Si1 and Si2) were constrained to share a σ^2 parameter (σ^2_{Si}). One O1-O2 double scattering path was used to represent two unique O1-O2 double scattering paths, the ΔR and σ^2 parameters were defined as $\Delta R_{O1}+\Delta R_{O2}$ and $\sigma^2_{O1}+\sigma^2_{O2}$, respectively. Three O1-O1 multiple scattering paths, non-forward linear, forward through absorber and rattle, were included in the fit. The ΔR and σ^2 parameters for the O1-O1 multiple scattering paths were defined as $2x\Delta R_{O1}$ and $2x\sigma^2_{O1}$. Two O2-Si2 multiple scattering paths, an obtuse triangle and a dog-leg, were also included in the fit. The ΔR and σ^2 parameters for the O2-Si2 multiple scattering paths were defined as $\Delta R_{O2}+0.5x\Delta R_{Si2}$ and $\sigma^2_{O1}+0.5x\sigma^2_{Si}$, respectively.

Table 4.SI.5. Fit parameters and uncertainties from EXAFS fits of $UMoO_6$ and Soddyite. Fit parameters: R-factor – measure of goodness of fit; ΔE – shift in E_0, which was constrained to be the same for all paths; S_0^2 – the amplitude reduction factor; N – degeneracy of a path; R – original path length; R_{calc} –new path length, sum of the calculated parameter ΔR and R; σ^2 – the Debye-Waller Factor; C3 – 3rd cumulant; C4 – 4th cumulant; V_i – calculated individual valence of a path; and BVS – sum of the valences for all paths in the first shell. Symbols * † ‡ ¤ § have been used to indicate the same parameter has been used. In the R_{calc} column any paths within a fit which share the same symbol share the same ΔR parameters, in the σ^2 column any paths within a fit which share the same symbol share the same σ^2 parameter. For paths which had ΔR and σ^2 parameters which were defined as the sum of more than one shared parameter, multiple symbols were used to indicate this. A through explanation of parameters used for each fit is given in the text.

Reference Compound	**R factor**	**S_0^2**	**ΔE**						
$UMoO_6$	0.0112	0.85	9.2(1.0)						
Path		**N**	**R** (Å)	**R_{Calc}** (Å)	**σ^2** (Å²)	**C_3** (Å³)	**C_4** (Å⁴)	**V_i**	**BVS**
O1		2	1.809	1.815(9)*	0.0044(11)*	0.0001(1)	0.00006(3)	1.63(3)	5.89(6)
O2		5	2.310	2.349(12)†	0.0102(10)†			0.53(1)	
O1-O2 double		4	3.570	3.616(21)*†	0.0145(21)*†				
O1-O2 double		6	3.588	3.633(21)*†	0.0145(21)*†				
O1-O1 rattle		2	3.618	3.630(18)*	0.0087(21)				
O1-O1 non-forward linear		2	3.658	3.671(18)*	0.0087(18)*				
O1-O1 forward through absorber		2	3.660	3.672(18)*	0.0087(18)*				
O1-O2 double		4	3.708	3.754(21)*†	0.0145(21)*†				
O2-O2 double		6	3.717	3.796(23)	0.0203(20)				
Mo1		1	3.758	3.823(58)	0.0097(15)‡				
Mo2		5	4.068	4.088(19)¤	0.0097(15)‡				
O2-Mo2 obtuse triangle		2	4.081	4.130(31)†¤	0.0150(25)†‡				
O2-Mo2 forward triangle		5	4.085	4.134(31)†¤	0.0150(25)†‡				
Reference Compound	**R factor**	**S_0^2**	**ΔE**						
Soddyite	0.0157	0.85	7.6(1.3)						
Path		**N**	**d** (Å)	**d_{final}** (Å)	**σ^2** (Å²)	**C_3** (Å³)	**C_4** (Å⁴)	**V_i**	**BVS**
O1		2	1.781	1.794(7)*	0.0017(6)*			1.70(2)	6.01(9)
O2		2	2.313	2.387(48)†	0.0079(24)†			0.49(5)	
O3		3	2.418	2.334(34)	0.0079(24)†			0.54(4)	
Si1		1	3.157	3.172(26)‡	0.0027(23)‡				
O1-O2 double		16	3.505	3.591(55)*†	0.0095(29)*†				
O1-O1 non forward linear		2	3.562	3.588(11)*	0.0033(11)*				
O1-O1 forward through absorber		2	3.562	3.588(11)*	0.0033(11)*				
O1-O1 rattle		2	3.562	3.588(11)*	0.0033(11)*				
Si2		2	3.805	3.855(43)	0.0027(23)‡				
U1		2	3.862	3.850(24)	0.0055(26)				
O2-Si1 obtuse triangle		4	3.874	3.973(60)†‡	0.0092(37)†‡				
O2-Si1 dog-leg		2	3.944	4.043(60)†‡	0.0092(37)†‡				

4.6. Acknowledgements

The authors are grateful to UKRI EPSRC for sponsorship for this research under grant references EP/R513313/1. CLC is grateful to EPSRC for the award of an Early Career Fellowship under grant reference EP/N017374/1.This research utilised the HADES/MIDAS facility and Henry Royce Institute at the University of Sheffield established with financial support from UKRI EPSRC and BEIS, under grant EP/T011424/1 [87]. We acknowledge the Diamond Light Source for time on B18 and I20-scanning under proposal numbers SP17782-1, SP24206-1 and SP31009-1, with thanks to Giannantonio Cibin, Stephen Parry, Fred Mosselmans and Shu Hayama. We acknowledge the European Synchrotron Radiation Facility for the provision of synchrotron radiation facilities under proposal number MA-4821, with thanks to Kristina Kvashnina, Sergei Butorin, and also to Tatiana Poliakova, Anastasiia Smirnova and Jurij Galanzew for their assistance in operating BM20 remotely. We acknowledge Brookhaven National Laboratory and the National Institute of Standards and Technology for time on X23A2 at the National Synchrotron Light Source with thanks to Bruce Ravel

4.7. References

[1] K. Maher, J.R. Bargar, G.E. Brown, Environmental Speciation of Actinides, Inorg. Chem. 52(7) (2013) 3510-3532.

[2] G.R. Choppin, J.-O. Lijenzin, J. Rydberg, Chapter 22 - Behavior of Radionuclides in the Environment, Radiochemistry and Nuclear Chemistry (Third Edition), Butterworth-Heinemann, Woburn, 2002, pp. 642-673.

[3] E.R. Vance, J.N. Watson, M.L. Carter, R.A. Day, B.D. Begg, Crystal chemistry and stabilization in air of brannerite, UTi_2O_6, J. Am. Ceram. Soc. 84(1) (2001) 141-144.

[4] J.A. Fortner, A.J. Kropf, R.J. Finch, A.J. Bakel, M.C. Hash, D.B. Chamberlain, Crystal chemistry of uranium (V) and plutonium (IV) in a titanate ceramic for disposition of surplus fissile material, J. Nucl. Mater. 304(1) (2002) 56-62.

[5] E.R. Vance, G.R. Lumpkin, M.L. Carter, D.J. Cassidy, C.J. Ball, R.A. Day, B.D. Begg, Incorporation of uranium in zirconolite ($CaZrTi_2O_7$), J. Am. Ceram. Soc. 85(7) (2002) 1853-1859.

[6] A.V. Soldatov, D. Lamoen, M.J. Konstantinovic, S. Van den Berghe, A.C. Scheinost, M. Verwerft, Local structure and oxidation state of uranium in some ternary oxides: X-ray absorption analysis, J. Solid State Chem. 180(1) (2007) 54-61.

[7] M. James, M.L. Carter, Z.M. Zhang, Y.J. Zhang, K.S. Wallwork, M. Avdeev, E.R. Vance, Crystal Chemistry and Structures of (Ca,U) Titanate Pyrochlores, J. Am. Ceram. Soc. 93(10) (2010) 3464-3473.

[8] A.F. Redkin, A.M. Ionov, N.P. Kotova, Hydrothermal synthesis of pyrochlores and their characterization, Phys. Chem. Miner. 40(9) (2013) 733-745.

[9] S.A. McMaster, R. Ram, F. Charalambous, M.I. Pownceby, J. Tardio, S.K. Bhargava, Synthesis and characterisation of the uranium pyrochlore betafite [$(Ca,U)_2(Ti,Nb,Ta)_2O_7$], J. Hazard. Mater. 280 (2014) 478-486.

[10] D.J. Bailey, M.C. Stennett, N.C. Hyatt, Synthesis and Characterization of Brannerite Compositions for MOX Residue Disposal, MRS Adv. 2(10) (2017) 557-562.

[11] D.J. Bailey, M.C. Stennett, B. Ravel, D. Grolimund, N.C. Hyatt, Synthesis and characterisation of brannerite compositions $(U_{0.9}Ce_{0.1})_{1-x}M_xTi_2O_6$ (M = Gd^{3+}, Ca^{2+}) for the immobilisation of MOX residues, RSC Adv. 8(4) (2018) 2092-2099.

[12] S.V. Stefanovsky, S.V. Yudintsev, A.A. Shiryaev, V.Y. Murzin, A.L. Trigub, Phase partitioning and uranium speciation in brannerite-based ceramics, J. Eur. Ceram. Soc. 37(2) (2017) 771-777.

[13] M.C. Dixon Wilkins, L.M. Mottram, E.R. Maddrell, M.C. Stennett, C.L. Corkhill, K.O. Kvashnina, N.C. Hyatt, Synthesis, Characterization, and Crystal Structure of Dominant Uranium(V) Brannerites in the $UTi_{2-x}Al_xO6$ System, Inorg. Chem. 60(23) (2021) 18112-18121.

[14] T. Subramani, J. Baker, H.W. Xu, A. Navrotsky, Synthesis, Characterization, and Enthalpies of Formation of Uranium Substituted Zirconolites, ACS Earth Space Chem. 4(10) (2020) 1878-1887.

[15] L.R. Blackburn, R. Crawford, S.A. Walling, L.J. Gardner, M.R. Cole, S.K. Sun, C. Gausse, A.R. Mason, M.C. Stennett, E.R. Maddrell, N.C. Hyatt, C.L. Corkhill, Influence of accessory phases and surrogate type on accelerated leaching of zirconolite wasteforms, NPJ Mater. Degrad. 5(1) (2021) 11.

[16] A.S. Yorkshire, M.C. Stennett, B. Walkley, S.E. O'Sullivan, L.M. Mottram, D.J. Bailey, J.L. Provis, N.C. Hyatt, C.L. Corkhill, Spectroscopic evaluation of U-VI-cement mineral interactions: ettringite and hydrotalcite, J. Synchrot. Radiat. 29 (2022) 89-102.

[17] Y. Yamamoto, Y. Takahashi, Y. Kanai, Y. Watanabe, T. Uruga, H. Tanida, Y. Terada, H. Shimizu, High-sensitive measurement of uranium L-III-edge X-ray absorption near-edge structure (XANES) for the determination of the oxidation states of uranium in crustal materials, Appl. Geochem. 23(8) (2008) 2452-2461.

[18] O. Stagg, K. Morris, A. Lam, A. Navrotsky, J.M. Velazquez, B. Schacherl, T. Vitova, J. Rothe, J. Galanzew, A. Neumann, P. Lythgoe, L. Abrahamsen-Mills, S. Shaw, Fe(II) Induced Reduction of Incorporated U(VI) to U(V) in Goethite, Environ. Sci. Technol. 55(24) (2021) 16445-16454.

[19] L.T. Townsend, G. Kuippers, J.R. Lloyd, L.S. Natrajan, C. Boothman, J.F.W. Mosselmans, S. Shaw, K. Morris, Biogenic Sulfidation of U(VI) and Ferrihydrite Mediated by Sulfate-Reducing Bacteria at Elevated pH, ACS Earth Space Chem. 5(11) (2021) 3075-3086.

[20] S.M. Butorin, S. Bauters, L. Amidani, A. Beck, S. Weiss, T. Vitova, O. Tougait, X-ray spectroscopic study of chemical state in uranium carbides, J. Synchrot. Radiat. 29 (2022) 295-302.

[21] K. Kvashnina, Y. Kvashnin, J.R. Vegelius, A. Bosak, P.M. Martin, S.M. Butorin, Sensitivity to Actinide Doping of Uranium Compounds by Resonant Inelastic X-ray Scattering at Uranium L-3 Edge, Anal. Chem. 87(17) (2015) 8772-8780.

[22] H. Smith, L.T. Townsend, R. Mohun, T. Cordara, M.C. Stennett, J.F.W. Mosselmans, K. Kvashnina, C.L. Corkhill, Cr2+ solid solution in UO2 evidenced by advanced spectroscopy, Comm. Chem. 5(1) (2022) 8.

[23] K. Yuan, M.R. Antonio, E.S. Ilton, Z.R. Li, U. Becker, Pentavalent Uranium Enriched Mineral Surface under Electrochemically Controlled Reducing Environments, ACS Earth Space Chem. 6(5) (2022) 1204-1212.

[24] A. Uehara, D. Matsumura, T. Tsuji, H. Yakumaru, I. Tanaka, A. Shiro, H. Saitoh, H. Ishihara, S. Homma-Takeda, Uranium chelating ability of decorporation agents in serum evaluated by X-ray absorption spectroscopy, Anal. Methods 14(24) (2022) 2439-2445.

[25] K.O. Kvashnina, S.M. Butorin, P. Martin, P. Glatzel, Chemical State of Complex Uranium Oxides, Phys. Rev. Lett. 111(25) (2013) 5.

[26] K.O. Kvashnina, F.M.F. de Groot, Invisible structures in the X-ray absorption spectra of actinides, J. Electron Spectrosc. Relat. Phenom. 194 (2014) 88-93.

[27] R. Bes, M. Rivenet, P.L. Solari, K.O. Kvashnina, A.C. Scheinost, P.M. Martin, Use of HERFD–XANES at the U L_3- and M_4-Edges To Determine the Uranium Valence State on $[Ni(H_2O)_4]_3[U(OH,H_2O)(UO_2)_8O_{12}(OH)_3]$, Inorg. Chem. 55(9) (2016) 4260-4270.

[28] X.F. Guo, E. Tiferet, L. Qi, J.M. Solomon, A. Lanzirotti, M. Newville, M.H. Engelhard, R.K. Kukkadapu, D. Wu, E.S. Ilton, M. Asta, S.R. Sutton, H.W. Xu, A. Navrotsky, U(V) in metal uranates: a

combined experimental and theoretical study of MgUO4, CrUO4, and FeUO4, Dalton Trans. 45(11) (2016) 4622-4632.

[29] G. Leinders, R. Bes, J. Pakarinen, K. Kvashnina, M. Verwerft, Evolution of the Uranium Chemical State in Mixed-Valence Oxides, Inorg. Chem. 56(12) (2017) 6784-6787.

[30] T. Vitova, I. Pidchenko, D. Fellhauer, P.S. Bagus, Y. Joly, T. Pruessmann, S. Bahl, E. Gonzalez-Robles, J. Rothe, M. Altmaier, M.A. Denecke, H. Geckeis, The role of the 5f valence orbitals of early actinides in chemical bonding, Nat. Commun. 8 (2017) 1-9.

[31] T. Vitova, R. Faizova, J.I. Amaro-Estrada, L. Maron, T. Pruessmann, T. Neill, A. Beck, B. Schacherl, F.F. Tirani, M. Mazzanti, The mechanism of Fe induced bond stability of uranyl(v), Chem. Sci. 13(37) (2022) 11038-11047.

[32] D. Akiyama, R. Kusaka, Y. Kumagai, M. Nakada, M. Watanabe, Y. Okamoto, T. Nagai, N. Sato, A. Kirishima, Study on the relation between the crystal structure and thermal stability of FeUO4 and CrUO4, J. Nucl. Mater. 568 (2022) 10.

[33] T. Yomogida, D. Akiyama, K. Ouchi, Y. Kumagai, K. Higashi, Y. Kitatsuji, A. Kirishima, N. Kawamura, Y. Takahashi, Application of High-Energy-Resolution X-ray Absorption Spectroscopy at the U L3-Edge to Assess the U(V) Electronic Structure in FeUO4, Inorg. Chem. 5.

[34] S. Calvin, XAFS for Everyone, Taylor and Francis, Boca Raton, 2013.

[35] W. Grunert, K. Klementiev, X-ray absorption spectroscopy principles and practical use in materials analysis, J. Taibah Univ. Med. Soc. 5(4) (2020) 35.

[36] M.A. Denecke, Actinide speciation using X-ray absorption fine structure spectroscopy, Coord. Chem. Rev. 250(7-8) (2006) 730-754.

[37] K.O. Kvashnina, Y.O. Kvashnin, S.M. Butorin, Role of resonant inelastic X-ray scattering in high-resolution core-level spectroscopy of actinide materials, J. Electron Spectrosc. Relat. Phenom. 194 (2014) 27-36.

[38] K.O. Kvashnina, H.C. Walker, N. Magnani, G.H. Lander, R. Caciuffo, Resonant x-ray spectroscopy of uranium intermetallics at the M-4,M-5 edges of uranium, Phys. Rev. B 95(24) (2017) 10.

[39] I. Pidchenko, K.O. Kvashnina, T. Yokosawa, N. Finck, S. Bahl, D. Schild, R. Polly, E. Bohnert, A. Rossberg, J. Gottlicher, K. Dardenne, J. Rothe, T. Schafer, H. Geckeis, T. Vitova, Uranium Redox Transformations after U(VI) Coprecipitation with Magnetite Nanoparticles, Environ. Sci. Technol. 51(4) (2017) 2217-2225.

[40] S.M. Butorin, K.O. Kvashnina, D. Prieur, M. Rivenet, P.M. Martin, Characteristics of chemical bonding of pentavalent uranium in La-doped UO2, Chem. Commun. 53(1) (2017) 115-118.

[41] H.E. Roberts, K. Morris, G.T.W. Law, J.F.W. Mosselmans, P. Bots, K. Kvashnina, S. Shaw, Uranium(V) Incorporation Mechanisms and Stability in Fe(II)/Fe(III) (oxyhydr)Oxides, Environ. Sci. Technol. Lett. 4(10) (2017) 421-426.

[42] L. Amidani, M. Retegan, A. Volkova, K. Popa, P.M. Martin, K.O. Kvashnina, Probing the Local Coordination of Hexavalent Uranium and the Splitting of 5f Orbitals Induced by Chemical Bonding, Inorg. Chem. 60(21) (2021) 16286-16293.

[43] M. Hunault, D. Menut, O. Tougait, Alkali Uranyl Borates: Bond Length, Equatorial Coordination and 5f States, Crystals 11(1) (2021) 9.

[44] K.O. Kvashnina, S.M. Butorin, High-energy resolution X-ray spectroscopy at actinide M-4,M-5 and ligand K edges: what we know, what we want to know, and what we can know, Chem. Commun. 58(3) (2022) 327-342.

[45] P. Glatzel, T.C. Weng, K. Kvashnina, J. Swarbrick, M. Sikora, E. Gallo, N. Smolentsev, R.A. Mori, Reflections on hard X-ray photon-in/photon-out spectroscopy for electronic structure studies, J. Electron Spectrosc. Relat. Phenom. 188 (2013) 17-25.

[46] R. Bes, G. Leinders, K. Kvashnina, Application of multi-edge HERFD-XAS to assess the uranium valence electronic structure in potassium uranate (KUO3), J. Synchrot. Radiat. 29 (2022) 21-29.

[47] G.L. Murphy, Z.M. Zhang, R. Tesch, P.M. Kowalski, M. Avdeev, E.Y. Kuo, D.J. Gregg, P. Kegler, E.V. Alekseev, B.J. Kennedy, Tilting and Distortion in Rutile-Related Mixed Metal Ternary Uranium Oxides: A Structural, Spectroscopic, and Theoretical Investigation, Inorg. Chem. 60(4) (2021) 2246-2260.

[48] International Atomic Energy Agency, G. Seidler, R. Bes, C. Schlesiger, Report from Consultancy Meeting on Current Developments of Laboratory Based Instruments for XAS or XES, in: R.P. Alvarez (Ed.) IAEA, 2019, pp. 1-19.

[49] R. Bes, T. Ahopelto, A.P. Honkanen, S. Huotari, G. Leinders, J. Pakarinen, K. Kvashnina, Laboratory-scale X-ray absorption spectroscopy approach for actinide research: Experiment at the uranium L-3-edge, J. Nucl. Mater. 507 (2018) 50-53.

[50] E.P. Jahrman, W.M. Holden, A.S. Ditter, D.R. Mortensen, G.T. Seidler, T.T. Fister, S.A. Kozimor, L.F.J. Piper, J. Rana, N.C. Hyatt, M.C. Stennett, An improved laboratory-based x-ray absorption fine structure and x-ray emission spectrometer for analytical applications in materials chemistry research, Rev. Sci. Instrum. 90(2) (2019) 15.

[51] L.M. Mottram, M.C.D. Wilkins, L.R. Blackburn, T. Oulton, M.C. Stennett, S.K. Sun, C.L. Corkhill, N.C. Hyatt, A Feasibility Investigation of Laboratory Based X-ray Absorption Spectroscopy in Support of Nuclear Waste Management, MRS Adv. 5(1-2) (2020) 27-35.

[52] S.E. O'Sullivan, Novel Oxides and Nitrides in the Nuclear Fuel Cycle, Materials Science and Engineering, The University of Sheffield, 2021, p. 287.

[53] M. James, M.L. Carter, J.N. Watson, The synthesis, crystal chemistry and structures of Y-doped brannerite ($U_{1-x}Y_xTi_2O_6$) and thorutite ($Th_{1-x}Y_xTi_2O_6$-delta) phases, J. Solid State Chem. 174(2) (2003) 329-333.

[54] S. Hayama, G. Duller, J.P. Sutter, M. Amboage, R. Boada, A. Freeman, L. Keenan, B. Nutter, L. Cahill, P. Leicester, B. Kemp, N. Rubies, S. Diaz-Moreno, The scanning four-bounce monochromator for beamline I20 at the Diamond Light Source, J. Synchrot. Radiat. 25 (2018) 1556-1564.

[55] A.C. Scheinost, J. Claussner, J. Exner, M. Feig, S. Findeisen, C. Hennig, K.O. Kvashnina, D. Naudet, D. Prieur, A. Rossberg, M. Schmidt, C.R. Qiu, P. Colomp, C. Cohen, E. Dettona, V. Dyadkin, T. Stumpf, ROBL-II at ESRF: a synchrotron toolbox for actinide research, J. Synchrot. Radiat. 28 (2021) 333-349.

[56] G.T. Seidler, D.R. Mortensen, A.J. Remesnik, J.I. Pacold, N.A. Ball, N. Barry, M. Styczinski, O.R. Hoidn, A laboratory-based hard x-ray monochromator for high-resolution x-ray emission

spectroscopy and x-ray absorption near edge structure measurements, Rev. Sci. Instrum. 85(11) (2014) 12.

[57] A.J. Dent, G. Cibin, S. Ramos, A.D. Smith, S.M. Scott, L. Varandas, M.R. Pearson, N.A. Krumpa, C.P. Jones, P.E. Robbins, B18: A core XAS spectroscopy beamline for Diamond, 14th International Conference on X-Ray Absorption Fine Structure (XAFS14), Iop Publishing Ltd, Camerino, ITALY, 2009.

[58] S. Diaz-Moreno, S. Hayama, M. Amboage, A. Freeman, J. Sutter, G. Duller, I20; the Versatile X-ray Absorption Spectroscopy Beamline at Diamond Light Source, 14th International Conference on X-Ray Absorption Fine Structure (XAFS14), Iop Publishing Ltd, Camerino, ITALY, 2009.

[59] K.O. Kvashnina, A.C. Scheinost, A Johann-type X-ray emission spectrometer at the Rossendorf beamline, J. Synchrot. Radiat. 23 (2016) 836-841.

[60] R. Bruce, in: L. Mottram (Ed.) 2023.

[61] P. Zimmermann, S. Peredkov, P.M. Abdala, S. DeBeer, M. Tromp, C. Muller, J.A. van Bokhoven, Modern X-ray spectroscopy: XAS and XES in the laboratory, Coord. Chem. Rev. 423 (2020) 28.

[62] easyXAFS LLC, easyXES100-extended Operator's Manual, Version 2.1, 2018.

[63] M.E. Seddon-Ferretti, L.M. Mottram, M.C. Stennett, C.L. Corkhill, N.C. Hyatt, HERMES - a GUI-based software tool for pre-processing of X-ray absorption spectroscopy data from laboratory Rowland circle spectrometers, J. Synchrot. Radiat. 29 (2022) 276-279.

[64] B. Ravel, M. Newville, ATHENA, ARTEMIS, HEPHAESTUS: data analysis for X-ray absorption spectroscopy using IFEFFIT, J. Synchrot. Radiat. 12 (2005) 537-541.

[65] A.L. Ankudinov, B. Ravel, J.J. Rehr, S.D. Conradson, Real-space multiple-scattering calculation and interpretation of x-ray-absorption near-edge structure, Phys. Rev. B 58(12) (1998) 7565-7576.

[66] M.A. Denecke, T. Reich, M. Bubner, S. Pompe, K.H. Heise, H. Nitsche, P.G. Allen, J.J. Bucher, N.M. Edelstein, D.K. Shuh, Determination of structural parameters of uranyl ions complexed with organic acids using EXAFS, J. Alloy. Compd. 271 (1998) 123-127.

[67] G. Murphy, B.J. Kennedy, B. Johannessen, J.A. Kimpton, M. Avdeev, C.S. Griffith, G.J. Thorogood, Z.M. Zhang, Structural studies of the rhombohedral and orthorhombic monouranates: CaUO4, alpha-SrUO4, beta-SrUO4 and BaUO4, J. Solid State Chem. 237 (2016) 86-92.

[68] C. Schlesiger, S. Praetz, R. Gnewkow, W. Malzer, B. Kanngießer, Recent progress in the performance of HAPG based laboratory EXAFS and XANES spectrometers, J. Anal. At. Spectrom. (2020).

[69] P. Wachulak, T. Fok, A. Bartnik, K.A. Janulewicz, H. Fiedorowicz, EXAFS of titanium L-III edge using a compact laboratory system based on a laser-plasma soft X-ray source, Appl. Phys. B-Lasers Opt. 126(1) (2020) 9.

[70] T. Vitova, K.O. Kvashnina, G. Nocton, G. Sukharina, M.A. Denecke, S.M. Butorin, M. Mazzanti, R. Caciuffo, A. Soldatov, T. Behrends, H. Geckeis, High energy resolution x-ray absorption spectroscopy study of uranium in varying valence states, Phys. Rev. B 82(23) (2010) 6.

[71] J.T. Szymanski, J.D. Scott, A crystal-structure refinement of synthetic brannerite, UTi_2O_6, and its bearing on rate of alkaline-carbonate leaching of brannerite in ore., Can. Mineral. 20(MAY) (1982) 271-280.

[72] L. Desgranges, G. Baldinozzi, G. Rousseau, J.C. Niepce, G. Calvarin, Neutron Diffraction Study of the in Situ Oxidation of UO_2, Inorg. Chem. 48(16) (2009) 7585-7592.

[73] P.G. Dickens, G.P. Stuttard, Structure of USbO5: powder neutron diffraction study, J. Mater. Chem. 2(7) (1992) 691-694.

[74] P. Garcia- Chain, R.M. Rojas, P. Herrero, J.R. Gunter, Microstructural Characterization of the Fluorite Phase in the U-La-O System : II. Hexagonal Microdomain Formation in $(U_{1-y}La_y)O_{2-x}$, $0.70 \leq y \leq 0.80$, J. Solid State Chem. 108(2) (1994) 236-242.

[75] B.O. Loopstra, The structure of β-U_3O_8, Acta Crystallographica Section B-Structural Crystallography and Crystal Chemistry B 26 (1970) 656-&.

[76] J. Holc, L. Golic, The Synthesis and Crystal Structure of α-Ca_3UO_6, J. Solid State Chem. 48(3) (1983) 396-400.

[77] G.L. Murphy, B.J. Kennedy, J.A. Kimpton, Q.F. Gu, B. Johannessen, G. Beridze, P.M. Kowalski, D. Bosbach, M. Avdeev, Z.M. Zhang, Nonstoichiometry in Strontium Uranium Oxide: Understanding the Rhombohedral-Orthorhombic Transition in SrUO4, Inorg. Chem. 55(18) (2016) 9329-9334.

[78] A.L. Klingensmith, K.M. Deely, W.S. Kinman, V. Kelly, P.C. Burns, Neptunium incorporation in sodium-substituted metaschoepite, Am. Miner. 92(4) (2007) 662-669.

[79] V.N. Serezhkin, V.K. Trunov, L.G. Makarevich, The Refined Crystal-Structure of Uranyl Molybdate, Kristallografiya 25(4) (1980) 858-860.

[80] R.A. Barry, J. Deveau, I. Korobkov, E.C. Corcoran, J. Scott, A facile and accurate preparation of pure UMoO6 and a crystallographic study of a Na-U-Mo-O intermediate, Polyhedron 108 (2016) 143-150.

[81] F. Demartin, C.M. Gramaccioli, T. Pilati, The importance of accurate crystal structure determination of uranium minerals. II. Soddyite $(UO_2)_2(SiO_4).2H_2O$, Acta Crystallogr. Sect. C-Cryst. Struct. Commun. 48 (1992) 1-4.

[82] A. Mesbah, S. Szenknect, N. Clavier, H.T. Lin, F. Baron, D. Beaufort, Y. Batonneau, J. Mercadier, A. Eglinger, M. Turuani, P. Goncalves, F. Choulet, V. Chapon, A.M. Seydoux-Guillaume, M. Pagel, N. Dacheux, Direct synthesis of pure brannerite UTi_2O_6, J. Nucl. Mater. 515 (2019) 401-406.

[83] R.W.G. Wyckoff, Crystal structures, 2nd ed., Interscience Publishers, New York, 1963.

[84] M. Bacmann, E.F. Bertaut, Structure du nouveau composé $UFeO_4$, Bulletin De La Societe Francaise Mineralogie Et De Cristallographie 90(2) (1967) 257-&.

[85] G. Hautier, C. Fischer, V. Ehrlacher, A. Jain, G. Ceder, Data Mined Ionic Substitutions for the Discovery of New Compounds, Inorg. Chem. 50(2) (2011) 656-663.

[86] A. Jain, S.P. Ong, G. Hautier, W. Chen, W.D. Richards, S. Dacek, S. Cholia, D. Gunter, D. Skinner, G. Ceder, K.A. Persson, Commentary: The Materials Project: A materials genome approach to accelerating materials innovation, APL Mater. 1(1) (2013) 11.

[87] N.C. Hyatt, C.L. Corkhill, M.C. Stennett, R.J. Hand, L.J. Gardner, C.L. Thorpe, The HADES facility for high activity decommissioning engineering & science: Part of the UK national nuclear user facility, IOP Conference Proceedings: Materials Science and Engineering 818 (2020) 012022.

5. X-ray absorption micro-spectroscopy analysis of uranium in a natural analogue for plutonium ceramic wasteforms

Mottram, L. M[1], Townsend, L. T[1], Ding H.[1], Tappero, R.[2], Nichols, S. L.[2], Stennett, M. C.[1], Hyatt, N. C.[2] and Corkhill, C. L.[1*]

[1]*NucleUS Immobilisation Science Laboratory, Department of Materials Science and Engineering, University of Sheffield, Sir Robert Hadfield Building, Sheffield, S1 3JD, UK*

[2]*Brookhaven National Laboratory, NSLS-II, Upton, NY 11973, USA*

**c.corkhill@sheffield.ac.uk*

Abstract

Natural analogues of ceramic titanate materials currently under consideration for the immobilisation of civil separated plutonium have been widely studied in the literature. These studies, typically on uranium (U) and thorium (Th) containing minerals of up to 1 billion years old, have given deeper insight to composition, alteration and radiation damage effects. However, to date, spatially resolved methods to quantify the local coordination chemistry of U in these minerals has not been performed. In this study, naturally occurring U titanate mineral from Crocker's Well, South Australia, was examined using μXRD, μXRF mapping, U L_3-edge μXANES and μEXAFS. These complementary chemical probes were used to determine that the U mineral was fully metamict and altered, with the majority of U speciation occurring as U^{6+} uranyl. Demonstration of multi-technique micro-focus X-ray techniques to these samples paves the way for future detailed analysis of altered natural analogue minerals, which may provide additional information to build safety arguments for the immobilisation of plutonium (Pu) in synthetic titanate ceramic materials.

5.1. Introduction

Although the currently preferred option for the UK's 140 tonne stockpile of separated civil plutonium (Pu) is reuse as MOX fuel, there is a small portion of the stockpile that is not suitable for this route and must, therefore, be immobilised [1]. The immobilisation of Pu requires a wasteform that is resistant to radiation damage and, because disposal of the UK's radioactive waste inventory will be in a deep geological disposal facility, the wasteform must also be resistant to leaching in groundwater. Any candidate wasteform should also be chemically flexible to accommodate known contaminants, e.g. Am^{3+} and Cl^{-}; moreover, there should be confidence that all these properties will persist over the long time scales required for geological disposal (ca. 1 million years) [2].

The study of analogues, either naturally occurring minerals or aged man-made materials, with a similar composition and structure to a potential wasteform, is essential to enable the confident prediction of such properties over the lifetime of the wasteform [3, 4]. Therefore, it is advantageous if potential wasteforms have available analogues. As such, synthetic wasteforms with compositions and structures of natural uranium (U) and thorium (Th) containing minerals, often hundreds of millions of years old, are attractive wasteform candidates. These include brannerite (UTi_2O_6), zirconolite ($CaZrTi_2O_7$) and materials in the pyrochlore groups ($A_2B_2O_7$ where A = Na, Ca, U, Th, Pu, Gd and B = Ti, Nb, Ta, Hf).

One factor on which wasteform properties are dependent is the speciation of the actinide (e.g. Pu, U) within the wasteform, since the solubility and relative mobility of these species in the sub-surface environment is highly dependent on the oxidation state. For example, the more oxidised U^{6+} containing uranyl and Pu^{6+} containing plutonyl ions are generally more soluble than reduced species of uranate U^{4+} [5] and plutonate Pu^{4+} [6]. Despite this, relatively few studies have investigated the oxidation state of U in natural analogue samples. Some speciation studies have been made on natural brannerite samples. Colella *et al.*, attempted to estimate the oxidation state of U in three mineral brannerite samples (composition $(U,Ca,Y,Pb,Th,Ce)(Ti,Si,Al,Fe)_2O_6$) using electron energy loss spectroscopy (EELS) and from the sample composition, obtained by energy-dispersive X-ray spectroscopy (EDX) [7]. Analysis of the EELS data gave an average U oxidation state of +4.6 and it was concluded that the majority

of the U present was U^{4+} with some oxidised U^{5+} or U^{6+}; however, the estimates of U speciation obtained from the composition were significantly different for two of the three brannerite samples investigated. René *et al.* performed electron probe micro-analysis (EPMA) [8] of brannerite minerals, producing estimates of concentrations of $U^{4+}O_2$ and $U^{6+}O_3$. From these estimates net U oxidation state can be calculated, giving values between +4.7 and +6.0. Finally, Vance *et al.* collected bulk X-ray absorption spectroscopy (XAS) data from an altered, metamict sample identified as brannerite and compared it to XAS data from synthetic UTi_2O_6 and $CaU^{6+}O_4$ to show qualitatively that the majority of U present in the brannerite sample was U^{6+} [9]. They also performed diffuse reflectance spectroscopy (DRS) which, in contrast to the bulk XAS, indicated that the brannerite sample contained U^{5+}.

In contrast to natural minerals, the speciation of U in synthetic U-containing titanate ceramics has been widely investigated by characterising the X-ray absorption near edge structure (XANES) and extended X-ray absorption fine structure (EXAFS) of U L_3-edge X-ray absorption spectroscopy (XAS) data [9-21] and the XANES of high energy resolution fluorescence detected (HERFD) U M_4-edge XANES [19]. Uranium L_3-edge XANES and EXAFS have features dependent on U oxidation state and coordination, and can, therefore, be characterised to determine the speciation of U [22]. Given that there tends to be a high amount of spatial variability and heterogeneity in natural mineral samples, an ideal probe to resolve some of the discrepancies that have been observed in the literature regarding the U oxidation state would be spatially resolved, ideally on the scale of several microns. X-ray fluorescence microprobe beamlines are a highly specialised tool which enable the collection of spatially resolved XAS data.

In this Chapter, the suitability of using an X-ray fluorescence microprobe to evidence U speciation is demonstrated, using spatially resolved XANES, EXAFS, X-ray diffraction (XRD) and X-ray fluorescence (XRF) to investigate a naturally-occurring U-titanate mineral, analogous to those under consideration for plutonium immobilisation.

5.2. Methodology

5.2.1. Sample provenance

The sample investigated in this work is reported to be from Crocker's Well, Olary Domain in South Australia, near Radium Hill and Broken Hill. The Olary Domain forms part of the Willyama Supergroup in Curnamona province [23]. At Crocker's Well, the primary U mineralisation occurs as the mineral brannerite (UTi_2O_6), which is associated with a pegmatite granite [24]. The other known U mineral occurrences are davidite ($(La,Ce,Ca)(Y,U)(Ti,Fe)_{20}O_{38}$) and uranothorite ($(Th,U)SiO_4$), which was found to be intimately mixed with brannerite in a sample from Crocker's well examined by Charalambous *et al.* [25]. Similar intimate mixing of a U-Th-rich silicate with brannerite, speculated to be uranothorite, has been observed in another brannerite sample from the same locality [26].

Ludwig and Cooper conducted U-Pb isotope dating of brannerite samples and host rock from the Crocker's well locality, giving an estimated age of ca. 1579.2 ± 1.5 Ma [24]. Given the age of this sample relative to the half-life of U isotopes in natural U, they are often metamict (i.e. amorphous through self-irradiation) due to alpha recoil damage [27]. The Olary Domain experienced the Delemerian orogeny (ca. 514-490 Ma) [28] during which deformation and localised low pressure and high temperature (typically 500-650°C [29]) metamorphism occurred [30]. The temperatures experienced by the sample during this event are not considered be sufficient to cause recrystallisation of brannerite or davidite [25, 31].

5.2.2. Sample preparation

The mineral sample was prepared by mounting onto a 25 x 50 x 1.0 mm Spectrosil slide and was then cut, ground to achieve a sample thickness of ca. 40 µm and polished to a 1 µm finish. Uranium reference compounds (Table 5.1) were prepared for XAS by combining powder samples with polyethylene glycol (PEG) to produce a homogenous dispersion and then pressed into pellets to achieve a thickness of one absorption length. U L_3-edge µXAS data were collected from a suite of U reference compounds with a range of U oxidation states and coordination numbers (Table 5.1) at 4-BM in March 2019. The mineral sample and complex U

mineral reference compounds metaschoepite, haiweeite and soddyite were measured in September 2019, as was UO_2 to allow alignment to the previous data set

Table 5.1. List of U reference compounds measured, with oxidation state and coordination

Standard	Uranium oxidation state	Uranium coordination
UTi_2O_6	4	6
UO_2	4	8
USbO5	5	7
$LaUO_4$	5	8
α-CaU_3O_6	6	6
$(UO_2)_8O_2(OH)_{12} \cdot 10H_2O$ (Metaschoepite)	6	7
$Ca(UO_2)_2Si_5O_{12}(OH)_2 \cdot 3(H_2O)$ (Haiweeite)	6	7
$(UO_2)_2SiO_4 \cdot 2H_2O$ (Soddyite)	6	7
$CaUO_4$	6	8

5.2.3. X-ray fluorescence microprobe (XFM) measurements

U L_3-edge microfocus XAS (μXAS), microfocus X-ray diffraction (μXRD) and microfocus X-ray fluorescence (μXRF) data were collected from the mineral sample on the X-ray Fluorescence Microscope beamline (XFM) at the National Synchrotron Light Source II (NSLS-II), Brookhaven National Laboratory, USA. Synchrotron radiation from a 3-pole wiggler was configured with a toroidal pre-focusing mirror, a vertical collimating mirror and a double crystal, Si (311) monochromator [32] detuned to 80%. A pair of Kirkpatrick Baez mirrors focused the beam [32] to a spot size of 10 μm x 10 μm. XAS data were acquired in air at room temperature in fluorescence mode from samples orientated at an incidence angle of 45° between the beam and the Vortex detector. μXRF data were collected at 17 keV on a Canberra 13-element Ge array detector, positioned at 90° to the incident beam. μXRD data were collected at 17 keV on a Perkin Elmer 1621 XRD area detector, positioned in the path of the beam behind the sample. Mapping was achieved by moving the sample, with the use of a mobile stage, into the path of the beam to achieve a raster-like motion and collecting μXRF spectra at regular spatial intervals. The two maps were collected with a step size of 0.01 mm: Region 1 had an area of 1.00 x 1.00 mm and Region 2 had an area of 0.50 x 0.50 mm.

5.2.4. Data processing and analysis

Processing of μXAS data and analysis of the XANES and EXAFS regions (μXANES and μEXAFS, respectively) were performed using the Athena and Artemis programs from the Demeter suite [33]. Athena was used to align, merge, background subtract and normalise data, in addition extract E_0 values and perform linear combination fitting (LCF) analysis on the μ-XANES data and multi electron excitation removal from the μEXAFS region. For estimates of U oxidation state using E_0 position, the E_0 half position, the point in energy on edge of a normalised spectrum where the normalised intensity is 0.5, was taken from the spectra of reference compounds, plotted against their known oxidation state and a linear fit was performed in Origin to produce an E_0 to oxidation state calibration line. The E_0 half positions were then taken and used to produce an estimate of net oxidation state of U at each point μXAS data were collected from. The uncertainties of E_0 positions were taken from the step size of the μXAS measurement (0.25 eV), the uncertainties of the oxidation state estimates were calculated from the uncertainties of the linear fit.

For linear combination fitting (LCF), a fitting range of $-20\ \text{eV} \leq E_0 \leq 30\ \text{eV}$ was applied, the weighting of each reference compound was constrained to $0 \leq w \leq 1$ and the sum of all weightings was not constrained. All combinations of reference compounds were allowed and the resulting fits were ranked by their R factor, a measure of goodness of fit calculated as part of the fitting process by Athena [33]. The weightings of the best fit were then normalised to sum to unity and the known U oxidation states of the reference compounds were used to estimate the net U oxidation state for each point (Table 5.2). The uncertainty of weighting of each reference compound and the net U oxidation states were calculated by the root mean square. μ-EXAFS data were fit using Artemis, scattering paths were calculated from CIF files of UO_2 [34], haiweeite ($Ca(UO_2)_2Si_5O_{12}(OH)_2{\cdot}3(H_2O)$) [35] and UTi_2O_6 [36], obtained through the Inorganic Crystal Structure Database.

μXRF and μXRD data were processed using GSE Mapviewer and Dioptas from the Larch suite [37]. Peak analysis of the μXRF spectra was also performed on GSE Mapviewer. Peaks in intensity associated with the emission lines of different elements were windowed, and then plotted against the position the spectra were collected from, generating a map of emission

intensity for each element windowed. The processed μXRD patterns were characterised using Diffrac.EVA and SIeve+.

5.3. Results

5.3.1. Thin-section Imaging and mapping

To identify regions of interest in the thin section and to investigate elemental differences across the sample, maps were produced using μXRF in two regions of interest (Figure 5.1a). From these μXRF maps, five points of interest, shown in Figure 5.1b and 5.1c, labelled A-E, were selected for collection of μXRD, μXANES and μEXAFS data. A net XRF spectrum, shown in Figure 5.2, taken from the whole area of Region 1 was calculated to allow characterisation of emission lines of different elements. This analysis identified the presence of Ca, Ti, Mn, Fe, Sr, Y, Zr, Ta, W, Pb, Th and U.

The elemental distribution maps in Figures 5.3 and 5.4 show the relative intensity of the selected emission line at each point measured in the map. It is not possible to quantify this intensity since this would require measurement of known standards and calibration of the detector to those standards, which is not possible for the instrument utilised; however, emission line intensity does indicate the relative concentration of the respective element. Region 1 (Figure 5.1b and Figure 5.3) exhibited three compositionally distinct phases (identified as Phase 1, 2 and 3 in Figure 5.1b): (1) a phase with high intensities of U Lα emissions, attributed to the main U mineral (thought to be brannerite); (2) a surrounding phase with comparatively very low or no U Lα emissions and high Ca Kα emissions and; (3) a phase with high intensities of Ti Kα emissions.

Phase 1 also contained Ca, Fe, Ti, Mn, Sr, Y, Zr, Ta, W, Pb and Th (Figure 5.2). These elements are all known constituents or impurities of brannerite identified in previous work [26, 29], except for Sr and W. Due to the low comparative intensity of the emissions of Fe Kα and Ca Kα in Phase 1 when compared to Phases 2 and 3, the presence of Fe and Ca in the Phase 1 is not is not readily apparent in Figure 5.3; however, μXRF data collected from point C (Figure 5.2) confirm the presence of these elements. In Figure 5.1b and Figure 5.3 it was also observed

that within Phase 1 there were regions that appeared to contain no elements at all (black areas indicated with arrows and L in Figure 5.1a). These regions of low intensity emission could be indicative of inclusions of minerals containing lighter elements that are not detectable by XRF at the energy range employed, alternatively these low intensity emission regions could also be caused by irregularities in the thickness of the sample or artefacts from sample preparation.

Importantly, there was clear evidence of alteration (i.e. either hydrothermal or aqueous alteration) in the Phase 1, with higher intensities of Pb, Sr and Y at the rim of the of the U-rich phase suggesting that they had "leached" out (Figure 5.3). Cracks in the Phase 3, which radiate outwards from Phase 1, contain concentrations of Fe and Pb similar to Phase 1, and much higher than in Phases 2 and 3, consistent with the migration of Fe and Pb from the Phase 1 into the cracks. It is also possible the Pb present at the rim of the Phase 1 and within the cracks originated from the migration of U to the rim of Phase 1 and cracks in Phase 3, which then subsequently underwent radioactive decay to Pb. Syverson *et al.* observed a 'spotty' distribution of Pb in their brannerite sample from Crocker's Well [38] and enrichment of Pb in cracks within the brannerite phase. Another brannerite sample from La Gardette Mine, France also presented a Pb rich rim [38]. Lumpkin *et al.* observed an alteration rim on the grain one of the samples they investigated from Crocker's Well [29], and the presence of a secondary U oxide phase in cracks in an adjacent rutile phase. They also observed the presence of secondary U oxide phases in cracks of the host rock surrounding a brannerite sample from Bou Azzer, Morocco, which displayed alteration along interior fractures and at the grain rims [29].

Phase 2, which was co-located within the Phase 1, was identified by µXRD (Figure 5.5, Point D) as rutile (TiO_2). Titanium oxides (either rutile or unspecified Ti oxide) commonly occur as both an accessory mineral and as grain inclusions on the scale of microns [38] and tens of microns [25, 29] in natural brannerite mineral samples.

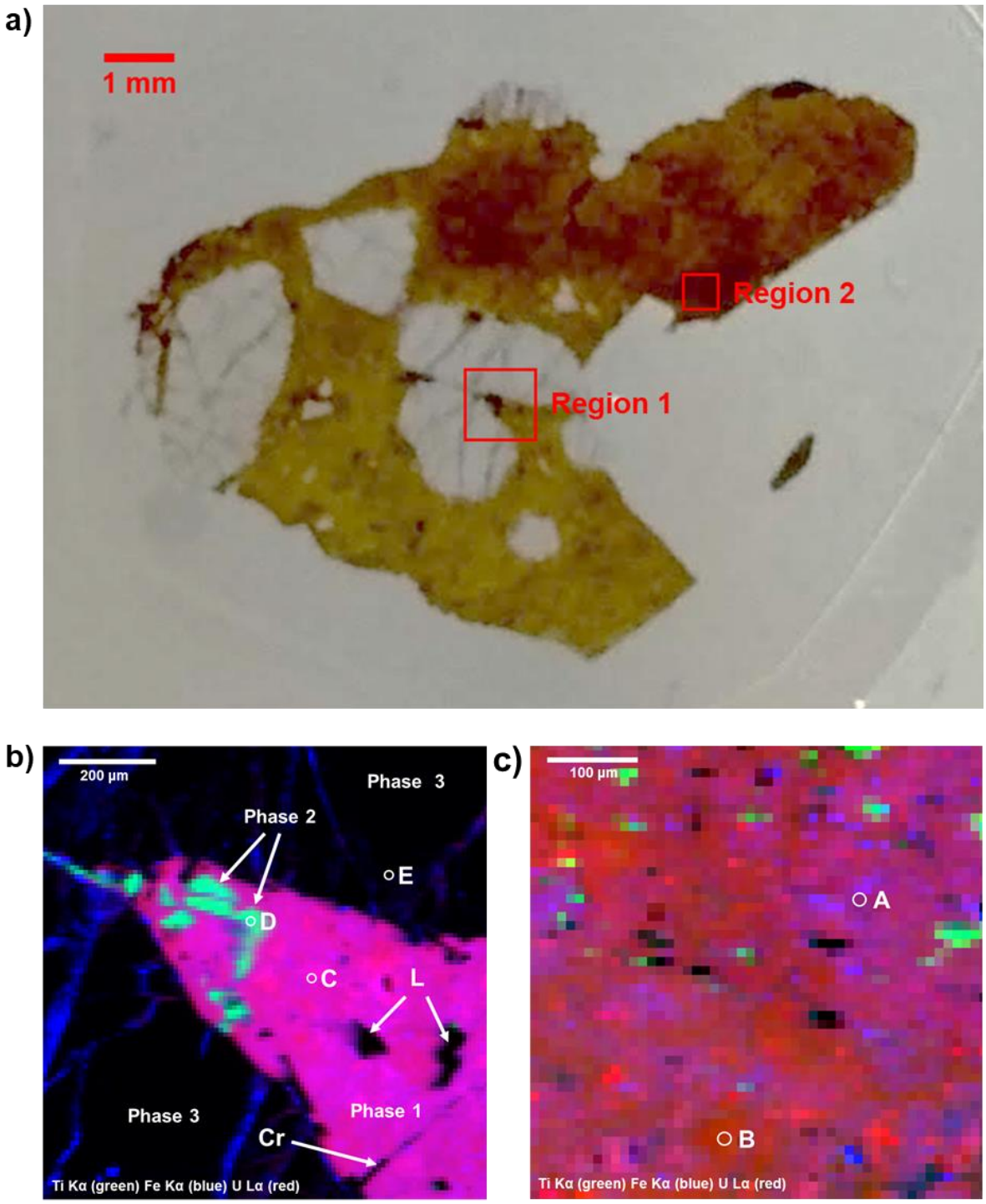

Figure 5.1. (a) Optical microscopy image of mineral thin section mounted on glass slide, with approximate scale and two regions of interest indicated. **(b)** Combined µ-XRF maps from Region 1 of Ti Kα (green), Fe Kα (blue) and U Lα (red) with: identified U rich (Phase 1), rutile (Phase 2) and fluorapatite (Phase 3) phases; regions of low concentration in all elements (L); crack feature (Cr); and points C-E indicated. **(c)** Combined µ-XRF maps from Region 2 of Ti Kα (green), Fe Kα (blue) and U Lα (red) with points A and B indicated.

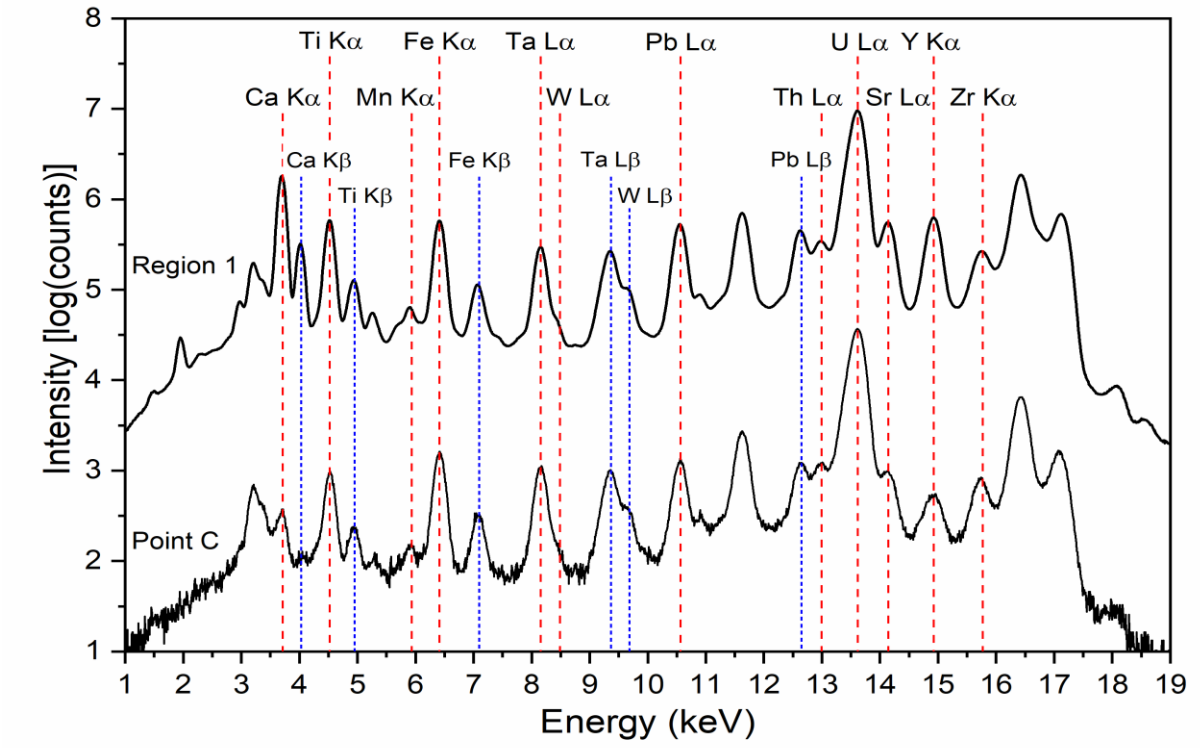

Figure 5.2. Summed µXRF spectra from the full area of Region 1 and from point C. Emission lines are indicated in red and blue (long and short dashed respectively), those emission peaks which were windowed for µXRF mapping are indicated in red.

Phase 3 was characterised by µXRD (Figure 5.5, Point E) as fluorapatite ($Ca_5(PO_4)_3F$), and was found to also contain Mn, Sr and Y, with relatively lower intensity emissions arising from Mn and Sr than from Phase 1. The fluorapatite phase (Phase 3) exhibited a number of cracks that radiated out from the Phase 1, possibly caused by expansion of the U mineral due to alpha recoil damage.

Region 2 was of an area within the main U mineral phase, indicated in Figure 5.1a. Similar to the U-rich phase in Region 1, heterogeneity in the distribution and intensity of some elements was apparent in Region 2 (Figure 5.4). While the Ta Lα, W Lα, U Lα and Th Lα emissions in this region appeared to be relatively homogeneous (with the exception of several hotspots), the distribution of intensity in the emission maps of Sr Kα and Pb Lα were dissimilar to all of the other elements, consistent with alteration. The phase was also found to contain hot spots of Ca, Ti, and Fe; the Ti hotspots, which were ca. 10 - 30 µm in size, could be Ti oxide grain inclusions.

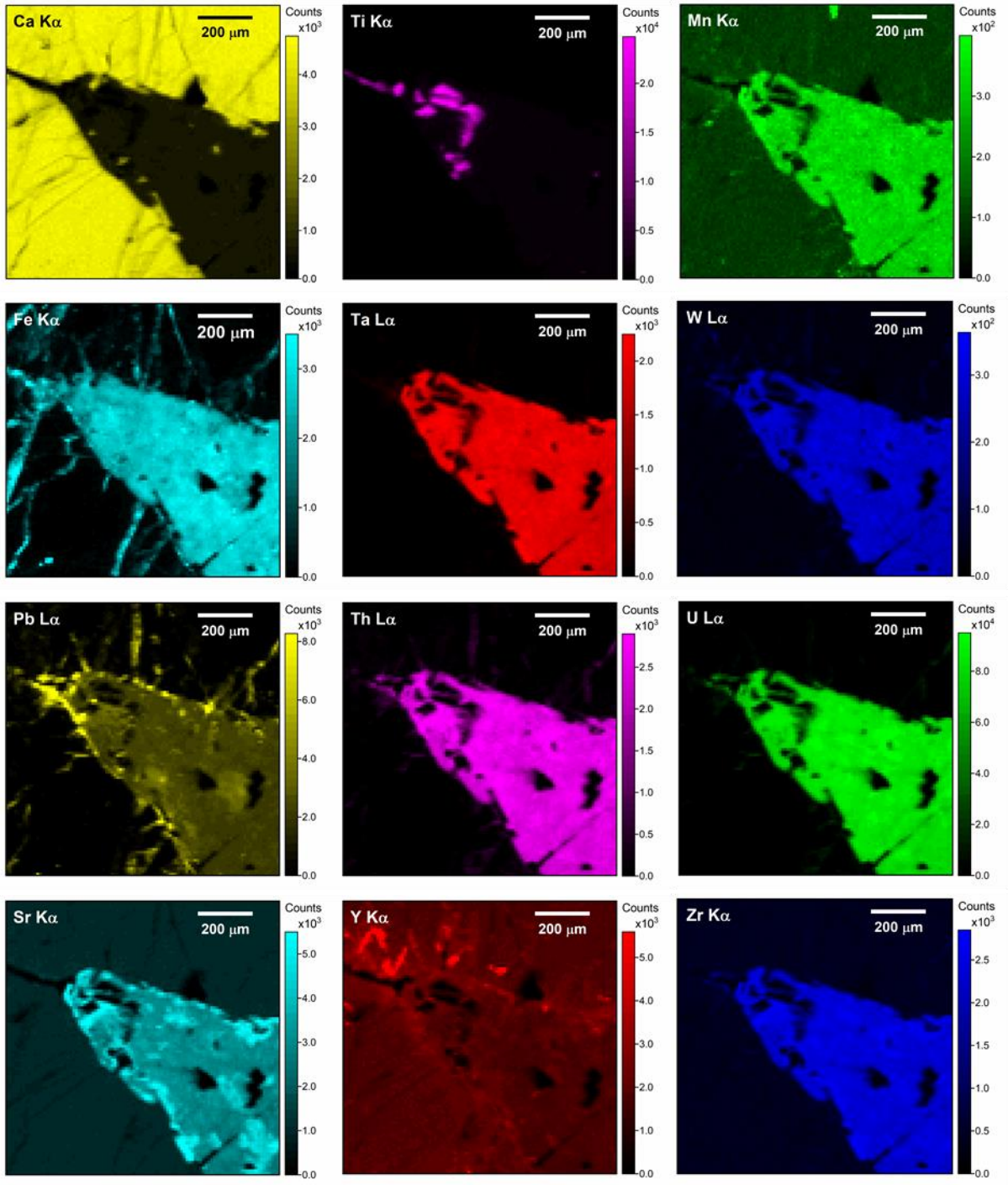

Figure 5.3. μXRF emission line maps of the natural uranium-containing mineral, Region 1. Size 1.0 by 1.0 mm, collected at 17 keV.

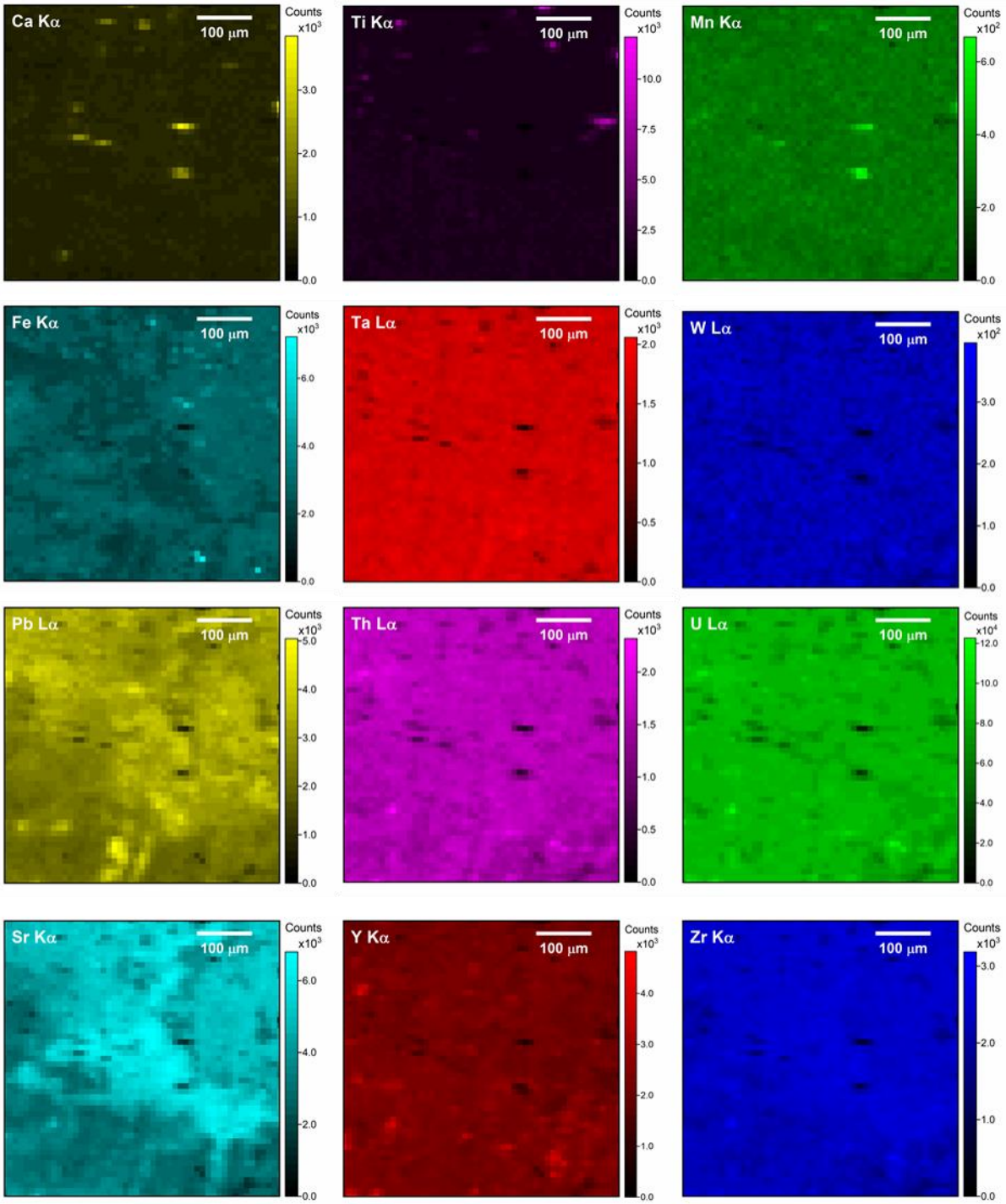

Figure 5.4. μXRF emission line maps of the natural uranium-containing mineral, Region 2. Size 0.5 by 0.5 mm, collected at 17 keV.

5.3.2. X-ray Diffraction

Figure 5.5 shows the processed 1D µXRD patterns relating to points in Region 1 (A-E). Due to the small beam size used to perform X-ray diffraction (1.5 by 1.5 µm), the diffraction patterns arise from crystals in specific orientations, rather a net representation of all possible orientations, which can make definitive phase assignment challenging. For example, the reflections of the measured pattern can have different relative intensities, dependent on orientation, to those of reference compounds measured by powder XRD, and some reflections may be missing.

The µXRD patterns of Points A-C in Region 1 all exhibited two regions of diffuse scattering, between $5.00 \leq 2\theta \leq 9.20°$ and $11.30 \leq 2\theta \leq 16.10°$, in addition to several distinct reflections. It can be concluded that the phase assemblage at these points is a mixture of amorphous (metamict) and crystalline minerals. Point D demonstrated reduced relative intensity in the regions of diffuse scattering when compared to points A-C, and similar distinct reflections, including one high intensity reflection at $\theta = 20.40°$. The majority of the reflections in Points A to D were attributed to rutile (TiO_2), a known associate mineral of brannerite at Crocker's Well. Point E appeared fully crystalline, with clearly defined reflections attributed to fluorapatite ($Ca_5(PO_4)_3F$); the apatite mineral group is another common associate mineral of brannerite [39]. Some reflections in the µXRD patterns of points A and D could also be attributed to fluorapatite and are indicated in Figure 5.5. The two reflections at $\theta = 10.0°$ and $\theta = 14.3°$ in the µXRD patterns of points A-E are artefacts which were a result of the background subtraction of the µXRD pattern collected from the glass slide.

As previously discussed, naturally occurring U mineral samples are often metamict [25, 26, 29, 38] due to the effects of alpha recoil decay, so a mainly amorphous material at points A-D was to be expected, as was the presence of fluorapatite and rutile. Ludwig and Cooper [24] commented that rutile is "*always associated*" with brannerite from Crocker's well including as "*intimate intergrowths within the brannerite grains*", as observed in Figure 5.3. The recent study by Turuani *et al.* identified inclusions of euhedral Ti oxides on the scale of microns within the brannerite phase of their Crocker's Well sample [26]. The presence of micron-sized inclusions could account for the reflections attributed to rutile for points A-D. It is also

possible that the peaks are from a rutile phase behind the main uranium mineral, since the μ-XRD patterns are measured in transmission and the samples are ca. 40 μm thick. Given the similarity of peak intensities between the μXRD patterns collected from all the spots, especially the (210) peak at θ = 20.40° which indicates that the rutile at points A-D have similar orientations, one large crystalline phase is more likely than several inclusions with similar orientations.

5.3.3. X-ray Absorption Near Edge Structure Analysis

Uranium L_3-edge μXAS data were collected at points A-E in Regions 1 and 2, with the μXANES data from each point shown in Figure 5.6. These were compared with XANES data from a suite of U reference compounds with a range of U coordination and oxidation states, some of which are also shown in Figure 5.6. The U L_3-edge XANES from the reference compounds demonstrate a linear trend between U oxidation state and edge position (E_0 half, all E_0 positons are E_0 half unless specified otherwise) as is shown in Figure 5.7; E_0 increased with U oxidation state, from $U^{4+}Ti_2O_6$ (17164.5 eV) to $CaU^{6+}O_4$ (17168.2 eV).

The XANES of points A-C were similar. They exhibited the similar or the same E_0 half positions (17167.4, 17167.4 and 1717674.3 eV, respectively) and the same E_0 1^{st} derivative (taken as the first maximum in the first derivative) position (17172.4 eV) and peak shape, including a flat shoulder feature between 17185 and 17200 eV and a second feature between 17205 and 17230 eV. The E_0 position of points A-C (Figure 5.7) were higher than those of the U^{5+} standards (17166.5 and 17166.9 eV) indicating the net U oxidation state is greater than 5+, and therefore the presence of U^{6+} at these points. However, the uncertainties of the E_0 positions of points A-C overlap with the uncertainties of the E_0 positions of both $LaU^{5+}O_4$ and metaschoepite ($(U^{6+}O_2)_8O_2(OH)_{12} \cdot 10H_2O$), so estimates of U oxidation state from the edge position of these points are indicative, but not robust.

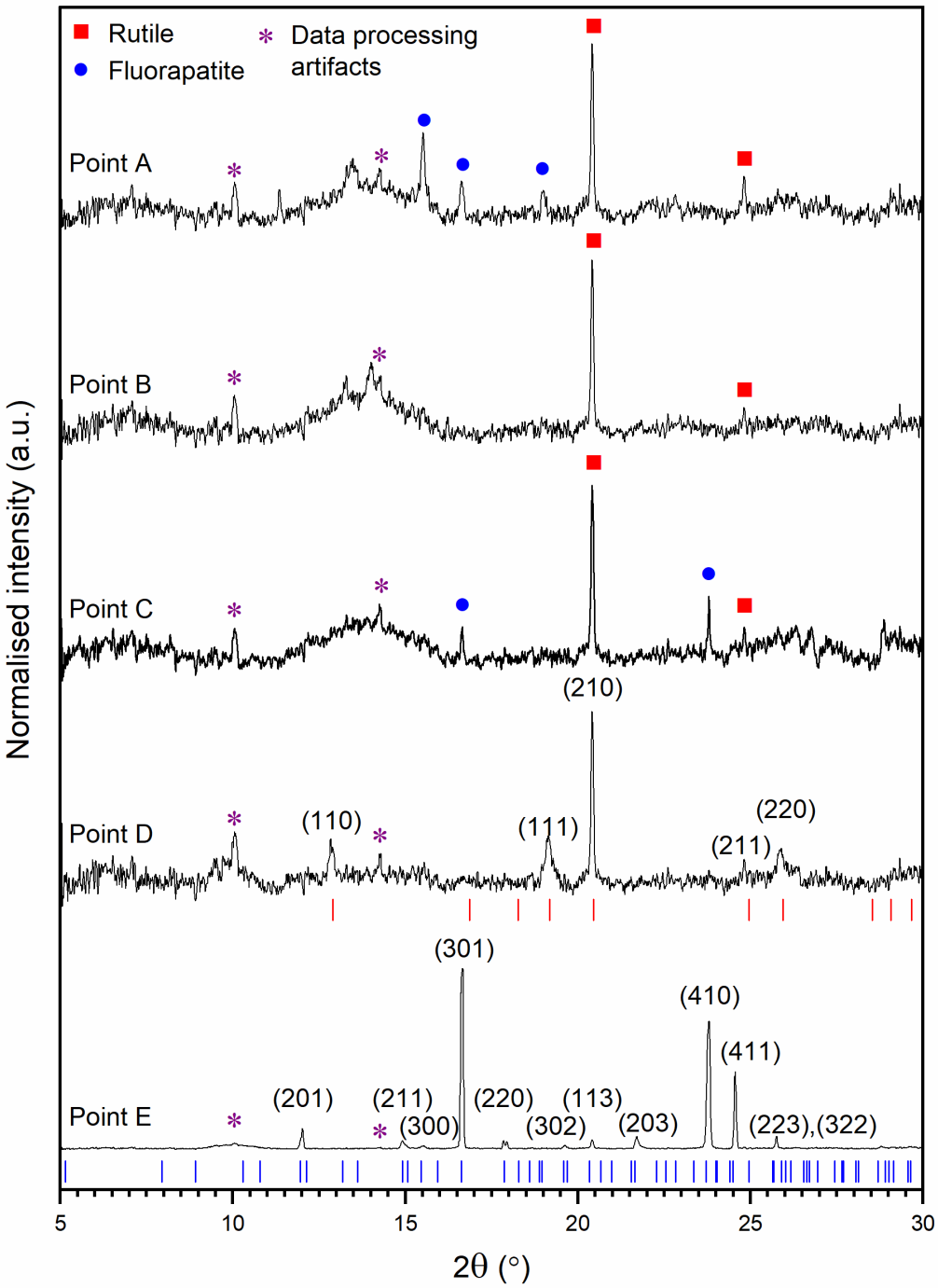

Figure 5.5. µXRD patterns collected from points A-F, with indexed phases of rutile (TiO_2; PDF no. 00-021-1276) and fluorapatite ($Ca_5(PO_4)_3F$; PDF no. 04-012-9849). Data processing artefacts are the result of subtracting the XRD pattern of the glass slide and adhesive.

The presence of a pronounced shoulder feature between 17185 and 17200 eV and a second feature between 17205 and 17230 eV is associated with the uranyl moiety (UO_2^{2+}) and was also observed in the XANES of known U^{6+} uranyl reference compounds metaschoepite ($(UO_2)_8O_2(OH)_{12} \cdot 10H_2O$) and soddyite ($(UO_2)_2SiO_4 \cdot 2(H_2O)$) (see **Chapter 4**). The presence of a slight feature in this region in the XANES of points A-C suggested that at these points in the sample U was partially speciated as U^{6+} uranyl.

The XANES region of point D was similar to points A-C, with the same maximum at 17219.0 eV and shoulder feature; however, the edge positon was higher (E_0 half = 17168.2 eV) (Figure 5.7) the shoulder feature was more prominent, and the white line (the crest of the absorption maximum) was narrower, which all indicated that a greater fraction of uranyl speciation was present at this point.

The XANES data collected from point E was different to that collected from the other points, as it did not appear to have the U^{6+} uranyl shoulder feature; however, it exhibited a lower U content and thus, the signal to noise ratio was high. As such, the possibility of U^{6+} uranyl speciation at this location cannot be discounted.

From observational analysis of the edge position and post-edge features of the U L_3-edge XANES, points A-C had features characteristic of the U^{6+} uranyl moiety. Therefore, the main U-containing mineral can be concluded to be, at least partially, U^{6+} uranyl. This is intriguing since U in both brannerite and davidite is prototypically U^{4+} [27, 40]. Certain synthetic compositions of brannerite have been found to contain higher net U oxidation states than 4+ [9, 17, 41-44], but never above 5+. For example, Bailey *et al.* confirmed, using U L_3-edge µXAS, that U with a net speciation greater than 4+ was present within brannerites of compositions $Gd_{0.1}U_{0.81}Ce_{0.09}Ti_2O_6$, $Gd_{0.2}U_{0.72}Ce_{0.08}Ti_2O_6$, $Gd_{0.25}U_{0.675}Ce_{0.075}Ti_2O_6$ and $Ca_{0.1}Gd_{0.1}U_{0.72}Ce_{0.08}Ti_2O_6$, sintered under various conditions [17], while Dixon Wilkins *et al.* successfully sintered brannerites with compositions $UTi_{1.4}Al_{0.6}O_6$, $UTi_{1.0}Al_{1.0}O_6$ and $UTi_{0.8}Al_{1.2}O_6$ which were confirmed to contain both U^{4+} and U^{5+} by applying U M_4-edge M_β HERFD [19]. Indeed, it is obvious that the edge positions (Figure 5.7) (17167.4, 17167.4, 17167.3, 17168.2 and 17167.7 eV, for points A-E) and shape of the XANES regions of points A-E were not similar those of the synthetic brannerite UTi_2O_6 standard (E_0 = 17169.2).

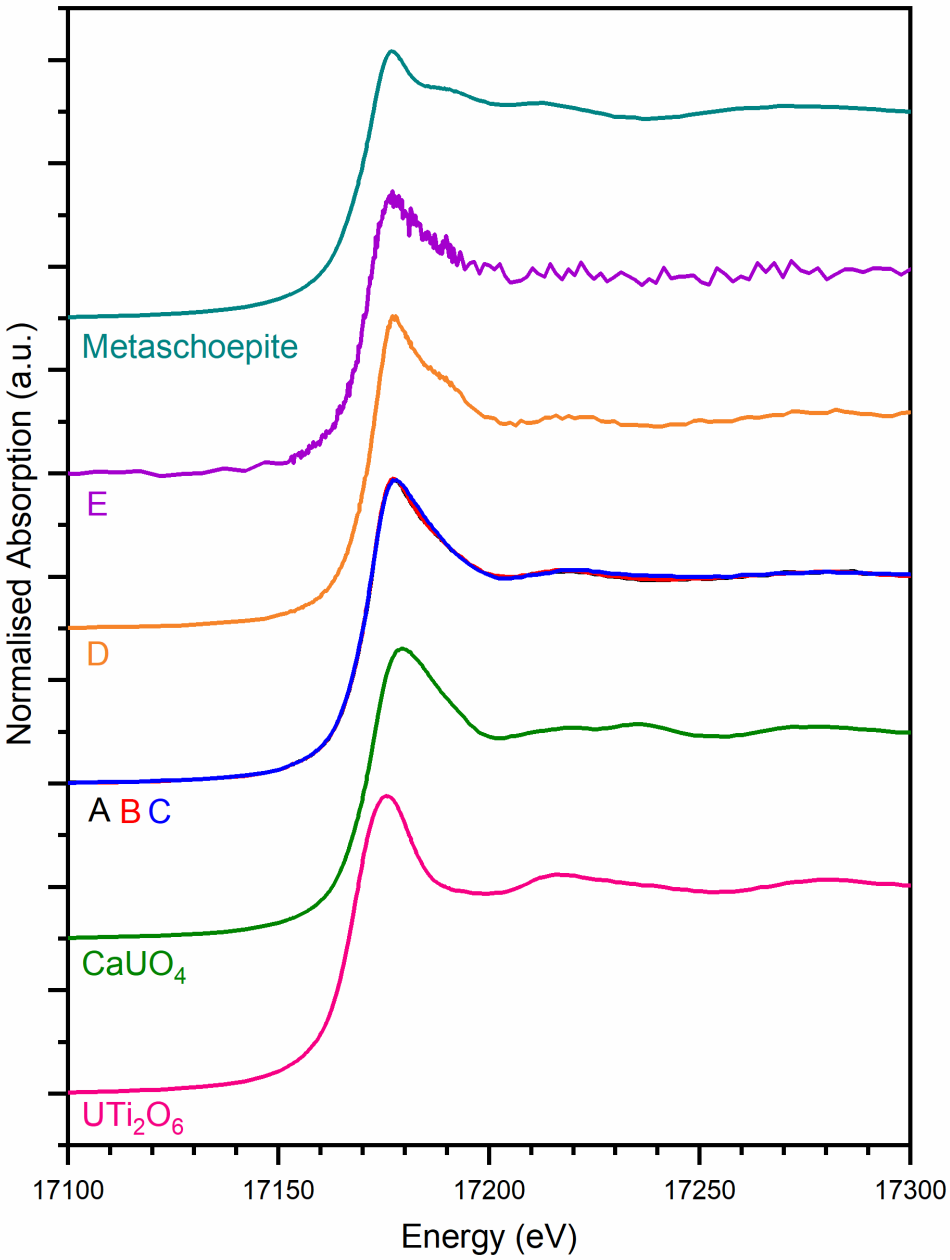

Figure 5.6. U L_3-edge µXANES data collected from of points A-E, with reference compounds $U^{4+}Ti_2O_6$, $CaU^{6+}O_4$ and metaschoepite ($(UO_2)_8O_2(OH)_{12} \cdot 10H_2O$)) for comparison.

An E_0 calibration line was constructed from the known oxidation states and E_0 positions of reference compounds (Figure 5.7), which was used to estimate U oxidation state, these estimates are given in Table 5.2. As discussed above, the estimates of U oxidation state from E_0 position for points A-C are not robust; however, the E_0 positions for points D and E do show a net U oxidation state greater than 5+, and therefore must contain U^{6+}.

Linear combination fitting (LCF) was performed to further investigate the nature of the U speciation observed in the XANES data from all points. The resulting mean weighted contributions calculated from LCF analysis of points A-E are shown in Table 5.2. The U speciation in points A-C are all best described by major contributions from the U^{6+}-containing $CaUO_4$ and haiweeite reference compounds, with a minor contribution from UO_2. The major contributions of two known U^{6+} reference compounds further evidences the U-rich phase as mainly having U^{6+} speciation, with particular emphasis on a possible uranyl moiety being present. Data acquired at each of the locations (points A-C) exhibited similar weightings of U^{4+} and U^{6+} (derived from the reference compounds) and, therefore, had similar estimated net U oxidation states (Table 5.2) of U of 5.7+. These estimates of net U oxidation state are in good agreement with estimates from E_0 position (5.7(2), 5.7(2), and 5.6(2) for A-C).

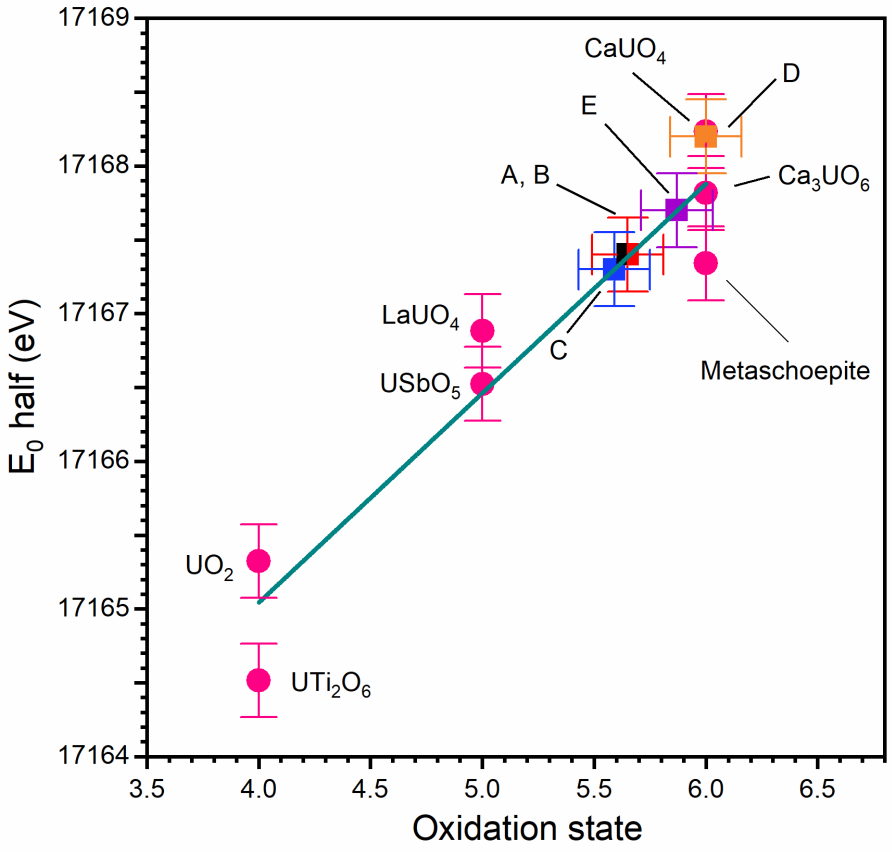

Figure 5.7. Plot of E_0 half positions of U reference compounds UTi_2O_6, UO_2, $USbO_5$, $LaUO_4$, Ca_3UO_6, $CaUO_4$ and metaschoepite ($(UO_2)_8O_2(OH)_{12} \cdot 10H_2O$)) against their known oxidation states, with linear regression applied to produce an E_0 oxidation state calibration line, from which the E_0 half positions of Points A-E have been estimated.

Table 5.2. Net weightings of each U oxidation state, scaled to sum to unity, and estimated net oxidation states relating to points A-E (Figure 5.4).

Point	LCF - Reference compound normalised weightings (%)			Estimated oxidation state from LCF	Estimated oxidation state from linear regression
	$U^{4+}O_2$	$CaU^{6+}O_4$	Haiweeite $Ca(U^{6+}O_2)_2(Si_5O_{12})(OH)\cdot 6H_2O$		
A	0.14(1)	0.37(1)	0.49(7)	5.7(2)	5.7(2)
B	0.15(1)	0.36(1)	0.49(7)	5.7(3)	5.7(2)
C	0.14(1)	0.50(2)	0.37(9)	5.7(3)	5.6(2)
D	-	0.37(2)	0.63(10)	6.0(4)	6.0(2)
E	0.14(2)	0.19(4)	0.67(30)	5.7(13)	5.9(2)

Point D was best described by contributions from only $CaUO_4$ and haiweeite (Table 5.2), of 0.37(2) and 0.63(10) respectively. The presence of a greater amount of U in a uranyl environment at point D than points A-C is in agreement with observations made from comparisons the XANES regions of these points. The U at point D appeared to be fully uranyl, with an estimated net U oxidation state of 6.0(4). This is in good agreement with the estimate from E_0 position of 6.0(2).

Point E was best described by a major contribution from haiweeite, and minor contributions from UO_2 and $CaUO_4$. The scaled weighting of UO_2 (0.14(2), Table 5.2), was the same as for points A and C. The net scaled weighting of U^{6+} reference compounds was also the same as for Points A and D (0.86); therefore, a similar net U oxidation state, of 5.7(13), was determined. A major contribution from haiweeite, a U^{6+} uranyl reference compound, was not expected from examination of the XANES region, as no uranyl shoulder feature appeared to be present. There were large errors for the weighted contributions from haiweeite (0.30), for this Point (E). The noise in the XAS data of Point E is at least, in part, the source of this errors; however, these errors could also indicate that the fit is missing key reference compounds to describe the U environment. Due to the noise of the data, the large errors in the LCF and the inconsistency between observational and LCF analysis, no definitive conclusions on the U speciation in the apatite phase can be made from LCF. However, the E_0 position gives a good

estimate of net oxidation state of 5.9(2) so therefore the majority of U at point E must be U^{6+}. 30

5.3.4. Extended X-ray Absorption Fine Structure Analysis

Fitting of the EXAFS data collected at points A-C was performed to further investigate the local structure of U within the U mineral phase, the data and fits are shown in Figure 5.8 and the final fit parameters are shown in Table 5.3. A fit was constructed using the EXAFS data collected from point A, which was then applied to points B and C. An amplitude reduction factor (S_0^2) of 0.8 was obtained by fitting the EXAFS of reference compound UO_2 using its known crystal structure [34], this value was then applied to the fits of unknown structures. A model of the EXAFS region of point A was first fitted by adapting the crystal structure of synthetic UTi_2O_6. However, as may be expected from the analysis of µXANES data, which favoured a uranyl speciation, these were unsuccessful and produced qualitatively and quantitatively poor fits. Whilst the method of applying a known or similar structure and then making adjustments to improve the fit is known to be effective for crystalline samples [45], this is not the case for the mineral sample investigated in the present study, since the precise composition is unknown and its structure is metamict. As such, fitting can be performed reliably on only the first and possibly the second shells of scatterers. Therefore, a different approach was applied which began without structural assumptions, instead paths and corresponding parameters were applied to create a model to best fit the data and, in turn, determine the structure.

5.3.4.1. Construction of EXAFS model

The best fit (Table 5.3) used three U-O backscattering paths; U-O1, a U-O axial path (initial distance of 1.791 Å) with a degeneracy of 2, taken from a CIF file of haiweeite [35]; U-O2, a U-O equatorial path (initial distance of 2.329 Å) with a degeneracy of 4, also taken from a CIF file of haiweeite [35]; and U-O3, a U-O path from a CIF file of UO_2 [34] (initial distance of 2.368 Å) with a degeneracy of 8.0. Each U-O path was assigned an individual σ^2 parameter. The U-

O3 path was treated as if fitting for a separate U environment and a weighting (W) was applied to the U-O_1 and U-O_2 paths, while a weighting W_{O3} where $W_{O3} = 1 - W$ was applied to the U-O_3 path. For the U-O1 path the associated rattle, non-forward and forward multi scattering paths were also included, these paths were assigned to share ΔR and σ^2 parameters with the U-O_1 path, with the multi scattering parameters equal to the single scatter parameters multiplied by a factor of 2.

When fitting the EXAFS with two U-O paths from the haiweeite CIF file only, it was not possible to adequately model the data in the region of 1.9 to 2.5 Å; the region which is dependent on the equatorial oxygen path. A third U-O path from UO_2 was introduced, representing a more distorted U speciation environment and accounting for the ca. 15% weighting of UO_2 indicated by analysis of the LCF data. This produced a significantly better fit to the data. Initially W was set to 0.85, taken from the fraction of U^{6+} speciation estimated by LCF.

U-O1 and U-O2 paths from a $CaUO_4$ CIF file were offered as an alternative to the use of U-O1 and U-O2 paths from haiweeite. Haiweeite and $CaUO_4$ both have short and long U-O paths; however, haiweeite, which contains U speciated as U^{6+} uranyl, has a shorter U-O1 path (1.791 Å) than the U^{6+} uranate $CaUO_4$ (1.957 Å). When U-O paths from $CaUO_4$ were used the new path length of U-O1 calculated by the fit was 1.806 Å (a Δd of -0.150 Å) and the goodness of fit was worse (0.0114 vs 0.0109 for point A) than when U-O paths from Haiweeite were used. The need to shorten of the $CaUO_4$ U-O1 path length to achieve a good fit is a strong indication that U^{6+} uranyl is present in the sample.

5.3.4.2. Fitting results

The best fit model was optimised using EXAFS data from point A, which was then applied to points B and C. Therefore, some parameter values for B and C are less than ideal (i.e. increased R-factors); however, this compromise was deemed worthy to keep a consistent fitting model throughout the dataset, as implied by the previously discussed XANES analyses. To improve the fits of B and C, different values for the W parameter were used (Table 5.2). In addition, the reduction in goodness of fit is also partially due to the collected data from points B and C

having more glitches than the data from point A. However, in the Fourier transform of the EXAFS data (Figure 5.9b) the fits all appear to match well to the data in the region associated with first shell oxygen paths, giving confidence that the fit adequately describes the first shell for all three points.

There are differences in the Fourier transform of EXAFS data of points A-C above 2.5 Å (Figure 5.9b), which could be indicative of variations in second shell structure between the different points, or these variations could be a product of noise. The lack of crystallinity in the sample significantly reduced the amount of second shell scattering that was experienced by the absorbing uranium atom. This low intensity, in combination with the limited number of variables available to use in fitting the data, precludes the modelling of second shell scatterers.

5.3.4.3. Bond Valence Sum

The bond valence of paths U-O1, U-O2 and U-O3 was calculated and summed using r_0 and B values from Gange *et al.* [46] to give an estimate of U oxidation state at each point (Table 5.3). The estimates were made by treating the U^{6+} uranyl and U^{4+} uranate paths as two separate U environments and applying values estimated by Gange *et al.* for U^{6+}-O and U^{4+}-O respectively. The estimated net U oxidation states for points A-C (5.5 to 5.7) are in good agreement with a majority fraction of uranyl speciation described by the fit and with estimates of net speciation from linear combination fitting (5.7) and E_0 position (5.6-5.7).

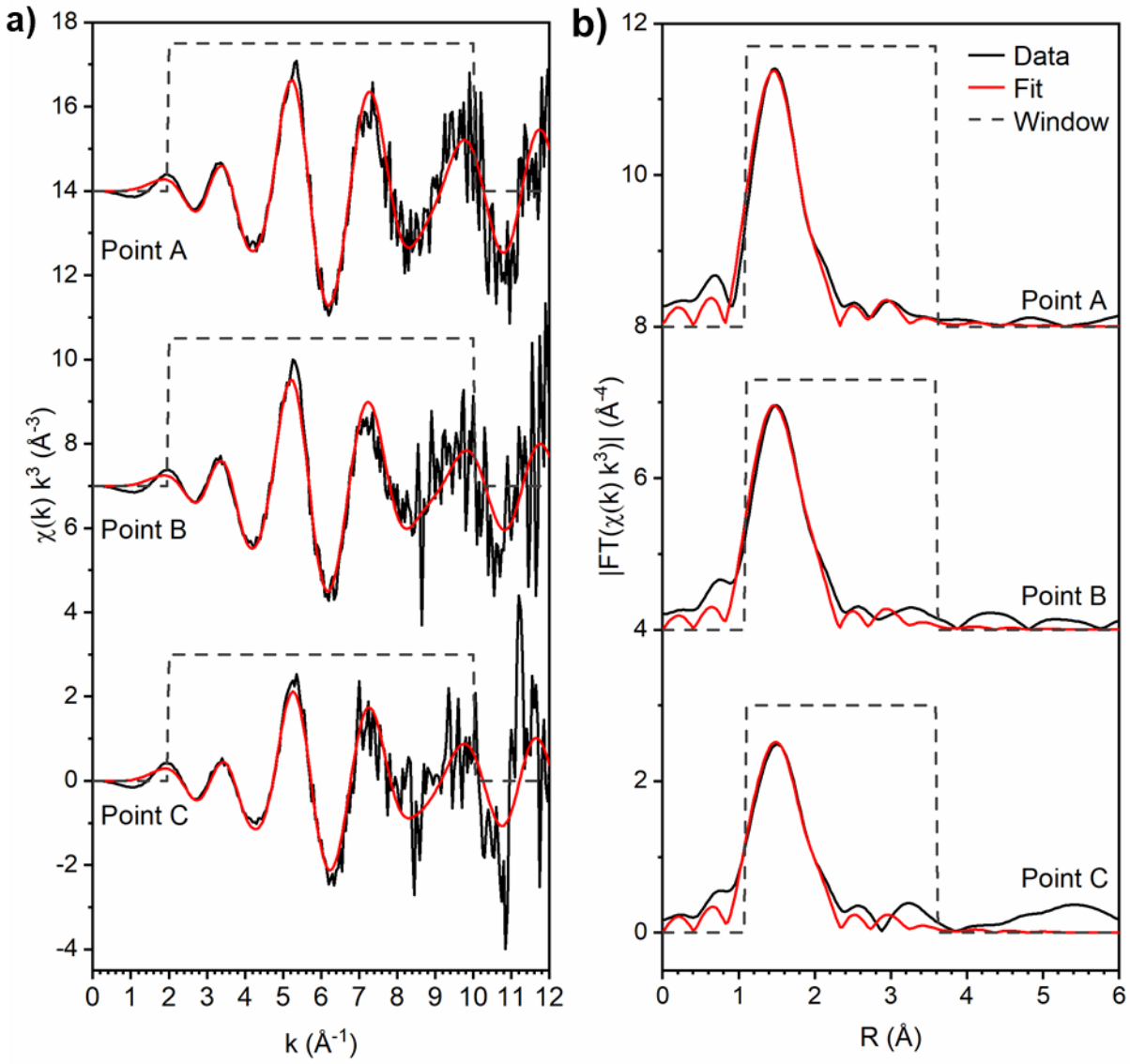

Figure 5.8: Final fits of U L_3-edge µEXAFS spectra from points A-C presented as **(a)** k^3 µEXAFS data and **(b)** as the magnitude of the respective Fourier transform.

Table 5.3: All fit parameters and uncertainties from EXAFS fits of points A-D. Fit parameters: R-factor – measure of goodness of fit; ΔE – shift in E_0, which was constrained to be the same for all paths; S_0^2 – the amplitude reduction factor; W – the weighting factor between the U-O paths from haiweeite and UO_2; N – degeneracy of a path; d – the new calculated path length; and σ^2 – the Debye-Waller Factor. Parameters which were set are indicated with*. Shared parameters between the U-O1 path and the O1-O1 multiple scattering paths are indicated with † and ‡.

Parameter	Point A	Point B	Point C
R-factor	0.0109	0.0173	0.0254
ΔE (eV)	0.8(1)	1.4(2)	1.3(2)
S_0^2*	0.8	0.8	0.8
W*	0.80	0.80	0.77
$N_{U\text{-}O1}$*	1.60	1.60	1.54
$d_{U\text{-}O1}$† (Å)	1.81(1)	1.81(1)	1.81(1)
$\sigma^2_{U\text{-}O1}$‡ (Å²)	0.003(1)	0.004(1)	0.005(2)
$N_{U\text{-}O2}$*	3.20	3.20	3.08
$d_{U\text{-}O2}$ (Å)	2.23(3)	2.25(4)	2.34(3)
$\sigma^2_{U\text{-}O2}$ (Å²)	0.012(4)	0.016(5)	0.005(3)
$N_{U\text{-}O3}$*	1.60	1.60	1.84
$d_{U\text{-}O3}$ (Å)	2.36(3)	2.35(4)	2.17(3)
$\sigma^2_{U\text{-}O3}$ (Å²)	0.004(3)	0.006(5)	0.005(4)
$N_{O1\text{-}O1\ MS}$*	2	2	2
$d_{O1\text{-}O1\ MS}$† (Å)	3.61(2)	3.62(2)	3.63(3)
$\sigma^2_{O1\text{-}O1\ MS}$‡ (Å²)	0.005(2)	0.008(2)	0.010(3)
CN	6.40	6.40	6.46
BVS	5.51(12)	5.63(7)	5.73(10)

5.4. Discussion

The U mineral investigated in this work is from Crocker's Well, South Australia. Since it is fully metamict, identification is challenging; the U minerals known to occur at Crockers Well are brannerite, davidite ($A_{1-x}M_{21}O_{38}$) and uranothorite ($(Th,U)SiO_4$). Uranothorite (or similar U-Th-silicates) has only been found to occur intimately mixed with brannerite [27, 40, 47, 48]. Qualitative analysis by µXRF does not disprove the presence of either mineral but the successful fitting of the µEXAFS data with an adapted brannerite structure is supportive of the U mineral being metamict brannerite.

Davidite-(La) is part of the crichtonite group, which has the idealised composition ($A_{1-x}M_{21}O_{38}$) [49]. Within the complex crichtonite structure there is one 12-fold coordinated A-site and five M-sites, including four octahedral sites and one tetrahedral site [40, 50]. The La rich form, davidite-(La) has the nominal composition $(La,Ce,Ca)(Y,U)(Ti,Fe)_{20}O_{38}$ [51] and U occupies the M(1) octahedral site [40]. When the structure was solved by Gatehouse *et al.* they concluded that the average ionic radius of the M(1) site (0.88Å) was suggestive of U^{4+} speciation [40]. Thus far, no work appears to have been undertaken to confirm the speciation of U in davidite-(La). Due to the variety of different sites, the crichtonite structure is also able to accommodate a variety of different elements.

As there is limited work available [48] on the characterisation of davidite-(La) there is little to compare the findings of this paper to, with regard to the possible presence of U^{6+}, or uranyl speciation within davidite-(La). Despite the lack of prior research, the possibility of oxidised U speciation within the crichtonite structure is of particular relevance as a another member of the crichtonite group, loveringite ($(Ca,REE)(Ti,Fe,Cr)_{21}O_{38}$) [52], was found to occur, with a small wt. % of U, in certain compositions of Synroc, a multi-phase synthetic titinate ceramic wasteform developed for the immobilisation of the radioactive waste [53].

Brannerite $(U,Ca,Y,Ce)(Ti,Fe)_2O_6$ [39] is a U titanate mineral with an idealised composition of $U^{4+}Ti_2O_6$; however, U is often partially oxidised [54]. Brannerite has the structure AB_2O_6, which can be described as layers of corner sharing A site octahedra between layers of edge sharing B site octahedra (BO_6) [54]. The brannerite structure can accommodate a variety of elements,

common impurities in mineral samples are Th, Pb and La on the A site and Al, Nb and Mn on the B site [29]. Brannerite is considered the third most abundant U^{4+} resource [27, 54, 55] in the world, but is also an attractive potential wasteform due to the abundance of natural analogues, its refractory nature, resistance to dissolution [55-58] and high waste loading (up to 55 wt. % U). Therefore, brannerite has been the subject of more extensive research as a potential wasteform than davidite.

As discussed previously, there have been some attempts at producing synthetic brannerites with U speciation greater than 4+. Dixon Wilkins *el al.* [19] demonstrated that the brannerite structure can accommodate pentavalent U. However, further work attempting to target U^{6+} speciation in synthetic brannerite has been unsuccessful [59]. Bailey *et al.* characterised samples using μXAS at the U L_3-edge, confirming a net U^{5+} speciation within the betafite phase itself, whereas other synthetic brannerites that have exhibited net U^{5+} speciation [9, 41, 42] also contained U_3O_8, in which U has a mixed 5+/6+ valence.

The presence of U^{6+} within a metamict, altered sample brannerite is much more credible, and supported by some previous work. As previously discussed, Colella *et al.* produced estimates of U oxidation state between +4.10 to +5.15 from EELS data and from the composition of the sample [7] that would require a contribution from U^{5+} or U^{6+}. However, the high intensity of the electron beam used in EELS can cause the sample to oxidise, resulting in the technique producing estimates of oxidation states that are too high. Previous attempts to characterise the composition of brannerite samples, using electron probe microanalysis (EPMA) [8], tend to attribute significant fractions of UO_3 (U^{6+}), by assuming ratios of U^{4+} and U^{6+} to achieve charge balance, and that there are a total of 3 cations per formula unit. In some brannerites such EPMA analysis has been used to infer that all U present was speciated at as U^{6+}. For example, René *et al.* characterised some regions of brannerite, that had been identified as unaltered, as only containing U speciated as 6+ on the basis of EPMA. However, they did not discuss which site U^{6+} would occupy in the brannerite structure.

One possible mechanism to produce U^{6+} in brannerite, through a combination of alteration and metamictisation was proposed by Singh *et al.* [60], according to Equation 1:

$$2U^{4+}Ti_2O_6 \rightarrow 2U^{6+}TiO_5 + 2TiO_2 \quad (1)$$

Equation 1. Oxidation mechanism of U in brannerite, proposed by Singh *et al.* [60]

The observations from the microstructure and composition of the Crocker's Well sample discussed here are consistent with this proposed mechanism: a majority U^{6+} speciation; the U-rich phase displayed evidence of alteration; and the U-rich phase was closely associated with rutile (TiO_2), which was present at all points investigated with µXRD. This mechanism is also consistent with previous work; for example, René *et al.* observed in a sample from the Rožná uranium deposit (Vysočina Region, Czech Republic) the decomposition of brannerite into a TiO_2 rich phase (> 90%), which was determined to contain U^{6+} by EPMA (as discussed above) [8]. The presence of Ti oxides has also been observed by Charalambous *et al.* (who characterised the Ti phase as rutile), Lumpkin *et al.* and Turuani *et al.* [25, 26, 29]. These authors all identified the presence of Ti oxide (characterised as rutile by) grains on the scale of microns [26] and tens of microns [25, 29] in the brannerite phase.

Vance *et al.* collected U L_3-edge XANES and diffuse reflectance spectroscopy (DRS) data from both a metamict brannerite sample from Spain and a heat treated, recrystallised equivalent [9]. Vance *et al.* identified that the edge position of the XANES from the natural sample appeared to be similar to the U^{6+} standard ($CaUO_4$) and concluded that the XANES from the heat-treated brannerite sample, which had a lower edge position, was indicative of a lower U oxidation state of "*just over +4*". However, they also found their DRS data indicated the presence of U^{5+} in both samples, neither spectra presented the green fluorescence characteristic of U^{6+}. It is worth noting that the DRS for synthetic UTi_2O_6 displayed no observable peaks, Vance *et al.* suggested the absence of U^{4+} peaks was due to the U^{4+} site having a centre of inversion which causes electric dipole transitions to be forbidden [9]. While the differences between the XANES and DRS analysis are not discussed in the text, from the discussion it can be inferred that the absence of green fluorescence characteristic of U^{6+} does

not prove or disprove the presence of U^{6+}. In addition, Vance *et al.* do not describe the condition of the metamict brannerite sample, i.e. to what extent, if any the sample had been altered, and unfortunately, no XRD data were included to determine what the thermally treated sample had recrystallised to.

Re-examination of the XANES data presented by Vance *et al.* provides further insight. Firstly, the XANES of the metamict mineral brannerite displays two features, one between 17185 and 17200 eV and a second between 17205 and 17230 eV which are characteristic of uranyl speciation, so the sample clearly contained a majority of U^{6+}, at least some of which is uranyl. Secondly, the XANES collected from the thermally treated sample did not have the same shape or features as the XANES collected from synthetic UTi_2O_6 (the synthetic UTi_2O_6 XANES data is consistent with XANES data presented here measured from synthetic UTi_2O_6) so the two samples clearly do not have the same structure. Therefore, the attempted recrystallisation of the metamict brannerite to the brannerite structure was unsuccessful. This suggests that the metamict brannerite sample was heavily altered, to the extent that recrystallisation to the original brannerite structure was not possible. This supports the supposition of the current study that the U rich phase in the Crocker's Well sample, which contains uranyl U^{6+}, is an altered brannerite, and also supports the mechanism proposed by Singh *et al.* of brannerite alteration that results in U^{4+} oxidation to U^{6+}.

Aside from the work discussed by Vance *et al.*, no other investigation of the effect of radiation-induced amorphisation on U speciation in brannerite has been undertaken, which would be beneficial to elucidating the process of U oxidation in natural brannerite.

Further work could be undertaken to confirm the original mineralogy of the Crocker's well sample, either by determining the composition using EDX, EPMA or laser ablation inductively coupled plasma mass spectrometry (LA-ICP-MS) or by attempting to recrystallise the sample using thermal treatment. However, whether the U-rich phase in the sample was originally brannerite, a crichtonite or another U mineral, it is questionable, given the extent of metamictization and alteration assumed to be required to achieve a majority U^{6+} speciation, if the sample should be classified as that original phase, even with the caveat of being heavily altered. Indeed, attempts to identify the original composition or structure, by compositional

analysis or recrystallisation may not be successful due to the extent of alteration. It is also possible that with further characterisation and re-examination from this perspective, some of the samples identified in previous work as U^{6+} containing altered brannerites would no longer be classified as brannerites.

If the U-phase is altered brannerite or davidite this implies that after alpha recoil damage and alteration, U^{6+} speciation could occur in a synthetic brannerite wasteform, or in certain compositions of Synroc under similar conditions to those experienced by the Crocker's Well sample. However, the hydrothermal event experienced by the Crocker's Well sample was 500 - 650^{o}C, whereas the temperatures experienced by a synthetic wasteform in a deep geological disposal facility will be restricted to 100 - 200^{o}C [61] so the probability of a wasteform containing either brannerite or davidite undergoing hydrothermal alteration is highly unlikely. In addition, µXRF maps only indicated low concentrations of U present in the cracks and surrounding fluorapatite phase, suggesting most U has been retained by the U-rich phase, even while speciated as U^{6+} uranyl. To fully understand the extent to which U has migrated from the U-rich phase the presence of radiogenic Pb in the rim of the U-rich phase and in the surrounding cracks in the apatite phase would require investigation.

5.5. Conclusions

Three phases were identified in the Crocker's well sample using μXRF and μXRD: fluorapatite, rutile and an altered, metamict U-rich phase. The known U minerals to occur at Crocker's Well are brannerite (UTi_2O_6), davidite-(La) ($(La,Ce,Ca)(Y,U)(Ti,Fe)_{20}O_{38}$) and uranothorite ($(Th,U)SiO_4$). The U-rich phase displayed strong evidence of alteration with spatial variations in composition. The speciation of U in the U-rich phase was investigated by U L_3-edge μXANES and μEXAFS at selected points. Analysis of both regions indicated that the majority of U present in the U-rich phase is in a U^{6+} uranyl moiety. Linear combination analysis (LCA) of XANES data determined that the U environment in the U-rich phase was best described by major contributions from $CaUO_4$ and haiweeite, both uranyl reference compounds, and a minor contribution from UO_2. This gave an average estimated net U oxidations state of 5.7.

Analysis of the μXRF, μXRD and μXANES data informed the construction of a fit to describe the structure of the first shell in the U-rich phase, which was then applied and adapted to better fit the μEXAFS data. The structure that best described the EXAFS data used three unique U-O scattering paths: two from haiweeite to represent a uranyl moiety; and one U-O scattering path from UO_2 to represent at U^{4+} contribution. These fits gave estimates of U coordination between 6.4 and 6.46 and U oxidation states between 5.5(1) and 5.7(1). The presence of U^{6+} in an altered, metamict sample would not be inconsistent with some previous analysis of altered brannerite samples.

Previous work characterising altered, metamict U titanate mineral samples, identified as brannerite, does not disprove the possibility of uranyl U^{6+} within an altered, metamict brannerite sample and re-examination of some previous work are supports the characterisation of U^{6+} uranyl in altered brannerite. This shows that when discussing and characterising brannerites care should be taken to determine to what extent a brannerite sample is altered and distinguish between altered and unaltered samples, as the compositions and U speciation are too different for the two types to be conflated.

If the Crocker's Well sample was originally brannerite, the occurrence of hydrothermal alteration at high temperatures and the retention of uranyl U^{6+} by the metamict, altered brannerite are supportive of brannerites candidacy as a wasteform, and the candidacy of multi ceramic wasteforms which contain brannerite phases.

An X-ray fluorescence microprobe beamline enabled the use of multiple complementary spatially resolved techniques, the data from which can be used to: identify regions of interest for further measurements; inform and support the analyses of data from other measurements; and therefore, gain a more extensive understanding of the sample with a greater confidence than could be achieved with the combined application of a bulk measurement of each technique. This suite of techniques is perfectly suited to the characterisation of samples with spatial variations in compositionally, structure and element speciation, such as analogue materials where such investigations are essential for the appraisal of potential wasteforms. This work demonstrates the necessity for further microfocus based studies on the natural analogues of all potential wasteforms.

5.6. Acknowledgments

The authors are grateful to UKRI EPSRC for sponsorship for this research under grant reference EP/R513313/1. CLC is grateful to EPSRC for the award of an Early Career Fellowship under grant reference EP/N017374/1.This research utilised the HADES/MIDAS facility and Henry Royce Institute at the University of Sheffield established with financial support from UKRI EPSRC and BEIS, under grant EP/T011424/1 [62]. We acknowledge the National Synchrotron Light Source II for provision of synchrotron radiation beamtime at beamline 4-BM, a US Department of Energy (DOE) Office of Science User Facility operated for the DOE Office of Science by Brookhaven National Laboratory under Contract No DE-SC0012704.

5.7. References

[1] N.C. Hyatt, Plutonium management policy in the United Kingdom: The need for a dual track strategy, Energy Policy 101 (2017) 303-309.

[2] R.C. Ewing, Long-term storage of spent nuclear fuel, Nat. Mater. 14(3) (2015) 252-257.

[3] J.L. Knight, Use of natural analogues in waste disposal, Interdiscip. Sci. Rev. 23(3) (1998) 233-241.

[4] G.R. Lumpkin, Y. Gao, R. Giere, C.T. Williams, A.N. Mariano, T. Geisler, The role of Th-U minerals in assessing the performance of nuclear waste forms, Mineral. Mag. 78(5) (2014) 1071-1095.

[5] K. Maher, J.R. Bargar, G.E. Brown, Environmental Speciation of Actinides, Inorg. Chem. 52(7) (2013) 3510-3532.

[6] G.R. Choppin, J.-O. Lijenzin, J. Rydberg, Chapter 22 - Behavior of Radionuclides in the Environment, Radiochemistry and Nuclear Chemistry (Third Edition), Butterworth-Heinemann, Woburn, 2002, pp. 642-673.

[7] M. Colella, G.R. Lumpkin, Z. Zhang, E.C. Buck, K.L. Smith, Determination of the uranium valence state in the brannerite structure using EELS, XPS, and EDX, Phys. Chem. Miner. 32(1) (2005) 52-64.

[8] M. Rene, Z. Dolnicek, Uraninite, Coffinite and Brannerite from Shear-Zone Hosted Uranium Deposits of the Bohemian Massif (Central European Variscan Belt), Minerals 7(4) (2017) 17.

[9] E.R. Vance, J.N. Watson, M.L. Carter, R.A. Day, B.D. Begg, Crystal chemistry and stabilization in air of brannerite, UTi_2O_6, J. Am. Ceram. Soc. 84(1) (2001) 141-144.

[10] J.A. Fortner, A.J. Kropf, R.J. Finch, A.J. Bakel, M.C. Hash, D.B. Chamberlain, Crystal chemistry of uranium (V) and plutonium (IV) in a titanate ceramic for disposition of surplus fissile material, J. Nucl. Mater. 304(1) (2002) 56-62.

[11] E.R. Vance, G.R. Lumpkin, M.L. Carter, D.J. Cassidy, C.J. Ball, R.A. Day, B.D. Begg, Incorporation of uranium in zirconolite ($CaZrTi_2O_7$), J. Am. Ceram. Soc. 85(7) (2002) 1853-1859.

[12] A.V. Soldatov, D. Lamoen, M.J. Konstantinovic, S. Van den Berghe, A.C. Scheinost, M. Verwerft, Local structure and oxidation state of uranium in some ternary oxides: X-ray absorption analysis, J. Solid State Chem. 180(1) (2007) 54-61.

[13] M. James, M.L. Carter, Z.M. Zhang, Y.J. Zhang, K.S. Wallwork, M. Avdeev, E.R. Vance, Crystal Chemistry and Structures of (Ca,U) Titanate Pyrochlores, J. Am. Ceram. Soc. 93(10) (2010) 3464-3473.

[14] A.F. Redkin, A.M. Ionov, N.P. Kotova, Hydrothermal synthesis of pyrochlores and their characterization, Phys. Chem. Miner. 40(9) (2013) 733-745.

[15] S.A. McMaster, R. Ram, F. Charalambous, M.I. Pownceby, J. Tardio, S.K. Bhargava, Synthesis and characterisation of the uranium pyrochlore betafite [$(Ca,U)_2(Ti,Nb,Ta)_2O_7$], J. Hazard. Mater. 280 (2014) 478-486.

[16] D.J. Bailey, M.C. Stennett, N.C. Hyatt, Synthesis and Characterization of Brannerite Compositions for MOX Residue Disposal, MRS Adv. 2(10) (2017) 557-562.

[17] D.J. Bailey, M.C. Stennett, B. Ravel, D. Grolimund, N.C. Hyatt, Synthesis and characterisation of brannerite compositions $(U_{0.9}Ce_{0.1})_{1-x}M_xTi_2O_6$ (M = Gd^{3+}, Ca^{2+}) for the immobilisation of MOX residues, RSC Adv. 8(4) (2018) 2092-2099.

[18] S.V. Stefanovsky, S.V. Yudintsev, A.A. Shiryaev, V.Y. Murzin, A.L. Trigub, Phase partitioning and uranium speciation in brannerite-based ceramics, J. Eur. Ceram. Soc. 37(2) (2017) 771-777.

[19] M.C. Dixon Wilkins, L.M. Mottram, E.R. Maddrell, M.C. Stennett, C.L. Corkhill, K.O. Kvashnina, N.C. Hyatt, Synthesis, Characterization, and Crystal Structure of Dominant Uranium(V) Brannerites in the $UTi_{2-x}Al_xO6$ System, Inorg. Chem. 60(23) (2021) 18112-18121.

[20] T. Subramani, J. Baker, H.W. Xu, A. Navrotsky, Synthesis, Characterization, and Enthalpies of Formation of Uranium Substituted Zirconolites, ACS Earth Space Chem. 4(10) (2020) 1878-1887.

[21] L.R. Blackburn, R. Crawford, S.A. Walling, L.J. Gardner, M.R. Cole, S.K. Sun, C. Gausse, A.R. Mason, M.C. Stennett, E.R. Maddrell, N.C. Hyatt, C.L. Corkhill, Influence of accessory phases and surrogate type on accelerated leaching of zirconolite wasteforms, NPJ Mater. Degrad. 5(1) (2021) 11.

[22] M.A. Denecke, Actinide speciation using X-ray absorption fine structure spectroscopy, Coord. Chem. Rev. 250(7-8) (2006) 730-754.

[23] L. Ruperto, P. de Caritat, Geological Review of the Southern Curnamona Region, Cooperative Research Centre for Landscape Environments and Mineral Exploration, 2006.

[24] K.R. Ludwig, J.A. Cooper, Geochronology of Precambrian granites and associated U-Ti-Th mineralization, northern Olary province, South Australia, Contrib. Mineral. Petrol. 86(3) (1984) 298-308.

[25] F.A. Charalambous, R. Ram, M.I. Pownceby, J. Tardio, S.K. Bhargava, Chemical and microstructural characterisation studies on natural and heat treated brannerite samples, Miner. Eng. 39 (2012) 276-288.

[26] M. Turuani, F. Choulet, A. Eglinger, P. Goncalves, J. Machault, J. Mercadier, A.M. Seydoux-Guillaume, S. Reynaud, F. Baron, D. Beaufort, Y. Batonneau, S. Gouy, A. Mesbah, S. Szenknect, N. Dacheux, V. Chapon, M. Pagel, Geochemical fingerprints of brannerite (UTi_2O_6): an integrated study, Mineral. Mag. 84(2) (2020) 313-334.

[27] R. Finch, T. Murakami, Systematics and Paragenesis of Uranium Minerals, Reviews in Mineralogy 38 (1999) 91-179.

[28] J. Foden, M.A. Elburg, J. Dougherty-Page, A. Burtt, The timing and duration of the Delamerian orogeny: Correlation with the Ross Orogen and implications for Gondwana assembly, J. Geol. 114(2) (2006) 189-210.

[29] G.R. Lumpkin, S.H.F. Leung, J. Ferenczy, Chemistry, microstructure, and alpha decay damage of natural brannerite, Chem. Geol. 291 (2012) 55-68.

[30] J. Foden, M. Elburg, S. Turner, C. Clark, M.L. Blades, G. Cox, A.S. Collins, K. Wolff, C. George, Cambro-Ordovician magmatism in the Delamerian orogeny: Implications for tectonic development of the southern Gondwanan margin, Gondwana Res. 81 (2020) 490-521.

[31] D. Malczewski, A. Grabias, M. Dziurowicz, Activation energy of annealed, partially metamict davidite by Fe-57 Mossbauer spectroscopy, J Geosci. 65(1) (2020) 37-44.

[32] Y.S. Chu, W.-K. Lee, R. Tappero, M. Ge, X. Huang, X. Xiao, H. Yan, P. Northrup, J. Thieme, A.M. Kiss, G.J. Williams, Y. Yang, S.L. Nicholas, A. Pattammattel, R. Smith, P. Ilinski, Y. Du, Multimodal, Multidimensional, and Multiscale X-ray Imaging at the National Synchrotron Light Source II, Synchrotron Radiation News 33(3) (2020) 29-36.

[33] B. Ravel, M. Newville, ATHENA, ARTEMIS, HEPHAESTUS: data analysis for X-ray absorption spectroscopy using IFEFFIT, J. Synchrot. Radiat. 12 (2005) 537-541.

[34] L. Desgranges, G. Baldinozzi, G. Rousseau, J.C. Niepce, G. Calvarin, Neutron Diffraction Study of the in Situ Oxidation of UO_2, Inorg. Chem. 48(16) (2009) 7585-7592.

[35] J. Plášil, K. Fejfarová, J. Čejka, M. Dušek, R.Š. Škoda, J. Sejkora, Revision of the crystal structure and chemical formula of haiweeite, $Ca(UO_2)_2(Si_5O_{12})(OH)_2 \cdot 6H_2O$, Am. Miner. 98(4) (2013) 718-723.

[36] J.T. Szymanski, J.D. Scott, A crystal-structure refinement of synthetic brannerite, UTi_2O_6, and its bearing on rate of alkaline-carbonate leaching of brannerite in ore., Can. Mineral. 20(MAY) (1982) 271-280.

[37] M. Newville, Larch: An Analysis Package for XAFS and Related Spectroscopies, 15th International Conference on X-Ray Absorption Fine Structure (XAFS), Iop Publishing Ltd, Beijing, PEOPLES R CHINA, 2012.

[38] D.D. Syverson, B. Etschmann, W.H. Liu, R. Ram, Y. Mei, T. Lanzirotti, J. Mercadier, J. Brugger, Oxidation state and coordination environment of Pb in U-bearing minerals, Geochimica Et Cosmochimica Acta 265 (2019) 109-131.

[39] J.W. Anthony, R.A. Bideaux, K.W. Bladh, M.C. Nichols, Handbook of Mineralogy. http://www.handbookofmineralogy.org/. (Accessed 05.09.2020 2020).

[40] B.M. Gatehouse, I.E. Grey, P.R. Kelly, The crystal structure of davidite, Am. Miner. 64(9-10) (1979) 1010-1017.

[41] M. James, J.N. Watson, The synthesis and crystal structure of doped uranium brannerite phases $U_{1-x}M_xTi_2O_6$ (M=Ca^{2+}, La^{3+}, and Gd^{3+}), J. Solid State Chem. 165(2) (2002) 261-265.

[42] M. James, M.L. Carter, J.N. Watson, The synthesis, crystal chemistry and structures of Y-doped brannerite ($U_{1-x}Y_xTi_2O_6$) and thorutite ($Th_{1-x}Y_xTi_2O_6$-delta) phases, J. Solid State Chem. 174(2) (2003) 329-333.

[43] D.J. Bailey, M.C. Stennett, N.C. Hyatt, Synthesis and characterization of brannerite wasteforms for the immobilization of mixed oxide fuel residues, Atalante 2016 International Conference on Nuclear Chemistry for Sustainable Fuel Cycles 21 (2016) 371-377.

[44] D.J. Bailey, M.C. Stennett, S.K. Sun, L.J. Gardner, S.A. Walling, C.L. Corkhill, B. Ravel, N.C. Hyatt, Iop, Ce and U speciation in wasteforms for thermal treatment of plutonium bearing wastes, probed

by L_3 edge XANES, THERAMIN Conference - Thermal Treatment of Radioactive Waste, Iop Publishing Ltd, Mech Inst, Manchester, England, 2020.

[45] S. Calvin, XAFS for Everyone, Taylor and Francis, Boca Raton, 2013.

[46] O.C. Gagne, Bond-length distributions for ions bonded to oxygen: results for the lanthanides and actinides and discussion of the f-block contraction, Acta Crystallogr. Sect. B-Struct. Sci.Cryst. Eng. Mat. 74 (2018) 49-62.

[47] F. Clifford, Systematic mineralogy of uranium and thorium, Geological Survey Bulletin 1064, Geological survey, U.S. Government, Washington, U.S.A., 1958.

[48] G.R. Lumpkin, M.G. Blackford, M. Colella, Chemistry and radiation effects of davidite, Am. Miner. 98(1) (2013) 275-278.

[49] W.L. Gong, R.C. Ewing, L.M. Wang, H.S. Xie, Crichtonite Structure Type ($AM_{21}O_{38}$ and $A_2M_{19}O_{36}$) as a Host Phase in Crystalline Waste Form Ceramics, 18th International Symposium on the Scientific Basis for Nuclear Waste Management, Materials Research Soc, Kyoto, Japan, 1994, pp. 807-815.

[50] I.E. Grey, D.J. Lloyd, J.S. White, The structure of crichtonite and its relationship to senaite, Am. Miner. 61(11-1) (1976) 1203-1212.

[51] R.J. Lauf, Minerology of Uranium and Thorium, Schiffer Publishing2016, pp. 291-293.

[52] P.R. Kelly, I.H. Campbell, I.E. Grey, B.M. Gatehouse, Additional data on loveringite (Ca,REE)$(Ti,Fe,Cr)_{21}O_{38}$ and mohsite discredited, Can. Mineral. 17 (1979) 635-638.

[53] G.R. Lumpkin, K.L. Smith, M.G. Blackford, Partitioning of uranium and rare earth elements in synroc: effect of impurities, metal additive, and waste loading, J. Nucl. Mater. 224(1) (1995) 31-42.

[54] A. Mesbah, S. Szenknect, N. Clavier, H.T. Lin, F. Baron, D. Beaufort, Y. Batonneau, J. Mercadier, A. Eglinger, M. Turuani, P. Goncalves, F. Choulet, V. Chapon, A.M. Seydoux-Guillaume, M. Pagel, N. Dacheux, Direct synthesis of pure brannerite UTi_2O_6, J. Nucl. Mater. 515 (2019) 401-406.

[55] R. Gilligan, A.N. Nikoloski, The process chemistry and mineralogy of brannerite leaching, J. S. Afr. Inst. Min. Metall. 117(8) (2017) 765-770.

[56] F.A. Charalambous, R. Ram, S. McMaster, M.I. Pownceby, J. Tardio, S.K. Bhargava, Leaching behaviour of natural and heat-treated brannerite-containing uranium ores in sulphate solutions with iron(III), Miner. Eng. 57 (2014) 25-35.

[57] S.K. Roberts, W.L. Bourcier, H.F. Shaw, Aqueous dissolution kinetics of pyrochlore, zirconolite and brannerite at 25, 50, and 75 degrees C, Radiochim. Acta 88(9-11) (2000) 539-543.

[58] Y. Zhang, G.R. Lumpkin, H. Li, M.G. Blackford, M. Colella, M.L. Carter, E.R. Vance, Recrystallisation of amorphous natural brannerite through annealing: The effect of radiation damage on the chemical durability of brannerite, J. Nucl. Mater. 350(3) (2006) 293-300.

[59] M.C. Dixon Wilkins, 2023.

[60] K. Singh, L. Bhargava, M. Ali, B. Swarnkar, An unusual brannerite from Tai, Arunachal Pradesh, India, Exploration and Research for Atomic Minerals (1990) 117-122.

[61] Radioactive Waste Management, Geological Disposal: Generic Disposal Facility Design, Nuclear Decommissioning Authority, 2016.

[62] N.C. Hyatt, C.L. Corkhill, M.C. Stennett, R.J. Hand, L.J. Gardner, C.L. Thorpe, The HADES facility for high activity decommissioning engineering & science: Part of the UK national nuclear user facility, IOP Conference Proceedings: Materials Science and Engineering 818 (2020) 012022.

6. Direct characterisation of a 1 billion-year old pentavalent uranium mineral

L. M. Mottram[1], L. T. Townsend[1], L. J. Gardner[1], K. Kvashnina[2,3], J. F. W. Mosselmans[4], M. C. Stennett[1], N. C. Hyatt[1] and C. L. Corkhill[1*]

[1]NucleUS Immobilisation Science Laboratory, Department of Materials Science and Engineering, University of Sheffield, S1 3JD, UK
[2]Helmholtz-Zentrum Dresden-Rossendorf (HZDR), Institute of Resource Ecology, PO Box 510119, 01314, Dresden
[3]The Rossendorf Beamline at ESRF – The European Synchrotron, CS40220, 38043 Grenoble Cedex 9, France
[4]Diamond Light Source, Harwell Science and Innovation Campus, Didcot, UK

Abstract

Historically, it was believed that uranium (U) does not naturally occur as U^{5+}, and the presence of any U^{5+} in minerals was attributed to weathering of U^{4+} minerals or as a result of auto-oxidation caused by radiogenic lead (Pb*). Here, we present the first direct measurement of U^{5+} speciation within a pyrochlore mineral sample from MacDonald Mine, Ontario, Canada. Uranium L_3- and U M_4-edge X-ray absorption spectroscopy, utilising a variety of data analysis techniques, were applied to characterise U speciation, which revealed that the mineral contained all three key U oxidation states (U^{4+}, U^{5+} and U^{6+}) with the majority (39%) attributed to U^{5+}. The mineral has an estimated age of 1.0 billion years old, with the U^{5+} component likely being present throughout the lifetime of the mineral. The presence of U^{5+}, within a pyrochlore structured mineral provides significant, long-term insight into the viability of potential future wasteforms for the disposal of radioactive waste.

6.1. Introduction

Formerly it was understood that U occurs in minerals only as U^{4+} or U^{6+} [1-3], and the occurrence of a mixed U speciation was rare [4]. To date, only four claimed U^{5+} minerals: wyartite ($Ca(CO_3)[U^{5+}(U^{6+}O_2)_2O_4(OH)](H_2O)_7$) [4]; shinkolobweite ($Pb_{1.25}[U^{5+}(H_2O)_2(U^{6+}O_2)_5O_8(OH)_2](H_2O)_5$) [5]; richetite ($Fe_{0.5}Pb_5[U^{5+}(U^{6+}O_2)_{17}O_{18}(OH)_{14}](H_2O)_{\sim 19.5}$) [6]; and nollomotzite ($Mg[U^{5+}(U^{6+}O_2)_2F_3O_4](H_2O)_4$) [7] have been verified. These minerals were all characterised by indirect crystallographic methods as containing U^{5+}. Pentavalent U has also been reported in meta-autunite ($Ca(U^{6+}O_2)_{2-x}(U^{5+}O_2)_x(H_3O^+)(PO_4)_2(6-x)H_2O$) [8] where electron paramagnetic resonance (EPR) and analysis of high temperature XRD data were applied to characterise the sample; however, this claim is disputed [9, 10]. Another reported occurrence of U^{5+} is in a U-rich hematite sample ($(Fe_{1.982}U_{0.014}Pb_{0.005})_2O_3$) [11] which was investigated by U L_3-edge X-ray absorption spectroscopy (XAS) [11] but, as is demonstrated and discussed in this work, the analysis of U L_3-edge XAS data alone is not adequate evidence to conclusively prove the presence of U^{5+}.

The occurrence of U minerals and their speciation is of particular relevance to strategies for radioactive waste disposal; for example, U-containing spent nuclear fuel, or Pu-bearing wastes, may be disposed of in a deep geological disposal facility. In such an environment, the release of U/Pu to the geo- and bio-sphere will be controlled by the dissolution of the waste by groundwater. As such, highly durable wasteforms are required.

The chemical speciation has a strong influence on the environmental mobility of any given actinide; for example, U^{6+} is highly mobile while U^{4+} is insoluble [12]. Therefore, synthetic wasteforms for U are designed to target U^{4+} speciation, with titanate minerals including brannerite (UTi_2O_6)[13-17], perovskite ($CaTiO_3$)[13, 15, 18], zirconolite ($CaZrTi_2O_7$)[13, 19-25] and oxide pyrochlores (a variety of compositions with the formula $A_2B_2O_7$ including those where A = Na, Ca, U, Th, Pu, Gd and B = Ti, Nb, Ta, Hf)[13, 15, 26] all being promising candidates. Importantly, all of these minerals have naturally occurring analogues that contain U and Th,[18] which range in age from 16 to 4400 million years [27, 28], providing confidence that they are long-lived, with a high aqueous durability and resistance to radiation damage. Indeed, many naturally occurring U-minerals are metamict (amorphous) as a result of self-

irradiation by alpha particles – yet, they retain their actinide inventory and remain resistant to degradation [29-31]. Determining the speciation of actinides in these natural analogues, within the context of the geochronology of the sample, is crucial to predicting and optimising the behaviour of synthetic wasteform materials over the timescales required for radioactive waste disposal (~100,000 years).

U-containing natural analogues for synthetic wasteforms are found in numerous geological localities, including the MacDonald Mine in Monteagle, Ontario, Canada, which is the focus of the present research. This region is well known as the origin of the first sample of 'ellsworthite', [32, 33] a U-containing mineral in the pyrochlore super-group, whose nomenclature was superseded by 'uranopyrochlore' $(Ca,U,Ce)_2(Nb,Ti,Ta)_2O_6(OH,F)$ [34, 35]'. Minerals of the pyrochlore super-group possess the structure $A_{2-m}B_2X_{6-w}Y_{1-n}$ ($Fd\bar{3}m$), [36] which consists, in its idealised form, of corner sharing BX_6 octahedra with A-site cations in the interstitials [37]. Pyrochlore super-group minerals are differentiated by both the dominant B-site valence and dominant cation concentration on the B site [38]. Groups include betafite, pyrochlore, roméite, microlite and elsmoreite, which have dominant B-site cations of Ti^{4+}, Nb^{5+}, Sb^{5+}, Ta^{5+} and W^{6+}, respectively; species are further distinguished by the dominant A site and Y site occupants (see **Chapter 2**).

The MacDonald Mine is in the Bancroft domain of the Central Metasedimentary belt in the south of the Grenville Orogen [39]. The mine is sited on a well segmented granite pegmatite dike, in which U-bearing minerals commonly occur in feldspar or calcite ($CaCO_3$) [40]. Lumpkin *et al.* assigned an age of 1 billion years to betafites and 'uranopyrochlores' from this locality [28], while U-Pb ages of titanites ($CaTiSiO_5$) from the Bancroft domain in close proximity to the MacDonald Mine locality were dated to the range of 1.043 to 1.060 billion years old [41].

In this work, we applied a suite of X-ray absorption spectroscopy (XAS) techniques as a unique and sensitive toolkit to directly characterise the speciation of low concentration elements in environmental samples. Furthering previous attempts to define speciation of U in minerals, we here specifically determine the presence and relative concentration of not only U^{4+} and U^{6+} in the MacDonald Mine sample, but also U^{5+}. Most importantly we utilised high energy resolution fluorescence detected (HERFD) U M_4-edge M_β XAS, which is the only XAS-based

technique that can confirm the presence of U^{5+} and enable the deconvolution of mixed U oxidation states [42, 43]. To further investigate the speciation of U within analogue samples, the extended X-ray absorption fine structure (EXAFS) was analysed, providing insight into the local U coordination environment [44-47], corroborating the presence of U^{5+} within the MacDonald Mine sample. Results from this work challenge the established preconception that U^{5+} is not an environmentally relevant U oxidation state and provides significant insight into future radioactive waste disposal and U mining techniques that may be employed.

6.2. Results

6.2.1. Characterisation of the partially-metamict, partially-altered MacDonald Mine sample

The main U-bearing phase (Fig. 1a) was identified as a pyrochlore. The majority of the sample was confirmed to be metamict by the diffuse scattering (i.e. there was no long range order) centred between 20° < 2θ < 40° in the XRD pattern (Fig. 1b). Low intensity reflections located at 29.9° (222) and 49.5° (440) were attributed to a pyrochlore structure (ICSD no. 72206 [48]). with observed reflections were attributed to a pyrochlore structure. The positions of these reflections gave d spacing values of 2.99 Å and 1.83 Å respectively, giving an estimated cell parameter of a = 10.3 Å, similar to that of a crystalline hydroxycalciopyrochlore, $(Ca_{0.73}Na_{0.57}U_{0.4}Ce_{0.05}Fe_{0.02}Y_{0.01}\square_{0.22})(Nb_{1.14}Ti_{0.79}Ta_{0.03}Al_{0.01}Mg_{0.01})O_{6.2}((OH)_{1.01}F_{0.09})$, [49] which had a unit cell parameter of a = 10.381(4), an oxycalciobetafite $(Ca_{1.29}Na_{0.18}U_{0.50}Ce_{0.03})(Ti_{1.09}Nb_{0.79}Zr_{0.14}F_{e0.04}Ta_{0.01})O_6(O_{0.98}F_{0.02})$ which had a unit cell parameter of a = 10.263(1) Å [50] and a possible oxyuranobetafite $(Ca_{0.46}U_{0.42}Fe_{0.11}Ba_{0.03}Pb_{0.02})(Nb_{1.1}Ti_{0.88}Ta_{0.02})O_{6.0}F_{0.04}\cdot 2.3H_2O$, which had a unit cell parameter a = 10.344(5) Å [51]. Synthetic $Ca_2Nb_2O_7$ and $Ca_{0.92}U_{1.08}Ti_2O_7$ have unit cell parameters of a = 10.444 [48] and 10.1579(5), [52] respectively.

EPMA analysis of this phase (Table 6.SI.1) produced an estimated composition of $(Na_{0.11}Ca_{1.02}Mn_{0.01}Fe_{0.08}Sr_{0.02}Ce_{0.01}Pb_{0.06}U_{0.30})(Al_{0.01}Ti_{0.88}Nb_{1.05}Ta_{0.05}W_{0.02})(O_{5.06}F_{0.10})$, identifying Ca as the dominant A-site cation and Nb as the dominant B-site cation. Under the classification system outlined by Atencio *et al.* [38], this established the phase as a calciopyrochlore. EDX data confirmed the presence of U in the sample (Fig 1c and 1d). The X and Y sites both appear to contain a significant fraction of vacancies, so this particular sample could be the first evidenced example of a kenocalciopyrochlore; there are currently only verified calciopyrochlore samples where the majority of Y sites = OH^- [49], F^- [53] and O_2^- [54, 55]. Other possible Y site occupiers include H_2O, K, Rb and Cs [38]. Only trace amounts of K and Cs were measured, and Rb was below the detection limits (Table 6.SI.1).

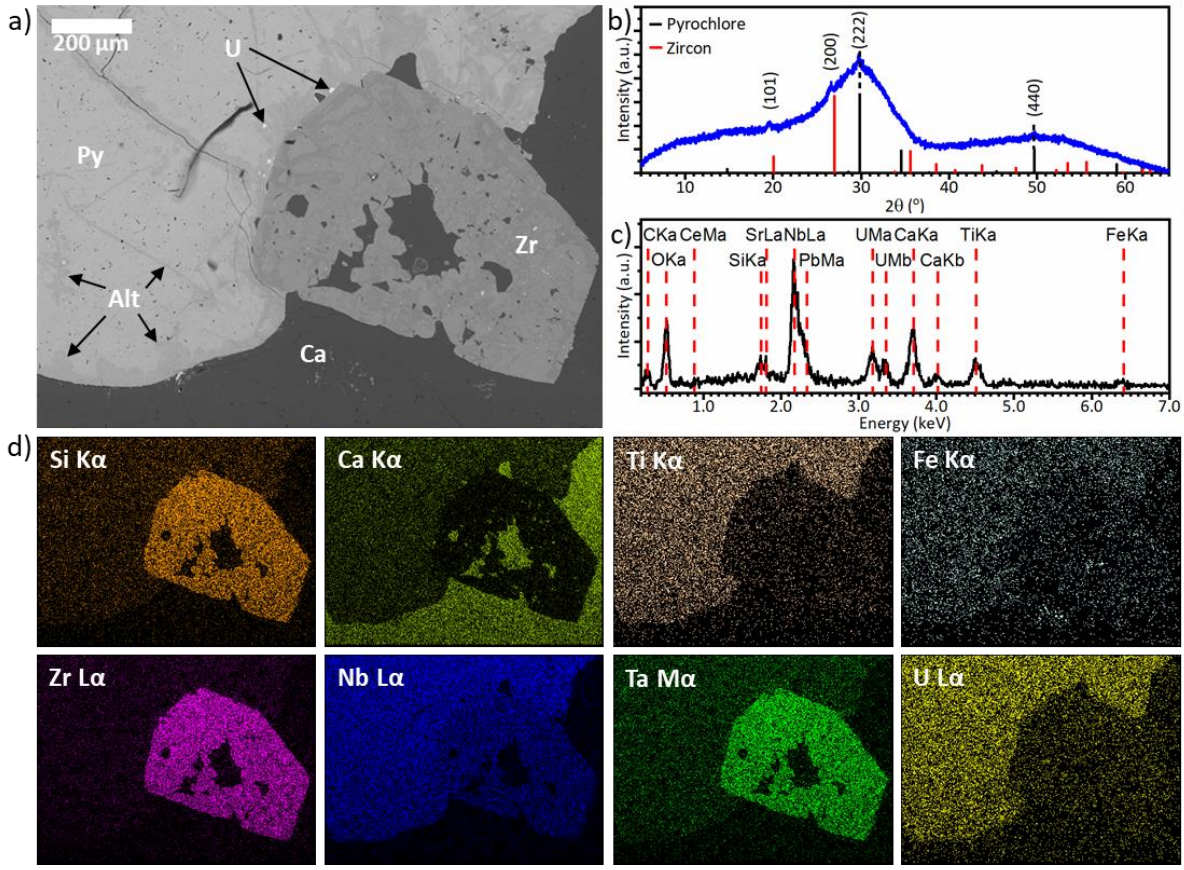

Figure 6.1. Microscopy and diffraction analysis of the MacDonald Mine calciopyrochlore mineral. Showing **(a)** BSE image with calcite (Ca), calciopyrochlore (Py), unidentified U rich phase (U) and zircon (Zr) phases indicated, as well as altered regions within the calciopyrochlore grain (Alt); **(b)** bulk XRD pattern collected from the MacDonald Mine sample, reflections were attributed as indicated to a pyrochlore structure with the composition ($Ca_2Nb_2O_7$), ICSD no. 72206 [48] and zircon, ICSD no. 9582 [56]; **(c)** an EDX spectrum collected from the unaltered region of the calciopyrochlore grain and; d) EDX element maps.

The high fraction of vacancies in the Y site could be indicative that the bulk of the calciopyrochlore phase has undergone alteration. Indeed, backscatter electron (BSE) imaging of the calciopyrochlore grain shows a distinct altered region present at the rim of the grain and in narrow channels in several places throughout the grain (Fig 1a). These altered regions, ranging between 5 – 60 µm in thickness, are thought to be secondary alteration, possibly caused by weathering, as they appear similar to those observed in samples from the Silver

Crater Mine (Bancroft, Ontario, Canada) by Lumpkin and Ewing [57]. Moreover, given that there are few A site vacancies (0.39 per formula unit), a high Ca and Na concentration on the A site, low concentrations of Sr, Ba and K, in addition to the fact that the sample is brown-yellow in colour, the observed alteration is thought to extend only to the rim and fractured regions, and not throughout the bulk. These features are entirely inconsistent with primary and transition alteration previously observed by Lumpkin and Ewing in two MacDonald Mine samples and in other samples from granitic pegmatites [58]. Therefore, we take the bulk of the calciopyrochlore phase to be unaltered. The presence of calcite ($CaCO_3$) (SI Fig. 1) and zircon ($ZrSiO_4$) (Fig. 1b), which are known accessory minerals of 'ellsworthite' at this locality [59] were also identified, with the latter identified by reflections located at 19.5°, 26.5° 2θ (ICSD no. 92740, Fig. 1b). In the BSE image of the sample (Fig. 1a), a bright U-rich phase is indicated, thought to be uraninite, which we were unable to identify as the concentration was either too low to detect by XRD, or is also metamict.

6.2.2. Presence of U^{5+} determined by analysis of U X-ray absorption near edge structure

A variety of XAS techniques were applied in combination to characterise the speciation of U and short-range structure in the calciopyrochlore. The techniques used were U L_3-edge transmission XAS, U L_3-edge $L_{1\alpha}$ HERFD XAS and M_4-edge M_β HERFD XAS, with each technique providing unique insight into the local speciation of U in the mineral sample. As these are all bulk techniques the results are representative of U in the calciopyrochlore, the U-rich phase and any other U-containing phases not identified. Estimates of the amounts of U^{4+}, U^{5+}, and U^{6+} present were obtained from both linear combination fitting (LCF) (Fig. 2a and 2b) and iterative target transformation factor analysis (ITTFA) of the U L_3-edge transmission and $L_{1\alpha}$ HERFD X-ray absorption near edge structure (XANES) region (Table 6.1). From these techniques, approximations of the net U speciation were calculated, with all analyses indicating that the net oxidation state was between +4.6 and +5.0.

For both the transmission and HERFD U L_3-edge XANES data, which is more sensitive to changes in the local atomic structure, regardless of the standards selected by the LCF and ITTFA analyses all estimates yielded a major weighted contribution from U^{4+} (32.4(5)% -

40.1(23)%, Table 6.1). Despite the discrepancies in the attributions of individual components (28.0(13)% to 59.9(5)% and 0.0(0)% to 35.1(14)% for U^{5+} and U^{6+}, respectively), all net U speciation estimates from LCF and ITTFA analyses of U L_3-edge XANES and U L_3-edge $L_{\alpha1}$ HERFD XANES were in good agreement, with a net oxidation state ranging between +4.60(4) and +4.98(6), indicating that U in the calciopyrochlore is partially oxidised. The significant weighting of a U^{5+} contribution in all of the U L_3-edge analyses suggests that U^{5+} is present in the sample. However, due to the linear shift in edge position (17169.9 to 17172.2 eV) at the U L_3-edge with U speciation (as shown in Fig. 2a and 2b), only the net U oxidation state of the bulk sample can be construed from the U L_3-edge XANES, i.e., these results show the presence of U^{4+} with either one of U^{5+} or U^{6+}, or both.

To resolve the presence of U^{5+}, LCF and ITTFA analyses of the U M_4-edge M_β HERFD, which has wider energy separation between the signal arising from U valence electrons, was performed. These data (Table 6.1) confirm the presence of U^{4+}, U^{5+} and U^{6+}, with a major contribution from U^{5+}, within the sample. Comparison of the spectra with the reference compounds, UTi_2O_6, $USbO_5$ and UO_3 (Figure 6.2c) shows that the features associated with each U species are sharp and distinct. Therefore, the presence of different U species in a mixed U oxidation state sample can be directly observed and the relative concentration of each species approximated.

In the HERFD U M_4-edge M_β XANES spectrum (Figure 6.2c) features consistent U^{4+} (3725.17 eV), U^{5+} (3726.20 eV) and U^{6+} (3726.75 eV) were identified, confirming a mixture of all three oxidation states exists within the calciopyrochlore mineral. Comparison of the weighted contributions of each U species, determined by LCF and ITTFA analyses of the HERFD U M_4-edge M_β XANES data (Table 6.1), showed good agreement between methods, with U^{4+}, U^{5+}, and U^{6+} weighted contributions of 25.2(8)% - 27.5(5)%, 40.4(17) - 38.0(11)%, and 34.4(9)% and 34.4(14)%, respectively. As such, the estimates of U net speciation determined by each method, of 5.09(7) and 5.07(5) for LCF and ITTFA, respectively, were similar. This analysis confirms that U^{5+} exists within the calciopyrochlore sample and that the net U^{5+} speciation observed in the U L_3-edge data is not merely indicative of equal amounts of U^{4+} and U^{6+}. Our analysis also strongly suggests that a major portion of U present in the sample occurs as U^{5+}.

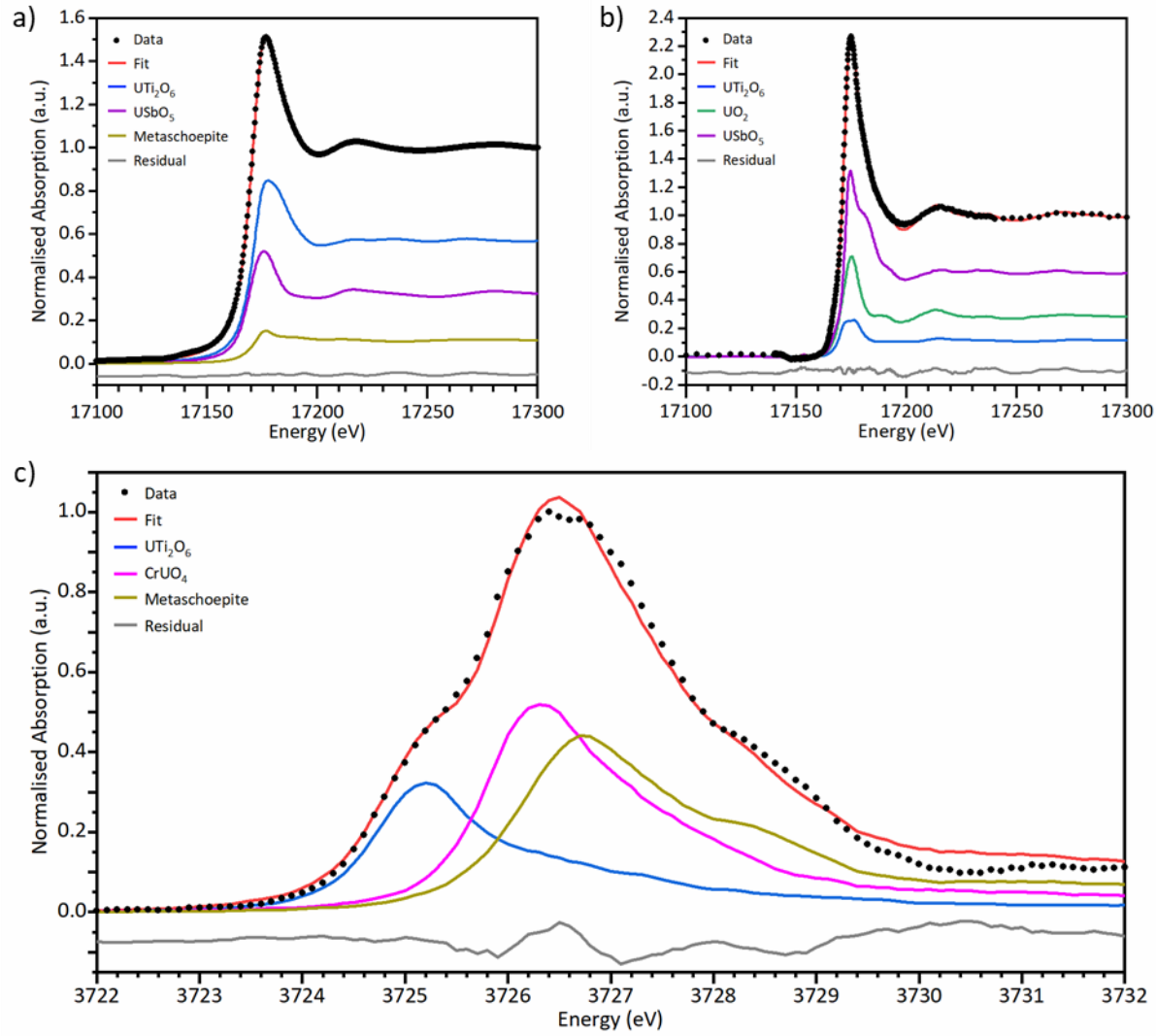

Figure 6.2. X-ray Absorption Near-Edge Spectroscopy analysis of the MacDonald Mine calciopyrochlore mineral. Showing linear combination fits of: **(a)** U L_3-edge transmission XANES; **(b)** U L_3-edge $L_{\alpha 1}$ HERFD XANES; and **(c)** U M_4-edge M_β HERFD XANES using XANES data from reference compounds $U^{4+}Ti_2O_6$, $U^{4+}O_2$, $CrU^{5+}O_4$, $U^{5+}SbO_5$ and metaschoepite ($(U^{6+}O_2)_8O_2(OH)_{12} \cdot 10H_2O$).

Table 6.1. Summary of U speciation analysis determined by X-ray absorption spectroscopy. Showing the estimated oxidation state from EXAFS bond valence sum (BVS) calculations, linear combination fitting (LCF) and iterative target transformation factor analysis (ITTFA), in addition to the relative weightings of different reference compounds used in the analysis.

Absorption Edge or Transition	Data and analysis type	Reference compound normalised weighting (%)					R factor (x100)	Estimated oxidation state
		$U^{(4+)}Ti_2O_6$	$U^{(4+)}O_2$	$CrU^{(5+)}O_4$	$U^{(5+)}SbO_5$	Metaschoepite $((U^{(6+)}O_2)_8O_2(OH)_{12}\cdot 10H_2O)$		
L_3	XANES LCF	32.4(5)	-	-	56.8(5)	10.9(5)	0.0054	4.79(3)
L_3	XANES ITTFA	35.3(9)	-	48.4(21)	-	16.3(21)	0.0055	4.81(10)
L_3	EXAFS BVS	-	-	-	-	-	0.0141	4.72(14)
L_3 L_{α_1}	XANES LCF	11.5 (10)	28.6(13)	-	59.9(5)	-	0.063	4.60(4)
L_3 L_{α_1}	XANES ITTFA	36.9(10)	-	28.0(13)	-	35.1(14)	0.057	4.98(6)
M_4 M_β	XANES LCF	25.2(8)	-	40.4(17)	-	34.4(14)	0.71	5.09(7)
M_4 M_β	XANES ITTFA	27.5(10)	-	38.0(5)	-	34.4(9)	0.22	5.07(5)

6.2.3. Elucidating the short-range structure from the extended X-ray absorption fine structure region

To gain further insight of the U local environment, the short-range order and coordination environment of the calciopyrochlore were investigated through fitting of the EXAFS region of the U L_3-edge transmission data (Figure 6.3, Table 6.2). The metamict nature of the sample made fitting difficult and so only the first two shells could be modelled.

The successful fit (R factor = 0.0141) (Table 6.2) of the EXAFS data was achieved using a modified pyrochlore structure, with the addition of a Nb scatterer (for full details of the EXAFS fitting see the Supplementary Information). The fit required a minimum of three U-O backscattering paths. The U-O1 path (R = 1.96(3) Å) is at a distance in the range of previously observed U^{5+} O_1 paths distances [60], corroborating the aforementioned XANES determination of U as a pentavalent species. However, this U-O1 path cannot be solely attributed to U^{5+} as the three U-O paths are merely a simplified representation of a multiple different U environments, but it is required in the fit and is indicative of a significant contribution from U^{5+}. The U-O3 path (R = 2.38(4) Å) is also within the range of previously observed U^{5+}-O_2 paths distances; [60] although it should be noted that path lengths of other U-O backscatters in likely sources of different U species such as uraninite and equatorial U-O paths in U^{6+} uranyl are similar and therefore difficult to distinguish. The successful adaptation of the pyrochlore structure in the fit, including the use of U-Ca and U-Nb paths, is good evidence that the U in the sample is present in a pyrochlore-like structure. In addition, the O1 and O3 path lengths (1.96(3) and 2.38(4) Å) are in agreement with estimates of bond lengths from a previous study (1.95 and 2.37 Å) that performed preliminary analysis of EXAFS data from a metamict sample with a composition that would now be classified as a calciopyrochlore ($(Ca_{0.46}U_{0.42}Fe_{0.11}Ba_{0.03}Pb_{0.02})(Nb_{1.1}Ti_{0.88}Ta_{0.02})O_{6.0}F_{0.04}\cdot 2.3H_2O$) [51].

To further reinforce the legitimacy of the EXAFS fitting models, a bond valence sum (BVS) was calculated for U in the fit (Table 6.2) which gave an estimated net U oxidation state of 4.72(14). This is in good agreement with the previous estimates calculated from ITTFA and LCF, giving greater confidence to the validity of the EXAFS fit.

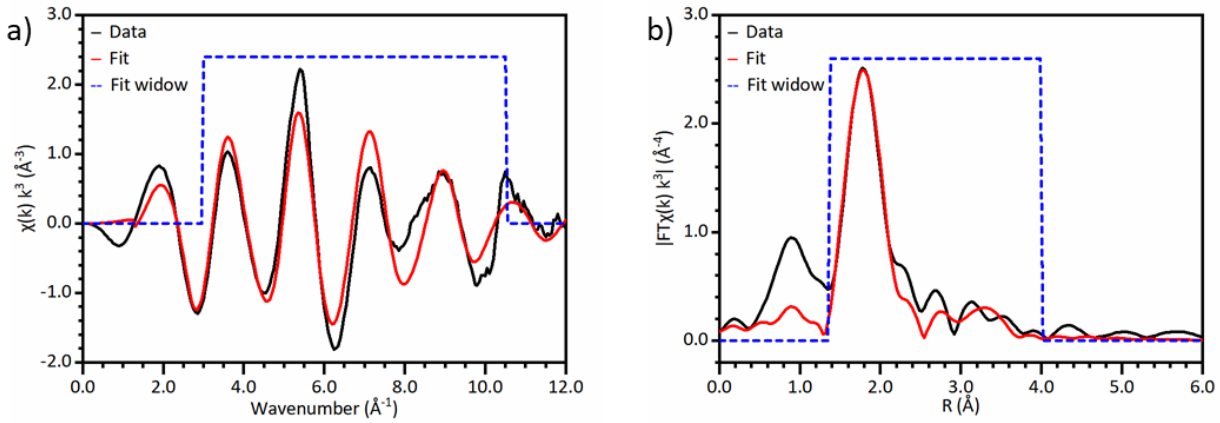

Figure 6.3. Fits of U L_3-edge EXAFS data from the MacDonald Mine calciopyrochlore. Showing **(a)** k^3-weighted EXAFS, **(b)** Fourier transform of k^3-weighted EXAFS using a Hanning window function. Black lines are data, red lines are the best modelled fits for the data, blue dashed lines show fitting windows.

Table 6.2. Fitting parameters for the best fit EXAFS model of the MacDonald Mine calciopyrochlore data. The amplitude reduction factor (S_2^0) was set to 0.84 for all paths. The shift in E_0 was constrained to be the same for all paths and was refined to be 6.4(15). The R-factor of the fit was 0.0141. *CN* is the degeneracy of the given path, *R* is the interatomic distance between U and the backscatterer (given in the path column), σ^2 is the Debye-Waller factor and V_i is the individual valence of the scattering path. * or † indicates the parameters were constrained to have the same variables. The BVS, as calculated from the summation of the V_i contributions from O1, O2, and O3, was found to be 4.72(14) (Table 6.1).

Path	CN	R (Å)	σ^2 (Å^{-2})	V_i
U-O1	1.3	1.96(3)	0.014(5)*	1.37(10)
U-O2	2.7	2.27(3)	0.009(3)	0.60(5)
U-O3	3.0	2.38(4)	0.014(5)*	0.45(5)
U-Ca	1.7	3.57(5)	0.019(6)†	–
U-Nb	2.4	3.52(5)	0.019(6)†	–

6.3. Discussion

The XAS data and analyses presented in this work are the first *direct* measurement of U^{5+} in a non-transient mineral sample, and, as such, a step change in the understanding of long-term chemical behaviour of uranium geochemistry is established. All of the U^{5+} containing minerals previously confirmed by crystallographic methods [4-7] also contained a higher concentration of U^{6+} (ratios of U^{5+}:U^{6+} varying from 1:2 – 1:17) than found in the present study and did not contain U^{4+}. The presence of minimal U^{5+} in these mineral samples and the very few number of U^{5+} containing minerals, had suggested that U^{5+} was unstable, and that the majority of any U^{5+} which occurred in minerals during formation or by the oxidation of U^{4+} had oxidised to U^{6+}. Here, the MacDonald Mine calciopyrochlore has been shown to be the first U mineral found to contain three U oxidation states, and the first with an apparent majority of U present occurring as 5+ with a ratio ca. 1:1.5:1.25 of U^{4+}:U^{5+}:U^{6+}.

The presence of previously characterised U^{5+} minerals has been attributed to the weathering (alteration) of uraninite [4, 6] and formation by solid state precipitation under partially reducing conditions [7]. Although alteration was observed in the calciopyrochlore examined in this work, it was confined to a narrow band around the rim of the mineral and in narrow veinlets, both of which are highly unlikely to be sufficient to produce the high fractions of U^{5+} and U^{6+} determined by XANES analysis. Another theorised cause of U^{5+} speciation in U minerals is auto-oxidation of U by radiogenic lead (Pb*). Lead is the final decay product of the ^{235}U, ^{238}U and Th decay chains (^{206}Pb, ^{207}Pb and Pb^{208} respectively) and is produced as Pb^{4+}, so a reduction of Pb^{4+} to Pb^{2+} or Pb^{0} with oxidation of U^{4+} to U^{5+} or U^{6+} could occur. However, even assuming all of the radiogenic Pb^{4+} produced in our sample (we estimate that 14% of the original U content would have decayed to radiogenic Pb, see methods for detail of calculation) was reduced to Pb^{0}, this would not be sufficient to account for the presence of the determined concentrations of U^{5+} (34% original U) and U^{6+} (30% original U). Moreover, recent work on the speciation of Pb in similar mineral samples found that all Pb was present as Pb^{2+} [61], further increasing our confidence that the U^{5+} in the MacDonald Mine cannot solely be the product of radiogenic Pb reduction. As such, it must be the case that at least some, and likely the majority, of the U^{5+} present in the calciopyrochlore is naturally occurring, and therefore has persisted in the mineral since formation, for a billion years.

The occurrence of U^{5+} may simply be a product of the A and B site occupancy in the calciopyrochlore phase. Attempts to target U^{5+} speciation by varying composition has been successful in synthetic brannerites [62], which have a similar structure and composition to calciopyrochlore; moreover, U^{5+} speciation is claimed in synthetic calciobetafites [63]. Both suggest that U^{5+} speciation in pyrochlore minerals may be dependent on composition. Several publications have claimed the production of U^{5+}-containing synthetic pyrochlores, including $Ca_{1.25}U^{4+}_{0.25}U^{5+}_{0.50}Ti_2O_7$ [63], $Ca_{1.40}U^{5+}_{0.60}U^{6+}_{0.10}Ti_{1.9}O_7$ [63] and $Ba_2U^{5+}{}_2O_7$ [64], by a range of synthesis processes [60, 63-66], demonstrating the ability of the pyrochlore structure to accept U^{5+}. Notably, despite reporting the successful synthesis of a U^{5+} containing pyrochlore, an investigation by Redkin *et al.* into a series of pyrochlore compositions led them to conclude that possibility of a pyrochlore with a significant concentration of U^{5+} and U^{6+} occurring naturally was unlikely [66]. These synthetic works have attributed the occurrence of U^{5+} to a distribution of U on both the A [63, 65] and B site [60, 64, 66]. Prior to this, it had been understood that U^{5+} would occur only on the B site, due to its ionic radius and the known occurrence of other 5+ cations on the B site (Ta,Nb,Sb) [37]. In the present study, due to limited data quality (short k-range) and the metamict nature of the sample, fitting of the EXAFS was non-trivial and limited in the medium-range order, so it was not possible to assign U^{5+} to a specific site.

In summary, this work represents the first characterisation of U^{5+} in a naturally occurring, long-lived mineral. It challenges the currently held assumptions surrounding U^{5+} longevity, in addition to those of U speciation in tailored ceramic materials for radioactive waste disposal. Due to the greater mobility of U^{5+} compared to U^{4+} [12], the potential presence of U^{5+} within a wasteform could be detrimental to the wasteforms ability to retain U. However, an increased mobility of U could make U-containing pyrochlores a more attractive prospect as a potential source of U for mining. Conversely, the presence of a majority of U^{5+} within a naturally occurring mineral, in which it has remained ca. 1 billion years, indicates that U^{5+} is more environmentally stable than previously thought and therefore a mixed U speciation within a wasteform may not be a cause for concern.

6.4. Methodology

6.4.1. Scanning electron microscopy

SEM was conducted on a Hitachi TM3030 in low charge build-up mode using backscattered electrons with an accelerating voltage of 15 keV and a working distance of approximately 9 mm. Energy dispersive X-ray (EDX) spectra were obtained on a Bruker Quantax Energy Dispersive X-ray Spectrometer connected to the Hitachi TM3030. Compositional data were obtained by identifying emission lines in the EDX spectra and attributing them to different elements, which was performed using the Quantax 70 software. The sample was mounted as a thin section on a spectrosil^{TM} slide, and polished to a thickness of 40 µm to a 1 µm finish.

6.4.2. Powder X-ray diffraction

p-XRD data were collected on a Bruker D2 Phaser diffractometer with Cu-K_α radiation (λ = 1.5418 Å) and a Lynxeye position sensitive detector. Data were collected from 5° to 65° 2θ with a step size of 0.02° and a total measurement time of 6 hours. The initial sample measured contained significant amounts of $CaCO_3$ (identified by comparison to ICSD no. 257801, SI Figure 6.1) so the sample was washed with HCl prior to re-analysis by p-XRD. Phase analysis was performed using Diffract.EVA.

6.4.3. Electron probe microanalysis

Electron probe microanalysis (EPMA) data were collected on a JEOL JXA-8530F Plus Hyper Probe with an accelerating voltage of 15 keV and a 100 nA beam current. A sample was mounted in epoxy resin, polished to a 1 µm finish and carbon coated in preparation for EPMA. Data were collected from 8 points on the bulk, unaltered region of the calciopyrochlore grain, the results of which are shown in Table 6.SI.1, as are the element standards used for calibration. When calculating the composition of the calciopyrochlore, the convention set by Atencio *et al.* [38] was followed, assuming that the B-site was fully occupied.

6.4.4. X-ray absorption spectroscopy

XAS was used to investigate the speciation and local coordination of U within the calciopyrochlore mineral. Three different XAS experiments were undertaken at three different beamlines. This involved the measurement of the sample and a set of reference compounds representative of a range of U oxidation states and coordination environments (Table 6.SI.2). The reference compounds measured at each beamline were prepared from the same original reference stock or mineral.

Transmission U L_3-edge XAS data were acquired at the B18 bending magnet beamline at the Diamond Light Source (DLS) Oxfordshire, UK. All samples were measured in air and at room temperature, in transmission mode, using a Si(111) monochromator. An in-line Y reference foil was used for energy calibration (the first peak in the first derivative of reference data were calibrated to 17038 eV).

U L_3-edge $L_{\alpha1}$ high resolution fluorescence detected (HERFD) XAS data were acquired at the I20-scanning beamline at DLS, Oxfordshire, UK. The beamline was configured with a Si(111) monochromator, and the measurements were performed on a Johann-type X-ray emission spectrometer with the sample, 5 striped Si(111) analyser crystals and Ge 64-element detector arranged in a vertical Rowland circle geometry to enable the collection of data at an emission energy of 13614.10 eV, which is the maximum intensity of the U $L_{\alpha1}$ emission line. Loss of photons was reduced by employing a He bag that was positioned between the sample, crystal analysers and detector. Samples were orientated at 45° to the beam direction. To minimise damage to the sample by the X-ray beam, each scan was measured on a new position on the sample.

U M_4-edge M_β HERFD XAS data were acquired at the Rossendorf beamline (BM20) at the European synchrotron radiation facility (ESRF), Grenoble, France. BM20 was configured with a double crystal Si(111) monochromator, and a Johann-type X-ray emission spectrometer with the sample, analyser crystals and detector arranged in a vertical Rowland circle geometry [67]. Five spherically bent (1.0 m) Si(220) striped analyser crystals aligned at a 75° Bragg angle

enabled the selection of the incident energy and the emission energy was fixed at 3337 eV, the maximum intensity of the U M_β emission line. The data were collected on a silicon drift detector (SDD).

For transmission U L_3-edge XAS measurements reference compounds and the sample were ground by hand and combined in powder form with 20 mg of polyethylene glycol (PEG) to form a homogenous dispersion and then pressed at 1 tonne for 1 minute into 6 mm pellets. Samples were prepared to obtain an absorber concentration of one absorption length, all calculations for which were performed in Hephaestus [68].

To ensure homogeneity for the more sensitive HERFD measurements, size reduction of powder samples was achieved by ball milling in a Fritsch Pulverisette 23 Micro Mill for 10 minutes at 30 RPM in IPA. The sample and PEG were carefully combined to ensure homogenous dispersion and then pressed into a pellets. For HERFD U L_3-edge $L_{\alpha1}$ XAS 10 mm pellets were prepared with 2 mg of sample and 50 mg of PEG and were pressed at 1 tonne for 1 minute. For HERFD U M_4-edge M_β XAS 6 mm pellets were prepared with 50 mg of sample, 50 mg of PEG and were pressed at 1 tonne for 1 minute.

6.4.5. X-ray absorption near edge spectra (XANES) analysis

All XAS data calibration, alignment, merging, normalisation and multi electron excitation (MEE) removal were performed in Athena, from the Demeter software suite [68]. Linear combination fitting (LCF) of the XANES region was also performed in Athena. All fits were constrained to give each component a weighting between 0 and 1 and the sum of weightings for each fit were not constrained to sum to unity. The initial fits on the Macdonald Mine sample for U L_3-edge transmission, U L_3-edge $L_{\alpha1}$ HERFD and U M_4-edge M_β HERFD data were initially performed utilising the same 12 reference compounds. The selection of reference compounds in the fits were then validated by applying principal component analysis (PCA) and iterative target transformation factor analysis (ITTFA) [69, 70]. The results of the initial LCF attempts with 12 reference compounds were used to identify an appropriate set of representative compounds for PCA and ITTFA. PCA in all cases identified that there were 3

distinct components, from this a constraint of a maximum of 3 reference compounds or components was applied to the final LCF and ITTFA attempts. For both LCF and ITTFA the fit range of U L_3-edge data was set to -20 to +30 eV from E_0 and for U M_4-edge M_β HERFD data the range was -6 to +8 eV from E_0. From the final fits, the weighted contributions were normalised to sum to unity to enable estimation of net U oxidation state for both ITTFA and LCF results.

It is possible that some of the variation between estimates could be improved by providing more compositionally similar reference compounds. All these analyses techniques are limited by the availability of appropriate reference compounds, which are used as a foundation for each technique. Analysis of HERFD U L_3-edge $L_{\alpha 1}$ and M_4-edge M_β data are especially sensitive to this limitation as the features that are fit are measured with a higher resolution. In the case of the M_4-edge, these features are more distinct, the effect of which can be seen in the goodness of fit parameter (Table 6.1, R factor).

6.4.6. Extended X-ray absorption fine structure (EXAFS) analysis

Artemis from the Demeter Suite [68] in combination with FEFF6 [71] was used to fit the U L_3-edge transmission EXAFS data. The fits were performed on the forward Fourier transform of EXAFS data which had been windowed in k-space between 2.5 and 11 $Å^{-1}$ and between 1.35 and 4 Å in R-space. This range provided 14 degrees of freedom in the fit with 9 number of variables being used for the fit (consistent with the Nyquist criterion). The amplitude reduction factor (S_0^2) for the fit of the MacDonald Mine sample was determined through EXAFS fitting of a UO_2 reference compound, prepared identically and measured concurrently to the mineral sample. Paths from two CIF files from synthetic pyrochlore structures, $Ca_2Nb_2O_7$ [48] and $CaUTi_2O_7$ [52], obtained through the Inorganic Crystal Structure Database (ICSD), were used as the basis for the EXAFS fitting. Input files were generated from the CIF files and edited to enable multiple occupancy on the A and B site of Ca and U, and Nb and Ti respectively. The bond valence sum of the U-O1, U-O2 and U-O3 paths were calculated using values from Brown and Altermatt [72].

6.4.7. Examination of U oxidation by radiogenic lead (Pb*) reduction

Taking the estimated age of the MacDonald Mine sample of 1.0 billion years, and the known half-lives of ^{235}U and ^{238}U, we were able to calculate the maximum amount of Pb* produced over the lifetime of our sample. Approximately 14% of the original U content would have decayed to Pb^{4+}. Assuming that the sample initially contained 100 atoms of U, 14 atoms would have undergone decay to become Pb*, while 86 atoms remain as U. To fully reduce the radiogenic Pb^{4+} to Pb^{0} the transfer of 56 electrons would be needed. Of the 86 U atoms in the sample, taking the mean of the two estimates of U speciation weighting from analysis of U M_4-edge M_β HERFD data, 34 (39.2%) are U^{5+} and 30 (34.4%) are U^{6+}, to produce this speciation by auto-oxidation would have required the removal of 94 electrons and so a deficit of 38 electrons is present.

6.5. Acknowledgments

The authors are grateful to UKRI EPSRC for sponsorship for this research under grant references EP/R513313/1. CLC is grateful EPSRC for the award of an Early Career Fellowship under grant reference EP/N017374/1.This research utilised the HADES/MIDAS facility and Henry Royce Institute at the University of Sheffield established with financial support from UKRI EPSRC and BEIS, under grant EP/T011424/1 [73]. We acknowledge Diamond Light Source for time on B18 and I20-scanning under proposal numbers SP17782-1, SP24206-1 and SP31009-1, with thanks to Giannantonio Cibin, Stephen Parry, Fred Mosselmans and Shu Hayama. We acknowledge the European Synchrotron Radiation Facility for the provision of synchrotron radiation facilities under proposal number MA-4821, with thanks to Kristina Kvashnina and Sergei Butorin, and also to Tatiana Poliakova, Anastasiia Smirnova and Jurij Galanzew for their assistance in operating BM20 remotely. LTT thanks Bruce Ravel for helpful correspondence.

6.6. Supplementary Information

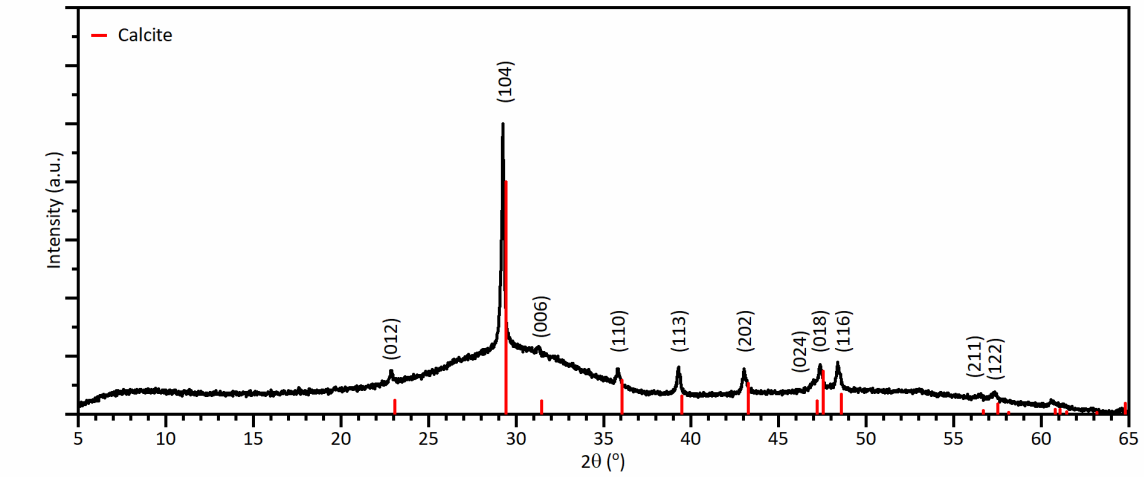

Figure 6.SI.1: XRD pattern collected from the Mac Donald sample, before washing in HCL, with the reflections of calcite (ICSD no. 257801) shown.

Table 6.SI.1: Electron probe microanalyses of bulk calciopyrochlore grain

Element	Mean wt.%	Range (wt.%)	SD		pfu	EPMA standard
Na	0.66	0.63–0.68	0.02	Na	0.11	Jadeite,
Ca	10.99	10.75–11.08	0.14	Ca	1.02	Wollastonite
Mn	0.12	0.10–0.15	0.02	Mn	0.01	Mn metal
Fe	1.24	1.16–1.32	0.05	Fe	0.08	Fe metal, Pyrite
Sr	0.41	0.31–0.48	0.07	Sr	0.02	SrF_2
Y	0.04	0.03–0.05	0.01	Y	0.001	Y metal, Y 12wt.% in Glass
Pd	0.01	0.00–0.02	0.01	Pd	0.000	Pd metal
Sn	0.09	0.08–0.09	0.003	Sn	0.003	Sn metal
Ba	0.02	0.02–0.04	0.01	Ba	0.000	BaF_2
La	0.02	0.01–0.03	0.01	La	0.000	LaB_6 La_2O_3 12 wt.% in glass
Ce	0.22	0.22–0.23	0.01	Ce	0.01	$CeAl_2$ Ce 12 wt.% in glass
Nd	0.06	0.05–0.06	0.003	Nd	0.001	NdF_3
Dy	0.07	0.05–0.08	0.01	Dy	0.002	Dy 12 wt.% in glass
Pb	3.09	3.04–3.20	0.05	Pb	0.06	PbTe
Th	0.18	0.16–0.19	0.01	Th	0.003	
U	19.31	19.17–19.55	0.13	U	0.30	
				ΣA	1.615	
Si	0.06	0.02–0.09	0.02	Si	0.01	Orthoclase, Wollastonite
Mg	0.01	0.01–0.02	0.004	Mg	0.002	MgO
Al	0.05	0.04–0.07	0.01	Al	0.01	Jadeite, Al_2O_3, Orthoclase, $CeAl_2$
Ti	11.26	11.17–11.37	0.08	Ti	0.88	Ti metal
Zr	0.03	0.03–0.04	0.003	Zr	0.001	Zr metal
Nb	26.12	25.82–26.55	0.28	Nb	1.05	Nb metal
Ta	2.23	1.98–2.41	0.16	Ta	0.05	Ta metal
W	0.80	0.77–0.83	0.02	W	0.02	W metal
				ΣB	2.000	
O	21.69	20.73–23.48	1.01	O	5.06	
F	0.49	0.37–0.57	0.09	F	0.10	SrF_2, BaF_2
K	0.01	0.00–0.10	0.004	K	0.0009	Orthoclase
Rb	–	–	–	Rb	–	
Cs	0.01	0.01–0.02	0.003	Cs	0.000	
				Σ(X+Y)	5.159	
Total	99.27					

Table 6.SI.2: List of reference compounds used for LCF, PCA and ITTFA, their oxidation states and coordination numbers.

Reference Compound	Oxidation state	Coordination Number
UTi_2O_6	4+	6
UO_2	4+	8
$CrUO_4$	5+	6
$USbO_5$	5+	7
Metaschoepite $((UO_2)_8O_2(OH)_{12} \cdot 10H_2O)$	6+	8

6.6.1. Fitting of the Extended X-ray Absorption Fine Structure.

The final fit utilised three U-O paths with bond lengths of 1.95(3) Å, 2.27(3) Å, and 2.38(4) Å with weightings of 1.3, 2.7 and 3.0 respectively, resulting in a U coordination of 7. These distances are shorter than those provided from the pyrochlore structure, 2.20 Å and 2.49 Å. It was found that using only one or two U-O paths could not fully reproduce the first shell, so three were used; however, due to the limited number of parameters available and concerns of overfitting four U-O paths was not attempted. The number of parameters used was reduced by setting the U-O1 and U-O3 paths to share a σ^2 parameter; however, the U-O2 path required an independent σ^2 parameter. The U-O1 and U-O3 paths are similar to those calculated previously for U^{5+} samples [4], including a synthetic U-Pu pyrochlore claimed to be U^{5+} for which EXAFS fitting gave paths at 2.05-2.07 Å and at 2.36 Å [60], with a degeneracy of 4 on the shorter path and 3 on the longer path, similar to the weighting of degeneracy in our fit. The U-O1 and U-O3 path distances are also similar to the path distances of metamict U bearing mineral sample investigated Greegor *et al.* which may be a calciopyrochlore, with the composition $(Ca_{0.46}U_{0.42}Fe_{0.11}Ba_{0.03}Pb_{0.02})(Nb_{1.1}Ti_{0.88}Ta_{0.02})O_{6.0}F_{0.04} \cdot 2.3H_2O$ [51], which had estimated path distances of 1.94 and 2.37 Å and also 2.03 and 2.51 Å for a thermally treated version. The U-O1 path is shorter than most of those measured previously, which were crystalline, possibly due to the fit attempting to describe both a U^{5+} contribution at c.a. 2.05-2.15 Å and a U^{6+} uranyl contribution at 1.8 Å [74], or the metamict nature of the sample [51]. The similarities between the U-O1 and U-O3 paths and those found by Fortner *et al.* [60] and

Greegor *et al.* in their synthetic U^{5+} pyrochlore are encouraging, however the U environment within the MacDonald Mine sample is complex, with at least 3 different U environments and a disordered structure, and the three paths in the fit are highly simplified representation of this so no strong conclusions can be drawn from these bond lengths.

Fits that assumed a total degeneracy of 6 and 8 for the U-O paths were attempted; however, it was found that a total degeneracy of 7 produced a better fit. A total degeneracy of 7 could be indicative of U occupying both the A and B site, or that the alpha recoil damage experienced by the pyrochlore has caused the A site, B site coordination to change to be closer to 7, 7 than 6, 8. However, due to the metamict nature of the sample, the quality of data and the range of data available to fit, no definite conclusions can be drawn.

The second shell of the final fit used a U-Ca path with a bond length of 3.57(5) Å and a degeneracy of 1.7 and a U-Nb path with a bond length of 3.52(5) Å and a degeneracy of 2.4. Both paths were taken from a CIF file of $Ca_2Nb_2O_7$ produced by Lewandowski *et al.* [48], edited to include U. Initial fitting used four paths from the highest concentration cations occurring in pyrochlore: Ca, U, Ti and Nb, from the EDX estimate of composition, to represent the scattering contributions of all cations in the A and B sites. The U-U and U-Ti paths were taken from a CIF file of $CaUTi_2O_7$ produced by Dickson *et al.* [52]. However, the A and B site cation paths presented very similar σ^2 and interatomic distances (R), so it was possible to represent all cation contributions with one U-Ca path and one U-Nb path.

Initial fits used degeneracy values taken from the estimated composition of the MacDonald mine calciopyrochlore, the simplified two cation path fits used degeneracies of 4.2 and 6 for the A and B site respectively. However, these fits gave high σ^2 values for the U-Ca and U-Nb paths and in the Fourier transform of the EXAFS data (Figure 6.3) it can be seen that the features in the second shell region (ca. 2.9-4.0 Å) are damped compared to the first shell and the second shells previously observed in EXAFS data of synthetic, crystalline pyrochlores [60]. The absorbing U atom appears to be experiencing less scattering from the second shell cations that would be expected from the calculated A and B site occupancies, likely due to disorder in the structure. To compensate for the damping of these features, an extra damping factor was introduced, which was applied to the U-Ca and U-Nb paths only. This method was applied

rather than to allow the degeneracy of both paths to vary in order to maintain the ratio of occupancy between the A and B sites. It was found that applying a damping factor of 0.4, equivalent to degeneracies of 1.7 and 2.4 for the U-Ca and U-Nb paths respectively, reduced the σ^2 values of the second shell paths and improved the goodness of fit.

To reduce the number of parameters used, the extra damping factor parameter was removed and the degeneracies of the two second shell paths were set to the new values. The fit was simplified further by forcing the U-Ca and U-Nb paths to share a σ^2 path, this gave a value for σ^2, 0.0189(6), which is slightly higher than ideal but reasonable for a σ^2 parameter that is representing two different paths. It was not possible to represent the second shell with just one path or reduce the number of parameters further by forcing the U-Ca and U-Nb paths to share an interatomic distance.

6.7. References

[1] S.I. Tomkeieff, The Geochemistry of Uranium, Scientific Progress 34(136) (1946) 696-712.

[2] F. Clifford, Systematic mineralogy of uranium and thorium, Geological Survey Bulletin 1064, Geological survey, U.S. Government, Washington, U.S.A., 1958.

[3] R. Finch, T. Murakami, Systematics and Paragenesis of Uranium Minerals, Reviews in Mineralogy 38 (1999) 91-179.

[4] P.C. Burns, R.J. Finch, Wyartite: Crystallographic evidence for the first pentavalent-uranium mineral, Am. Miner. 84(9) (1999) 1456-1460.

[5] T.A. Olds, A.J. Lussier, A.G. Oliver, V. Petříček, J. Plášil, A.R. Kampf, Burns, P. C., M. Dembowski, S.M. Carlson, I.M. Steele, IMA No. 2016-095 Shinkolobweite, Mineral. Mag. 81 (2017) 403-409.

[6] J. Plášil, Crystal structure of richetite revisited: Crystallographic evidence for the presence of pentavalent uranium, Am. Miner. 102(9) (2017) 1771-1775.

[7] J. Plášil, A.R. Kampf, R. Škoda, J. Čejka, Nollmotzite, $Mg[U^{V}(U^{VI}O_2)_2O_4F_3]\cdot 4H_2O$, the first natural uranium oxide containing fluorine, Acta Crystallogr. Sect. B-Struct. Sci.Cryst. Eng. Mat. 74 (2018) 362-369.

[8] V. Bermanec, R. Wegner, G. Kniewald, B. Rakvin, L.A. Palinkas, M. Rajic, N. Tomasic, K. Furic, The role of uranium(V) ion in the chemical composition of meta-autunite from pegmatites of Quintos de Baixo, Brazil, Neues Jahrb. Mineral.-Abh. 181(1) (2005) 27-38.

[9] A.J. Locock, Comments on " Bermanec, V., Wegner, R., Kniewald, G., Rakvin, B., Palinkas, L. A., Rajic, M., Tomasic, N. & Furic, K. (2005): The role of uranium(V) ion in the chemical composition of meta-autunite from pegmatites of Quintos de Baixo, Brazil". N. Jb. Miner. Abh. 181 : 27-38, Neues Jahrb. Mineral.-Abh. 182(2) (2006) 213-216.

[10] V. Bermanec, G. Kniewald, Response to Comments by A. J. Locock on the paper: Bermanec et al. "The role of uranium(V) ion in the chemical composition of meta-autunite from pegmatites of Quintos de Baixo, Brazil". N. Jb. Miner. Abh. 181 : 27-38, Neues Jahrb. Mineral.-Abh. 182(2) (2006) 217-219.

[11] E.S. Ilton, R.N. Collins, C.L. Ciobanu, N.J. Cook, M. Verdugo-Ihl, A.D. Slattery, D.J. Paterson, S.T. Mergelsberg, E.J. Bylaska, K. Ehrig, Pentavalent Uranium Incorporated in the Structure of Proterozoic Hematite, Environ. Sci. Technol. 8.

[12] K. Maher, J.R. Bargar, G.E. Brown, Environmental Speciation of Actinides, Inorg. Chem. 52(7) (2013) 3510-3532.

[13] G.R. Lumpkin, Ceramic waste forms for actinides, Elements 2(6) (2006) 365-372.

[14] F.A. Charalambous, R. Ram, S. McMaster, J. Tardio, S.K. Bhargava, An investigation on the dissolution of synthetic brannerite (UTi_2O_6), Hydrometallurgy 139 (2013) 1-8.

[15] S.V. Stefanovsky, S.V. Yudintsev, Titanates, zirconates, aluminates and ferrites as waste forms for actinide immobilization, Russ. Chem. Rev. 85(9) (2016) 962-994.

[16] S.V. Stefanovsky, S.V. Yudintsev, A.A. Shiryaev, V.Y. Murzin, A.L. Trigub, Phase partitioning and uranium speciation in brannerite-based ceramics, J. Eur. Ceram. Soc. 37(2) (2017) 771-777.

[17] D.J. Bailey, M.C. Stennett, B. Ravel, D. Grolimund, N.C. Hyatt, Synthesis and characterisation of brannerite compositions $(U_{0.9}Ce_{0.1})_{1-x}M_xTi_2O_6$ ($M = Gd^{3+}$, Ca^{2+}) for the immobilisation of MOX residues, RSC Adv. 8(4) (2018) 2092-2099.

[18] G.R. Lumpkin, Y. Gao, R. Giere, C.T. Williams, A.N. Mariano, T. Geisler, The role of Th-U minerals in assessing the performance of nuclear waste forms, Mineral. Mag. 78(5) (2014) 1071-1095.

[19] S.X. Wang, B.D. Begg, L.M. Wang, R.C. Ewing, W.J. Weber, K.V.G. Kutty, Radiation stability of gadolinium zirconate: A waste form for plutonium disposition, J. Mater. Res. 14(12) (1999) 4470-4473.

[20] S.K. Roberts, W.L. Bourcier, H.F. Shaw, Aqueous dissolution kinetics of pyrochlore, zirconolite and brannerite at 25, 50, and 75 degrees C, Radiochim. Acta 88(9-11) (2000) 539-543.

[21] E.R. Vance, G.R. Lumpkin, M.L. Carter, D.J. Cassidy, C.J. Ball, R.A. Day, B.D. Begg, Incorporation of uranium in zirconolite ($CaZrTi_2O_7$), J. Am. Ceram. Soc. 85(7) (2002) 1853-1859.

[22] R.A. Day, S. Moricca, M. Stewart, B.D. Begg, E. Maddrell, C.R. Scales, N. Gawthorpe, Demonstration of Zirconolite Glass-Ceramics Processed in a hot Isostatic Press: An option for Immobilisation of Actinide Containing Residues at Sellafield, ICEM'05: the 10th International Conference on Environmental Remediation and Radioactive Waste Management, Glasgow, Scotland, 2005.

[23] B.I. Omel'yanenko, T.S. Livshits, S.V. Yudintsev, B.S. Nikonov, Natural and artificial minerals as matrices for immobilization of actinides, Geol. Ore Depos. 49(3) (2007) 173-193.

[24] M. Gilbert, J.H. Harding, Energetics of Ce and Pu incorporation into zirconolite waste-forms, Phys. Chem. Chem. Phys. 13(28) (2011) 13021-13025.

[25] L.R. Blackburn, D.J. Bailey, S.K. Sun, L.J. Gardner, M.C. Stennett, C.L. Corkhill, N.C. Hyatt, Review of zirconolite crystal chemistry and aqueous durability, Adv. Appl. Ceram. 120(2) (2021) 69-83.

[26] R.C. Ewing, W.J. Weber, J. Lian, Nuclear waste disposal-pyrochlore ($A_2B_2O_7$): Nuclear waste form for the immobilization of plutonium and "minor" actinides, J. Appl. Phys. 95(11) (2004) 5949-5971.

[27] J.W. Valley, A.J. Cavosie, T. Ushikubo, D.A. Reinhard, D.F. Lawrence, D.J. Larson, P.H. Clifton, T.F. Kelly, S.A. Wilde, D.E. Moser, M.J. Spicuzza, Hadean age for a post-magma-ocean zircon confirmed by atom-probe tomography, Nat. Geosci. 7(3) (2014) 219-223.

[28] G.R. Lumpkin, R.C. Ewing, Alpha-decay damage in minerals of the pyrochlore group, Phys. Chem. Miner. 16(1) (1988) 2-20.

[29] Q.X. Cao, S.V. Krivovichev, B.E. Burakov, X.D. Liu, X.T. Liu, Natural metamict minerals as analogues of aged radioactive waste forms, J. Radioanal. Nucl. Chem. 304(1) (2015) 251-255.

[30] R.C. Ewing, B.C. Chakoumakos, G.R. Lumpkin, T. Murakami, R.B. Greegor, F.W. Lytle, Metamict minerals: Natural analogues for radiation damage effects in ceramic nuclear waste forms, Nucl. Instrum. Methods Phys. Res. Sect. B-Beam Interact. Mater. Atoms 32(1-4) (1988) 487-497.

[31] R.C. Ewing, The metamict state: 1993 — the centennial, Nucl. Instrum. Methods Phys. Res. Sect. B-Beam Interact. Mater. Atoms 91(1-4) (1994) 22-29.

[32] T.L. Walker, A.L. Parsons, Ellsworthite and Associated Minerals from Hybla, Ontario, The University of Toronto1923.

[33] H.V. Ellsworth, Ellsworthite crystals from Haliburton County, Ontario, Am. Miner. 12(2) (1927) 48-53.

[34] D.D. Hogarth, Classification and Nomenclature of Pyrochlore Group, Am. Miner. 62(5-6) (1977) 403-410.

[35] A.G. Christy, D. Atencio, Clarification of status of species in the pyrochlore supergroup, Mineral. Mag. 77(1) (2013) 13-20.

[36] B.C. Chakoumakos, Systematics of the Pyrochlore Structure Type, Ideal $A_2B_2X_6Y$, J. Solid State Chem. 53(1) (1984) 120-129.

[37] M.A. Subramanian, G. Aravamudan, G.V.S. Rao, Oxide Pyrochlores - A Review, Prog. Solid State Chem. 15(2) (1983) 55-143.

[38] D. Atencio, M.B. Andrade, A.G. Christy, R. Giere, P.M. Kartashov, The Pyrochlore Supergroup of Minerals: Nomenclature, Can. Mineral. 48(3) (2010) 673-698.

[39] K. Mezger, E.J. Essene, B.A. Vanderpluijm, A.N. Halliday, U-Pb geochronology of the Grenville Orogen of Ontario and New York: constraints on ancient crustal tectonics, Contrib. Mineral. Petrol. 114(1) (1993) 13-26.

[40] J. Satterly, D.F. Hewitt, Some Radioactive Mineral Occurrences in the Bancroft Area, in: O.D.o. Mines (Ed.) Baptist Johnston, Printer to the Queen's Most Excellent Majesty, Toronto, 1955.

[41] K. Mezger, B.A. Vanderpluijm, E.J. Essene, A.N. Halliday, Synorogenic Collapse: A Perspective from the Middle Crust, the Proterozoic Grenville Orogen, Science 254(5032) (1991) 695-698.

[42] K.O. Kvashnina, S.M. Butorin, P. Martin, P. Glatzel, Chemical State of Complex Uranium Oxides, Phys. Rev. Lett. 111(25) (2013) 5.

[43] R. Bes, M. Rivenet, P.L. Solari, K.O. Kvashnina, A.C. Scheinost, P.M. Martin, Use of HERFD–XANES at the U L_3- and M_4-Edges To Determine the Uranium Valence State on $[Ni(H_2O)_4]_3[U(OH,H_2O)(UO_2)_8O_{12}(OH)_3]$, Inorg. Chem. 55(9) (2016) 4260-4270.

[44] F. Farges, R.C. Ewing, G.E. Brown, The structure of aperiodic, metamict (Ca, Th)$ZrTi_2O_7$ (zirconolite): An EXAFS study of the Zr, Th, and U sites, J. Mater. Res. 8(8) (1993) 1983-1995.

[45] F. Farges, The structure of metamict zircon: A temperature-dependent EXAFS study, Phys. Chem. Miner. 20(7) (1994) 504-514.

[46] M. Harfouche, F. Farges, J.P. Crocombette, A.M. Flank, XAFS and molecular dynamics study of natural minerals, analogues of ceramics for nuclear waste storage, Phys. Scr. T115 (2005) 928-930.

[47] M. Harfouche, F. Farges, XAFS Study of Actinides in Natural Minerals Analogues of Ceramics for Nuclear Waste, Acta Crystallogr. Sect. A 65 (2009) S118-S118.

[48] J.T. Lewandowski, I.J. Pickering, A.J. Jacobson, Hydrothermal synthesis of calcium-niobium and tantalum oxides with the pyrochlore structure, Mater. Res. Bull. 27(8) (1992) 981-988.

[49] G.M. Yang, G.W. Li, M. Xiong, B.M. Pan, C.J. Yan, Hydroxycalciopyrochlore, A New Mineral Species from Sichuan, China, Acta Geol. Sin.-Engl. Ed. 88(3) (2014) 748-753.

[50] F. Camara, C.T. Williams, G. Della Ventura, R. Oberti, E. Caprilli, Non-metamict betafite from Le Carcarelle (Vico volcanic complex, Italy): occurrence and crystal structure, Mineral. Mag. 68(6) (2004) 939-950.

[51] R.B. Greegor, F.W. Lytle, B.C. Chakoumakos, G.R. Lumpkin, R.C. Ewing, An Investigation of Uranium L-Edges of Metamict and Annealed Betafite, MRS Proceedings 50 (1985) 387.

[52] F.J. Dickson, K.D. Hawkins, T.J. White, Calcium Uranium Titanate - A New Pyrochlore, J. Solid State Chem. 82(1) (1989) 146-150.

[53] G.W. Li, G.M. Yang, F.D. Lu, M. Xiong, X.K. Ge, B.M. Pan, J. de Fourestier, Fluorcalciopyrochlore, a new mineral species from Bayan Obo, Inner Mongolia, P.R. China, Can. Mineral. 54(5) (2016) 1278-1284.

[54] P. Černý, F.C. Hawthorne, J.H.G. Laflamme, J.R. Hinthorne, Stibiobetafite, a new member of the pyrochlore group from Venza, Czechoslovakia, Can. Mineral. 17 (1979) 583-588.

[55] D. Atencio, Pyrochlore-Supergroup Minerals Nomenclature: An Update, Front. Chem. 9 (2021) 6.

[56] L.W. Finger, Refinement of the Crystal Structure of Zircon, Year Book - Carnegie Institution of Washington 73 (1974) 544-547.

[57] G.R. Lumpkin, R.C. Ewing, Geochemical alteration of pyrochlore group minerals: Betafite subgroup, Am. Miner. 81(9-10) (1996) 1237-1248.

[58] G.R. Lumpkin, R.C. Ewing, Geochemical alteration of pyrochlore group minerals - Pyrochlore subgroup, Am. Miner. 80(7-8) (1995) 732-743.

[59] D.F. Hewitt, Pegmatite Mineral Resources of Ontario, in: O.D.o. Mines (Ed.) Toronto, 1967.

[60] J.A. Fortner, A.J. Kropf, R.J. Finch, A.J. Bakel, M.C. Hash, D.B. Chamberlain, Crystal chemistry of uranium (V) and plutonium (IV) in a titanate ceramic for disposition of surplus fissile material, J. Nucl. Mater. 304(1) (2002) 56-62.

[61] D.D. Syverson, B. Etschmann, W.H. Liu, R. Ram, Y. Mei, T. Lanzirotti, J. Mercadier, J. Brugger, Oxidation state and coordination environment of Pb in U-bearing minerals, Geochimica Et Cosmochimica Acta 265 (2019) 109-131.

[62] M.C. Dixon Wilkins, L.M. Mottram, E.R. Maddrell, M.C. Stennett, C.L. Corkhill, K.O. Kvashnina, N.C. Hyatt, Synthesis, Characterization, and Crystal Structure of Dominant Uranium(V) Brannerites in the $UTi_{2-x}Al_xO6$ System, Inorg. Chem. 60(23) (2021) 18112-18121.

[63] M. James, M.L. Carter, Z.M. Zhang, Y.J. Zhang, K.S. Wallwork, M. Avdeev, E.R. Vance, Crystal Chemistry and Structures of (Ca,U) Titanate Pyrochlores, J. Am. Ceram. Soc. 93(10) (2010) 3464-3473.

[64] A.V. Soldatov, D. Lamoen, M.J. Konstantinovic, S. Van den Berghe, A.C. Scheinost, M. Verwerft, Local structure and oxidation state of uranium in some ternary oxides: X-ray absorption analysis, J. Solid State Chem. 180(1) (2007) 54-61.

[65] S.A. McMaster, R. Ram, F. Charalambous, M.I. Pownceby, J. Tardio, S.K. Bhargava, Synthesis and characterisation of the uranium pyrochlore betafite (Ca,U)(2)(Ti,Nb,Ta)(2)O-7, J. Hazard. Mater. 280 (2014) 478-486.

[66] A.F. Redkin, A.M. Ionov, N.P. Kotova, Hydrothermal synthesis of pyrochlores and their characterization, Phys. Chem. Miner. 40(9) (2013) 733-745.

[67] K.O. Kvashnina, A.C. Scheinost, A Johann-type X-ray emission spectrometer at the Rossendorf beamline, J. Synchrot. Radiat. 23 (2016) 836-841.

[68] B. Ravel, M. Newville, ATHENA, ARTEMIS, HEPHAESTUS: data analysis for X-ray absorption spectroscopy using IFEFFIT, J. Synchrot. Radiat. 12 (2005) 537-541.

[69] A. Rossberg, T. Reich, G. Bernhard, Complexation of uranium(VI) with protocatechuic acid - application of iterative transformation factor analysis to EXAFS spectroscopy, Anal. Bioanal. Chem. 376(5) (2003) 631-638.

[70] A. Rossberg, K.U. Ulrich, S. Weiss, S. Tsushima, T. Hiemstra, A.C. Scheinost, Identification of Uranyl Surface Complexes an Ferrihydrite: Advanced EXAFS Data Analysis and CD-MUSIC Modeling, Environ. Sci. Technol. 43(5) (2009) 1400-1406.

[71] A.L. Ankudinov, B. Ravel, J.J. Rehr, S.D. Conradson, Real-space multiple-scattering calculation and interpretation of x-ray-absorption near-edge structure, Phys. Rev. B 58(12) (1998) 7565-7576.

[72] I.D. Brown, D. Altermatt, Bond-valence parameters obtained from a systematic analysis of the Inorganic Crystal Structure Database, Acta Crystallogr. Sect. B-Struct. Commun. 41(AUG) (1985) 244-247.

[73] N.C. Hyatt, C.L. Corkhill, M.C. Stennett, R.J. Hand, L.J. Gardner, C.L. Thorpe, The HADES facility for high activity decommissioning engineering & science: Part of the UK national nuclear user facility, IOP Conference Proceedings: Materials Science and Engineering 818 (2020) 012022.

[74] P.C. Burns, R.C. Ewing, F.C. Hawthorne, The crystal chemistry of hexavalent uranium: Polyhedron geometries, bond-valence parameters, and polymerization of polyhedra, Can. Mineral. 35 (1997) 1551-1570.

7. Development and application of laboratory X-ray absorption spectroscopy for the support of nuclear waste disposal

This results chapter is an initial investigation into the application of laboratory X-ray absorption spectroscopy. It consists of three published papers, in which a lab XAS system has been used to measure Fe K-edge, U L_3 edge and Ce L_3 edge XAS in standards and materials relevant to nuclear waste and the speciation of Fe, U and Ce were characterised successfully.

This chapter is a synthesis of three papers:

Paper 1: A Feasibility Investigation of Laboratory Based X-ray Absorption Spectroscopy in Support of Nuclear Waste Management – *Initial U and Ce speciation paper*

Paper 2: A feasibility investigation of speciation by Fe K-edge XANES using a laboratory X-ray absorption spectrometer – *Initial Fe speciation paper*

Paper 3: Laboratory Based X-ray Absorption Spectroscopy of Iron Phosphate Glasses for Radioactive Waste Immobilisation: A Preliminary Investigation – *Speciation of Fe in glass wasteform paper*

MRS Advances

A Feasibility Investigation of Laboratory Based X-ray Absorption Spectroscopy in Support of Nuclear Waste Management

L.M. Mottram, M.C. Dixon Wilkins, L.R. Blackburn, T. Oulton, M.C. Stennett, S.K. Sun, C.L. Corkhill, and N.C. Hyatt

Immobilisation Science Laboratory, University of Sheffield, Department of Materials Science and Engineering, Sir Robert Hadfield Building, Mappin Street, S13JD, UK

ABSTRACT

X-ray Absorption Spectroscopy is a technique of fundamental importance in nuclear waste management, as an element specific probe of speciation, which governs radionuclide solubility, immobilisation and migration. Here, we exploit recent developments in laboratory instrumentation for X-ray Absorption Spectroscopy, based on a Rowland circle geometry with a spherically bent crystal analyser, to demonstrate speciation in prototype ceramic and glass-ceramic waste forms. Laboratory and synchrotron XANES data acquired from the same materials, at the Ce and U L_3 edges, were found to be in excellent quantitative agreement. We establish that analysable laboratory XANES data may be acquired, and interpreted for speciation, even from quite dilute absorber concentrations of a few mol%, albeit with data acquisition times of several hours. For materials with suitable absorber concentrations, this approach will enable routine element specific speciation studies to support rapid optimisation of radioactive waste forms and analysis of radiological materials in a purpose designed laboratory, without the risk associated with transport and manipulation at a synchrotron radiation facility.

INTRODUCTION

As an element specific probe of speciation X-ray absorption spectroscopy (XAS) finds ubiquitous and powerful application in the field of nuclear waste management, in particular in the development of waste form materials[1-16]. The fundamental requirement for a tunable broadband source of high brilliance X-rays, has, hitherto, generally required exploitation of synchrotron radiation sources for application of XAS techniques. However, recent advances in laboratory XAS instrumentation, exploiting spherically bent crystal analysers (SBCAs) in Rowland circle geometry, or bent cylindrical analysers in von Hamos geometry[17-26]. The use of SBCAs generally

delivers higher spectral resolution in the region of the X-ray Absorption Near Edge Structure (XANES), but the requirement to work close to back scattering geometry requires several monochromator crystals to cover the range 5 – 18 keV, and a precision motor driven system to maintain optical alignment[17-21]. In contrast, the von Hamos geometry utilises only a single bent crystal analyser and does not necessarily require movement of components for acquisition of spectra, however, the achievable resolution in the XANES region is comparatively lower[22-26]. These developments in instrumentation offer the potential to transform the application of XAS techniques in many scientific fields, by enabling routine studies of materials in which the absorbing element is moderately dilute to concentrated. With regard to research involving radioactive materials, laboratory instrumentation offers the inherent advantage of allowing characterisation to be completed, or at least preliminary investigation performed, without the need to move samples to the synchrotron source, reducing the risk, cost and timescale of research. Recently, Jahrman *et al.*, reported the first Ce and U L_3 XANES from reference compounds, achieved with a laboratory spectrometer using a SBCA[20]. Bes *et al* developed this approach with the report of laboratory U L_3 XANES data acquired from UO_2, UO_3 and KUO_3[27]. In this contribution we present the results of our preliminary investigation in the application of laboratory XAS to the characterisation of element speciation in materials for radioactive waste immobilisation.

EXPERIMENTAL

The spectrometer utilised in this study was an EasyXAFS 100 extended spectrometer, produced by EasyXAFS LLC, Seattle, USA, based on the design of Seidler et al [17-20]. The instrument is the first of its kind to be installed and commissioned in the UK, within the HADES facility at the University of Sheffield. The optical arrangement of the spectrometer is shown in Figure 1 and is based on a Rowland circle of 1m diameter. Energy scanning involves symmetrical movement of source and detector on a linear translation stage to increment Bragg angle steps. The X-ray source is a low power, air cooled, X-ray tube with a maximum output of 100 W. The sample is located in front of a Hitatchi Vortex Silicon Drift Detector (SDD), with a 5 mm exit slit to minimise stray scatter. The energy resolution of the SDD is ca. 140 eV, enabling rejection of the harmonic content of the incident beam and background scatter. Alignment of source, SBCA and detector is maintained by steering bars. With robust initial SBCA alignment, change over and alignment of SBCAs is straightforward and can be achieved in 30 minutes or less, the spectrometer is also easily adapted to perform X-ray Emission Spectroscopy experiments.

Laboratory Ce and U L_3 edge XANES data were acquired in transmission mode using, respectively the (422) and (1266) harmonic of a Si (211) SBCA. A step size of 0.75 eV and count time of 10s / step were used in the XANES region. A He flight path (welded steel enclosure with kapton windows) was employed to minimise air scatter and absorption. Data were acquired with ($I_t(E)$) and without the sample ($I_0(E)$), using the same scan parameters. The absolute energy scale was calibrated using a Cr foil (E_0 = 5989.00 eV)[29] or Y_2O_3 (E_0 = 17042.30 eV) reference, for the Ce L_3 and U L_3 edges respectively (E_0 set as first peak in first derivative). The Bragg angle, θ_m, corresponding to the first peak in the derivative spectrum of the reference, was set equivalent $E_c = E_0$, enabling the energy scale to be calibrated according to:

$$E_c = \frac{E_m sin(\theta)}{sin(\theta + \Delta\theta)}$$

where, E_m is the measured energy, E_c the calibrated energy, and $\Delta\theta$ is the difference between the measured Bragg angle at E_c and at E_m

Synchrotron Ce and U L_3 edge XANES data were acquired in transmission mode at beamline B18, Diamond Light Source, configured with a collimating mirror, a fixed-exit double crystal Si(111) monochromator, and a double toroidal focussing mirror. The step size in the XANES region was 0.5 eV for all measurements. The absolute energy scale was calibrated using a Cr foil (E_0 = 5989.00 eV) or Y foil (E_0 = 17038.00 eV)[29] reference, for the Ce L_3 and U L_3 edges respectively. Additionally, we calibrated the E_0 of our Y_2O_3 secondary standard against an Y foil utilising the BMM beamline, NSLS II; data were acquired in transmission mode, using a Si (111) monochromator, utilising a harmonic rejection mirror and toroidal focusing mirror. Incident and transmitted beam intensities were measured using ionization chambers, filled with mixtures of He and Ar or N_2, operated in a stable region of their I/V curve, for synchrotron data.

Samples were prepared for XANES analysis by diluting the material to be investigated in polyethylene glycol to yield a thickness of $\mu x = 1$. All XANES data were dead time corrected and processed in Athena using standard background subtraction and normalisation procedures[30].

The materials investigated by Ce and U L_3 XANES were CeO_2, $CePO_4$, $Ca_{0.75}ZrCe_{0.25}Ti_{1.5}Al_{0.5}O_7$, UTi_2O_6, $U_{0.55}Yb_{0.45}Ti_2O_6$, UO_3 and a brannerite glass ceramic comprising nominally UTi_2O_6 (50 wt%) crystallised in $Na_2AlBSi_2O_6$ glass (50 wt%). CeO_2, $CePO_4$, UTi_2O_6, and $U_{0.55}Yb_{0.45}Ti_2O_6$ were synthesized as reported previously[2,10,31]. UO_3 was utilized as stock material, originally produced by British Drug Houses. $Ca_{0.75}Ce_{0.25}ZrTi_{1.5}Al_{0.5}O_7$ was synthesized from stoichiometric quantities of $CaTiO_3$, TiO_2, CeO_2 and Al_2O_3, ball milled for 30 min at 300 r.p.m.; the mixture was pressed as a 13 mm pellet and subject to reaction – sintering at 1350°C for 4h in air. All materials were confirmed to be single phase by powder X-ray diffraction. The brannerite glass-ceramic was synthesized by first calcining a homogenized and stoichiometric mixture of SiO_2, H_3BO_3, Na_2CO_3, and Al_2O_3 at 600 °C for 6 hours, this was then ball milled with the required quantity of UO_2 and TiO_2 at 300 r.p.m. for 30 min. The recovered powder batch was pressed into 13 mm pellets and heat treated at 1200°C for 12h under Ar gas flow. X-ray diffraction analysis showed the material to comprise UTi_2O_6 and an amorphous phase (evident from diffuse scattering), plus trace UO_2. SEM/EDX analysis demonstrated U to be partitioned primarily into the brannerite ceramic phase, but with minor uptake into the glass phase – estimated as 2.5 wt% UO_2 by EDX analysis.

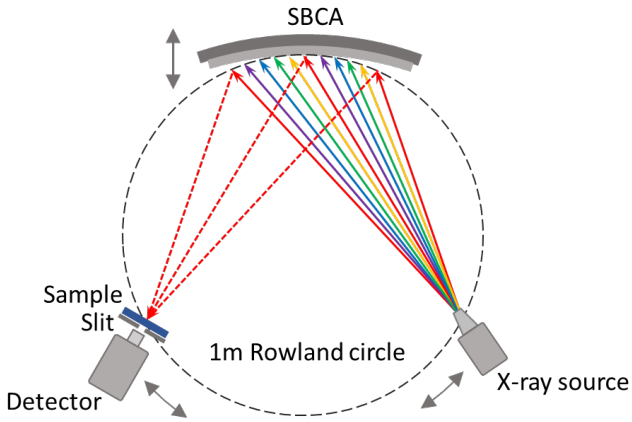

Fig. 1: Schematic representation of Rowland circle geometry for laboratory transmission X-ray Absorption Spectroscopy, as described in the text; note, the He flight path (a welded steel enclosure with kapton windows) is not shown.

RESULTS AND DISCUSSION

Ce L_3 XANES

Ce is often used as a Pu surrogate in development of ceramic, glass, and glass-ceramic waste forms, given that both elements adopt oxidation states $Ce^{3/4+}$ and $Pu^{3/4+}$, which controls partitioning in the phase assemblage[2,6-8,10]. Consequently, routine determination of $Ce^{3+}/^{4+}$ ratios in prototype waste form materials is essential for understanding surrogate partitioning mechanisms, governed by redox behavior and hence the processing conditions of the material. Figure 1 shows a comparison of laboratory and synchrotron XANES data acquired at the Ce L_3 edge of $CePO_4$ and CeO_2 reference compounds. The laboratory data sets were each acquired in 3h, whereas the synchrotron data sets were each acquired in 10 minutes. The laboratory and synchrotron data of the reference compounds are in excellent overall agreement, although some minor variation in the intensity of XANES features can be discerned. These variations are caused by small differences in the thickness of the different individual samples prepared for the laboratory and synchrotron experiments, combined with some contribution from "leakage" effects as described below. The Ce L_3 absorption edge of Ce^{3+} species, such as in $CePO_4$, is characterized by a single intense feature attributed to the transition from an initial $2p^64f^15d^0$ state to a $2p^54f^15d^1$ final state [8,10,30-32]. In contrast the absorption edge of Ce^{4+} species, such as in CeO_2, is characterized by three features attributed to the transition from an initial $2p^64f^05d^0$ state to a $2p^54f^25d^1\underline{L}^2$, $2p^54f^15d^1\underline{L}^1$, and $2p^54f^05d^1$ final states, in order of increasing energy[8,10,31-33]. These features are well resolved in the laboratory XANES data and led us to investigate the potential for speciation of an unknown. Figure 1 also shows Ce L_3 edge XANES data acquired from a zirconolite ceramic with composition $Ca_{0.75}Ce_{0.25}ZrTi_{1.5}Al_{0.5}O_7$ developed for immobilization of UK separated civil plutonium. These data are the summation of 10 individual data sets, with a total data collection time of ca. 8h; note that the concentration of the Ce absorber species is only 2.3 mol%.

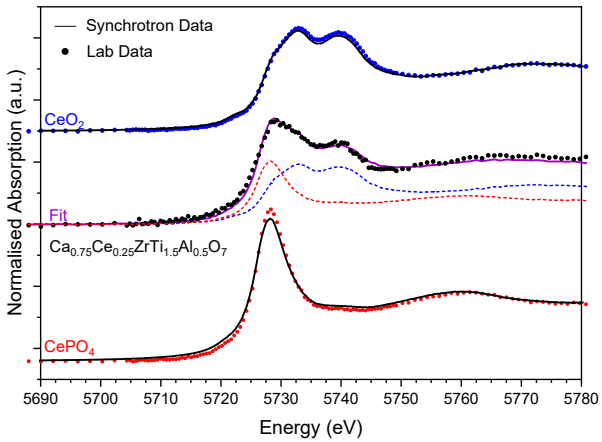

Fig. 2: Laboratory Ce L_3 XANES of $CePO_4$ (Ce^{3+}) and CeO_2 (Ce^{4+}) reference compounds (solid points) and linear combination fit (solid pink line)) to Ce L_3 XANES data of $Ca_{0.75}Ce_{0.25}ZrTi_{1.5}Al_{0.5}O_7$ (solid points), contributions of reference compounds to linear combination fit are shown by dotted lines, see text for details; synchrotron data are shown as a solid black line.

X-ray powder diffraction and SEM / EDX analysis of ceramic $Ca_{0.75}Ce_{0.25}ZrTi_{1.5}Al_{0.5}O_7$ demonstrated the phase assemblage of this material to be 84.9 wt% zirconolite, with 13.5 wt% (Ca,Ce)TiO_3 perovskite and 1.6 wt% Al_2O_3. The Ce L_3 XANES data acquired from the zirconolite ceramic show features characteristic of both Ce^{3+} and Ce^{4+} species, by comparison with the reference compounds. Linear combination fitting of the reference spectra to that of the zirconolite ceramic afforded an estimate of 57.2 % Ce^{3+} and 42.8 % Ce^{4+} species, with the constraint of $(1 - x)$ Ce^{4+} + x Ce^{3+} = 1 (where x is the weight fraction). The fitted linear combination of $CePO_4$ and CeO_2 spectra is excellent (R factor = 0.003) and demonstrates that effective Ce speciation may be achieved using laboratory XANES with reasonable data collection time, even for quite low absorber concentrations. The presence of Ce^{3+} is consistent with the formation of a significant minor fraction of perovskite phase, in which this species is known to preferentially partition, given the identical ionic radii for Ce^{3+} and Ca^{2+} (1.48Å), with respect to the 12- co-ordinate site in the perovskite structure[34].

U L_3 XANES

Uranium shows a rich redox chemistry in the nuclear fuel cycle, involving oxidation states U^{4+}, U^{5+} and U^{6+}, which is often of critical importance in understanding structure – property – function relations in chemical and materials systems[9,13]. The investigation of uranium bearing materials at a synchrotron source is, understandably, governed by strict safety protocols relating to sample transport and experimental procedure. Routine analysis of U L_3 XANES would therefore be of considerable impact in nuclear fuel cycle research, including radioactive waste management and disposal. Figure 4 compares U L_3 laboratory and synchrotron XANES data acquired from UTi_2O_6; the data collection parameters are summarized in Table 1. Comparison of the laboratory and synchrotron XANES data shows that the near edge features are well reproduced in the laboratory data, albeit with lower signal to noise as a result of the low photon flux. However, there is some mismatch in the measured absorption in the region of the white line. Such distortions are symptomatic of sample thickness and/or "leakage" effects. In the present case, the sample was prepared to yield an effective thickness of $\mu x = 1$, with due regard to homogeneity, and thus cannot be considered to be overly thick. "Leakage" effects incorporate a multitude of signal distortions arising from the contribution to the measured transmission of harmonics, stray scatter, and the low energy tail of the monochromator function (I_{lk})[35]. Consequently, $\mu = \ln (I_0 - I_{0,lk}) / (I_t - I_{t,lk})$, and thus μ no longer strictly depends on I_0 and I_t. In simple terms, I_{lk} makes a significant contribution to the measured I_t, which is small because μ is a maximum at the white line and the sample is strongly attenuating. The data can be effectively corrected for this "leakage" effect, by measurement of $I_{0,lk}$ and $I_{t,lk}$, which is achieved by using a large detector offset, in this case 4.0°, as shown by comparison of Figure 3 and 4.

Figure 4 shows a comparison of laboratory and synchrotron U L_3 XANES acquired on reference compounds UTi_2O_6, $U_{0.55}Yb_{0.45}TiO_6$, and UO_3, with correction of laboratory data for "leakage" effects. In Figure 4, the laboratory and synchrotron data are shown as points and solid lines, respectively, and are clearly in excellent agreement. A small deviation in laboratory and synchrotron XANES data of UO_3 is apparent in the region of the white line, which is thought to arise from the fact that this sample was strongly self-attenuating. Table 1 summarises the energy E_0 associated with the X-ray

absorption edge, from laboratory and synchrotron XANES data, determined as the first peak in the first derivative. The agreement between laboratory and synchrotron determined E_0 values is remarkable, within 0.1 eV for each compound. The chemical shift range of E_0 for the reference compounds is certainly resolvable using laboratory XAS, which should enable the routine speciation of "unknown" uranium oxidation states,

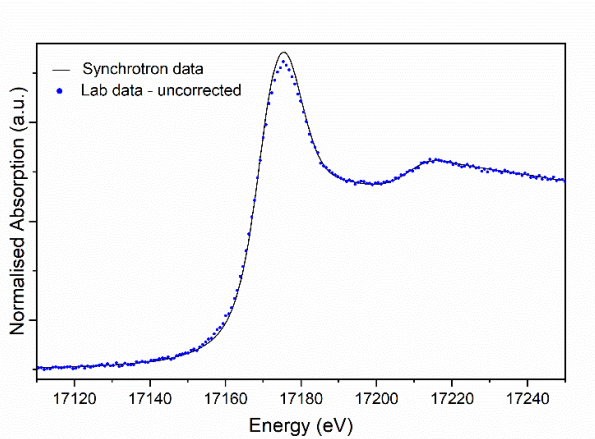

if the absorber is sufficiently concentrated. To test that hypothesis, we acquired laboratory U L_3 XANES data from a brannerite glass ceramic, comprising nominally 50wt% UTi_2O_6 crystallised in 50wt% $Na_2AlBSi_2O_6$ glass. The data and E_0, presented in Figure 4 and Table 1, are in excellent agreement with those acquired from crystalline UTi_2O_6.

Fig. 3. Comparison of laboratory and synchrotron U L_3 XANES data from UTi_2O_6, without correction of laboratory data for "leakage" effects – see text for details.

Assuming E_0 to have a linear dependence on oxidation state for the brannerite structure, then by interpolation between UTi_2O_6 and $U_{0.55}Yb_{0.45}TiO_6$, we estimate the bulk U oxidation state in the glass ceramic to be 4.2 ± 0.1. The marginally higher oxidation state compared to the bulk ceramic is thought to arise from the minor contribution of U incorporated in the glass phase as U^{5+} or U^{6+}. Note that these data also demonstrate the potential for performing U L_3 XANES speciation studies on relatively dilute absorber concentrations, using a commercially available laboratory XAS spectrometer.

Compound	U Mol%	Oxidation State	Laboratory			Synchrotron		
			No. scans	Time (h)	E_0 (eV)	No. scans	Time (min)	E_0 (eV)
UTi_2O_6	11.1	4.0+	20	15	17,164.51	3	15	17,164.65
$U_{0.55}Yb_{0.25}Ti_2O_6$	6.1	5.0+	20	15	17,166.04	3	15	17,166.15
UO_3	25.9	6.0+	20	15	17,169.47	3	15	17,169.87
UTi_2O_6 GC	2.8	4.2 (±0.1)+	20	15	17,164.65			

Table 1. Data collection parameters for laboratory and synchrotron U L_3 XANES data; precision in E_0 estimated to be ± 0.4 and ± 0.3 eV respectively; note GC – glass ceramic.

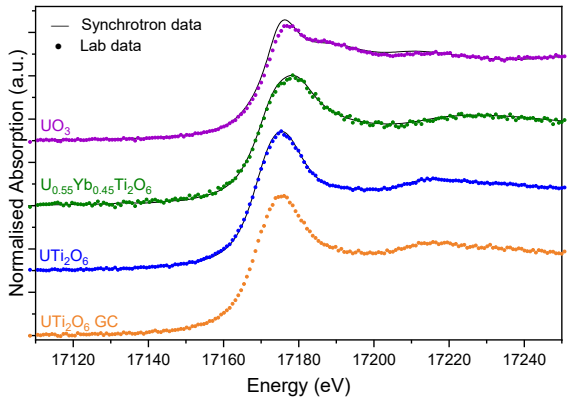

Fig 4. Comparison of laboratory (points) and synchrotron (black solid line) U L_3 XANES data from reference compounds incorporating U^{4+} – UTi_2O_6, U^{5+} – $U_{0.55}Yb_{0.45}Ti_2O_6$, U^{6+} – UO_3, and a brannerite glass ceramic with unknown U oxidation state; note: laboratory data were corrected for "leakage" effects; GC – glass ceramic.

CONCLUSIONS

Laboratory XANES at the Ce L_3 and U L_3 edge were successfully demonstrated for speciation studies in ceramic and glass-ceramic waste forms, by comparison to reference compounds. At the U L_3 edge, XANES data are susceptible to "leakage" effects which suppress the white line and XANES features, however, it is possible to correct data for this effect by measurement and subtraction of the total background scatter and harmonic contribution. The XANES features of Ce^{3+} and Ce^{4+} allow straightforward determination of these oxidation states and, by linear combination fitting of reference compounds, determination of the average of mixed oxidation states. With respect to the U L_3 edge, the chemical shift of E_0 with oxidation state, for three reference compounds, was found to be in excellent agreement between laboratory and synchrotron data. By comparison with the chemical shift of these reference compounds bulk speciation of U was effectively achieved for a brannerite glass-ceramic. This investigation also demonstrated the application of laboratory XANES to materials with absorber concentrations of only a few mol%, which is relevant to optimization of the materials chemistry of waste form materials through routine characterisation, albeit with data acquisition times of several hours. In this context, laboratory XANES is of particular utility in enabling the analysis of radiological materials within a dedicated hot lab, without necessitating transport to a synchrotron radiation facility, for which there is a significant administrative overhead, and very stringent safety controls, even for kBq quantities of uranium and thorium.

ACKNOWLEDGEMENTS

We are grateful for financial support from the Nuclear Decommissioning Authority and EPSRC under grant numbers EP/M026566/1, EP/S01019X/1, EP/N017870/1 and EP/R511754/1. This research utilised the HADES / MIDAS facility at The University of Sheffield established with financial support from EPSRC and BEIS, under grant

EP/T011424/1. We gratefully acknowledge G.T. Seidler and D.R. Mortensen for useful discussions in support of this study. This research was performed, in part, at Diamond Light Source, Beamline B18, with beamtime awarded under proposal SP17243. This research used resources [or insert beamline if applicable] of the National Synchrotron Light Source II, a U.S. Department of Energy (DOE) Office of Science User Facility operated for the DOE Office of Science by Brookhaven National Laboratory under Contract No. DE-SC0012704.

References

1. D.J. Bailey, M.C. Stennett, A.R. Mason, N.C. Hyatt, J. Nucl. Mater., **503**, 164 (2018).
2. D.J. Bailey, M.C. Stennett, B. Ravel, D. Grolimund, N.C. Hyatt, RSC Advances, **8**, 2092 (2018).
3. D.S. Patil, M. Konale, M. Gabel, O.K. Neill, J.V. Crum, A. Goel, M.C. Stennett, N.C. Hyatt, J.S. McCloy, J. Nucl. Mater., **510**, 539 (2018).
4. K. Joseph, M.C. Stennett, N.C. Hyatt, R. Asuvathraman, C.L. Dube, A.S. Gandy, K.V.G. Kutty, K. Jolley, P.R.V. Rao, R. Smith, J. Nucl. Mater., **494**, 342 (2017).
5. M.A. Kim, J.H. Song, W. Um, N. Hyatt, S.K. Sun, J. Heo, Ceram. Int., **43**, 4687 (2017).
6. C.L. Corkhill, D.J. Bailey, F.Y, Tocino, M.C. Stennett, J.A. Miller, J.L. Provis, K.P. Travis, N.C. Hyatt, ACS Appl. Mater. Interf., **8**, 20562 (2016).
7. J. Squire, E.R. Maddrell, N.C. Hyatt, M.C. Stennett, Int. J. Appl. Tech., **12**, 92 (2015).
8. N.C. Hyatt, R.R. Schwarz, P.A. Bingham, M.C. Stennett, C.L. Corkhill, P.G. Heath, R.J.Hand, M. James, A. Pearson, S. Morgan, J. Nucl. Mater., **444**, 186 (2014).
9. A.J. Connelly, N.C.Hyatt, K.P. Travis, R.J.Hand, M.C. Stennett, A.S. Gandy, A.P. Brown, D.C. Apperley, J. Non Cryst. Solids, **378**, 282 (2013).
10. M.C. Stennett, C.L. Freeman, A.S. Gandy, N.C. Hyatt, J. Solid State Chem., **192**, 172 (2012).
11. N.J. Cassingham, M.C. Stennett, P.A. Bingham, N.C. Hyatt, G. Aquilanti, Int. J. Appl. Glass Sci., **2**, 343 (2011).
12. P.A. Bingham, A.J.Connelly, N.J. Cassingham, N.C. Hyatt, J. Non Cryst. Solids, **357**, 2726 (2011).
13. A.J. Connelly, N.C. Hyatt, K.P. Travis, R.J. Hand, E.R. Maddrell, R.J. Short, J. Non Cryst. Solids, **357**, 1647 (2011).
14. D.P. Reid, M.C. Stennett, B. Ravel, J.C. Woicik, N. Peng, E.R. Maddrell, N.C. Hyatt, Nucl. Inst. Meth. Phys. Res. B, **268**, 1847 (2010).
15. R.J. Short, R.J. Hand, N.C. Hyatt, G, Mobus, J. Nucl. Mater., **340**, 179 (2005).
16. N.C. Hyatt, R.J. Short, R.J. Hand, W.E. Lee, F. Livens, J.M. Charnock, R.L. Bilsborrow, Ceramic Transactions, **168**, 179 (2005).
17. G.T. Seidler, D.R. Mortensen, A.J. Remesnik, J.I. Pacold, N.A. Ball, N. Barry, M. Styczinski, O.R. Hoidn, Rev. Sci. Instr., **85**, 113906 (2014).
18. D.R. Mortensen, G.T. Seidler, A.S. Ditter, P. Glatzel, J. Phys. Conf. Ser., **712**, 012036 (2016).
19. G.T. Seidler, A.S. Ditter, N.A. Ball, A.J. Remesnik, J. Phys. Conf. Ser., **712**, 012015 (2016).
20. E.P. Jahrman, W.M. Holden, A.S. Ditter, D.R. Mortensen, G.T. Seidler, T.T. Fister, S.A. Kozimor, L.F.J. Piper, J. Rana, N.C. Hyatt, M.C. Stennett, Rev. Sci. Instr., **90**, 024106 (2019).
21. A.P. Honkanen, S. Ollikkala, T. Ahopelto, A.J. Kallio, M. Blomberg, S. Huotari, Rev. Sci. Instr., 90, 033107 (2019).
22. C. Schlesiger, L. Anklamm, H. Stiel, W. Malzer, B. Kanngiesser, J. Anal. Atomic Spectr., **30**, 1080 (2015).
23. Z. Nemeth, J. Szlachetko, E.G. Bajnoczi, G. Vanko, Rev. Sci. Instr., **87**, 103105 (2016).
24. W. Malzer, G. Grotzsch, R. Gnewkow, C. Schlesiger, F. Kowalewski, B. Van Kuiken, S. DeBeer, B. Kanngiesser, Rev. Sci. Instr., **89**, 113111 (2018).
25. W. Blachucki, J. Czapla-Masztafiak, J. Sa, J. Szlachetko, J. Anal. Atomic Spectr., **34**, 1409 (2019).
26. F. Zeeshan, J. Hoszowska, L. Loperetti-Tornay, J.C. Dousse, Rev. Sci. Instr., **90**, 073105 (2019).
27. R.Bès, T.Ahopelto, A.-P.Honkanen, S.Huotari, G.Leinders, J.Pakarinen, K.Kvashnina, J. Nucl. Mater., 507, 50 (2018).
28. B. Ravel, M. Newville, J. Synch. Rad., **12**, 537 (2005).
29. J.A. Bearden, A.F. Burr, Rev. Mod. Phys., 39, 125 (1967).
30. M. C. Dixon Wilkins, M.C. Stennett, N.C. Hyatt, in review, MRS Advances (2019).
31. A. Bianconi, A. Marcelli, H. Dexpert, R. Karnatak, A. Kotani, T. Jo, J. Petiau, Phys. Rev. B, **35**, 806 (1987)
32. A. Soldatov, T. Ivanchenko, S. Dellalonga, A. Kotani, Y. Iwamoto, A. Bianconi, Phys. Rev. B, **50**,

5074 (1994).
33. D.P. Reid, M.C. Stennett, N.C. Hyatt, J. Solid State Chem., **191**, 2 (2012).
34. R.D. Shannon, Acta Cryst., **A32**, 751 (1976).
35. E. A. Stern and K. Kim, Phys. Rev. B, **23**, 3781 (1981).

DOI: 10.3190/jgeosci.XXX

Original paper

A feasibility investigation of speciation by Fe K edge XANES using a laboratory X-ray absorption spectrometer

Lucy M. Mottram[1], Samuel Cafferkey, [1] Amber R. Mason, Tom Oulton,[1] Shi Kuan Sun,[1] Daniel J. Bailey,[1] Martin C. Stennett[1], and Neil C. Hyatt[1*]

1 Department of Materials Science and Engineering, The University of Sheffield, Mappin Street, Sheffield, S1 3JD, UK;

n.c.hyatt@sheffield.ac.uk

* *Corresponding author*

Keywords: XANES, X-ray Absorption Spectroscopy, iron, speciation, laboratory.

Running title: Speciation by laboratory Fe K-edge XANES

Abstract

We demonstrate effective speciation of Fe in model compounds from analysis of the weak pre-edge features in Fe K-edge XANES spectra, with a commercially available laboratory X-ray spectrometer, using a spherically bent crystal analyser, and a low power X-ray tube, in Rowland circle geometry. Direct comparison with XANES data acquired from a third generation synchrotron bending magnet beamline, using the same specimens, validated quantitative agreement in determination of the total integrated intensity and centroid position of the pre-edge feature, which are a probe of the electronic configuration and symmetry of the absorber atom, and hence oxidation state and co-ordination number. This work opens the door to rapid and routine speciation studies of Fe by laboratory XANES, even for materials with relatively dilute absorber concentration of only a few mol%.

1. Introduction

The redox chemistry of iron is of fundamental importance in Earth science and plays a crucial role in geochemical and biogeochemical processes (Taylor and Konhauser 2011). Iron is so far known to adopt formal oxidation states from Fe^{2-} to Fe^{6+}, although the most common oxidation states are ferrous Fe^{2+} and ferric Fe^{3+} (Greenwood and Earnshaw 1997). Redox transformations involving Fe^{2+} and Fe^{3+} are of critical importance in geological, environmental, biological and material processes, and, for example, the Fe^{2+} / Fe^{3+} ratio is commonly exploited to constrain the conditions of mineral and glass formation (Wood and Virgo 1989; Taylor and Konhauser 2011; Joseph et al. 2017). X-ray absorption spectroscopy (XAS) has proven a powerful tool for the determination of Fe speciation in minerals and materials (Waychunas et al. 1983; Bajt et al. 1994; Galoisy et al. 2001; Petit et al. 2001; Wilke et al. 2001; Berry et al. 2003; Joseph et al. 2017), however, routine application is inhibited by the requirement to access XAS beamlines at synchrotron radiation facilities, which is highly competitive, time limited, and not immediate. The weak pre-edge features in the Fe K-edge X-ray Absorption Near Edge Structure (XANES), located ca. 15 - 20 eV below the edge step, have been shown to be a particularly sensitive probe of Fe speciation (Waychunas et al. 1983; Bajt et al. 1994; Galoisy et al. 2001; Petit et al. 2001; Wilke et al. 2001; Berry et al. 2003; Joseph et al. 2017). These features are associated with 1s – 3d (quadrupole) and/or 1s – 4p (dipole) electronic transitions in the Fe absorber atom and, therefore, are sensitive to both the electronic configuration and symmetry, from which oxidation state and co-ordination number are inferred.

Wilke *et al.* developed a systematic methodology to extract the normalised pre-edge features from Fe K-edge XANES data and determination of the centroid energy position and total integrated intensity, which was effectively correlated with Fe oxidation state and co-ordination number (Petit et al. 2001; Wilke et al. 2001). This methodology utilised high

resolution XANES data from mineral reference compounds, primarily acquired using the undulator beamline ID26 with a Si (220) double crystal monochromator, at the European Synchrotron Radiation Facility. This methodology has subsequently been widely applied (685 citations up to the end of 2019 (Wilke et al. 2001)).

In recent years, a renaissance in laboratory instrumentation for X-ray absorption and emission spectroscopy, has been driven by exploitation of Spherically Bent Crystal Analysers (SBCAs) in a Rowland circle geometry or bent cylindrical monochromators in von Hamos geometry (Seidler et al. 2014, 2016; Schlesiger et al. 2015; Mortensen et al. 2016; Nemeth et al. 2016; Holden et al. 2017; Malzer et al. 2018; Jahrman et al. 2019; Blachucki et al. 2019; Honkanen et al. 2019; Jahrman et al. 2019; Zeeshan et al. 2019; Mottram et al. 2020). In principle, such instrumentation may allow good quality X-ray absorption or emission spectroscopy to be *routinely* acquired from materials with moderately dilute to concentrated absorbers in a matter of hours, without recourse to a synchrotron light source. Here, we report the results of a preliminary comparative investigation of Fe speciation by analysis of weak pre-edge features in Fe K-edge X-ray Absorption Near Edge Structure (XANES) using a commercially available laboratory spectrometer based on the design of Seidler *et al*., which is also capable of acquisition of the full Extended X-ray Absorption Fine Structure (EXAFS) in favourable circumstances (Seidler et al. 2014, 2016; Mortensen et al. 2016; Jahrman et al. 2019). The spectrometer arrangement utilises SBCAs in a 1m Rowland circle geometry, Fig. 1 and Fig. 2, in which energy scanning is achieved through symmetrical movement of detector and source. Linear translation stages are used to increment Bragg angle steps, with the alignment of source, SBCA and detector maintained by steering bars. The spectrometer operates close to back scattering geometry to maximise resolution and thus requires a different SBCA to scan several hundred eV. In our set up, the high efficiency of the SBCAs enables the use of a relatively inexpensive, low power, air cooled, X-ray source (100 W), which is sufficient for

transmission mode investigation of moderately dilute absorbers in a favourable matrix, with a data collection time of several hours (it is also possible to utilise a fixed X-ray source of 1.5kW with suitable modification of the optical arrangement, as highlighted by Honkanen et al. 2019) With robust initial SBCA alignment (Mortensen et al. 2017), change over and alignment of SBCAs is straightforward and can be achieved in 20 minutes or less. In the following, we first compare the resolution performance of this laboratory spectrometer in comparison with a synchrotron bending magnet beamline at a third generation synchrotron source. Using the well established methodology of Wilke *et al.* (Petit et al. 2001; Wilke et al. 2001), we then demonstrate that laboratory XANES data from reference compounds can be analysed to accurately infer Fe speciation from the weak pre-edge features, even in the case of a relatively dilute Fe concentration of a few mol %.

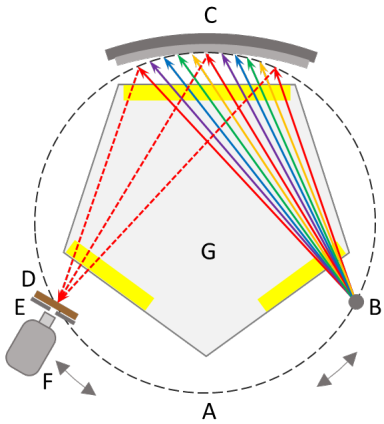

Fig. 1 Schematic representation of Rowland circle geometry for laboratory transmission X-ray Absorption Spectroscopy, as described in the text, showing: Rowland circle (A), broadband low power X-ray source (B); spherically bent crystal analyser (C); sample (D) and slit (E) arrangement; silicon drift detector (F); and helium filled beam path with kapton windows (G).

Fig. 2 Photograph of EasyXAFS XES100 spectrometer arrangement shown in Fig. 1, with helium filled beam path removed, to show linear translation stages and steering bars used to maintain alignment of X-ray source (A), spherically bent crystal analyser (B); and sample, slit and detector assembly (C).

2. Materials and Methods

2.1. Materials

The materials investigated in this study are summarised in Tab. 1. $NaFeSi_2O_6$ and $FePO_4$ are characterised by Fe^{3+}, co-ordinated by oxygen in an octahedral and tetrahedral co-ordination, respectively (Arnold 1986; Baum et al. 1988). Fe_2SiO_4 and $Fe_{1.5}Mg_{0.5}Al_{9.1}Si_{3.9}(OH)_2$ are characterised by Fe^{2+}, co-ordinated by oxygen in an octahedral and tetrahedral co-ordination, respectively (Smyth 1975; Hawthorne et al. 1993). Polycrystalline $FePO_4$ and Fe_2SiO_4 were, respectively, synthesised by: solid state reaction of Fe_2O_3 and $NH_4H_2PO_4$ at 900 °C in air for 16 h; and solid state reaction of stoichiometric quantities of Fe, Fe_2O_3 and SiO_2 at 750 °C for

48 h in a sealed, evacuated, quartz tube. Mineral specimens of agerine - $NaFeSi_2O_6$ (Langesund Fjord, Norway), and staurolite – $Fe_{1.5}Mg_{0.5}Al_{9.1}Si_{3.9}(OH)_2$ (Georgia, USA), were provided from our own collection. All materials were confirmed to be single phase by powder X-ray diffraction. The expected Fe speciation was verified by ^{57}Fe Mossbauer analysis.

Material	Fe oxidation state	CN	Fe Concentration (mol%)	Lab data collection time (h)
$NaFeSi_2O_6$ *Agerine: Langesund Fjord (Norway)*	3+	6 (O_h)	10.0	6
$FePO_4$ *Synthetic*	3+	4 (T_d)	16.7	5
Fe_2SiO_4 *Synthetic*	2+	6 (O_h)	28.6	4
$Fe_{1.5}Mg_{0.5}Al_{9.1}Si_{3.9}(OH)_2$ *Staurolite: Georgia (USA)*	2+	4 (T_d)	3.7	8

Tab. 1 Materials analysed in this study, summarising Fe oxidation state, co-ordination number by oxygen (and symmetry), Fe concentration, and data collection time.

2.2. *X-ray absorption spectroscopy*

Fe K-edge XANES data were acquired in transmission mode using a commercially available laboratory spectrometer and the DUBBLE beamline, BM 26, of the European Synchrotron Radiation Facility.

The laboratory spectrometer, based on the design of Seidler *et al*. (Seidler et al. 2014, 2016; Mortensen et al. 2016; Jahrman et al. 2019), was an EasyXAFS XES100 system, equipped with an air cooled X-ray tube operating at 25 kV and 4 mA, with a Hitatchi Vortex Silicon Drift Detector (SDD). The spectrometer was configured with a Ge (620) SBCA to scan the energy range 6970 – 7340 eV, with a step size of 0.25 – 1.00 eV and constant count time of 4s / point in the XANES region (total scan time 30 min for 0.25 eV step size). The energy resolution of the SDD is ca. 140 eV, enabling rejection of the harmonic content of the incident beam and background scatter. A He flight path was used to minimise air scatter and

absorption. Transmission data were acquired with ($I_t(E)$) and without the sample ($I_0(E)$), using the same scan parameters. The Ge (620) monochromator was aligned using the clock angle procedure of Mortensen and Seidler, to account for the crystal miscut (Mortensen et al. 2017).

The DUBBLE beamline is situated on a bending magnet and was configured with a Si (111) channel cut monochromator and Si mirror for harmonic rejection (Borsboom et al. 1988). Incident and transmitted beam intensities were measured using ionization chambers, filled with mixtures of He and N_2, operated in a stable region of their I/V curve. For synchrotron data, a step size of 0.25 eV was used in the XANES region with a count time of 1s / point. Samples were prepared from finely ground specimens dispersed in 70 mg of polyethylene glycol, pressed into 13 mm diameter pellets, to achieve a thickness of one absorption length. Data reduction and analysis was performed using the programs Athena and Hephaestus (Ravel et al. 2005). Calibration of the energy scale was achieved by reference to a 5 μm Fe foil (Goodfellow Cambridge Ltd.), for which the first peak in the derivative spectrum was set to 7112.00 eV, as defined by Bearden and Burr for the Fe K absorption edge (Bearden et al. 1967). For laboratory XANES data, Fe foil data were acquired using the same methods as for the sample materials. The Bragg angle of $\theta = 77.7084^{o}$, corresponding to the first peak of the derivative spectrum was set equivalent to 7112.00 eV, enabling the energy scale to be calibrated according to:

$$E_c = \frac{E_m sin(\theta)}{sin(\theta + \Delta\theta)}$$

where, E_m is the measured energy, E_c the calibrated energy, $\Delta\theta$ is the difference between the Bragg angle corresponding to E_c and E_m.

For synchrotron XANES data, an Fe foil was measured simultaneously with the samples, and the energy scale calibrated using the alignment tool in the Athena program (Ravel et al.

2005). Extraction and analysis of the pre-edge feature in Fe K-edge XANES data was achieved using Microsoft Excel software, to first fit a spline function to model and subtract the contribution of the edge step. The pre-edge envelope was then deconvoluted by fitting Gaussian components using a linear least squares refinement to optimise the normalised height, full width at half height, and energy position, so as to minimise the difference between the observed and calculated envelope determined from the sum of the fitted Gaussian components. Fitting initially utilised two Gaussian components with the significance of a third component tested by inspection of the improvement in goodness of fit. The total integrated intensity and centroid energy of the pre-edge feature were determined, respectively, from the sum of the integrated intensities and intensity weighted average energy position of the Gaussian components. The same initial parameters were used for all data sets, and several sets of different initial parameters trialled, to ensure that convergence did not arise in a local minimum. This approach is a simplification of that applied by Wilke *et al*., which employed pseudo-Voigt components (Petit et al. 2001; Wilke et al. 2001).

3. Results

3.1. Spectrometer performance at Fe K-edge

The robustness of the laboratory spectrometer and resolution at the Fe K-edge was investigated by acquisition and analysis of XANES data from an Fe foil. Fig. 3 shows the result of a merging 10 individual XANES scans (0.25 eV resolution, black line), between each individual scan, the sample carousel was removed and the Fe foil unmounted. Data were background subtracted and normalised prior to merging, but were not aligned. The resulting standard deviation in the merged data (red line) shown in Fig. 3, attests to robustness of the spectrometer alignment and scan to scan reproducibility. Next, as shown in Fig. 4, laboratory data were acquired at step sizes of 0.25, 0.50, 0.75 and 1.00 eV in the XANES region (points)

and compared with synchrotron data from the DUBBLE beamline acquired at 0.25 eV step size (solid line), as the first derivative to amplify the XANES features. Comparison of these spectra shows that a step size of 0.5 eV accurately approximates the synchrotron data, but a step size of 0.75 eV or greater does not fully resolve features apparent in the synchrotron data. The resolution of our laboratory data are therefore comparable with that achievable with a Si (111) monochromator on a bending magnet beamline at a third generation synchrotron source, providing confidence in the characterisation of weak pre-edge features. Note that the core-hole life time is estimated to impose a limiting resolution of 1.25 eV at the Fe K-edge (Krause et al. 1979), which dominates the resolution of both our laboratory and synchrotron data. For the purpose of head to head comparison a step size of 0.25 eV was maintained for acquisition of XANES data from Fe reference compounds.

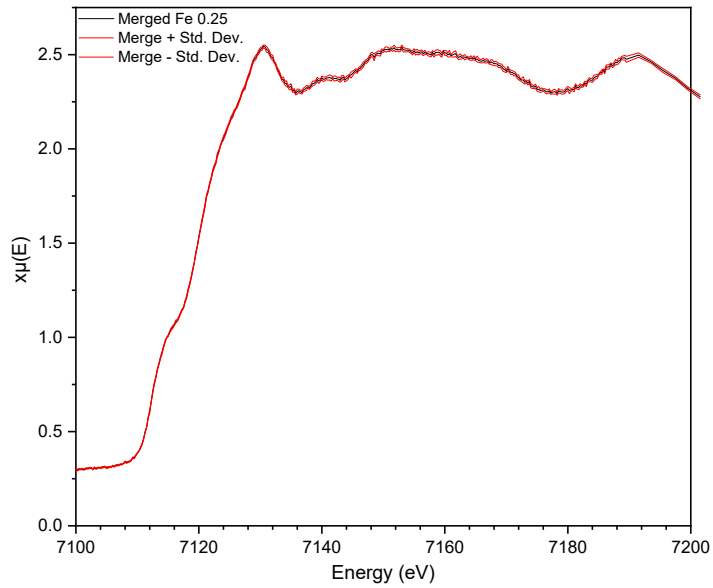

Fig. 3 – Merge of 10 independent XANES data sets from Fe foil (0.25 eV resolution, black line) with standard deviation (red line).

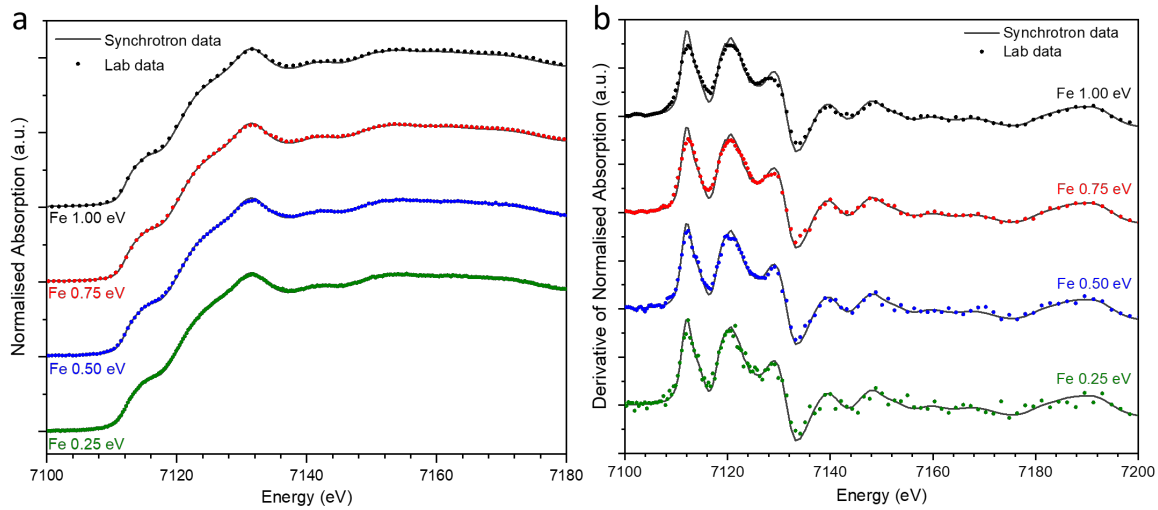

Fig 4a – Comparison of synchrotron (0.25 eV resolution, black line) and laboratory (0.25 – 1.00 eV resolution, points) acquired XANES data; **b** - Comparison of first derivative of synchrotron (0.25 eV resolution, black line) and laboratory (0.25 – 1.00 eV resolution, points) acquired XANES data, to emphasise correspondence of features.

3.2. *Laboratory and synchrotron Fe K-edge XANES of model compounds*

Fig. 5 compares the laboratory and synchrotron Fe K-edge XANES data acquired from the reference compounds in Tab. 1. Overall, the observed chemical shift and XANES features are in excellent agreement between the data sets, when the synchrotron data are convoluted by a Lorenztian function of 0.75 eV full width at half maximum (FWHM). For the staurolite data in particular, which presents relatively sharp features in the region of the white line, this convolution greatly improves the agreement between synchrotron and laboratory data. We also corrected laboratory data for the "leakage" effect, which arises from contamination of I_0 and I_t by photons arising from the low energy tail of the monochromator function, harmonics and scattering (I_{lk}) (Stern et al. 1981). Consequently, $\mu = \ln (I_0 - I_{0,lk}) / (I_t - I_{t,lk})$, and thus μ no longer strictly depends on I_0 and I_t. In simple terms, the distortion arises because, at the white line, where μ is a maximum, I_{lk} makes a non-negligible contribution to the measured I_t,

which is small because of the dilute concentration in a relatively absorbing matrix: thus, the measured absorption is less than the true absorption. In the present investigation, this correction had marginal impact on the laboratory XANES data.

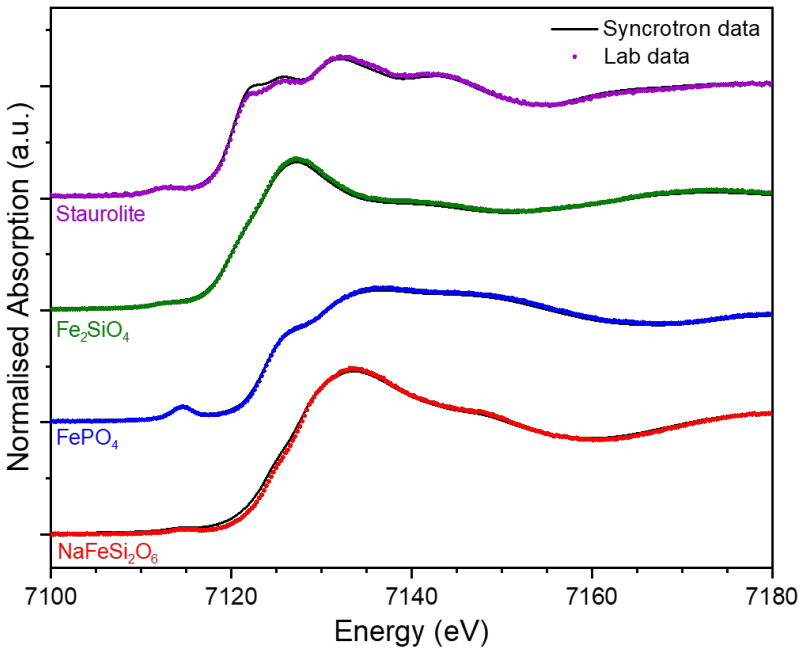

Fig. 5 Comparison of normalised transmission mode Fe K-edge XANES spectra from reference compounds $NaFeSi_2O_6$, $FePO_4$, Fe_2SiO_4, and staurolite – $Fe_{1.5}Mg_{0.5}Al_{9.1}Si_{3.9}(OH)_2$, (prepared to $\mu x = 1$), acquired using laboratory XAS spectrometer (points) and DUBBLE beamline (solid line); syncrotron data were broadened by a Lorentzian function of 0.75 eV FWHM.

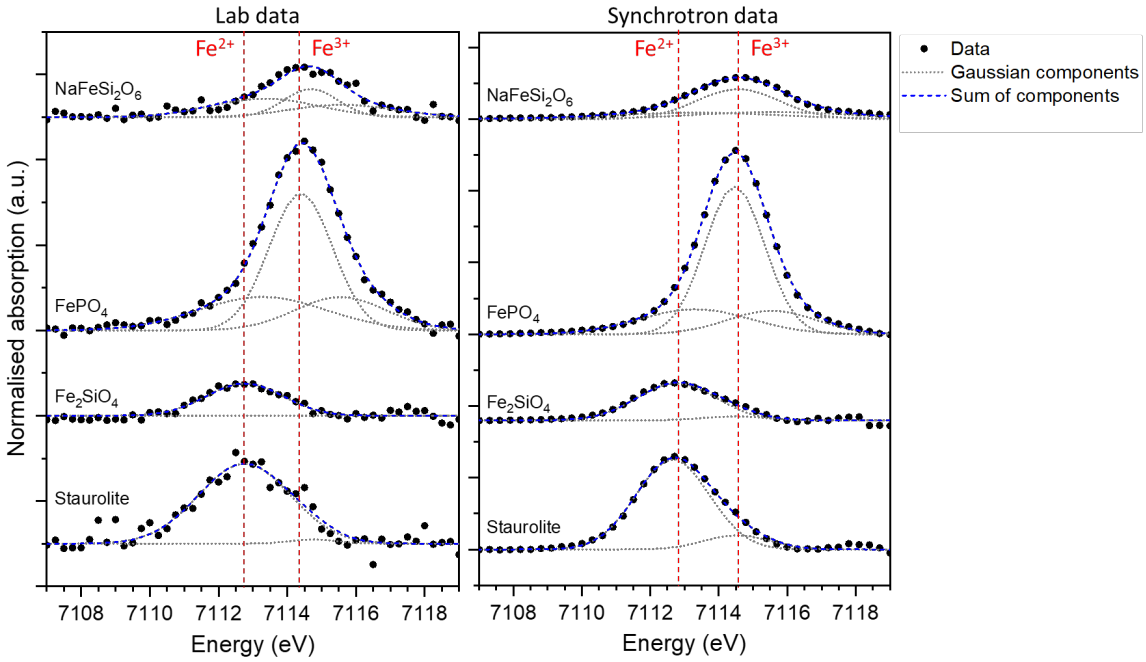

Fig. 6 Normalised pre-edge spectra at Fe K edge (points) from reference compounds $NaFeSi_2O_6$, $FePO_4$, Fe_2SiO_4, and $Fe_{1.5}Mg_{0.5}Al_{9.1}Si_{3.9}(OH)_2$, acquired using laboratory XAS spectrometer and DUBBLE beamline, showing fitted Gaussian components (grey dotted line) and their summation envelope (blue dotted line).

Fig. 7 and Tab. 2 compare the extracted pre-edge features from laboratory and synchrotron XANES data and the modelled envelope of the Gaussian components (here the synchrotron data are not convoluted by Lorentzian broadening). For each material, the pre-edge features of the laboratory and synchrotron XANES data were adequately modelled using the same number of Gaussian components (either two or three). Although the laboratory data clearly demonstrate more scatter in comparison to the synchrotron data, as expected due to lower signal to noise ratio, the correspondence between the data sets is remarkable. The centroid energy of the pre-edge features of Fe^{2+} and Fe^{3+} species are clearly distinguished at 7112.9 ± 0.1 eV and 7114.5 ± 0.1 eV respectively, in both the laboratory and synchrotron data. For each Fe species, the measured normalised intensity of the pre-edge feature is also in excellent

agreement between laboratory and synchrotron data sets. As expected, the pre-edge features of the tetrahedral Fe species present in $FePO_4$ and $Fe_{1.5}Mg_{0.5}Al_{9.1}Si_{3.9}(OH)_2$, have considerably greater intensity than those of the octahedral species present in $NaFeSi_2O_6$ and Fe_2SiO_4. As noted above, and discussed below, the pre-edge features are primarily associated with 1s – 3d quadrupole transitions, which are only weakly allowed for octahedral Fe since the initial and final states are centrosymmetric. In the non-centrosymmetric tetrahedral environments, the transition probability is enhanced due to admixture of unoccupied 4p orbitals in the final state.

Material	Gaussian 1		Gaussian 2		Gaussian 3		Centroid Energy (eV)	Total integrated intensity (a.u).
	Energy (eV)	Intensity (a.u.)	Energy (eV)	Intensity (a.u.)	Energy (eV)	Intensity (a.u.)		
$NaFe_2SiO_6$	**7113.3**	**0.042**	**7114.7**	**0.032**	**7115.6**	**0.027**	**7114.5**	**0.102**
Agerine: Langesund Fjord (Norway)	7113.4	0.027	7114.6	0.063	7115.6	0.028	7114.6	0.117
$FePO_4$	**7113.3**	**0.091**	**7114.5**	**0.186**	**7115.4**	**0.065**	**7114.4**	**0.343**
Synthetic	7113.3	0.071	7114.5	0.225	7115.5	0.053	7114.4	0.349
Fe_2SiO_4	**7112.7**	**0.063**	**7115.8**	**0.002**	-	-	**7112.8**	**0.063**
Synthetic	7112.8	0.075	7114.5	0.006			7112.9	0.081
$Fe_{1.5}Mg_{0.5}Al_{9.1}Si_{3.9}(OH)_2$	**7112.8**	**0.157**	**7114.8**	**0.004**	-	-	**7112.9**	**0.161**
Staurolite: Georgia (USA)	7112.7	0.169	7114.5	0.024			7112.9	0.192

Tab. 2 Integrated intensity and centroid energy for Gaussian components fitted to pre-edge features, and intensity weighted centroid position and total integrated intensity of fitted pre-edge envelope. Values in bold type are derived from laboratory data; values in normal type are derived from synchrotron data.

Fig. 7 compares the total integrated intensity and centroid energy of modelled pre-edge features extracted from our laboratory and synchrotron XANES data, and the synchrotron data reported by Wilke *et al*. (Petit et al. 2001; Wilke et al. 2001). To construct this plot, the data of Wilke *et al*. (calibrated to E_0 = 7111.08 eV), were shifted by +0.92 eV, consistent with our absolute energy scale. Fig. 7 shows that Fe speciation is clearly differentiated according to the total integrated intensity and centroid position of the pre-edge feature. The data points determined from laboratory and synchrotron data, acquired from identical materials, and

corresponding data points acquired by Wilke *et al*. on their materials, are seen to be in good overall agreement (solid points in Fig. 7). A systematic difference of ca. 0.25 eV is apparent between the pre-edge centroid energy determined from our laboratory and synchrotron data. This is of the order of the measurement step size and, therefore, likely arises from a small difference in calibration of the absolute energy scale (see also Tab. 2). The spread in determined total integrated intensities is approximately 15 – 20 % relative, with the laboratory determination systematically lower than our synchrotron determination. In the case of our laboratory data, the contribution of intensity in the tails of the pre-edge features is underestimated by the fitted Gaussian components, due to the lower signal to noise. Nevertheless, it is clear that both our laboratory and synchrotron data fall within the known Fe^{2+} and Fe^{3+} speciation fields, as shown by Fig. 7. Some scatter is apparent between our synchrotron data points and those of Wilke *et al*., for the same nominal materials, however, given that the samples, experimental set ups, and data analysis methods are not identical, we believe the overall agreement between the studies to validate the determination of Fe speciation by laboratory XANES data.

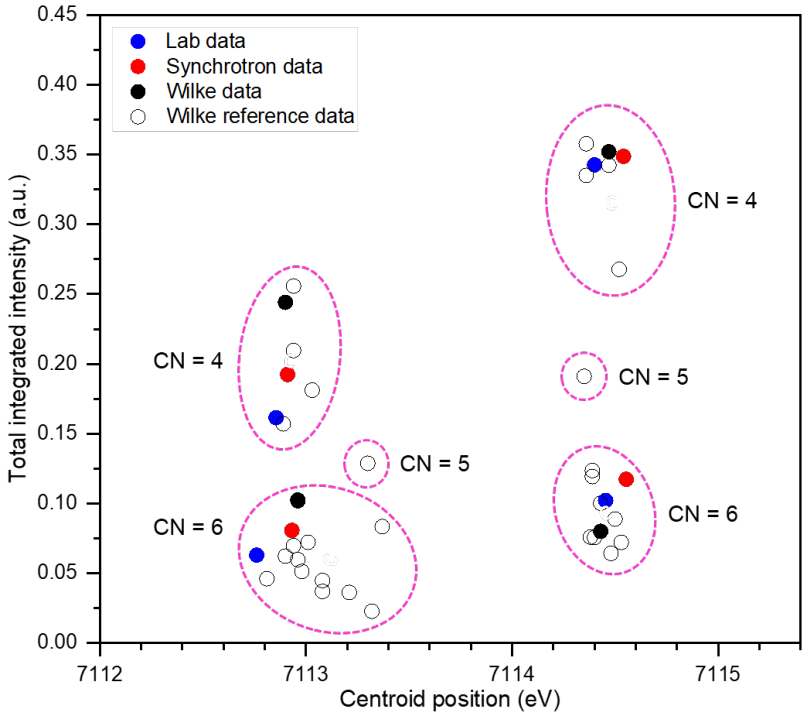

Fig. 7 Speciation field diagram, based on total integrated intensity and centroid energy of pre-edge feature of Fe K-edge XANES data. Data points derived from analysis of our laboratory and synchrotron data are shown as solid blue and red circles, respectively, equivalent data points from Wilke *et al*. (Wilke et al. 2001) shown as solid black circles. Other reference data from Wilke *et al*., shown as open black circles. Note data from Wilke *et al.*, are shifted by +0.92 eV consistent with our absolute energy scale as described in the text.

4. Discussion

The data presented in Fig. 5-7 show that good quality XANES data may be acquired in a matter of hours from compounds with moderately dilute to high Fe concentration, using a commercially available spectrometer, enabling routine speciation of Fe in the laboratory. Optimisation of the data acquisition strategy may yield efficiency gains for routine application. Good signal to noise, and a sufficiently small step size, are essential in the region

of the pre-edge and rising absorption edge, to enable accurate isolation of the pre-edge feature with optimal resolution. However, outside of this range, the density of data points used in this study could potentially be reduced by a factor of 2-4, without impacting on accuracy or precision of the pre-edge analysis, for high throughput routine analysis.

The weak pre-edge features observed in Fe K-edge XANES data are associated primarily with 1s – 3d (quadrupole) and 1s – 4p (dipole) electronic transitions (Waychunas et al. 1983; Bajt et al. 1994; Galoisy et al. 2001; Petit et al. 2001; Wilke et al. 2001; Berry et al. 2003; Joseph et al. 2017). The pre-edge envelope is typically comprised of two or more components which arise from transitions to 3d final states which are non-degenerate as a result of the crystal field imposed by the local environment of the Fe absorber. Thus, crystal field theory predicts two and three allowed transitions, respectively, for Fe^{2+} ([Ar]$3d^6$ *hs*) in tetrahedral and octahedral field, whereas, two allowed transitions are predicted for Fe^{3+} ([Ar]$3d^5$ *hs*) in tetrahedral and octahedral crystal fields respectively (*hs*: high spin) (Westre et al. 1997; Baker et al. 2017). Additional contributions to the pre-edge feature have been reported for some distorted Fe^{3+} octahedral environments (such as in Fe_2O_3) which are attributed to admixture of 4p states and availability of unoccupied delocalised states (Dräger et al. 1988; de Groot et al. 2009). In this investigation, and others (Petit et al. 2001; Wilke et al. 2001), deconvolution of the pre-edge feature requires fewer components than the number of allowed transitions, due to a combination of the magnitude of the crystal field splitting, distortion from ideal co-ordination geometry, limited spectral resolution compared to the core-hole life time, and other factors. Nevertheless, as demonstrated by Fig. 7, the total integrated intensity and centroid energy of the pre-edge feature can be accurately estimated by fitting of Gaussian or pseudo-Voigt functions, and is correlated with the electronic configuration and symmetry of the absorber and hence oxidation state and co-ordination number.

The chemical shift between the centroid energy of Fe^{2+} and Fe^{3+} species determined in this investigation was 1.6 ± 0.1 eV for both laboratory and synchrotron XANES data, in excellent agreement with the value of 1.4 ± 0.1 eV determined by Wilke *et al*. (Wilke et al. 2001). Our laboratory and synchrotron data can be brought into approximate co-incidence in Fig. 6, by a shift of approximately 0.25 eV in energy and 0.025 a.u. in total integrated intensity, which implies that the differences between our measurements arise principally from systematic error. Consequently, it is preferable that a comprehensive reference data set (including reference mixtures) be acquired to define the speciation fields (and their joins), for each specific instrument (whether laboratory or synchrotron) to enable the most accurate speciation. This will form the objective of the next phase of this study.

As pointed out by Wilke *et al*. (Wilke et al. 2001), Fe speciation can be determined unambiguously in the case of a single dominant species or a binary mixture, from analysis of the pre-edge feature in Fe K-edge XANES. However, unique determination of more complex mixtures, or the presence of 5 co-ordinate Fe, is more difficult to ascertain, although the location of extracted data in the structure field map of Fig. 7 at least provides some insight into the likely component species. For such cases, modelling of the extended X-ray absorption fine structure, additional ^{57}Fe Mossbauer data, and/or simulation of XANES spectra, are required to give a unique determination.

5. Conclusions

We have successfully validated the methodology of Wilke *et al.* (Petit et al. 2001; Wilke et al. 2001), for analysis of weak pre-edge features in Fe K-edge XANES for determination of Fe speciation, using data acquired from model compounds in a matter of hours on a commercially available laboratory X-ray spectrometer. Quantitative agreement was observed

between the total integrated intensity and centroid energy of the pre-edge features determined from laboratory and synchrotron data, and with previously published independent data. The primary sources of discrepancy in these parameters within our study were systematic error, arising from marginal difference in calibration of the absolute energy scale and underestimation of total integrated intensity due to lower signal to noise ratio in the laboratory data (which could be compensated, to an extent, by increased effective counting time). Therefore, for accurate speciation, data from a library of reference compounds should be established for the particular laboratory or synchrotron instrument. This proof of concept study has also clearly established the feasibility of data acquisition and analysis for relatively dilute Fe absorber concentrations. The rate of core-hole generation in our set up is not favourable for fluorescence data acquisition as a result of the low power 100W X-ray source, however, successful laboratory fluorescence XAS measurements using a 1.5 kW X-ray source were recently reported by Honkanen et al. 2019. Nevertheless, as we have demonstrated here, transmission mode XANES may be acquired from relatively dilute absorber concentrations without heroic data acquisition times, in favourable circumstances. Indeed, we have recently reported further exploitation this approach to speciation of Ce and U L_3 edge XANES, with absorber concentrations of only a few mol% (Mottram et al. 2020).

Acknowledgements. We are grateful for financial support from the Nuclear Decommissioning Authority and EPSRC under grant numbers EP/M026566/1, EP/S01019X/1, EP/N017870/1 and EP/R511754/1. This research utilised the HADES / MIDAS facility at The University of Sheffield established with financial support from EPSRC and BEIS, under grant EP/T011424/1. This research was undertaken, in part, at the DUBBLE beamline, BM 26, at the European Synchrotron Radiation Facility. We gratefully acknowledge G.T. Seidler and D.R. Mortensen for useful discussions in support of this study.

References

ARNOLD H (1986) Crystal structure of $FePO_4$ at 294 and 20 K. Zeitschrift für Kristallographie - Crystalline Materials 177: 139–142

BAJT S, SUTTON SR, DELANEY JS (1994) X-ray microprobe analysis of iron oxidation states in silicates and oxides using X-ray absorption near edge structure (XANES). Geochimica et Cosmochimica Acta 58: 5209-5214

BAKER ML, MARA MW, YAN JJ, HODGSON KO, HEDMAN B, SOLOMON EI (2017) K- and L-edge X-ray Absorption Spectroscopy (XAS) and Resonant Inelastic X-ray Scattering (RIXS) Determination of Differential Orbital Covalency (DOC) of Transition Metal Sites. Coordination Chemistry Reviews 345: 182-208

BAUM E, TREUTMANN W, BEHRUZI M, LOTTERMOSER W, AMTHAUER G (1988) Structural and magnetic properties of the clinopyroxenes $NaFeSi_2O_6$ and $LiFeSi_2O_6$. Zeitschrift für Kristallographie 183: 273–284

BEARDEN JA, BURR AF (1967) Reevaluation of X-Ray Atomic Energy Levels. Reviews of Modern Physics 39: 125

BERRY AJ, O'NEILL HS, JAYASURIYA KD, CAMPBELL SJ, FORAN GJ (2003) XANES calibrations for the oxidation state of iron in a silicate glass. American Mineralogist 88: 967-977

BLACHUCKI W, CZAPLA-MASZTAFIAK, J, SA J, SZLACHETKO J (2019) A laboratory-based double X-ray spectrometer for simultaneous X-ray emission and X-ray absorption studies. Journal of Analytical Atomic Spectrometry 34: 1409-1415

BORSBOOM M, BRAS W, CERJAK I, DETOLLENAERE D, GLASTRA VAN LOON D, GOEDTKINDT P, KONIJNENBURG M, LASSING P, LEVINE YK, MUNNEKE B, OVERSLUIZEN M, VAN TOL R, VLIEG E (1988) The Dutch-Belgian beamline at the ESRF. Journal of Synchrotron Radiation 5: 518-520

DE GROOT F, VANKO G, GLATZEL P (2009) The 1s x-ray absorption pre-edge structures in transition metal oxides. Journal of Physics Condensed Matter: 21 104207

DRÄGER G, FRAHM R, MATERLIK G, BRÜMMER O (1988) On the Multipole Character of the X-Ray Transitions in the Pre-Edge Structure of Fe K Absorption Spectra - An Experimental Study. Physica Status Solidi B - Basic Research 146: 287-294

GALOISY L, CALAS G, ARRIO MA (2001) High-resolution XANES spectra of iron in minerals and glasses: structural information from the pre-edge region. Chemical Geology 174: 307-319

GREENWOOD N, EARNSHAW A (1997) Chemistry of the Elements, 2nd Edition. Butterworth-Heinemann, Oxford pp 1-1342

HAWTHORNE FC, UNGARETTI L, OBERTI R, CAUCIA F, CALLEGARI A (1993) The crystal chemistry of staurolite; 1. Crystal structure and site populations. The Canadian Mineralogist 31: 551-582

HOLDEN WM, HOIDN OR, DITTER AS, SEIDLER GT, KAS J, STEIN JL, COSSAIRT BM., KOSIMOR SA, GUO JH, YE YF, MARCUS MA, FAKRA S (2017) A compact dispersive refocusing Rowland circle X-ray emission spectrometer for laboratory, synchrotron, and XFEL applications. Reviews of Scientific Instruments 88: 073904

HONKANEN AP, OLLIKKALA S, AHOPELTO T, KALLIO AJ, BLOMBERG M, HUOTARI S (2019) Johann-type laboratory-scale x-ray absorption spectrometer with versatile detection modes. Reviews of Scientific Instruments 90: 033107

JAHRMAN EP, HOLDEN WM, DITTER AS, MORTENSEN DR, SEIDLER GT, FISTER TT, KOZIMOR SA, PIPER LFJ, RANA J, HYATT NC, STENNETT M (2019) An improved laboratory-based x-ray absorption fine structure and x-ray emission spectrometer for analytical applications in materials chemistry research. Reviews of Scientific Instruments 90: 024106.

JOSEPH K, STENNETT MC, HYATT NC, ASUVATHRAMAN R, DUBE CL, GANDY AS, KUTTY KVG, JOLLEY K, RAO PRV, SMITH R (2017) Iron phosphate glasses: Bulk properties and atomic scale structure. Journal of Nuclear Materials 494: 342-353.

KRAUSE MO, OLIVER J H (1979) Natural widths of atomic K and L levels, Kα X-ray lines and several KLL Auger lines. Journal of Physical and Chemical Reference Data 8: 320-338

MALZER W, GROTZSCH G, GNEWKOW R, SCHLESIGER C, KOWALEWSKI F, VAN KUIKEN B, DEBEER S, KANNGIESSER B (2018) A laboratory spectrometer for high throughput X-ray emission spectroscopy in catalysis research. Reviews of Scientific Instruments 89: 113111

MORTENSEN DR, SEIDLER GT, DITTER AS, GLATZEL P (2016) Benchtop Nonresonant X-ray Emission Spectroscopy: Coming Soon to Laboratories and XAS Beamlines Near You? Journal of Physics Conference Series 712: 012036

MORTENSEN DR, SEIDLER GT (2017) Robust optic alignment in a tilt-free implementation of the Rowland circle spectrometer. Journal of Electron Spectroscopy and Related Phenomena 215: 8-15

MOTTRAM LM, DIXON WILKINS MC, BLACKBURN LR, OULTON T, STENNETT MC, SUN SK, CORKHILL CL, HYATT NC (2020), A Feasibility Investigation of Laboratory Based X-ray Absorption Spectroscopy in Support of Nuclear Waste Management. MRS Adv 5: 27-35.

NEMETH Z, SZLACHETKO J, BAJNOCZI EG, VANKO G (2016) Laboratory von Hamos X-ray spectroscopy for routine sample characterization. Reviews of Scientific Instruments 87: 103105

PETIT PE, FARGES F, WILKE M, SOLÉ VA, Determination of the iron oxidation state in Earth materials using XANES pre-edge information, Journal of Synchrotron Radiation, 8, 2001, 952-954

RAVEL B, NEWVILLE M, (2005) ATHENA, ARTEMIS, HEPHAESTUS: data analysis for X-ray absorption spectroscopy using IFEFFIT. Journal of Synchrotron Radiation 12: 537-541

SCHLESIGER C, ANKLAMM L, STIEL H, MALZER W, KANNGIESSER B (2015) XAFS spectroscopy by an X-ray tube based spectrometer using a novel type of HOPG mosaic crystal and optimized image processing. Journal of Analytical Atomic Spectrometry 30: 1080-1085.

SEIDLER GT, MORTENSEN DR, REMESNIK AJ, PACOLD JI, BALL NA, BARRY N, STYCZINSKI M, HOIDN OR (2014) A laboratory-based hard x-ray monochromator for high-resolution x-ray emission spectroscopy and x-ray absorption near edge structure measurements. Reviews of Scientific Instruments 85: 113906

SEIDLER GT, DITTER AS, BALL NA, REMESNIK AJ (2016) A Modern Laboratory XAFS Cookbook. Journal of Physics Conference Series 712: 012015

SMYTH JR (1975) High Temperature Crystal Chemistry of Fayalite. American Mineralogist 60: 1092-1097

STERN EA, KIM K, (1981) Thickness effect on the extended-x-ray-absorption-fine-structure amplitude. Physical Review B 23: 3781-3787

TAYLOR KG, KONHAUSER KO (2011) Iron in Earth Surface Systems: A Major Player in Chemical and Biological Processes. Elements 7: 83-87

WAYCHUNAS GA, APTED MJ, BROWN GE (1983) X-ray K-edge Absorption-Spectra of Fe Minerals and Model Compounds - Near-Edge Structure. Physics and Chemistry of Minerals 10: 1-9

WESTRE TE, KENNEPOH P, DEWITT JG, HEDMAN B, HODGSON KO, SOLOMON EI (1997) A Multiplet Analysis of Fe K-Edge 1s f 3d Pre-Edge Features of Iron Complexes. Journal of the American Chemical Society 119: 6297-6314

WILKE M, FARGES F, PETIT PE BROWN, GE, MARTIN F (2001) Oxidation state and coordination of Fe in minerals: An Fe K-XANES spectroscopic study, American Mineralogist 86: 714-730

WOOD BJ, VIRGO D (1989) Upper mantle oxidation state: Ferric iron contents of Iherzolite spinels by 57Fe Mössbauer spectroscopy and resultant oxygen fugacities. Geochimica et Cosmochimica Acta 53: 1277-1291

ZEESHAN F, HOSZOWSKA J, LOPERETTI-TORNAY L, DOUSSE JC (2019) In-house setup for laboratory-based x-ray absorption fine structure spectroscopy measurements. Reviews of Scientific Instruments 90: 073105

IOP Conf. Series: Materials Science and Engineering **818** (2020) 012020 doi:10.1088/1757-899X/818/1/012020

Laboratory Based X-ray Absorption Spectroscopy of Iron Phosphate Glasses for Radioactive Waste Immobilisation: A Preliminary Investigation

L M Mottram,[1] M C Stennett,[1] S K Sun[1] and N C Hyatt[1]*

Department of Materials Science & Engineering, The University of Sheffield, Mappin Street, Sheffield, S1 3JD.

*n.c.hyatt@sheffield.ac.uk

Abstract. We report the application of laboratory based X-ray absorption spectroscopy to the speciation of Fe in iron phosphate glasses prepared by conventional and microwave melting. Analysis of the weak pre-edge features in Fe K-edge XANES data demonstrated glasses produced by microwave melting to have a higher fraction of reduced Fe^{2+} species, since microwave melts do not have sufficient time to equilibrate with the prevailing oxygen partial pressure, compared to counterparts produced by conventional melting. Furthermore, our laboratory XANES data are consistent with the formation of octahedral Fe^{2+} at the expense of tetrahedral Fe^{3+} species, with increasing Fe^{2+} content. These findings are consistent with the previous findings of our ^{57}Fe Mossbauer study, synchrotron XANES data, and current understanding of the structure of iron phosphate glasses, and demonstrate the utility of laboratory based XANES for routine speciation of Fe in these and other materials.

1. Introduction

The baseline treatment option for intermediate level wastes in the UK is encapsulation in an ordinary portland cement matrix, combined with super-compaction, where appropriate. However, there is a growing appreciation that some wastes, such as reactive metals and organic materials, are not compatible with this approach [1-3]. Furthermore, cement encapsulation technology results in a dilution of the radioactive waste feed and a projected increase in the packaged waste volume by typically 30%. In principal, thermal treatment technologies challenge these shortcomings, through at least partial oxidation of metallic and organic waste components, to produce a passively safe product, with retention of radioactive and chemotoxic elements [3-10].

Iron phosphate glasses are one matrix of interest for the vitrification of some challenging radioactive wastes [11-13]. The $40Fe_2O_3$–$60P_2O_5$ (mol%) glass composition, has been extensively studied for radioactive waste immobilisation, due to the high incorporation rate of elements which have low solubility in borosilicate melts (e.g. F, Cl, S and Bi), good chemical durability, and reasonable processing temperature and melt viscosity [14-16].

X-ray absorption and ^{57}Fe Mossbauer spectroscopy studies of iron phosphate glasses have demonstrated the Fe^{2+} / Σ Fe ratio to be sensitive to melt composition and processing conditions (temperature, time and atmosphere) [16-19]. This redox ratio is determined by the equilibrium: $2\ FeO_{(melt)} + ½\ O_{2\,(g)} = Fe_2O_{3\,(melt)}$, and, in the case of the $40Fe_2O_3$–$60P_2O_5$ glass composition, up to 60% of the total Fe may be present as Fe^{2+} [17]. An increased fraction of Fe^{2+} is reported to be both detrimental to glass forming ability and radiation stability [16, 19-22], whereas chemical durability is

reported to be insensitive to the fraction of Fe^{2+} [18]. The Fe^{2+} / Σ Fe ratio also governs the electrical conductivity of Fe_2O_3-P_2O_5 glass melts, which is an important consideration for some melter designs, in the context of application to radioactive waste treatment [19].

From the preceding discussion, it will be appreciated that routine determination of Fe^{2+} / Σ Fe ratio in Fe_2O_3-P_2O_5 glasses is of importance for formulation and development of such waste forms. ^{57}Fe Mossbauer spectroscopy has been widely exploited for the determination of Fe^{2+} / Σ Fe ratio, according to the distinctive isomer shift and quadrupole splitting of Fe^{2+} and Fe^{3+} species, which are also sensitive to co-ordination number [13, 16-18, 23]. However, the determination of average Fe co-ordination number is complicated by the overlap of ^{57}Fe isomer shift and quadrupole splitting ranges, particularly for amorphous materials [13, 23]. Whilst ^{57}Fe Mossbauer spectroscopy can conveniently be applied in a laboratory environment, data acquisition is dependent on ^{57}Fe concentration, ^{57}Co source activity, and sample characteristics, which translate to data acquisition time of days per sample.

Fe K-edge X-ray absorption spectroscopy has also been applied to determination of Fe^{2+} / Σ Fe ratio in Fe_2O_3-P_2O_5 glasses. The weak pre-edge features in the Fe K-edge X-ray Absorption Near Edge Structure (XANES), located ca. 15–20 eV below the edge step, have been shown to be a sensitive probe of Fe speciation [24-29]. These features are associated with 1s – 3d (quadrupole) and/or 1s – 4p (dipole) electronic transitions in the Fe absorber atom and, therefore, are sensitive to both the electronic configuration and symmetry, from which oxidation state and co-ordination number are inferred. Wilke *et al.* developed a systematic methodology to extract the normalised pre-edge features from Fe K-edge XANES data and determination of the centroid energy position and total integrated intensity, which were effectively correlated with Fe oxidation state and co-ordination number [27, 28]. Conventionally, acquisition of XANES data has required access to a synchrotron radiation beamline, which is highly competitive, time limited, and not immediate. Recently, however, we demonstrated the first proof of concept Fe K-edge XANES speciation studies, using a commercially available laboratory X-ray spectrometer, from analysis of weak pre-edge features [30]. This approach enables routine Fe speciation in materials with data acquisition times of only a few hours. Here, we build on this recent study to demonstrate the potential for Fe redox determination in $40Fe_2O_3$–$60P_2O_5$ glasses prepared by conventional and microwave melting. Our preliminary results demonstrate that laboratory based Fe K-edge XANES has sufficient resolution and sensitivity to routinely determine Fe^{2+} / Σ Fe ratio in iron phosphate glasses.

2. Experimental

2.1. Synthesis of iron phosphate glasses

Iron phosphate glasses of $40Fe_2O_3$–$60P_2O_5$ (mol%) composition were prepared by conventional and microwave heating, as previously described [23, 31, 32]. Conventional melting used a stoichiometric mixture of Fe_3O_4 and P_2O_5 (PO) or $NH_4H_2PO_4$ (AP), in covered silica crucibles, heated at 1150ºC for 5h in air. Microwave melting used a stoichiometric mixture of Fe_3O_4 and P_2O_5 or $NH_4H_2PO_4$, in covered silica crucibles, heated for 12 minutes at 800W power in a domestic microwave oven (DMO). Fe_3O_4 was selected as the iron source since it is known to strongly couple to the 2.45 GHz frequency of domestic microwaves, resulting in rapid self heating. After approximately 20 seconds of microwave irradiation a dull red glow emanating from the crucible was observed through the silica lid. The intensity of the glow increased until, after approximately 1 minute, an incandescent red glow could be clearly observed. This continued until the DMO was switched off. The peak temperature of melting was estimated to be 1150ºC, using a grounded thermocouple. Glasses were quenched in air and confirmed to be amorphous by X-ray diffraction.

2.2. Reference compounds

Fe K-edge XANES data were acquired from four selected reference compounds. $NaFeSi_2O_6$ (aegirine) and Fe_2SiO_4 (fayalite) are characterised by Fe^{3+} and Fe^{2+}, respectively, in octahedral FeO_6 co-ordination (CN = 6); whereas $FePO_4$ and $Fe_{1.5}Mg_{0.5}Al_{9.1}Si_{3.9}(OH)_2$ (staurolite) are characterised by Fe^{3+} and Fe^{2+}, respectively, in tetrahedral FeO_4 co-ordination (CN = 4) [33-36]. Polycrystalline $FePO_4$ and Fe_2SiO_4

were, respectively, synthesised by: solid state reaction of Fe_2O_3 and $NH_4H_2PO_4$ at 900 °C in air for 16 h; and solid state reaction of stoichiometric quantities of Fe, Fe_2O_3 and SiO_2 at 750 °C for 48 h in a sealed, evacuated, quartz tube. Mineral specimens of aegirine (Langesund Fjord, Norway), and staurolite (Georgia, USA), were provided from our own collection. All materials were confirmed to be single phase by powder X-ray diffraction. The expected Fe speciation was verified by ^{57}Fe Mossbauer analysis.

2.3. Fe K-edge XANES

Fe K-edge XANES data were acquired on an EasyXAFS XES100 spectrometer, Figure 1, based on the design of Seidler *et al.*, equipped with an air cooled X-ray tube operating at 25 kV and 4 mA, with a Hitatchi Vortex Silicon Drift Detector (SDD) [37-40]. The spectrometer was configured with a Ge (620) SBCA to scan the energy range 6970 – 7340 eV, with a step size of 0.25 eV and constant count time of 4s / point in the XANES region (total scan time 30 min per data set). The energy resolution of the SDD is ca. 140 eV, enabling rejection of the harmonic content of the incident beam and background scatter. A He flight-path was used to minimise air scatter and absorption. Transmission data were acquired with (I_t(E)) and without the sample (I_0(E)), using the same scan parameters. The Ge (620) monochromator was aligned using the clock angle procedure of Mortensen and Seidler, to account for the crystal miscut [41]. Data integration time was typically 4h per spectrum.

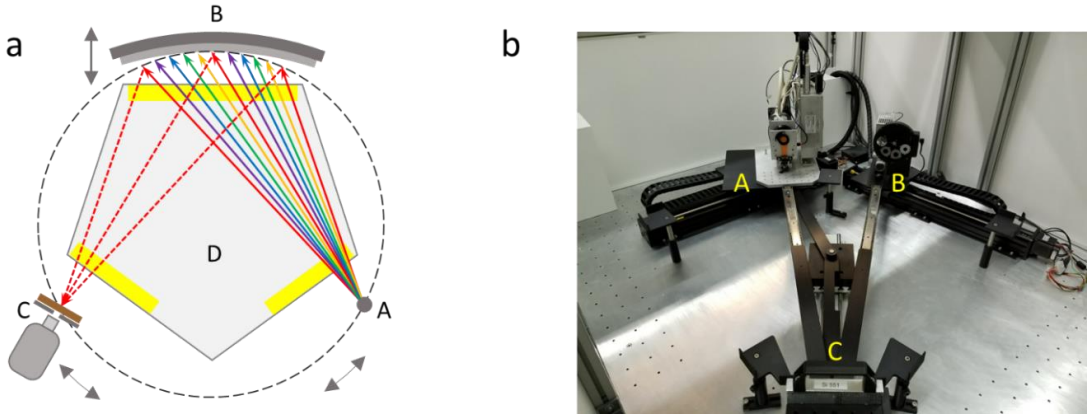

Figure 1. a) Schematic representation of Rowland circle geometry for laboratory transmission X-ray Absorption Spectroscopy, as described in the text, showing: broadband low power X-ray source (A); spherically bent crystal analyser (B); sample / detector assembly (C); and helium filled beam path with kapton windows (D); **b)** Photograph of EasyXAFS XES100 spectrometer arrangement shown in Fig. 1a, with helium filled beam path removed, to show linear translation stages and steering bars used to maintain alignment of X-ray source (A), analyser (B), and sample / detector assembly (C).

Fe K-edge XANES data were also acquired on the KMC-2 beamline at the BESSY-II synchrotron. The KMC-2 beamline is situated on a bending magnet and was configured with a Si (111) channel cut monochromator and mirror for harmonic rejection. Incident and transmitted beam intensities were measured using ionization chambers, filled with mixtures of He and N_2, operated in a stable region of their I/V curve. For synchrotron data, a step size of 0.25 eV was used in the XANES region with a count time of 1s / point. Data integration time was typically 0.5h per spectrum.

Samples were prepared from finely ground specimens of glasses or reference compounds dispersed in 70 mg of polyethylene glycol, pressed into 13 mm diameter pellets, to achieve a thickness of one absorption length. Data reduction and analysis was performed using the programs Athena and Hephaestus [42]. Calibration of the energy scale were achieved by reference to a 5 μm Fe foil (Goodfellow Cambridge Ltd.), for which the first peak in the derivative spectrum was set to 7112.00 eV, as defined by Bearden and Burr for the Fe K absorption edge [43]. Data from the reference foil

were acquired periodically for the laboratory and synchrotron experiments, the absolute energy scale for the laboratory XANES data was calibrated as previously described [30, 44].

Extraction and analysis of the pre-edge feature in Fe K-edge XANES data were achieved using Microsoft Excel software, to first fit a spline function to model and subtract the contribution of the edge step. The pre-edge envelope was then deconvoluted by fitting Gaussian components using a linear least squares refinement to optimise the normalised height, full width at half height, and energy position, so as to minimise the difference between the observed and calculated envelope determined from the sum of the fitted Gaussian components. Fitting initially utilised two Gaussian components with the significance of a third component tested by inspection of the improvement in goodness of fit. The total integrated intensity and centroid energy of the pre-edge feature were determined, respectively, from the sum of the integrated intensities and intensity weighted average energy position of the Gaussian components. The same initial parameters were used for all data sets, and several sets of different initial parameters trialled, to ensure that convergence did not arise in a local minimum. This approach is a simplification of that applied by Wilke *et al.*, which employed pseudo-Voigt components [28, 30].

3. Results and discussion

Figure 2 shows a head to head comparison of Fe K-edge XANES data acquired from $40Fe_2O_3$–$60P_2O_5$ (mol%) glasses, where, respectively, C and M are used to denote materials processed by conventional and microwave heating, and PO and AP denote the use of P_2O_5 and $NH_4H_2PO_4$ reagents. Excellent correspondence is observed between the laboratory (points) and synchrotron (solid line) XANES data, demonstrating that acquisition of good quality Fe K-edge XANES data using the laboratory set up, with reasonable data integration times. Note that the synchrotron data have *not* been convoluted by Gaussian or Lorentzian broadening for this comparison.

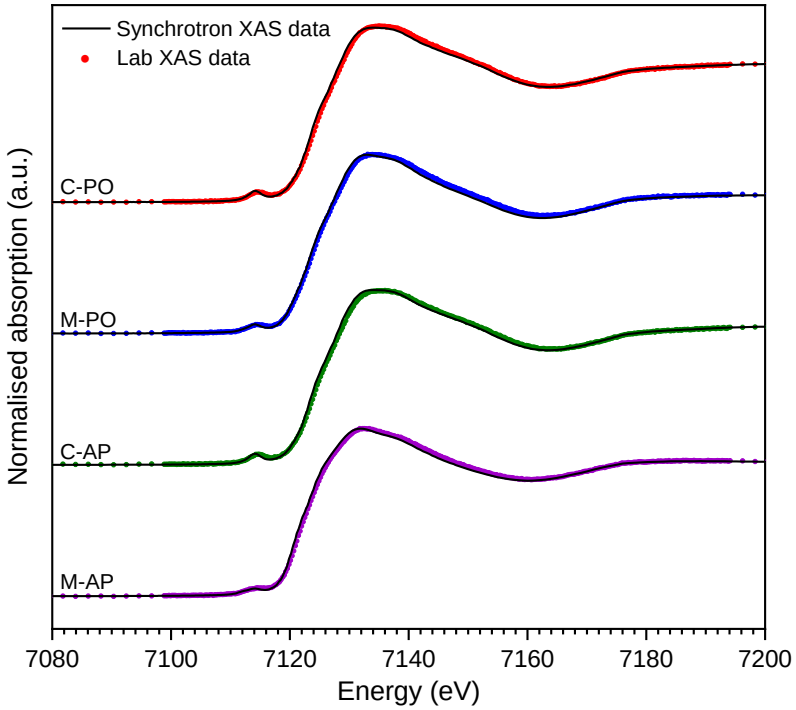

Figure 2. Comparison of normalised transmission mode Fe K-edge XANES spectra from $40Fe_2O_3$–$60P_2O_5$ glasses prepared by microwave (M) or conventional (C) heating of Fe_3O_4 with P_2O_5 (PO) or $NH_4H_2PO_4$ (AP), acquired using laboratory XAS spectrometer (points) and KMC-2 synchrotron beamline (solid line).

Figure 3 shows the extracted pre-edge features from the laboratory XANES data of the glass samples and the modelled envelope of the Gaussian components. Although the laboratory data show some scatter, as a result of the relatively low signal to noise ratio, the pre-edge features are evidently resolvable and measurable relative to the background. For each material, the pre-edge features of the laboratory and synchrotron XANES data were adequately modelled using three Gaussian components, the fitted parameters are summarised in Table 1. The fitted centroid position and integrated intensity of the pre-edge features are plotted in Figure 4, together with data from the reference compounds analysed in this study and that of Wilke *et al.* [28]. Note that the data of Wilke *et al.* (calibrated to E_0 = 7111.08 eV), were shifted by +0.92 eV, consistent with our absolute energy scale.

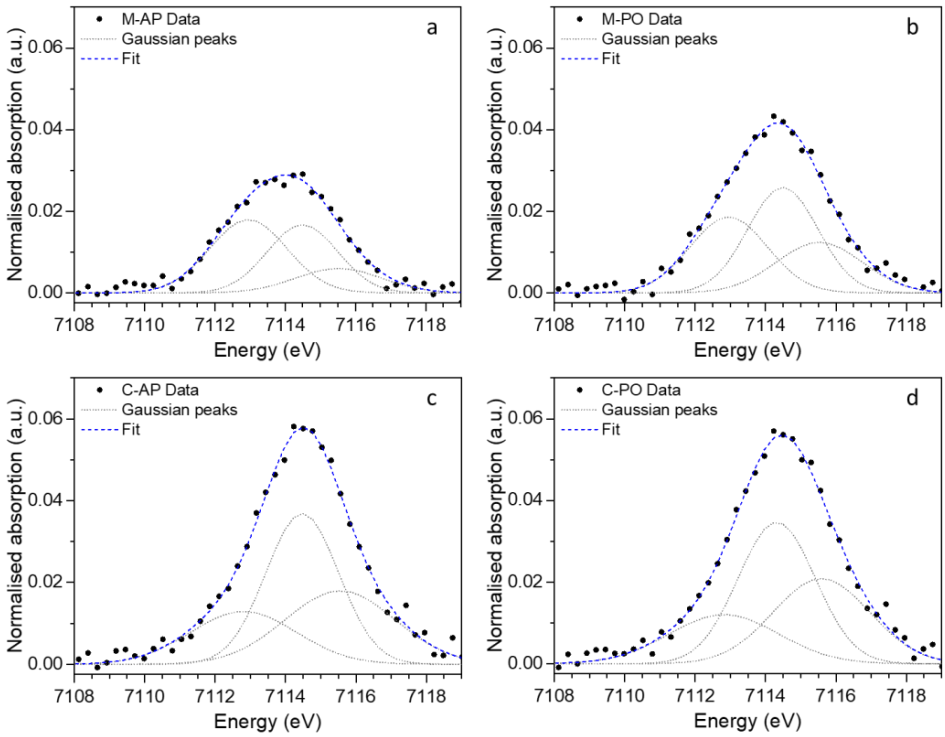

Figure 3. Normalised pre-edge spectra at Fe K edge (points) from $40Fe_2O_3$–$60P_2O_5$ glasses prepared by microwave (M) or conventional (C) heating of Fe_3O_4 with P_2O_5 (PO) or $NH_4H_2PO_4$ (AP), acquired using laboratory XAS spectrometer (points), showing fitted Gaussian components (grey dotted line) and their summation envelope (blue dotted line).

Table 1. Integrated intensity and centroid energy for Gaussian components fitted to pre-edge features of $40Fe_2O_3$–$60P_2O_5$ glasses prepared by microwave (M) or conventional (C) heating of Fe_3O_4 with P_2O_5 (PO) or $NH_4H_2PO_4$ (AP). Values in bold type are derived from laboratory data; values in normal type are derived from synchrotron data.

Sample	Gaussian 1		Gaussian 2		Gaussian 3		Centroid Energy (eV)	Total integrated intensity (a.u)
	Energy (eV)	Intensity (a.u.)	Energy (eV)	Intensity (a.u.)	Energy (eV)	Intensity (a.u.)		
C-AP	**7112.8**	**0.049**	**7114.5**	**0.096**	**7115.5**	**0.070**	**7114.4**	**0.215**
	7112.9	0.046	7114.4	0.103	7115.4	0.068	7114.4	0.217
C-PO	**7112.8**	**0.047**	**7114.3**	**0.095**	**7115.6**	**0.072**	**7114.4**	**0.213**
	7112.8	0.049	7114.3	0.120	7115.5	0.043	7114.3	0.212
M-AP	**7113.0**	**0.049**	**7114.5**	**0.042**	**7115.5**	**0.018**	**7114.0**	**0.110**
	7112.4	0.041	7114.4	0.073	7115.5	0.002	7113.7	0.116
M-PO	**7113.0**	**0.051**	**7114.5**	**0.065**	**7115.5**	**0.038**	**7114.2**	**0.154**
	7112.8	0.045	7114.3	0.094	7115.5	0.021	7114.1	0.160

As shown in the speciation plot of Figure 4, the data points for the Fe^{3+} reference compounds $NaFeSi_2O_6$ (octahedral, FeO_6) and $FePO_4$ (tetrahedral, FeO_4) are in excellent agreement between the laboratory data (solid blue circles) and synchrotron data (solid red circles), and the data reported by Wilke *et al.* (solid black circles) [28]. The Fe^{2+} reference compounds $Fe_{1.5}Mg_{0.5}Al_{9.1}Si_{3.9}(OH)_2$ (octahedral, FeO_6) and Fe_2SiO_4 (tetrahedral, FeO_4) were investigated using only the laboratory set up, but these data (solid blue circles) but are also in reasonable agreement with the data reported by Wilke *et al.* (solid black circles) [28]. Both the laboratory and synchrotron data points fall within the known field for Fe^{2+} / Fe^{3+} speciation for octahedral (CN = 6) and tetrahedral (CN = 4) co-ordination, defined by the reference compounds reported by Wilke *et al.* (solid / open black circles). Figure 4 demonstrates that laboratory XANES is effective in distinguishing Fe^{2+} and Fe^{3+} species according to the centroid of the pre-edge features at 7112.9 ± 0.1 eV and 7114.5 ± 0.1 eV respectively. The chemical shift between the centroid energy of Fe^{2+} and Fe^{3+} species determined in this investigation was thus 1.6 ± 0.1 eV for laboratory XANES data, which is in excellent agreement with the value of 1.4 ± 0.1 eV determined by Wilke *et al.* and our previous feasibility study [28, 30]. Figure 4 demonstrates that laboratory XANES is also effective in differentiating tetrahedral and octahedral Fe^{2+} / Fe^{3+} species, according to the relative total integrated intensity of the pre-edge feature. As noted above, the pre-edge feature is associated with 1s – 3d quadrupole transitions, which are only weakly allowed for a centrosymmetric octahedral environment but have enhanced transition probability in non-centrosymmetric tetrahedral environments, due to admixture of unoccupied 4p orbitals in the final state.

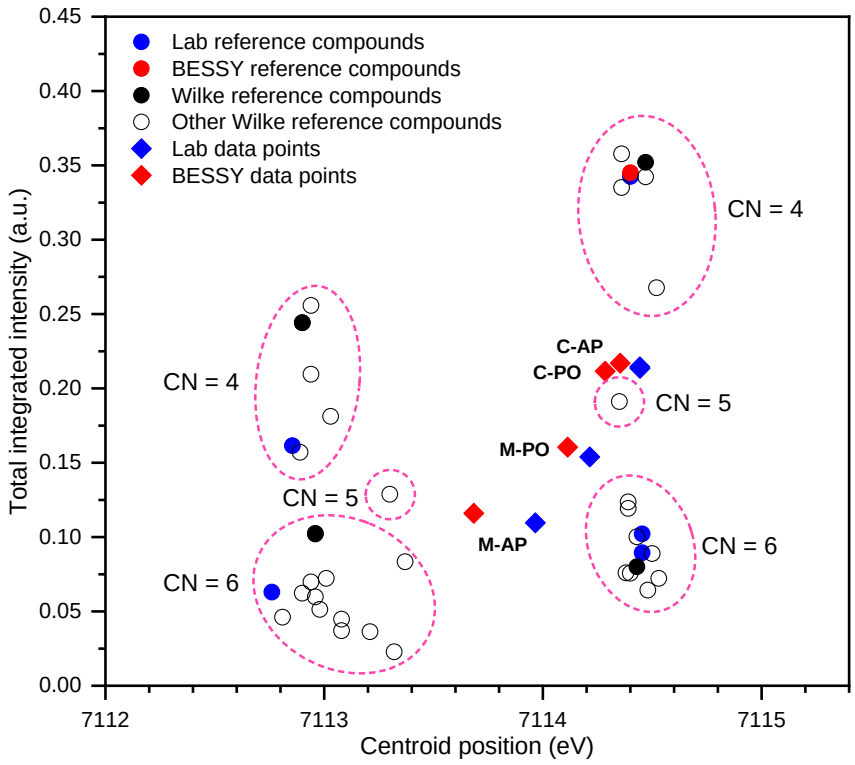

Figure 4. Speciation field diagram, based on total integrated intensity and centroid energy of pre-edge feature of Fe K-edge XANES data. Data points derived from analysis of our laboratory XANES are shown by solid blue circles (reference compounds) or diamonds (glasses); data points derived from synchrotron XANES are shown as solid red circles (reference compounds) or diamonds (glasses); equivalent data points of reference compounds from Wilke *et al.*, are shown as solid black circles (other reference data from Wilke *et al.*, shown as open black circles) [28]. Note data from Wilke *et al.*, are shifted by +0.92 eV consistent with our absolute energy scale as described in the text.

Turning to the analysis of the $40Fe_2O_3$–$60P_2O_5$ glass compositions, Figure 4 shows reasonably good agreement between the laboratory and synchrotron data points, demonstrating that laboratory XANES has, in principle, sufficient resolution and sensitivity to probe Fe^{2+} / Σ Fe ratio in iron phosphate glasses. The centroid energy of the pre-edge feature of glasses produced by microwave heating (M) is displaced toward lower energy compared to glasses produced by conventional melting (C), implying the presence of a greater concentration of Fe^{2+} species in the microwave processed materials. This is in agreement with our previous ^{57}Fe Mossbauer investigation [23], which estimated the Fe^{2+} / Σ Fe ratio to be 0.43 for glass M-AP, 0.22 for glass M-PO, and 0.10 for glass C-AP and C-PO. The centroid position of the pre-edge feature is known to show a non-linear dependence on Fe^{2+} / Σ Fe ratio, when both average oxidation state and co-ordination number vary at the same time [28], which is clearly inferred in this case from Figure 4 (see below). Hence, the Fe^{2+} / Σ Fe ratio cannot yet be reliably estimated from our XANES data without further careful calibration using mixtures of reference compounds. Nevertheless, it is evident from Figure 4 that glasses produced by microwave heating are characterised by a higher Fe^{2+} / Σ Fe redox ratio compared to the counterparts prepared by conventional melting. The higher Fe^{2+} / Σ Fe ratio for the microwave processed glasses, previously demonstrated by ^{57}Fe Mossbauer spectroscopy [23], is a reflection of the rapid processing time, which does not allow the melt to reach equilibrium with the prevailing oxygen partial pressure, compared to the conventionally processed counterparts. It is also evident from Figure 4, that the highest Fe^{2+} / Σ Fe ratio is observed for the microwave processed glass using $NH_4H_2PO_4$ as the phosphate source, also in agreement with our earlier ^{57}Fe Mossbauer investigation [23]. Decomposition of $NH_4H_2PO_4$ during the rapid microwave heating evolves NH_3 gas which maintains a sufficiently reducing environment to assist incorporation of Fe^{2+} within the melt, potentially also inducing partial reduction of Fe^{3+}. It is notable that the synchrotron determined data points in Figure 4 (red diamonds) are displaced to slightly higher centroid energy, compared to those determined by laboratory analysis (blue diamonds) on the same glass materials. This may suggest a small systematic difference in Fe^{2+} / Σ Fe ratio determined by laboratory and synchrotron XANES, however, this should be considered with due caution given the expected non-linear dependence of centroid energy on Fe^{2+} / Σ Fe ratio, which must be determined for both data sets.

Figure 4 also reveals a measurable difference of average Fe co-ordination in the microwave and conventionally melted glasses. In the case of conventionally melted glasses, the integrated intensity of the pre-edge feature implies a mixture of tetrahedral and octahedral, and/or pentahedral, Fe^{3+} species are present. This is in agreement with more recent Fe K-edge synchrotron XANES and ^{57}Fe Mossbauer studies of iron phosphate glasses, which point to a mixture of tetrahedral and octahedral, and or pentahedral, Fe^{3+} species, when Fe^{2+} / Σ Fe < 0.2 [13, 45, 46]. The microwave processed glasses are characterised by pre-edge features of lower integrated intensity, compared to their conventionally processed counterparts. This implies that the higher Fe^{2+} / Σ Fe ratio of the microwave processed glasses is associated with an increased proportion of octahedral Fe^{2+} (which would be expected to prefer octahedral co-ordination on the basis of crystal field stabilisation energy). This observation is consistent with the current understanding of the structure of iron phosphate glasses, in which an increase in Fe^{2+} / Σ Fe ratio, results in conversion of network forming tetrahedral Fe^{3+} to network modifying octahedral Fe^{2+} polyhedra [13,45,46]. Further work to accurately estimate the Fe^{2+} / Σ Fe ratio using mixtures of reference compounds, should also allow the proportion of co-ordination environments to be determined from laboratory XANES data,

4. Conclusions

Analysis of the weak pre-edge features in Fe K-edge XANES data from a laboratory XAS spectrometer demonstrated microwave processed iron phosphate glasses to incorporate a higher fraction of Fe^{2+} species, compared to counterparts produced by conventional melting, consistent with our previous ^{57}Fe Mossbauer spectroscopy study. Laboratory and synchrotron Fe K-edge XANES data from the same suite of glass materials were found to be in excellent agreement. Accurate determination of Fe^{2+} / Σ Fe ratio by laboratory XANES analysis, will require careful calibration against centroid energy of the pre-edge features, due to the known non-linear dependence when both average oxidation state and co-ordination number vary at the same time. Nevertheless, this preliminary study has established that

laboratory XANES data are of sufficient resolution and sensitivity, in principle, to routinely probe Fe^{2+} / Σ Fe ratio in iron phosphate glasses and other materials.

5. References

[1] NDA 2016 *Nuclear Decommissioning Authority Strategy effective from April 2016*
[2] NDA/RWM 2016 *Geological Disposal Science and Technology Plan*.
[3] NDA 2019 *5-year R&D Plan 2019 to 2024*
[4] Hyatt N C and James M 2013 *Nucl. Eng. Int*. **2** 10-3
[5] Bingham P A, Hyatt N C and Hand R J 2012 *Glass Technol. Part A* **53** 83.
[6] Bingham P A, Hyatt N C, Hand R J and Forder S D 2013 *Glass Technol. Part A* **54** 1.
[7] Bingham P A, Hyatt N C, Hand R J and Wilding C R 2009 *Mat. Res. Soc. Symp. P*. **1124** 161.
[8] Heath P G, Corkhill C L, Stennett M C, Hand R J, Whales K M and Hyatt N C 2018 *J. Nucl. Mater*. **508** 203.
[9] Hyatt N C, Morgan S, Stennett M C, Scales C R, Deegan D, 2007 *Mat. Res. Soc. Symp. P*. **985** 293
[10] Hyatt N C, Schwarz R R, Bingham P A, Stennett M C, Corkhill C L, Heath P G, Hand R J, James M, Pearson A and Morgan S 2013 *J. Nucl. Mater*. **444** 186.
[11] Brow R K, Kim C W and Reis S T 2020 *Int. J. Appl. Glass Sci.* **11** 4.
[12] Day D E, Wu Z, Ray C S and Hrma P 1998 *J Non-Cryst. Solids* **241** 1.
[13] Joseph K, Stennett M C, Hyatt N C, Asuvathraman R, Dube C L, Gandy A S, Kutty K V G, Jolley K, Rao P R V and Smith R 2017 *J. Nucl Mater*. **494** 342.
[14] Kim C W and Day D E 2003 *J. Non-Cryst. Solids* **331** 20.
[15] Mesko M G, Day D E and Bunker B C 2000 *Waste Manag.* **20** 271-8.
[16] Marasinghe G K, Karabulut M, Ray C S, Day D E, Shumsky M G, Yelon W B, Booth C H, Allen P G and Shuh D K 1997 *J. Non-Cryst. Solids* **222** 144.
[17] Karabulut M, Marasinghe G K, Ray C S, Day D E, Waddil G D, Booth C H, Allen P G, Bucher J J, Caulder D L and Shuh D K 2002 *J. Non-Cryst. Solids* **306** 182.
[18] Ray C S, Fang X, Karabulut M, Marasinghe G K and Day D E 1999 *J. Non-Cryst. Solids* **249** 1.
[19] Fang X, Ray C S, Moguš-Milanković A and Day D E 2001 *J. Non-Cryst. Solids* **283** 162.
[20] Griscom D L, Merzbacher C I, Bibler N E, Imagwa H, Uchiyama S, Namiki A, Marasinghe G K, Mesko M and Karabulut M 1998 *Nucl. Instr. and Meth. In Phys. Res. B* **141** 600.
[21] Joseph K, Jolley K and Smith R 2015 *J. Non-Cryst. Solids*, **411** 137.
[22] Jolley K and Smith R 2016 *Nucl. Instr. Methods Phys. Res. Sec. B.* **374** 8.
[23] Forder S D, Bingham P A, McGann O J, Stennett M C and Hyatt N C 2013 *Hyperfine Interact.* **217** 83.
[24] Waychunas G A, Apted M J and Brown G E 1983 *Phys. Chem. Miner.* **10** 1.
[25] Bajit S, Sutton S R and Delaney J S 1994 *Geochim. Cosmochim. Acta* **58** 5209.
[26] Galoisy L, Calas G and Arrio M A 2001 *Chem. Geol.* **174** 307.
[27] Petit P E, Farges F, Wilke M and Solé V A 2001 *J. Synchrotron Radiat.* **8** 952.
[28] Wilke M, Farges F, Petit P E, Brown G E and Martin F 2001 *Am. Mineral.* **86** 714.
[29] Berry A J, O'Neill H S, Jayasuriya K D, Campbell S J and Foran G J 2003 *Am. Mineral.* **88** 967.
[30] Mottram L M, Cafferkey S, Mason A R, Oulton T, Sun S K, Bailey D J, Stennett M C and Hyatt N C 2020 *J. Geosci.,* **65** 27.
[31] Stennett M C and Hyatt N C 2009 *Mat. Res. Soc. Symp. P*. **1124** 147.
[32] Mayzan M Z H, Stennett M C, Hyatt N C and Hand R J 2014 *J. Nucl. Mater.* **454** 343.
[33] Arnold H 1986 *Z. Kristallogr. Cryst. Mater.* **177** 139.
[34] Baum E, Treutmann W, Behruzi M, Lottermoser W and Amthauer G 1988 *Z. Kristallogr.* **183** 273.
[35] Smyth J R 1975 *Am. Mineral.* **60** 1092.
[36] Hawthorne F C, Ungaretti L, Oberti R, Caucia F and Callegari A 1993 *Can. Mineral.* **31** 551.
[37] Seidler G T, Mortensen D R, Remesnik A J, Pacold J I, Ball N A, Barry N, Styczinski M and Hoidn O R *2014 Rev. Sci. Instrum.* **85** 113906.
[38] Seidler G T, Ditter A S, Ball N A and Remesnik A J 2016 *J. Phys. Conf. Ser.* **712** 012015.

[39] Mortensen D R, Seidler G T, Ditter A S and Glatzel P 2016 *J. Phys. Conf. Ser.* **712** 012036.
[40] Jahrman E P, Holden W M, Ditter A S, Mortensen D R, Seidler G T, Fister T T, Kozimor S A, Piper L F J, Rana J, Hyatt N C and Stennett M 2019 *Rev. Sci. Instrum.* **90** 024106.
[41] Mortensen D R and Seidler G T 2017 *J. Electron. Spectrosc. Relat. Phenom.* **215** 8.
[42] Ravel B and Newville M 2005 *J. Synchrotron Radiat.* **12** 537.
[43] Bearden J A and Burr A F 1967 *Rev. Mod. Phys.* **39** 125.
[44] Mottram L M, Dixon Wilkins M C, Blackburn L R, Oulton T, Stennett M C, Sun S K, Corkhill C L and Hyatt N C 2020 *MRS Adv.* **5** 27.
[45] Wang G, Wang Y and Jin B 1994 *Proc. SPIE* **2287** 214.
[46] Karabulut M, Marasinghe G K, Ray C S, Day D E, Waddill G D, Allen P G, Booth C H, Bucher J J, Caulder D L, Shuh D K, Grimsditch M, Saboungi M L 2000 *J. Mater. Res.* **15** 1972.

Acknowledgment
We are grateful for financial support from the Nuclear Decommissioning Authority and EPSRC under grant numbers EP/M026566/1, EP/S01019X/1, EP/N017870/1 and EP/R511754/1. This research utilised the HADES / MIDAS facility at The University of Sheffield established with financial support from EPSRC and BEIS, under grant EP/T011424/1. This research was undertaken, in part, at the KMC-2 beamline at the BESSY-II synchrotron radiation source.

8. Conclusions

In this Chapter, the overall conclusions of the Thesis are drawn together. They are discussed through compilation of the findings from each chapter, under the key themes that have been prevalent throughout the Thesis.

8.1. Capabilities of Bulk U XAS measurements

In Chapter 4, the capabilities of several different U XAS measurements were investigated by collecting data from a large set of reference compounds and comparing the data and results of different analysis techniques. From this, the benefits and limitations of different techniques were identified, including the novel identification that the first peak in the first derivative of the U L_1-edge is an excellent indicator of net U oxidation state. This work also highlighted the importance of using multiple U XAS measurements and analysis techniques to thoroughly investigate U environment in samples. However, it should be noted that the key limitation of these studies was that the reference compounds investigated in Chapter 4 had high concentrations of U and, as such, the application of some of these techniques (particularly U L_1-edge) may not usable when applied to lower concentration mineral samples.

Chapter 6 progressed this work by utilising multiple U XAS measurements to investigate the nature of U in a U-bearing natural calciopyrochlore (MacDonald Mine, Ontario, Canada), a mineral analogue to synthetic U titanate pyrochlores that have previously been considered as ceramic wasteforms for Pu. This included the application of multiple analysis techniques including assessment of E_0 positions, peak fitting by LCF and PCA with ITTFA, and also structural investigation by EXAFS. This study investigated the full extent of what may be achieved using bulk U XAS measurements and analysis methods to characterise a mineral analogue sample. The benefits of using multiple measurements and analyses was also demonstrated, including U M_4-edge M_β HERFD XAS to directly investigate U speciation, U L_3-edge EXAFS to probe short range order, and U L_3-edge transmission and $L_{\alpha 1}$ HERFD XANES data to estimate net U oxidation state. All findings were supported by bulk XRD and SEM/EDX data and, overall, the results provide a clear demonstration of the efficacy of XAS when applied to U speciation determination.

8.2. Capabilities of spatially-resolved X-ray techniques

In Chapter 5, the techniques available at a microprobe beamline were utilised to examine the U environment in a metamict U- and Ti-rich mineral from Crocker's Well, South Australia, which is likely to be an altered brannerite. This work demonstrates what characterisation can be achieved using spatially resolved X-ray techniques. The U oxidation state and the short-range structure were successfully determined by analysis of μXANES and μEXAFS. Hydrothermal alteration within the sample was examined using μXRF element maps, and other phases in the sample were characterised by μXRF element maps and μXRD analysis. However, the lack of quantitative compositional data and long-range structure data, due to the metamict nature of the sample, prevented the confirmation of the original composition and structure (brannerite) of the sample.

8.3. Capabilities of laboratory X-ray spectrometers to investigate wasteforms

Chapter 4 compared U L_3-edge transmission XANES data collected from U reference compounds on a laboratory spectrometer and at a beamline. The two data sets showed excellent agreement, demonstrating that U L_3-edge XANES data collected on a laboratory instrument was, like U L_3-edge XANES data measured on a beamline, sensitive to variations in U oxidation state and coordination, and therefore could be used to characterise U in concentrate samples. The first paper presented in Chapter 7, '*A Feasibility Investigation of Laboratory Based X-ray Absorption Spectroscopy in Support of Nuclear Waste Management*' advances this work by applying laboratory XAS to investigate two examples of synthetic potential actinide wasteforms: a Ce-doped zirconolite ($Ca_{0.75}Ce_{0.25}ZrTi_{1.5}Al_{0.5}O_7$) and a brannerite glass-ceramic (50 wt% UTi_2O_6 50 wt% $Na_2AlBSi_2O_6$), in conjunction with some Ce and U reference compounds. These samples contained representative concentrations of Ce and U, and the successful measurement and characterisation of Ce L_3-edge and U L_3-edge XANES data. The Ce in the zirconolite sample, which was used as a surrogate of Pu, was analysed by LCF to determine the presence of a mixed oxidation state with a Ce^{3+}:Ce^{4+} ratio of 57:43. The U within the brannerite glass-ceramic was determined to have a net U oxidation

state of 4.2+ by analysis of the U L_3-edge E_0 position. In addition, work was undertaken to improve the accuracy of XAS data measured on this type of instrument by the introduction of a leakage correction measurement and calculation.

In the remaining papers presented in Chapter 7: *'Laboratory Based X-ray Absorption Spectroscopy of Iron'* and '*A feasibility investigation of speciation by Fe K edge XANES using a laboratory X-ray absorption spectrometer',* the potential to characterise Fe using a laboratory spectrometer was established. The first Fe K-edge paper demonstrated that it was possible to collect Fe K-edge XANES on a laboratory instrument which were in good agreement with data collected on a beamline, and sensitive enough to have distinguishable pre-edge features which could be analysed to determine Fe oxidation state and coordination. It was also shown that the difference between the results from data analysis on laboratory instruments and synchrotrons was similar to the difference between two sets of synchrotron data. The second Fe K-edge paper expanded on this work by utilising Fe K-edge XANES to investigate the oxidation state and coordination of Fe in iron phosphate glasses, an example of a potential glass wasteform. This study demonstrated that it was possible to collect Fe XANES from glass material which contains concentrations of Fe representative of potential wasteforms.

This work has established the capability of laboratory spectrometers characterise U, Ce and Fe in both concentrate reference compounds and in samples relevant to wasteforms for nuclear waste disposal.

8.4. U speciation in U- and Ti-bearing mineral analogues and implications for synthetic U titanates

In Chapter 5, analysis of the calciopyrochlore sample found that it contained U speciated as U^{4+}, U^{5+} and U^{6+}, with U^{5+} as a major fraction of U speciation. As already discussed, this is the first known direct characterisation of a U^{5+} containing mineral. Analysis of U M_4-edge M_β HERFD XANES data determined the relative concentration of each U oxidation state, this was supported by analysis of U L_3- edge transmission and U L_3-edge $L_{\alpha 1}$ HERFD XANES which showed the presence of U oxidation states higher than U^{4+}. Furthermore, analysis of the U L_3-

edge transmission EXAFS data which produced estimates of U-O bond distances consistent with U^{5+} speciation. The U^{5+} present in the sample was also determined to have been present since mineral formation, rather than having occurred as a product of alteration or caused by the reduction of radiogenic Pb. This suggests that U^{5+} is more stable than previously assumed, and that the occurrence of U^{5+} within a synthetic U titanate pyrochlore wasteform would not be detrimental to the ability of a wasteform to immobilise U over the timescales required for geological disposal.

In Chapter 6, the investigation of the U- and Ti -bearing metamict, altered mineral phase thought to be brannerite, used spatially resolved X-ray techniques to show the majority of U was speciated as U^{6+} uranyl. Analysis of the edge position and LCF both gave estimates of net U oxidation state between 5.5+ and 5.7+, evidencing the presence of some U^{6+} within the sample, with observational and LCF analysis of the U L_3-edge μXANES region also indicating uranyl speciation. Fitting of the μEXAFS region determined the majority of U in the U-rich phase as U^{6+} uranyl, with weightings of U^{6+} uranyl paths of 0.77 - 0.80. Re-examination of previous literature produced evidence for a previous example of uranyl speciation in an altered brannerite sample, and of a mechanism by which this oxidation could have occurred, which were consistent with the observations from the Crocker's Well sample. The alteration undergone by the sample can be attributed to a known geological event at that locality which involved aqueous solutions at temperatures much higher than those that a wasteform would experience in a GDF. Therefore, if the U-rich phase is confirmed as brannerite, these findings would demonstrate its suitability as a potential actinide wasteform from the point of view of dissolution.

Chapters 5 and 6 provided important insight into the alteration, and mobility, of U in these analogue minerals over their lifetimes. The ability of both analogues to retain U and to resist alteration within the specified conditions of a GDF are encouraging and supportive of the candidacy of U titanate pyrochlores and brannerites as potential wasteforms.

9. Future Work

9.1. Further evaluation of U XAS

Analysis of the E_0 position from the first peak in the first derivative of U L_1-edge data was found to be an excellent technique to estimate net U oxidation state. The full extent of the information that can be gained from the U L_1-edge should be investigated further, including a similar study to the work shown here with U L_1-edge EXAFS and U L_1-edge $L_{\alpha1}$ HERFD XAS data. A further study should be undertaken with lower U concentration reference compounds, which are analogous to environmental samples, to see if the results of the utility of the U L_1-edge to diagnose net oxidation state may be readily transposed to a wider range of samples (expanding its impact to new areas of research, such as environmental science).

To further probe the capabilities of estimating U oxidation state using edge position, or other analysis techniques such as LCF or PCA with ITTFA, it would be beneficial to undertake a series of experiments where XAS data are collected from a set of mixtures of U reference compounds with different oxidation states, and compare known net U oxidation states to estimates by different analysis techniques.

9.2. Mineral dating and recrystallisation

The age of *other* minerals from the localities of both U titanate minerals investigated in Chapters 5 and 6 is known; however, the exact minerals investigated in this Thesis have not been determined. It would be beneficial to confirm directly the ages of both samples, for example by U-Pb dating using a laser ablation inductively coupled plasma mass spectrometer (LA-ICP-MS).

Since both mineral samples are metamict, another avenue of investigation would be recrystallisation by thermal treatment and subsequent characterisation to further understand the nature of alteration. Although, if the composition of the sample has been sufficiently changed, it may not be possible to recrystallise the sample back to the original structure. These experiments may enable the investigation of the original structure. Thermogravimetric

analysis (TGA) and differential thermal analysis (DTA) could be collected while the sample is undergoing heat treatment, or XRD data could be collected at intermittent temperatures during heating, to probe the recrystallisation process. These heat-treated samples could then be characterised by pXRD (to determine the structure and confirm if recrystallisation has occurred), bulk U L_3-edge XANES (to investigate the net U speciation present), and U M_4-edge HERFD XANES to investigate the relative amount of each U species present.

9.3. Spatially-resolved investigation of natural calciopyrochlore minerals

The calciopyrochlore mineral (MacDonald Mine, Ontario, Canada), which is the subject of Chapter 5, presented a clear altered region, which spatially resolved XAS techniques are ideally suited to investigate. Indeed, µXRF, µXRD and µXANES data were collected from the sample during the course of this Thesis; however, limitations on time (due to Covid-19) did not allow a detailed investigation. Ideally, µEXAFS data would be collected to investigate any variation in short-range structure in the altered and non-altered regions. The initial investigations already performed are detailed in Appendix I.

9.4. Compositional analysis of Crocker's Well sample

The composition of the Crocker's Well sample could be quantitatively investigated by EDX, EPMA or LA-ICP-MS measurement, enabling the conclusive determination of the composition, i.e., confirming whether or not the sample is indeed a metamict brannerite. The variation of U oxidation state within the sample could be further investigated by attempting oxidation state mapping through the use of µXANES, to provide further insight into the extent of alteration. This was not possible during the course of the Thesis, since the sample is at the NSLS-II facility and cannot be returned.

9.5. Expand applications of Laboratory XAS for nuclear applications

Further work to obtain laboratory-derived XAS data from different materials that are relevant to radioactive waste disposal should continue, to expand the confidence in the measurement of the Fe K, Ce L_3 and U L_3-edge data, and also increase the number of feasible elements that can be measured. Moreover, the limitations for lab U L_3-edge XANES and Ce L_3-edge XANES should be probed further by measuring lower concentration samples. This could include exploring the potential of lab U L_3-edge XANES as a tool for characterising environmental U samples, e.g. from land contaminated by U.

The initial Fe K-edge study using Fe reference compounds could benefit from being supported by a more extensive study where Fe K-edge data is collected from a much broader set of reference compounds that contain multiple examples of different combinations of Fe oxidation state and coordination.

One edge to target would be the Ti K-edge that was measured by several of the investigations of U speciation in synthetic U titanate materials discussed in Chapter 2. This would help to support the findings from analysis of the U L_3-edge. Analysis of the U L_1-edge was identified in Chapter 4 as a promising technique to investigate U oxidation state; however, thus far, no attempts have been made to measure U L_1-edge XAS data on a laboratory instrument. Whether this is feasible or practical could be investigated.

9.6. Further investigation of U in synthetic and mineral U titanates

As highlighted in Chapter 2, thus far there has been limited investigation into U speciation, U environmental mobility, and alteration history within mineral analogues to inform the design of synthetic U titanates. The characterisation of mineral analogues in Chapters 5 and 6 is the first step towards developing an understanding of how mineral analogues inform the design of synthetic wasteforms. As demonstrated in this Thesis, XAS techniques could support the development of a database of mineral analogues, including information about U environment by XAS, as well as sample composition and age. Such a database could be supported by development of synthetic versions of the estimated original mineral compositions, subjected to radiation damage and dissolution. Such an approach could inform our understanding of

the mineral analogue compositions, their alteration and metamictisation. Some initial work has been undertaken throughout the course of this Thesis, by measuring other mineral samples at microprobe beamlines (see Appendix II for data), and also by attempting the synthesis of betafites targeting U^{5+} speciation. It was not possible to complete the latter work due to covid-19 induced laboratory closures.

10. Appendix I

Initial analysis of spatially resolved X-ray measurements from calciopyrochlore, MacDonald Mine, Ontario, Canada. µXRF mapping informed the selection of points for U L_3-edge µXANES from the bulk, altered region and rim of a U containing calciopyrochlore ((Ca,U)(Nb,Ti)O_7) grain (MacDonald Mine, Ontario, Canada), where the altered region contained less U than the bulk, and U hotspots. The µXANES data were found to clearly show an increase in in net U speciation (positive shift in edge position) from the bulk (points A-C) to the altered region and rim (points D-J).

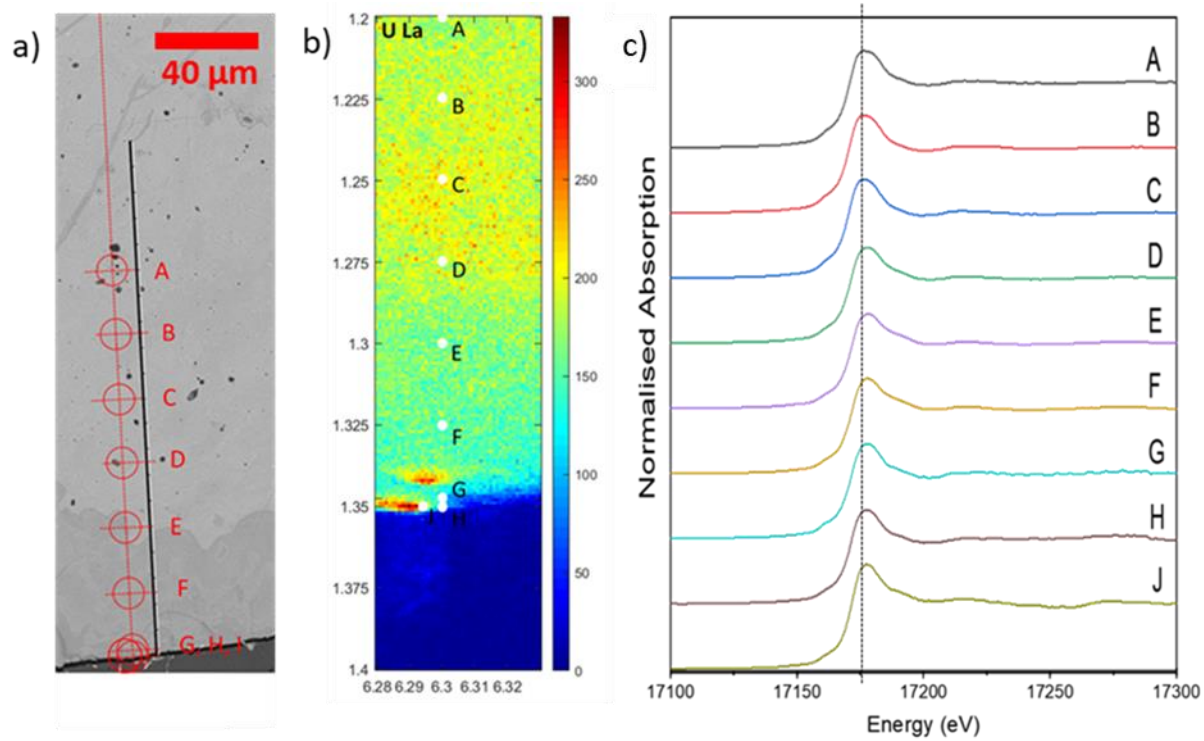

Figure 10.1. (a) SEM image of calciopyrochlore grain (MacDonald Mine, Ontario, Canada), with spots A-J indicated, **(b)** µXRF map of U Lα intensity, collected at 18100 eV, with spots A-J indicated. **(c)** U L_3-edge µXANES data collected from spots A-J. µXRF and µXANES data presented in this figure were collected at the microXAS beamline, Swiss Light Source (SLS), Paul Scherrer Institute (PSI), Switzerland.

11. Appendix II

A highly altered U and Ti rich mineral, thought to have the pyrochlore structure, from Beryl Hill, Upper Gascoyne Shire, Australia has been investigated using µXRF, µXANES and µEXAFS. Initial observations from µXRF data found varying relative concentrations of Pb and U in a crack feature (Figure 11.1a). Points (1-3) were selected for U L_3-edge µXANES (Figure 11.1b) to investigate U speciation across this feature. It was found that a shift in edge positon occurred between Points 1, 2 and 3 in addition to a clear difference in peak intensity and features past the white line (17180 - 17200eV) between the µXANES spectrum acquired at point 1 and the spectra acquired at points 2 and 3. To further investigate the variation in speciation and short range structure at these points, µEXAFS data were also collected from points 1-3 (Figure 11.1c and 11.1d). The µEXAFS data showed a distinct difference between the U environments at all three points. It was not possible to complete the analysis of data presented in these examples within the timeframe of this PhD. µXRD was also used to confirm that the U-rich phase was amorphous at all the points selected for µXANES and µEXAFS, which will inform the analysis of the data collected.

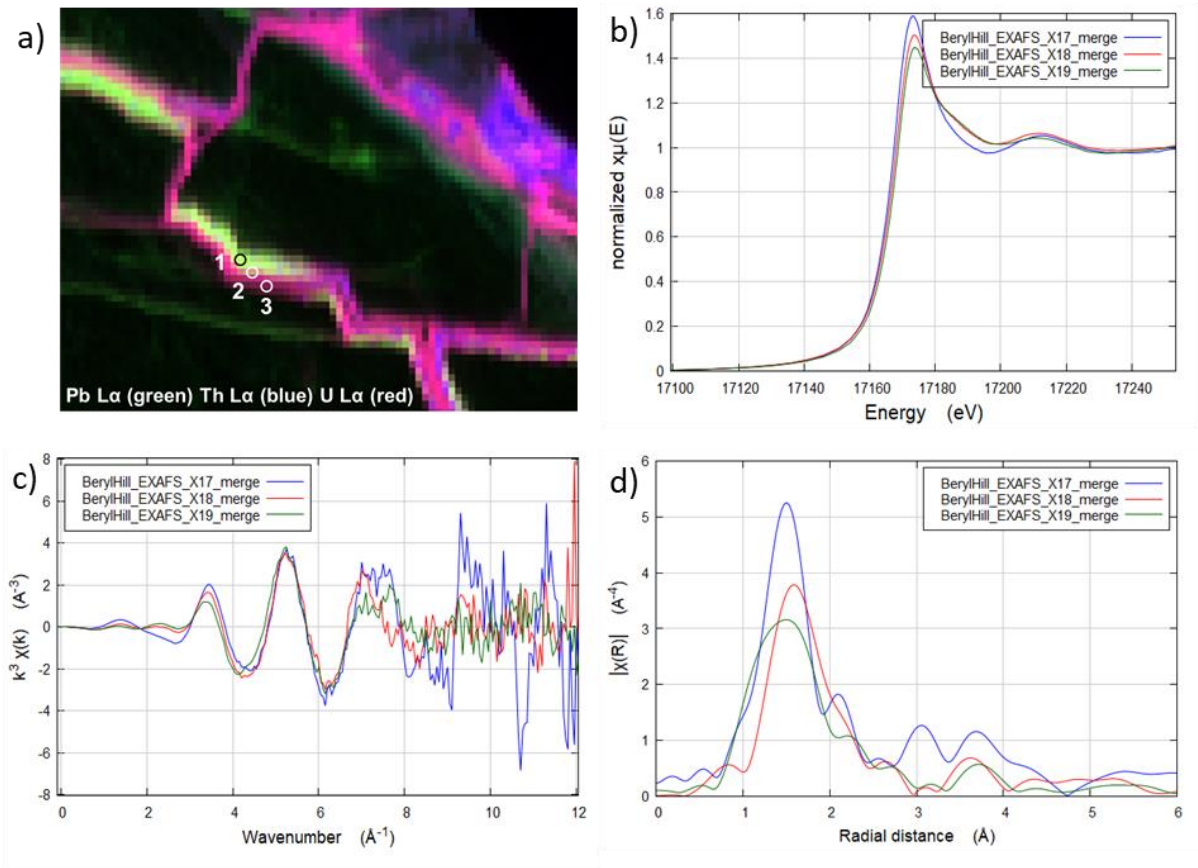

Figure 11.1. (a) Combined μXRF maps from Pb Lα (green), Th Lα (blue) and U Lα (red) with points 1-3 indicated. **(b)** U L_3-edge μXANES collected from points 1-3. **(c)** U L_3-edge μEXAFS spectra from points 1-3 C presented as k^3 μEXAFS data **(d)** U L_3-edge μEXAFS spectra presented as the magnitude of the respective Fourier transform. Data were collected at the X-ray Fluorescence Microprobe (XFM) beamline, National Synchrotron Light Source-II (NSLS-II), Brookhaven National Lab (BNL), USA.